

UNIVERSITY OF SPLIT
FACULTY OF ELECTRICAL ENGINEERING, MECHANICAL
ENGINEERING AND NAVAL ARCHITECTURE

Boris Delipetar

**DEVELOPMENT OF MICROSTRUCTURED SUBSTRATES
FOR MECHANOTAXIS AND ELECTROTAXIS OF PRIMARY
AUDITORY NEURONS**

DOCTORAL THESIS

Split, 2026

The doctoral thesis was prepared within the postgraduate university doctoral study programme in Mechanical Engineering at the Faculty of Electrical Engineering, Mechanical Engineering and Naval Architecture, University of Split. The research was carried out at the University of Split, and the Department of Physics, Faculty of Science, University of Split, with support from the Croatian Science Foundation “Young Researchers’ Career Development Project – Training New Doctoral Students” (ESF-DOK-2018-01) and the STIM-REI project (KK.01.1.1.01.0003).

Supervisors: Prof. Emeritus Frano Barbir, PhD, FESB, University of Split, Croatia and Associate Professor Damir Kovačić, PhD, Faculty of Science, University of Split, Croatia

Doctoral thesis number:

BIBLIOGRAPHIC INFORMATION

Keywords (ključne riječi): primary auditory neurons, neuroanatomical gap, microstructured substrates, surface characterization, mechanotaxis, electrotaxis, extracellular electrophysiology (primarni auditorni neuroni; neuroanatomska šupljina; mikrostrukturirani supstrati; karakterizacija površine; mehanotaksija, elektrotaksija, izvanstanična elektrofiziologija)

Scientific area (Znanstveno područje): Technical sciences (Tehničke znanosti)

Scientific field (Znanstveno polje): Mechanical engineering (Strojarstvo)

Scientific branch (Znanstvena grana): Production engineering (Proizvodno strojarstvo)

Institution of PhD completion: University of Split, Faculty of Electrical Engineering, Mechanical Engineering and Naval Architecture

Supervisors of the thesis: Prof. Emeritus Frano Barbir, PhD and Associate Professor Damir Kovačić, PhD

Number of pages: 191

Number of figures: 102

Number of tables: 20

Number of references: 98

Committee for assessment of doctoral thesis:

1. Professor Sonja Jozić, PhD, University of Split, FESB
2. Professor Dražen Bajić, PhD, University of Split, FESB
3. Professor Antonio Šarolić, PhD, University of Split, FESB
4. Professor Saša Zelenika, PhD, University of Rijeka, RITEH
5. Assistant Professor Jure Krolo, PhD, University of Split, FESB

Committee for defence of doctoral thesis:

1. Xxxx. dr. sc. Xxxx Yyyyy, Institution name and City/Town
2. Xxxx. dr. sc. Xxxx Yyyyy, Institution name and City/Town
3. Xxxx. dr. sc. Xxxx Yyyyy, Institution name and City/Town
4. Xxxx. dr. sc. Xxxx Yyyyy, Institution name and City/Town
5. Xxxx. dr. sc. Xxxx Yyyyy, Institution name and City/Town

Development of microstructured substrates for mechanotaxis and electrotaxis of primary auditory neurons

Abstract

This doctoral thesis investigates the development of microstructured substrates and a neuroelectronic interface for in vitro studies of primary auditory neurons. The work is motivated by the neuroanatomical gap between cochlear implant electrodes and target neurons, which limits the precision and efficiency of electrical stimulation. The central hypothesis is that microstructured substrates, through mechanotaxis and electrotaxis, can support neuronal growth and directed organization while preserving electrophysiological function.

The study includes the design and characterization of three-dimensional MEA-based substrates, development of a neuroelectronic interface for extracellular recording and stimulation, and implementation of a magnetic field stimulator for inducing an electric field. Experiments were performed on dissociated spiral ganglion neurons isolated from rat pups under four conditions: glass without stimulation, chip without stimulation, glass with electric field stimulation, and chip with electric field stimulation. Morphometric analyses included soma area, neurite length, and neurite alignment, while electrophysiological analysis covered spontaneous activity.

The results show that substrate microtopography produces a strong mechanotactic effect, particularly by promoting neurite elongation and alignment, whereas the electric field has a weaker modulatory influence. The developed interface also enabled extracellular detection of spontaneous activity, supporting its value as a platform for studying neuron–electrode interactions.

Keywords:

primary auditory neurons, neuroanatomical gap, microstructured substrates, surface characterization, mechanotaxis, electrotaxis, extracellular electrophysiology

Razvoj mikrostrukturiranih supstrata za mehanotaksiju i elektrotaksiju primarnih auditornih neurona

Sažetak

Ova doktorska disertacija bavi se razvojem mikrostrukturiranih supstrata i neuroelektroničkog sučelja za in vitro ispitivanje primarnih auditornih neurona, s posebnim naglaskom na mehanizme mehanotaksije i elektrotaksije kao mogućim pristupima smanjenju neuroanatomske šupljine između neurona i elektroda u umjetnim pužnicama. Polazište rada jest hipoteza da supstrati prilagođene mikrotopografije, uz djelovanje vanjskog električnog polja, mogu potaknuti rast, produljenje i usmjeravanje neurita uz očuvanje elektrofiziološke aktivnosti neurona.

U radu su razvijeni i opisani mikroelektrodni supstrati s trodimenzionalnom mikrotopografijom integrirani u neuroelektroničko sučelje za ekstracelularno snimanje i stimulaciju te sustav za induciranje električnog polja promjenjivim magnetskim poljem. Na kulturama neurona spiralnih ganglija štakora provedena je karakterizacija kvalitete i uniformnosti supstrata, morfometrijska analiza površine some, duljine i poravnanja neurita te elektrofiziološka analiza spontane aktivnosti uz demonstraciju evocirane aktivnosti. Uspoređeni su učinci glatke kontrolne staklene podloge i mikrostrukturiranog čipa, sa i bez stimulacije električnim poljem.

Rezultati pokazuju da mikrotopografija supstrata ima snažan i dosljedan učinak na morfologiju neurona, osobito na produljenje i poravnanje neurita, dok je učinak električnog polja manje izražen. Dodatno, potvrđena je sposobnost neurona za generiranje spontanih električnih aktivnosti na neuroelektroničkom sučelju u uvjetima mehanotaksije. Dobiveni rezultati potvrđuju potencijal mikrostrukturiranih MEA supstrata kao eksperimentalne platforme za proučavanje interakcije neurona i elektroda te kao polazišta za budući razvoj naprednijih neuroelektroničkih sustava s ciljem poboljšanja umjetnih pužnica.

Ključne riječi:

primarni auditorni neuroni, neuroanatomska šupljina, mikrostrukturirani supstrati, karakterizacija površine, mehanotaksija, elektrotaksija, ekstracelularna elektrofiziologija

Acknowledgments

Contents

1	INTRODUCTION.....	1
1.1	Subject of research.....	1
1.1.1	Hearing impairment.....	1
1.1.2	Auditory system.....	3
1.1.3	Hearing prosthetics.....	16
1.1.4	Limitations and strategies for advancement.....	21
1.2	Hypothesis.....	26
1.3	Research methodology.....	26
1.4	Scientific contribution.....	29
1.5	Structure of the dissertation.....	29
2	LITERATURE REVIEW.....	31
2.1	Mechanotaxis.....	31
2.2	Electrotaxis.....	34
2.3	Electrophysiological recording methods.....	36
2.4	Literature review: summary.....	40
3	EXPERIMENTAL INTERFACE DESIGN.....	42
3.1	Microelectrode array substrate.....	43
3.2	Neuroelectronic interface.....	45
3.3	Magnetic field stimulator.....	50
4	EXPERIMENTAL METHODS.....	54
4.1	Sample preparation.....	54
4.1.1	Experimental animals and cochlear tissue dissection.....	55
4.1.2	Spiral ganglion neurons dissociation and culture medium.....	55
4.1.3	Cell seeding and culture maintenance.....	56
4.1.4	Fixation, immunostaining and imaging.....	56
4.2	Magnetic field stimulator experiment.....	57
4.2.1	Magnetic field stimulator: stimulation protocol.....	58
4.2.2	Morphometrics and image processing.....	59
4.2.3	Statistical methods and data processing.....	62
4.3	Neuroelectronic interface experiment.....	66
4.3.1	Validation of mechanotaxis on microelectrode array substrates.....	67
4.3.2	Acquisition and stimulation of extracellular neuronal activity.....	68
4.3.3	Postprocessing in a MATLAB application.....	70

5	SUBSTRATE CHARACTERIZATION.....	73
5.1	Quantitative analysis of chip composition.....	74
5.2	Chip coverage with culture medium.....	79
5.3	Summary.....	85
6	INDIVIDUAL AND COMBINED EFFECTS OF MECHANOTAXIS AND ELECTROTAXIS ON MICROSTRUCTURED SUBSTRATES.....	87
6.1	Mechanotaxis on microstructured substrates.....	87
6.1.1	Soma area.....	89
6.1.2	Neurite length.....	92
6.1.3	Neurite alignment.....	95
6.1.4	Summary.....	98
6.2	Electrotaxis on glass substrates.....	99
6.2.1	Soma area.....	101
6.2.2	Neurite length.....	103
6.2.3	Neurite alignment.....	105
6.2.4	Summary.....	108
6.3	Mechanotaxis and electrotaxis: combined effect.....	109
6.3.1	Soma area.....	110
6.3.2	Neurite length.....	117
6.3.3	Neurite alignment.....	125
6.3.4	Summary.....	132
6.4	Discussion and summary.....	133
7	EXTRACELLULAR RECORDING WITH NEUROELECTRONIC INTERFACE.....	136
7.1	Validation of mechanotaxis on microelectrode array.....	137
7.1.1	The effect of mechanotaxis on neurite length on microelectrode array.....	139
7.1.2	The effect of mechanotaxis on neurite alignment on microelectrode array.....	141
7.2	Recording of spontaneous neurophysiological activity from a single source.....	144
7.3	Recording of spontaneous neurophysiological activity from different independent sources ...	149
7.4	Recording of evoked neurophysiological activity.....	156
7.5	Discussion and summary.....	157
8	SCIENTIFIC CONTRIBUTION.....	161
9	CONCLUSION.....	162
	REFERENCES.....	165

List of tables

Table 3.1 Fabrication parameters of the chip carrier PCB.....	48
Table 3.2 Wire bonding process parameters for the chip carrier	48
Table 4.1 Experimental groups used in the MFS mechanotaxis and electrotaxis experiments	58
Table 4.2 Measurement plan for mechanotaxis parameters for the NEI experiment	67
Table 5.1 EDS sampling plan (empty chip).....	75
Table 5.2 SEM/EDS acquisition settings (empty chip)	75
Table 5.3 Atomic percentage for empty chip (D1–Z4–P2)	76
Table 5.4 Ti_index per chip and zone on empty chip.....	77
Table 5.5 Two-factor ANOVA with replication for Ti_index on empty chip.....	78
Table 5.6 Data acquisition plan for NB-A coverage assessment.....	79
Table 5.7 EDS acquisition settings for NB-A coverage assessment	79
Table 5.8 Atomic percentage for covered chip (Z3-V5).....	80
Table 5.9 NaCl_index per chip (Ch1–Ch4) and zone (Z1–Z4)	83
Table 5.10 Two-factor ANOVA with replication for NaCl_index.....	84
Table 7.1 Descriptive statistics of neurite length across 4 zones for S1-S5	139
Table 7.2 Two-factor ANOVA test: Neurite length	141
Table 7.3 Descriptive statistics of NA across 4 zones for S1-S5.....	142
Table 7.4 Two-factor ANOVA test: Biaxial index of neural alignment.....	143
Table 7.5 Single signal source (S4-Z3): detection parameter settings.....	144
Table 7.6 Multiple signal sources (S3-Z4-D19/22): detection parameter settings	149

List of figures

Figure 1.1 Anatomical structure of the ear	5
Figure 1.2 Main parts of the inner ear.....	6
Figure 1.3 Cross-sectional view of the cochlea	7
Figure 1.4 Organ of Corti.....	7
Figure 1.5 Depolarization of sensory cells	8
Figure 1.6 Image of stereocilia acquired with SEM	9
Figure 1.7 Schematic overview of auditory mechanotransduction.....	9
Figure 1.8 Schematic representation of a neuron.....	10
Figure 1.9 Action potential segments	13
Figure 1.10 Mechanism of signal propagation along the axon.....	15
Figure 1.11 Overview of the historical development of the cochlear implants	17
Figure 1.12 Model of implanted cochlear implant.....	18
Figure 1.13 Internal and external signal processing components	19
Figure 1.14 Waveform and extracted envelope of a speech signal.....	20
Figure 1.15 Amplitude modulated pulse train	20
Figure 1.16 Probe-assisted electrode insertion	21
Figure 1.17 EABR with respect to electrode position	22
Figure 1.18 Relationship between NAG and neuronal excitability	23
Figure 1.19 X-ray of a section of an implant with electrodes in the cochlea	23
Figure 1.20 Relationship between electrode width, impedance and RMS	24
Figure 2.1 Neurite orientation and elongation of rat embryonic hippocampal neurons on square micropillar arrays with different spacings	33
Figure 2.2 Finite element analysis of current-density and voltage-gradient distributions in DC and charge-balanced biphasic pulsed electric fields	36
Figure 2.3 Electrophysiological recording methods	37
Figure 2.4 Superimposed fluorescence image and electrical footprint of the same neuron at DIV 14, 17 and 20.....	40
Figure 3.1 Schematic relation between MFS, NEI and MEA as their common substrate.....	42
Figure 3.2 Schematic view of the MEA substrate with: (a) zone layout, (b) electrode top view and (c) electrode cross-section.....	44

Figure 3.3 Structure and composition of the chip: (a) SEM image of the chip surface (b) EDS image of the chip surface	45
Figure 3.4 Schematic view of the NEI.....	46
Figure 3.5 Two-level PCB architecture: (a) KiCad layout of the connector PCB (b) KiCad layout of the chip carrier PCB (c) Connector PCB (left) and chip carrier PCB (right).....	47
Figure 3.6 Chip carrier PCB before (a) and after (b) epoxy coating and attachment of the glass ring	49
Figure 3.7 Fully assembled experimental setup for NEI/MEA combination	50
Figure 3.8 Schematic representation of the relationship between the position of the MEA and the MFS coil.....	50
Figure 3.9 Magnetic field stimulator: main components	53
Figure 4.1 Flow chart of the experiment.....	54
Figure 4.2 Whole-chip composite fluorescence image of SGN cultures on the MEA	57
Figure 4.3 Schematic of the MFS stimulation waveform	59
Figure 4.4 Representative ImageJ morphometric measurements: (a) soma area, (b) neurite length and (c) neurite alignment	61
Figure 4.5 Electrode arrangement per chip zone	69
Figure 4.6 The home page of the MATLAB application interface.....	71
Figure 4.7 Main plot window with basic functions	72
Figure 5.1 SEM view of chip zones with micropillar diameters: (a) zone 1: 1.0 μm (b) zone 2: 1.8 μm (c) zone 3: 2.8 μm (d) zone 4: 4.0 μm	73
Figure 5.2 EDS elemental maps of O (a), Si (b) and Ti (c) for D1-Z4-P2	76
Figure 5.3 View of the chip surface partially covered with NB-A.....	81
Figure 5.4 Sample (Ch1-Z2-V3): (a) SEM view (b) Spectra of Na, Cl, Si and Al.....	82
Figure 5.5 NaCl_index: V3 vs V30 per zone.....	85
Figure 5.6 Δ NaCl_index; V3 vs V30 per zone	85
Figure 6.1 Representative ROI measurements on Glass control: (a) SA (b) NL (c) NA	88
Figure 6.2 Representative ROI measurements on Chip control: (a) SA (b) NL (c) NA.....	89
Figure 6.3 SA (Glass control vs Chip control): (a) Box-and-whisker plot (b) Histogram	90
Figure 6.4 SA: Permutation null distribution of Δ _median (Glass control vs Chip control)	92
Figure 6.5 NL (Glass control vs Chip control): (a) Box-and-whisker plot (b) Histogram	93

Figure 6.6 NL: Permutation null distribution of Δ_{median} (Glass control vs Chip control)	95
Figure 6.7 NA (Glass control vs Chip control): Half-polar plot (0–180°).....	96
Figure 6.8 Biaxial alignment index (AI _{bi}): Glass control vs Chip control.....	97
Figure 6.9 Angle to the nearest substrate axis ($\delta\theta_{\text{ax}}$): Glass control vs Chip control	98
Figure 6.10 Representative ROI measurements on Glass EF: (a) SA (b) NL (c) NA	100
Figure 6.11 SA (Glass control vs Glass EF): (a) Box-and-whisker plot (b) Histogram.....	101
Figure 6.12 SA: Permutation null distribution of Δ_{median} (Glass control vs Glass EF).....	103
Figure 6.13 NL (Glass control vs Glass EF): (a) Box-and-whisker plot (b) Histogram.....	104
Figure 6.14 NL: Permutation null distribution of Δ_{median} (Glass control vs Glass EF).....	105
Figure 6.15 NA (Glass control vs Glass EF): Half-polar plot (0–180°).....	106
Figure 6.16 Circular alignment index (AI _{circ}): Glass control vs Glass EF.....	107
Figure 6.17 Angle to local field tangent ($\delta\theta_{\text{circ}}$): Glass control vs Glass EF	108
Figure 6.18 Representative ROI measurements on Chip EF: (a) SA (b) NL (c) NA	109
Figure 6.19 SA (Glass control vs Chip EF): (a) Box-and-whisker plot (b) Histogram	111
Figure 6.20 SA: Permutation null distribution of Δ_{median} (Glass control vs Chip EF)	112
Figure 6.21 SA (Chip control vs Chip EF): (a) Box-and-whisker plot (b) Histogram	113
Figure 6.22 SA: Permutation null distribution of Δ_{median} (Chip control vs Chip EF)	114
Figure 6.23 SA: Glass EF vs Chip EF: (a) Box-and-whisker plots (b) Histogram.....	116
Figure 6.24 SA: Permutation null distribution of Δ_{median} (Glass EF vs Chip EF).....	117
Figure 6.25 NL (Glass control vs Chip EF): (a) Box-and-whisker plots (b) Histogram	119
Figure 6.26 NL: Permutation null distribution of Δ_{median} (Glass control vs Chip EF).....	120
Figure 6.27 NL (Chip control vs Chip EF): (a) Box-and-whisker plots (b) Histogram	121
Figure 6.28 NL: Permutation null distribution of Δ_{median} (Chip control vs Chip EF).....	122
Figure 6.29 NL (Glass EF vs Chip EF): (a) Box-and-whisker plots (b) Histogram.....	124
Figure 6.30 NL: Permutation null distribution of Δ_{median} (Glass EF vs Chip EF).....	125
Figure 6.31 NA (Glass control vs Chip EF): Half-polar plot (0–180°)	126
Figure 6.32 Circular alignment index (AI _{circ}): Glass control vs Chip EF.....	126
Figure 6.33 Angle to local field tangent ($\delta\theta_{\text{circ}}$): Glass control vs Chip EF.....	127
Figure 6.34 NA (Chip control vs Chip EF): Half-polar plot (0–180°)	128
Figure 6.35 Circular alignment index (AI _{circ}): Chip control vs Chip EF.....	129
Figure 6.36 Angle to local field tangent ($\delta\theta_{\text{circ}}$): Chip control vs Chip EF.....	130

Figure 6.37 NA (Glass EF vs Chip EF): Half-polar plot (0–180°).....	131
Figure 6.38 Circular alignment index (AI_circ) for Glass EF vs Chip EF	131
Figure 6.39 Angle to local field tangent ($\delta\theta_{\text{circ}}$): Glass EF vs Chip EF	132
Figure 7.1 Experimental samples: SGN cultures on MEA substrates	137
Figure 7.2 Cropped examples of ROI-based measurements: (a) Raw image (b) NL measurement (c) NA measurement	138
Figure 7.3 Distribution of neurite length for Zone 1-Zone 4.....	140
Figure 7.4 Distribution of NA for Zone 1-Zone 4	142
Figure 7.5 Single signal source (S4-Z3): cropped view of an electrode array on an MEA substrate with SGN cultures.....	144
Figure 7.6 Single signal source (S4-Z3): search time window	145
Figure 7.7 Single signal source (S4-Z3-D18): amplitude distribution histogram	146
Figure 7.8 Single signal source (S4-Z3-D18): width distribution histogram	147
Figure 7.9 Single signal source (S4-Z3-D18): ISI histogram.....	148
Figure 7.10 Multiple signal sources (S3-Z4-D19/22): cropped view of an electrode array on an MEA substrate with SGN cultures.....	150
Figure 7.11 Multiple signal sources (S3-Z4-D19/22): search time window	150
Figure 7.12 Multiple signal sources (S3-Z4-D19/22): correlogram	151
Figure 7.13 Multiple signal sources (S3-Z4-D19/21): amplitude distribution histogram	152
Figure 7.14 Multiple signal sources (S3-Z4-D19/21): width distribution histogram	153
Figure 7.15 Multiple signal sources (S3-Z4-D19/21): ISI histogram.....	154
Figure 7.16 Bright field view: stimulating and recording electrodes	156
Figure 7.17 Evoked APs (upper graph); Stimulation pulses (lower graph); (a) Evoked AP: magnified (b) Stimulation pulse (magnified).....	157

List of abbreviations, symbols and indices

ANOVA	Analysis of variance
AP	Action potential
at %	Atomic percentage
Chip EF	Cultures on chip stimulated with an electric field
Chn	Chip with NB-A number
CMOS	Complementary metal-oxide semiconductor
CNS	Central nervous system
CoV	Coefficient of variation
CSV	Comma-separated values
df	Degrees of freedom
DIV	Days in vitro
Dn	Empty chip number
EABR	Evoked auditory brainstem responses
EDS	Energy-dispersive X-ray spectroscopy
EF	Electric field
FOV	Field of view
Glass EF	Cultures on glass stimulated with an electric field
GUI	Graphical user interface
IQR	Interquartile range
ISI	Interspike interval
MEA	Microelectrode array
MFS	Magnetic field stimulator
MS	Mean square
NA	Neurite alignment
NaCl_index	Index of the percentage of sodium and chlorine in the surface cover
NAG	Neuroanatomical gap
NB-A	Neurobasal-A-based culture medium

NEI	Neuroelectronic interface
NL	Neurite length
PCB	Printed circuit board
RMP	Resting membrane potential
RMS	Root mean square
ROI	Region of interest
SA	Soma area
SD	Standard deviation
SE	Standard error
SEM	Scanning electron microscope
SGN	Spiral ganglion neurons
Sn	Sample number
SNR	Signal-to-noise ratio
SS	Sum of squares
Ti_index	Index of the percentage of titanium in the surface cover
WD	Working distance
Zn	Zone number

1 INTRODUCTION

1.1 Subject of research

1.1.1 Hearing impairment

Hearing impairment is one of the most common sensory deficits and causes of disability worldwide. According to the World Health Organization, almost 20 % of the world's population, i.e., more than 1.5 billion people, live with some degree of hearing impairment, of which approximately 430 million have a level of impairment that requires some rehabilitation [1]. It is estimated that by 2050 that number will exceed 700 million [1]. Disabling hearing loss is considered any hearing loss in which the pure-tone average threshold is greater than 35 dB in the healthier ear. For comparison, normal hearing is considered a response to threshold frequencies \leq 20 dB [1]. The distribution of hearing impairment in the world population is uneven. Almost 80 % of people with disabling hearing loss live in low- and middle-income countries, while the prevalence increases sharply with age and affects a quarter of the population over 60 [1]. Hearing loss is a significant health problem in pediatric practice as well. It is estimated that 34 million children worldwide have deafness or disabling hearing loss, with almost 60 % of the impairment attributed to preventable causes such as infections, perinatal complications and ototoxic exposures [1].

Apart from hearing problems themselves, hearing impairments cause a wide range of negative consequences for the individual and society. Even moderate unilateral hearing loss in children can slow down the development of speech and language learning resulting in lower academic performance years later [1]. In adults, in addition to communication difficulties, hearing loss is also associated with a less favorable position on the labor market, social withdrawal and even an increased risk of depression and earlier cognitive decline [2]. From a socioeconomic point of view, it is estimated that hearing impairments at the world level indirectly cause almost 1 trillion US dollars in costs through health care costs, reduced productivity and educational support [1]. These data suggest the importance of hearing impairment as an important challenge in public health and the importance of developing effective diagnostic and restorative strategies.

From a clinical perspective, hearing loss is classified on several grounds. According to the location of the lesion, it is divided into conductive, sensorineural, mixed and central. There are differences

between unilateral and bilateral hearing loss, sudden and progressive and stable and fluctuating. Each hearing impairment differs according to the configuration of the audiogram, and according to the degree, they are divided into mild, moderate, moderately severe, severe and profound hearing loss. In the context of this dissertation, the most relevant classification is according to the location of the lesion due to its direct connection with the structural integrity of the cochlea and auditory nerve, which directly affects the design and limitations of auditory prostheses.

Conductive hearing loss is caused by the difficult transmission of sound waves through the structures of the outer or middle ear. The most common causes of this type of damage are cerumen impaction, otitis media with effusion, tympanic membrane perforation, ossicular chain discontinuity or fixation (e.g., otosclerosis) and congenital malformations of the auricle or ear canal [3]. Pure conductive hearing loss is usually at least partially reversible with medical or surgical treatment, and in the event that the cause cannot be removed, conventional hearing aids can often provide a satisfactory level of speech understanding. Although the pathology of conductive impairments is clinically important, the focus of this dissertation leans toward hearing impairments of sensorineural etiology.

Sensorineural hearing loss is caused by damage to the structures of the inner ear (outer and inner hair cells) and/or the auditory nerve and is the most common form of permanent hearing loss in children and adults. The etiology of sensorineural hearing loss varies and includes genetic mutations, exposure to noise, aging (presbycusis), ototoxic drugs, autoimmune diseases of the inner ear, infections or hypoxia [4]. In sensorineural hearing loss, outer hair cell dysfunction reduces selectivity of frequencies and cochlear amplification, while inner hair cell and synaptic damage degrades temporal precision and neural coding of suprathreshold sounds even when audiometric thresholds are relatively preserved. The loss or degeneration of spiral ganglion neurons (SGNs), which represent the primary auditory neurons, impairs signal transmission from the cochlea to the central nervous system (CNS) and is of particular importance for electrical stimulation strategies, such as those used in cochlear implants.

Mixed hearing loss is characterized by the simultaneous presence of conductive hearing loss and sensorineural hearing loss, such as the combination of otitis media with presbycusis [3]. This type of hearing impairment can complicate rehabilitation due to the often simultaneously affected mechanical and neural structures of the auditory system, therefore the optimal treatment often

includes a combination of surgical interventions on the conductive components and the installation of implantable devices for targeting the sensorineural components.

In addition to these three main types of hearing loss, hearing loss caused by damage to the CNS is also distinguished. This type of hearing loss is caused by lesions of the auditory pathways or cortical areas in the brain and can manifest as difficulties in sound localization, temporal processing, or speech comprehension despite near-normal peripheral sensitivity. Such forms of impairment emphasize the importance of considering the entire auditory pathway in the design of neuroelectronic interfaces (NEIs) for stimulation and rehabilitation strategies. Additionally, a part of hearing impairment is attributed to auditory neuropathy spectrum disorder, which is characterized by preserved outer hair cells function with impaired or unsynchronized transmission at the level of inner hair cells, their synapses, or the auditory nerve. These patients may have relatively mild elevation of pure-tone thresholds but disproportionately poor speech perception, especially in noise [5].

The degree of hearing loss is defined based on the pure-tone average in the healthier ear: mild (20–34 dB), moderate (35–49 dB), moderately severe (50–64 dB), severe (65–79 dB) and profound (≥ 80 dB) [1]. Even mild and moderate degrees of loss, which are often under-diagnosed and under-treated, have been shown to significantly impact quality of life, communication and occupational functioning [6].

1.1.2 Auditory system

The main role of the auditory system is to receive sound from the environment, convert it into information understandable to the CNS, and forward this information to specialized parts of the CNS. Sound propagates through space in the form of a longitudinal wave, in which periodic oscillations of particles compress and rarefy the medium (air, water, tissue, solid materials) parallel to the direction of propagation. The basic characteristics of sound as a wave phenomenon include waveform, phase, amplitude, and frequency. The standard equations presented in this chapter are based on formulations reported in [7].

Sound intensity is defined as the power transmitted by a sound wave per unit area perpendicular to that surface. The unit of intensity is W/m^2 . It is expressed by the formula:

$$I = 2\pi^2 v^2 \delta^2 \rho c \quad (1.1)$$

where:

ν – frequency / Hz

δ – amplitude / m

ρ – density of the medium / kg/m³

c – speed of sound through a medium / m/s

Sound loudness is the ratio of the sound intensity I and the reference value of the intensity in the medium I_0 . It is defined by the formula:

$$L = 10 \log_{10} \left(\frac{I}{I_0} \right) \quad (1.2)$$

where:

L – sound level / dB

I – sound intensity / W/m²

I_0 – reference sound intensity / W/m²

The reference value for air I_0 is 1 pW/m². Under constant conditions, the intensity of a sound (expressed in decibels / dB) is proportional to the amplitude of the sound wave, with the perception of loudness being logarithmic. The pitch of a sound is defined by its frequency (expressed in hertz, Hz), with the perception of pitch increasing with increasing frequency. The audible frequency range of a healthy human ear is in the range of 20 Hz to 20 kHz [8].

1.1.2.1 Ear anatomy

Figure 1.1 shows the anatomical structure of the ear, divided into three functional units: the outer, middle, and inner ear.

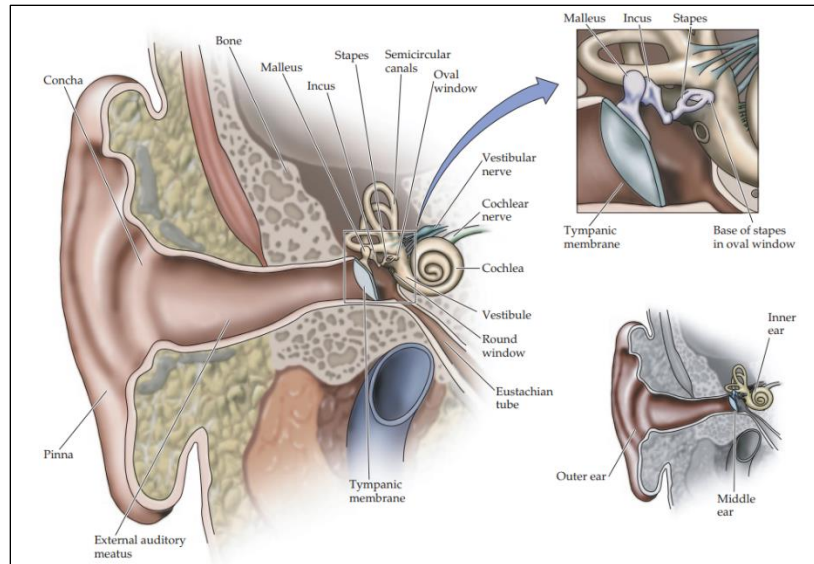


Figure 1.1 Anatomical structure of the ear [7]

A) Outer ear

The basic function of the outer ear is to collect and conduct sound waves from the environment to the middle ear. It consists of the auricle (also called the pinna), the ear opening and the ear canal. The auricle is a cartilaginous structure that, with its shape, partially directs sound waves towards the ear opening. Through the ear opening (lat. *concha*) the sound wave enters the ear canal through which it propagates to the middle ear.

B) Middle ear

The middle ear consists of the tympanic membrane, i.e., the eardrum, three auditory ossicles, and the middle ear muscles. The middle ear system acts as a mechanical amplifier of sound from the environment, transmitting vibrations to the cochlea with minimal energy loss. The main problem in transmitting sound signals from the environment is the attenuation that occurs when sound passes from air to liquid. Since the liquid in the cochlea has a significantly higher acoustic resistance than air, without an intermediate amplifier, more than 99.9 % of the sound wave energy would be attenuated. The described problem is solved by the system of the eardrum and three auditory ossicles. Sound waves reach the eardrum through the outer ear and cause the tensioned membrane to vibrate. The central part of the eardrum is connected to the malleus (lat. *malleus*), one of the auditory ossicles to which the vibration of the membrane is transmitted. The malleus transmits the vibration to the incus (lat. *incus*), and the incus further to the stapes (lat. *stapes*). The

stapes then transmits the vibration to the oval window of the cochlea located on the edge of the inner ear. The middle ear system amplifies all frequencies in the audible range (from 20 Hz to 20 kHz), but the amplification is not uniform for all frequencies. The greatest amplification occurs in the interval from 2 kHz to 5 kHz, which contains many sounds from the natural environment. In addition to mechanical stimuli, damage to the eardrum and auditory ossicles can also be caused by sounds of extremely high intensity. This phenomenon is partially prevented by two middle ear muscles, the tensor tympani and stapedius, which, by tightening the eardrum, reduce the intensity of the vibrations, protecting the structures of the middle ear.

C) Inner ear

The inner ear is the most complex part of the auditory system, connecting the middle ear to the CNS. The main parts of the inner ear are shown in Figure 1.2.

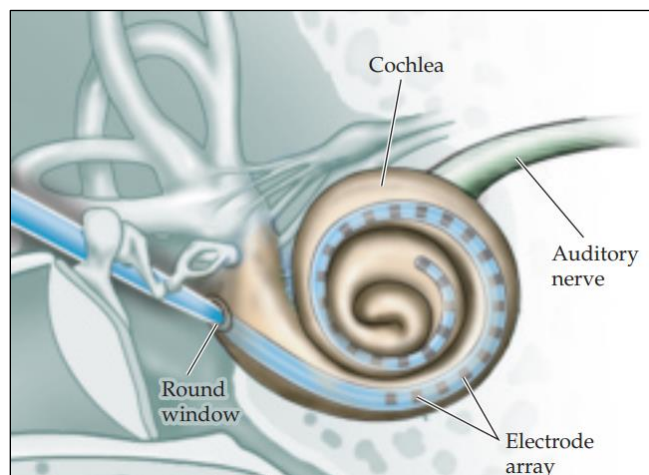


Figure 1.2 Main parts of the inner ear [7]

The main part of the inner ear is the cochlea (lat. *cochlea*). It is spirally twisted approximately two and a half times around its axis and owes its name to its characteristic appearance. The cochlea, by means of a complex mechanism, converts periodic oscillations of sound waves into interpretable electrical nerve signals. The cochlea is approximately circular in cross-section, 10 mm in diameter, and 35 mm in length when stretched. The cochlea consists of two partially separate cavities, the scala vestibuli and the scala tympani, which extend from the basal to the apical part. These cavities are filled with perilymph and are separated by the helicotrema, an opening through which the perilymph passes between the two cavities. The scala media is separated and filled with endolymph. A cross-section of the cochlea is shown in Figure 1.3. The

process of converting vibrations into a nerve signal takes place in the organ of Corti. The vibrations of the perilymph, caused by the action of a sound wave on the oval window via the middle ear system, in the scala media, cause the basilar membrane to vibrate regularly. The basilar membrane is home to hair cells, topped by stereocilia, hair-like structures with their tips resting on the tectorial membrane fixed to the supporting tissue. By moving the basal membrane, the stereocilia make contact with the fixed tectorial membrane. Under the action of shear force, the stereocilia change their orientation, whereby potassium ions, which participate in the process of generating a nerve signal, enter the sensory cells, as shown in Figure 1.4.

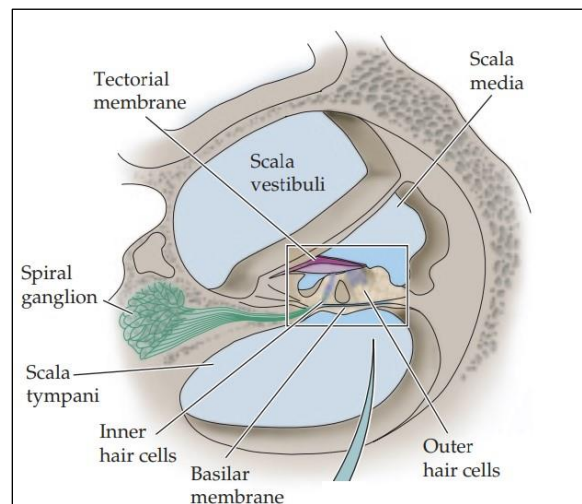


Figure 1.3 Cross-sectional view of the cochlea [7]

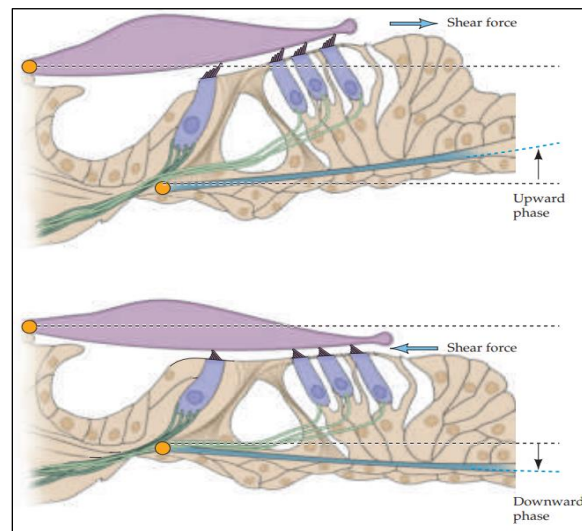


Figure 1.4 Organ of Corti [7]

Figure 1.5 shows a more detailed view of the mechanism. At the tips of bundle-like clusters of approximately 30 stereocilia are ion channels permeable to K^+ ions from the endolymph. As the stereocilia move, due to the vibration of the basilar membrane towards the tallest stereocilium in the bundle, i.e., the kinocilium, potassium channels open and allow ions to enter the sensory cell. The potential in the cytoplasm depolarizes, which causes the opening of Ca^{2+} permeable channels, which cause the release of neurotransmitters from the sensory cell to the bipolar SGN. The SGN conducts the signal by the mechanism of action potential to the central nervous system.

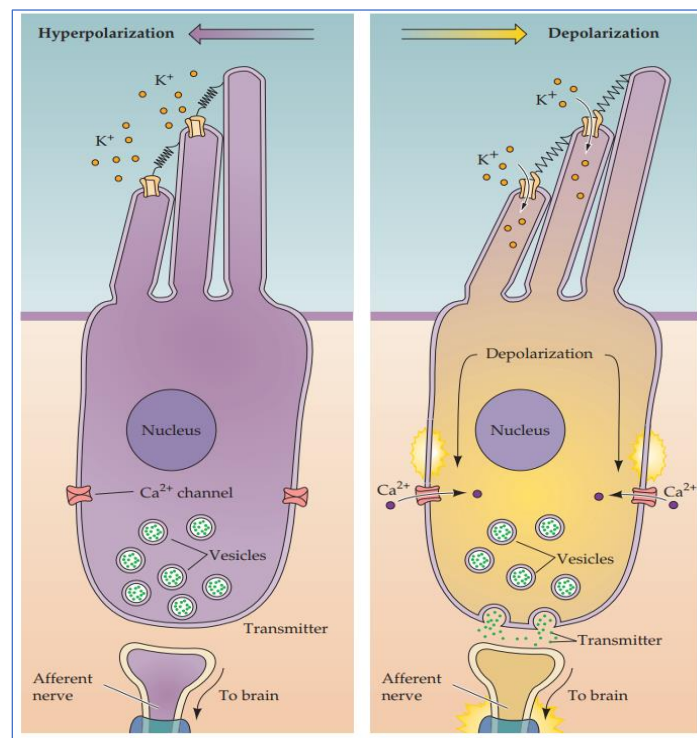


Figure 1.5 Depolarization of sensory cells [7]

Images of stereocilia acquired with a scanning electron microscope (SEM) are shown in Figure 1.6. Moving in the opposite direction towards the smallest stereocilia, the opposite process occurs: ion channels close, which leads to hyperpolarization. The reaction of the system from the entry of sound into the ear to depolarization is approximately 10 ms.

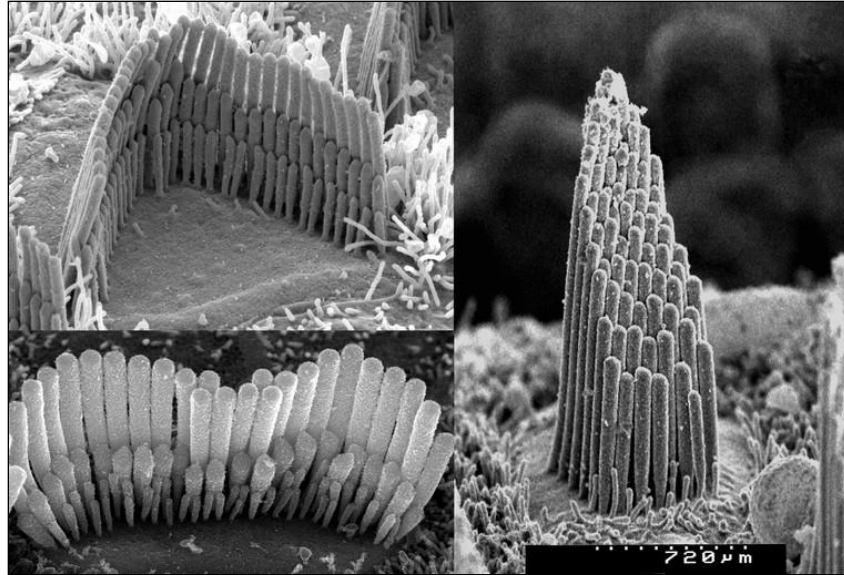


Figure 1.6 Image of stereocilia acquired with SEM [9]

1.1.2.2 Signal transmission in the auditory system

This process of converting mechanical stimuli into electrochemical activity is called mechanotransduction and can be represented in the auditory system in Figure 1.7.

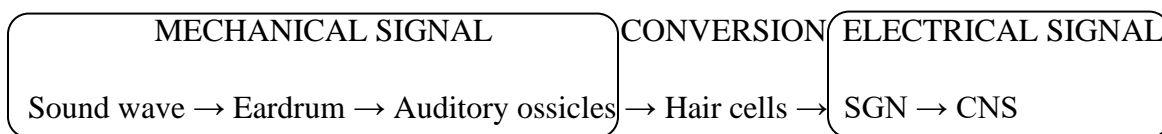


Figure 1.7 Schematic overview of auditory mechanotransduction

The nervous system, according to the common definition, is a specialized system in multicellular organisms that receives and transmits information from the environment and the inside of the body, processes it, and prepares appropriate responses. The basic building blocks of the nervous system are neurons. In the human body, according to some estimates, there are about 86 billion neurons in the brain alone [10]. Their task is to conduct sensory and motor information in the form of electrical signals. The basic building blocks of neurons are the soma and neurites, which are divided into axons and dendrites. The soma is the body of the cell that contains the nucleus. Protein synthesis and other basic processes important for the life of the cell take place in it. The axon is a long shoot that conducts electrical signals, and dendrites are short shoots that receive stimuli from the environment. Most neurons have a single axon and one or more dendrites. According to the number of processes emerging from the soma, they are classified as unipolar, bipolar, tripolar or multipolar neurons. There are also anaxonic neurons in which it is not possible to distinguish

neurites. In addition to the basic units, a neuron also consists of others, which are shown with their corresponding functions in Figure 1.8.

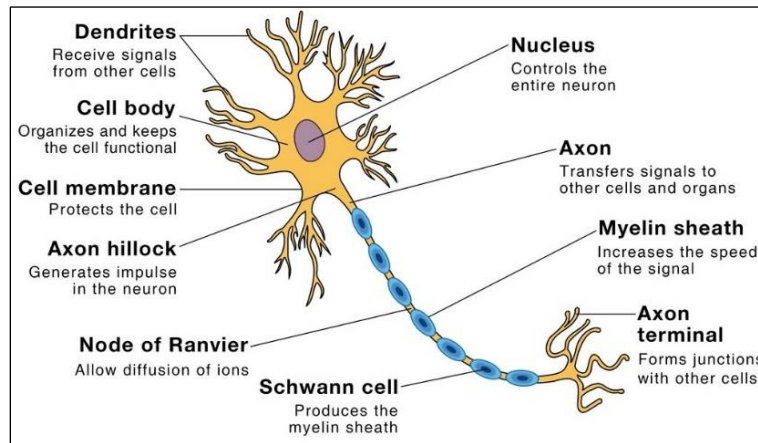


Figure 1.8 Schematic representation of a neuron [11]

According to the organizational principle, the nervous system is divided into central and peripheral. The CNS includes the brain and spinal cord, and the peripheral includes cranial nerves (12 pairs) and spinal neurons nerves (31 pair), which branch out throughout the rest of the body [7]. In the peripheral part, sensory information from the environment is transmitted to the CNS, where the information is analyzed and integrated into motor information that the peripheral system performs.

According to the direction of information flow, the nervous system is divided into afferent and efferent. Afferent (sensory) neurons transmit information from the environment to the CNS, and efferent (motor) neurons receive information from the CNS and perform actions.

Communication between neurons occurs via synapses, narrow gaps between the ends of axons and dendrites. The emitting neuron of an electrical signal at the end of the axon releases neurotransmitters, exciting the neighboring neuron, which continues the signal propagation. Neurons are classified as excitatory or inhibitory with respect to their synaptic effect on postsynaptic activity. Information is transmitted in the nervous system by the mechanism of action potential (AP). AP represents a change in the electrical potential on the membrane in a precisely defined amount that propagates along the axon at a precisely defined speed. The fundamental problem of transmitting information electrically is the length over which it is necessary to preserve the signal due to insufficient passive electrical conductivity of the tissue. The AP mechanism

preserves the signal amplitude along the entire length of the axon, ensuring the stability of information from the periphery to the CNS and vice versa, regardless of the distance of the stimulus site from the CNS. Body fluids, intracellular and extracellular, contain numerous ions, the ratio of which determines the electrical potential at a particular location.

The resting membrane potential (RMP) ranges from -40 mV to -90 mV, depending on the type and function of the neuron. The exact value of the RMP depends on the ratio of ion concentrations inside and outside the cell and is defined by the Nernst equation:

$$E_X = \frac{RT}{zF} \ln \frac{[X]_2}{[X]_1} \quad (1.3)$$

where:

E_x – equilibrium potential / mV

R – gas constant / J mol⁻¹ K⁻¹

T – absolute temperature / K

z – valence of ions

F – Faraday's constant / C mol⁻¹

x_2 – concentration of ions outside the cell / mol/L

x_1 – concentration of ions inside the cell / mol/L

Ion exchanges on the cell membrane take place in two basic ways: ion channels and ion transporters. Ion channels transport ions down a concentration gradient, i.e., from an area of higher to an area of lower concentration. Ion transporters transport ions against the concentration gradient, i.e., from an area of lower to an area of higher concentration. Channels and transporters are usually permeable to only one type of ion. With a larger number of different ions, the RMP is determined by the permeability of the membrane (of ion channels, not ion transporters) for a specific ion. For example, if there are significantly more Na⁺ ions outside the neuron than inside the neuron, then the electric potential inside the cell will be more positive, the greater the permeability to Na⁺, because in this case it enables a greater influx of positive ions into the neuron. For the potassium ion K⁺, whose concentration is significantly higher inside the cell with an increase in membrane

permeability, the RMP will fall due to the outflow (efflux) of positive ions from the neuron. In that case, the RMP is defined by the Goldman equation:

$$V = 58 \text{ mV} \log \frac{P_K [K]_2 + P_{Na} [Na]_2 + P_{Cl} [Cl]_1}{P_K [K]_1 + P_{Na} [Na]_1 + P_{Cl} [Cl]_2} \quad (1.4)$$

P_K , P_{Na} and P_{Cl} denote relative ion permeabilities and are therefore dimensionless, while ion concentrations are expressed in the same concentration unit, e.g., mol/L.

AP occurs when an external stimulus (mechanical, acoustic, thermal or light stimulus, neurotransmitter, etc.) through its indirect action causes an increase in the RMP to a value greater than the AP activation threshold, whereby the neuron switches from passive conduction to active conduction. This creates a signal that propagates along the entire neuron with a constant amplitude. The activation threshold for human neurons is around -50 mV.

Let us consider two cases:

In the first case, a stimulus occurs that causes a spike in potential that does not exceed the activation threshold. In this case, no AP is initiated and no stable information is transmitted. The neuron behaves like a passive conductor (e.g., a metal wire) and the amplitude of such a signal decreases in space according to equation 1.5 which reads:

$$V_x = V_0 e^{-\frac{x}{\lambda}} \quad (1.5)$$

where:

V_0 – electrical potential at the site of stimulation / mV

V_x – electric potential at a distance x from the stimulus site / mV

x – distance from the stimulus location / m

λ – axon length constant / m

The length constant is defined by equation 1.6 which reads:

$$\lambda = \sqrt{\frac{r_m}{r_i + r_e}} \quad (1.6)$$

where:

λ – length constant / m

r_m – membrane resistance per unit length / $\Omega \cdot \text{m}$

r_i – intracellular axial resistance per unit length / Ω/m

r_e – extracellular axial resistance per unit length / Ω/m

The phases of AP are shown in Figure 1.9.

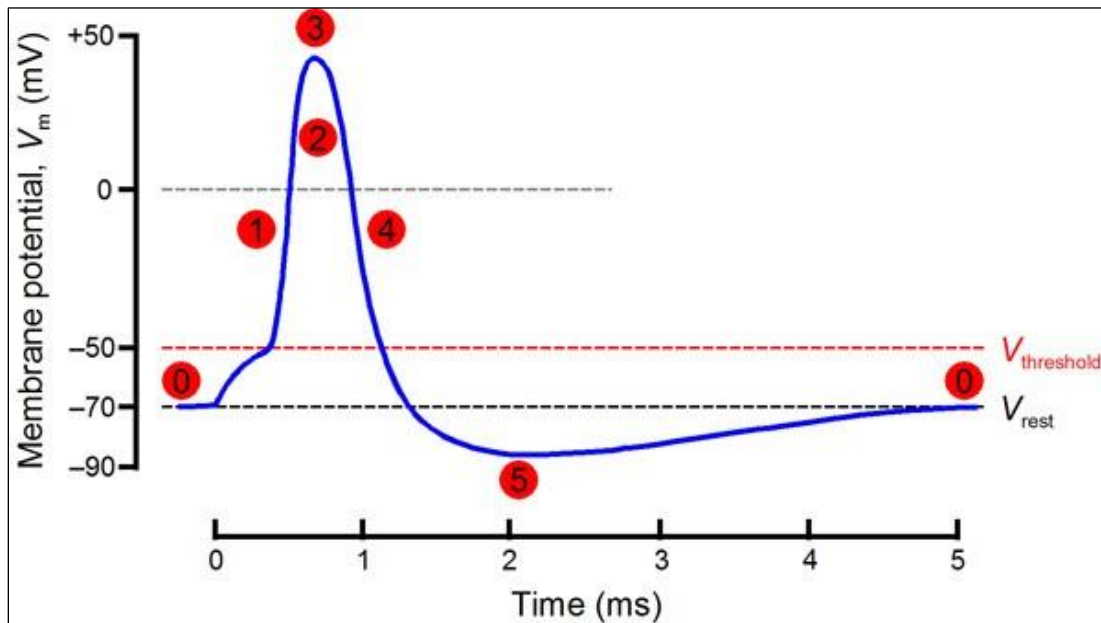


Figure 1.9 Action potential segments [12]

Area 0: Let us assume that the initial RMP of the neuron is -70 mV. When an external stimulus arrives at the neuron membrane, it produces a local graded depolarization of the membrane potential. The membrane potential increases slowly but remains below the activation threshold, so voltage-gated Na^+ channels are not yet activated in the manner required for action potential initiation. At this point, the signal can still only propagate along the axon passively.

Area 1: The intensity of the opening of the ion channels depends on the electrical potential that acts on the structure and arrangement of the building proteins of the channel. When the potential reaches the activation threshold value (in the observed case -50 mV), the ion channels permeable to sodium open significantly, resulting in a sudden influx of a large number of Na^+ ions, which cause rapid depolarization of the neuron.

Area 2 and 3: The influx of Na^+ ions through voltage-gated sodium channels raises the signal amplitude to its maximum value, i.e., peak. As the membrane potential approaches its peak, voltage-gated Na^+ channels become inactivated. At the same time, a significant increase in the potential in the neuron causes the rapid opening of voltage-gated potassium channels, resulting in a sudden efflux of K^+ ions.

Area 4: A sudden efflux of potassium ions causes rapid repolarization, with the potential again taking a negative value.

Area 5: A drop in potential causes potassium ion channels to close, but due to the difference in structure compared to sodium channels, potassium channels close more slowly resulting in repolarization to an amount lower than the initial RMP (undershoot). This segment of the AP signal is called the refractory period. Ion transporters eventually compensate for the resulting difference by slow exchange and return the potential to the initial RMP value.

The propagation of the action potential along the axon is described by the Hodgkin-Huxley model, for which the Nobel Prize in Medicine and Physiology was awarded in 1963. Neuron elements are represented by capacitors (lipid membrane layer), electrical conductivity (ion channels) and voltage (electrochemical gradient) and current (ion transporters) sources.

A simplified mechanism of signal propagation along the axon is shown in Figure 1.10.

At time t_1 , an external stimulus depolarizes the membrane in area A, opening sodium ion channels. Na^+ ions, with their positive charges, passively depolarize the adjacent area B within the neuron to the potential level at which sodium ion channels open in that area.

At time t_2 , due to the sudden opening of sodium ion channels, AP is generated in area B. The influx of Na^+ ions in area B depolarizes the adjacent area C. In area A, the efflux of K^+ ions is complete and the potential is returned to the RMP level.

At time t_3 , area C is depolarized, resulting in an influx of Na^+ ions. In area B, the potential is returned to the RMP level. Na^+ ions depolarize the next area, and the signal continues to propagate to the end of the axon.

The undershoot of K^+ ions during the refractory period repolarizes the potential to a low enough level to prevent redepolarization of Na^+ ions from the neighboring area, thus preventing signal back-propagation.

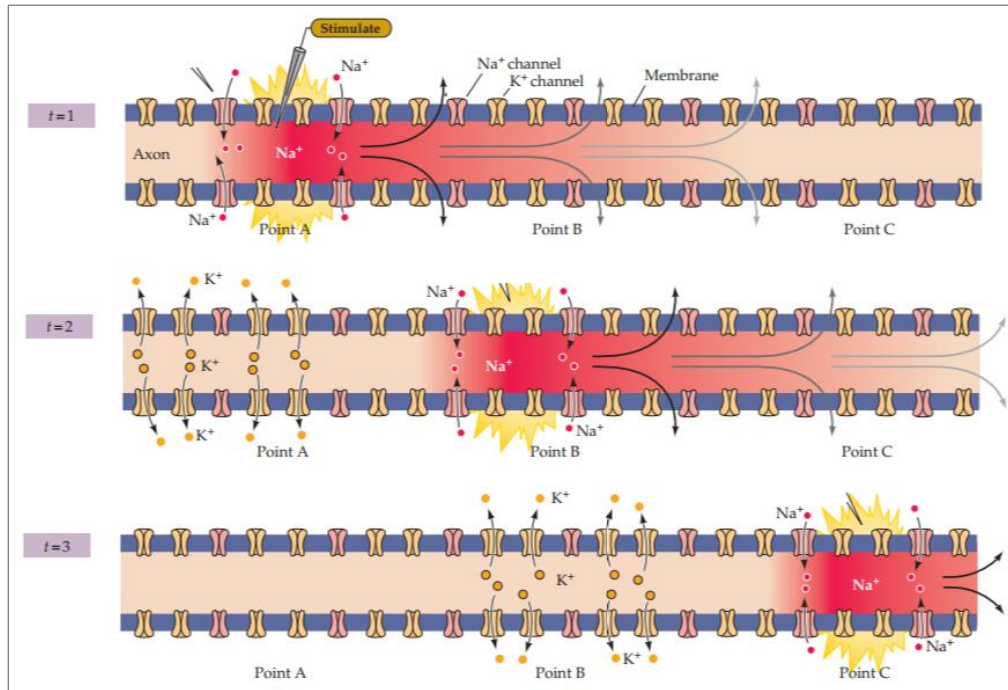


Figure 1.10 Mechanism of signal propagation along the axon [7]

The speed of action potential propagation along the axon ranges from 1 to 100 m/s. Factors that affect the speed are:

- Temperature: increase in temperature \rightarrow increase in transmembrane diffusion of ions \rightarrow increase in propagation speed
- Axon diameter: larger axon diameter \rightarrow lower resistance (passive conductor model) \rightarrow increase in propagation speed
- Myelin sheath: The myelin sheath wraps axon segments at regular intervals and prevents continuous transmembrane ion exchange along the entire length of the axon. Ion exchange occurs exclusively at segments without a myelin sheath, i.e., the nodes of Ranvier, enabling saltatory signal propagation and preventing return depolarization (animation at the link: https://upload.wikimedia.org/wikipedia/commons/thumb/4/48/Saltatory_Conduction.gif/1024px-Saltatory_Conduction.gif).

Along with RMP and activation threshold, latency, duration, amplitude and accommodation are also important characteristic values of the AP signal [13]. The readings of some values may vary depending on the recording technique.

Accommodation is the way a neuron responds to a stimulus. There are three types of response:

- Unitary accommodation: one stimulus → one AP; independent of stimulus duration
- Rapid accommodation: one stimulus → a certain number of APs; independent of stimulus duration
- Slow accommodation: one stimulus → generation of APs in a regular rhythm for the duration of the stimulus; dependent on stimulus duration

For reference, during AP activation along an axon with a diameter of 10 μm , the surface of the membrane where ion exchange takes place is about 314 μm^2 . If the standard amounts of Na^+ and K^+ ion concentrations are assumed, the amount of approximately 2 000 000 Na^+ ions and 2 000 000 K^+ ions changed during one activation is obtained. In addition to stimulated neurophysiological activity, there are also spontaneous action potentials, i.e., the generation and propagation of AP without an external stimulus. Such cases are common in neurons in the early stages of development and in some neurological disorders [14].

1.1.3 Hearing prosthetics

1.1.3.1 Hearing aid

A hearing aid is a device that works on the principle of amplifying frequencies that the user can hear less well due to damage. The three basic components of a hearing aid are:

- a unit for receiving signals from the environment
- a unit for processing signals
- a unit for sending signals to the user

Hearing aids are an effective solution for a wide range of hearing problems. Their advantages include ease of use and maintenance, and rapid adjustment and implementation that do not require complex medical treatment. In the United States, 4.23 million different hearing aids were sold in

2019, representing a 6.5 % increase over the previous year [15]. Given the generally satisfactory results among users with presbycusis, as well as trends in the aging population and improving healthcare standards, further growth in their use is expected in the near future.

However, despite the above advantages, hearing aids are not the optimal solution for all users, especially for people with severe hearing loss, certain forms of sensorineural hearing loss, as well as congenital hearing loss [16]. In such cases, it is necessary to use another type of technology.

1.1.3.2 Cochlear implant

The cochlear implant is the pinnacle of technological progress in hearing prosthetics and is generally the most successful neural prosthetic device. The forerunner of the cochlear implant dates back to 1957, when French doctors Journo and Eyriès, by electrically stimulating the auditory nerve endings with an induction coil, restored hearing to the level of gross pitch discrimination in a patient with a cochlear ablation [17]. In the following decades, the cochlear implant became an effective solution for patients for whom conventional hearing aids did not provide adequate assistance [18]. The total number of cochlear implants implanted worldwide by 2022 exceeded one million [19]. An overview of the historical development of artificial cochlear technology is given in Figure 1.11.

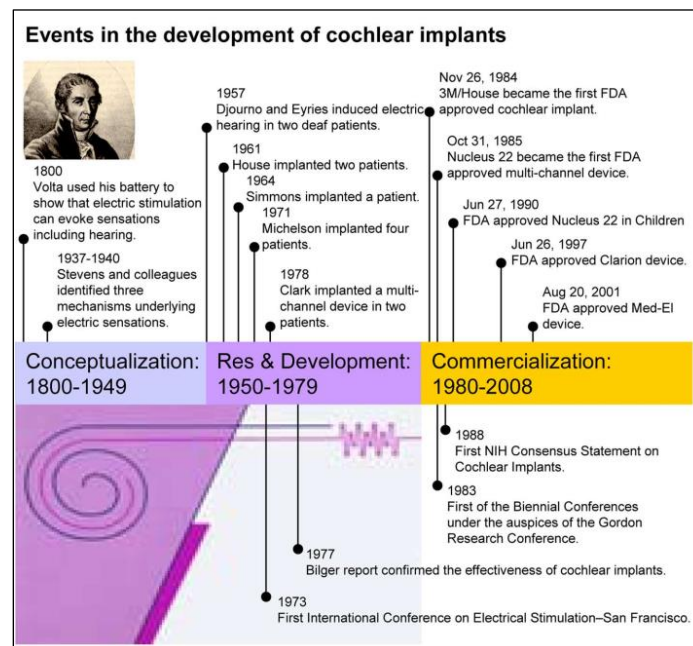


Figure 1.11 Overview of the historical development of the cochlear implants [20]

The principle of operation of the cochlear implant is based on the conversion of sound waves into an electrical signal that is fed directly to the cochlea, which translates the signals into information interpretable by the CNS. An illustration of the implanted artificial cochlea with its main components is given in Figure 1.12. The microphone (2) collects sound waves from the environment, which are then processed according to the user's needs in a microprocessor (1). Signal processing generally consists of converting the signal into a digital form, which is then converted into a radiofrequency signal and sent by a transmitter, i.e., an antenna (3), to an internal receiver (4) installed under the user's skin. The antenna is magnetically attached to the internal receiver. The radiofrequency signal from the internal receiver is decoded in an electrical stimulator (5) and converted into an electrical signal, from where it is sent by wire (6) to electrodes (7) implanted in the scala tympani, stimulating primary auditory neurons (8).

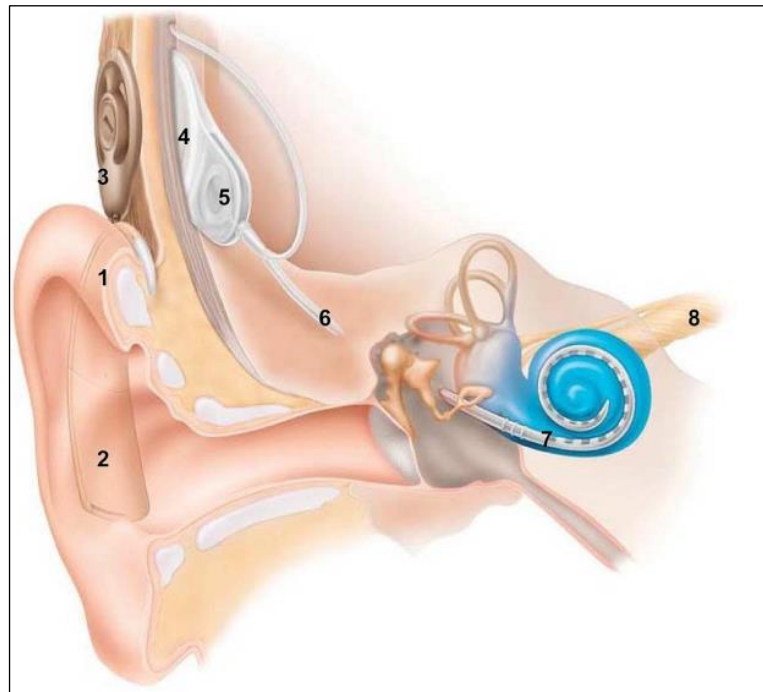


Figure 1.12 Model of implanted cochlear implant [20]

Cochlear implant can be divided into internal components that are surgically implanted, and external components that can be easily removed as needed. A schematic representation of the internal and external signal processing components is shown in the block diagram in Figure 1.13.

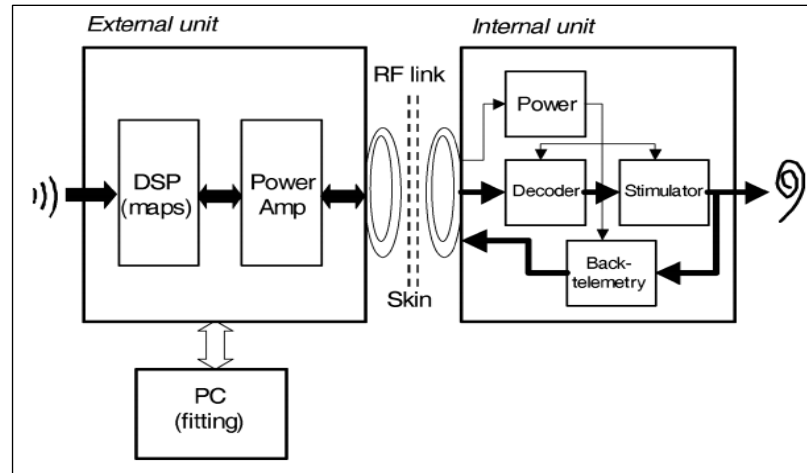


Figure 1.13 Internal and external signal processing components [20]

The most important process in cochlear implant is the conversion of the sound signal into an electrical impulse in the processor. A frequently used principle of signal processing is continuous interleaved sampling and is performed in 4 steps:

1) Filtering: In the first step of filtering, the sound wave from the environment recorded by the microphone is separated into different frequency bands, where each band is paired with one electrode. Electrodes with higher frequency filters were connected to the basal part of the cochlea, and electrodes with lower frequency filters to the apical part according to the characteristics.

2) Band envelope: By rectifying the wave and using a low-pass filter, a signal envelope is formed to determine the amplitude of each electrical pulse. Figure 1.14 shows the frequencies of the originally recorded sound of the sentence "drive round picked my children back up" and its envelope.

3) Compression: Using the nonlinear mapping method, the signal is compressed from the ambient noise level (approx. up to 100 dB) to the level of the electrically evoked potential (approx. 10 dB).

4) Modulation: The compressed envelope is used as the modulation signal, which modulates amplitudes of the biphasic pulses with fixed duration and firing rate.

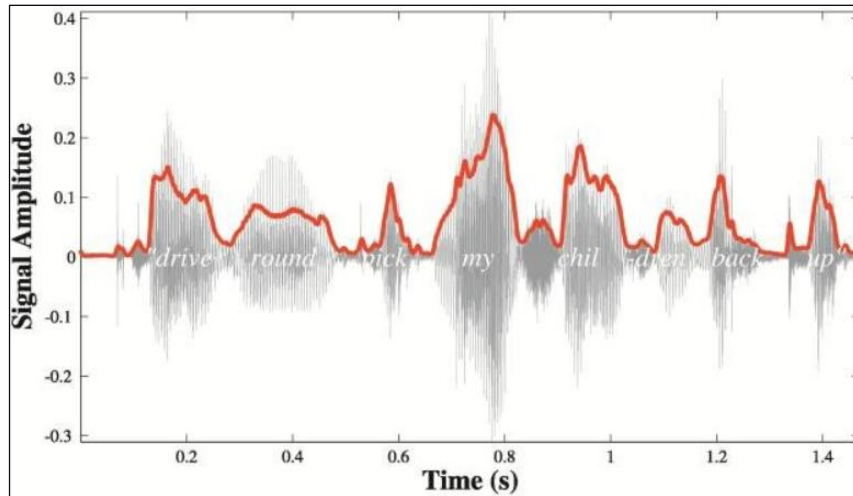


Figure 1.14 Waveform and extracted envelope of a speech signal [21]

Biphasic pulses modulated in this way trigger non-simultaneously on the electrodes, i.e., they do not trigger multiple electrodes simultaneously, which prevents the negative consequences of possible inter-electrode interference. Modern devices provide a stimulation frequency (firing rate) of approximately 1 000 to 2 000 pulses per second per electrode. The amplitude modulated sequence of pulses (pulse train) shown in Figure 1.15 represents the final output of one of the electrodes.

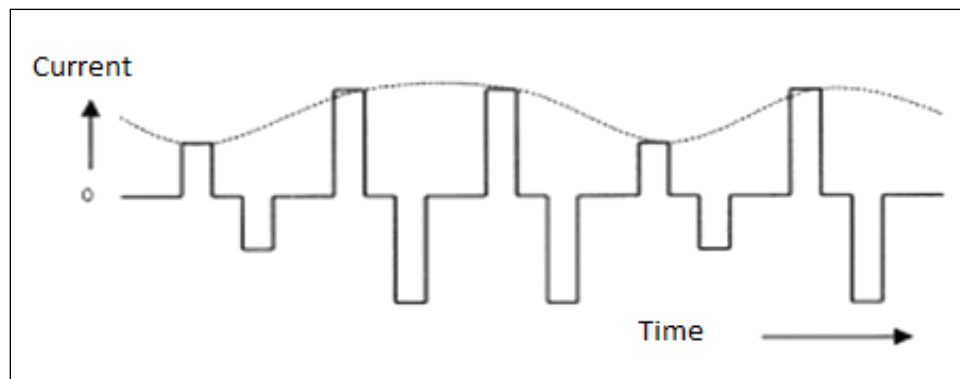


Figure 1.15 Amplitude modulated pulse train [22]

Communication between the internal and external unit takes place via radio frequencies through the skin. The processed signal from the microprocessor is sent through the induction coil to the internal unit where it is decoded accordingly. The parameters that are passed to the stimulator are the target electrode, the pulse amplitude and duration, and the distance between pulses for each electrode (pulse gap). The pulses must be biphasic because long-term stimulation with monophasic

pulses of positive or negative charge can cause a disturbance of the equilibrium potential at the stimulation site. Before sending the signal, it is necessary to perform bit coding, most often according to the amplitude-shift keying procedure, frame coding and back telemetry [20]. In addition to sound information, the induction coil also transmits energy for the operation of the internal unit. The RF link delivers approximately 20–40 mW of power to the internal unit, with about 40 % transmission efficiency [20]. Energy transfer increases with the height of the coil, but is limited by the practical and ergonomic requirements of the user.

1.1.4 Limitations and strategies for advancement

During the process of implantation, i.e., insertion of electrodes into the cochlea, it is necessary to take into account the method and depth of insertion in order not to damage the sensitive structures in the scala tympani. In some designs, insertion is assisted by a probe (stylet) with the aim of reducing rough contacts with internal structures as in Figure 1.16. Due to the dimensions of the scala tympani and the still insufficiently flexible and tissue-friendly electrode designs, insertion up to 400° is considered safe and routine. The surgical procedure itself is a routine procedure and lasts 3 to 4 hours.

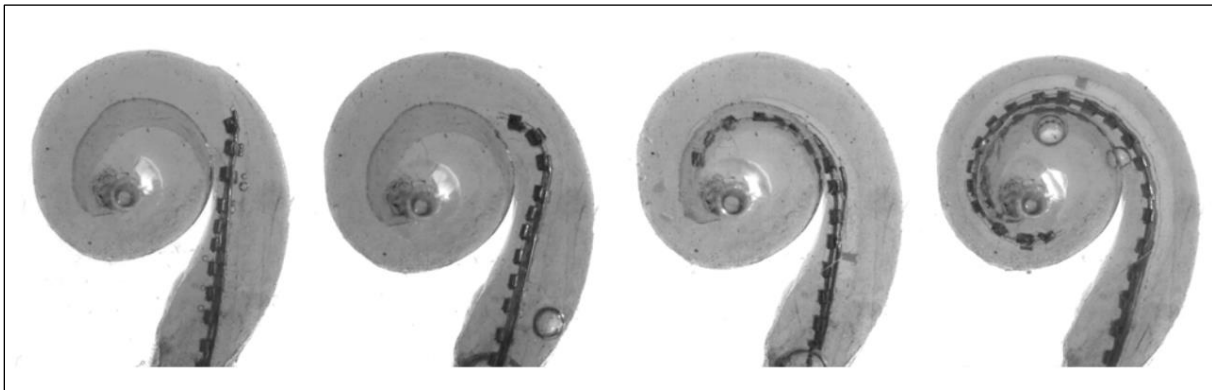


Figure 1.16 Probe-assisted electrode insertion [20]

However, despite increasingly advanced surgical techniques, due to the dimensions of the implants and anatomical structures and the high sensitivity of the inner ear structures, when inserting the implant carrier with electrodes into the cochlea, it is not possible to achieve ideal contact of all electrodes with the targeted primary auditory neurons, which leads to the lack of precise stimulation inside the cochlea. The distance between the electrodes and the neurons is called the neuroanatomical gap (NAG) and represents one of the main reasons for high variability and

unpredictability of the implantation outcome [20, 23, 24]. This problem is further accentuated by the disparity in the number of neurons in the cochlea and electrodes in implants, since the human cochlea typically contains about 30 000 spiral ganglion neurons [25], and most modern cochlear implants do not exceed 24 electrodes and most electrodes are made mainly of a platinum-iridium alloy in a ratio of 9:1 [20]. These spatial and numerical discrepancies can severely reduce the electrical coupling efficiency, causing poor pitch perception and speech perception in noise [26, 27], since the effect of stimulation heavily relies on electrical coupling, which depends on the position of the electrode and the distance between electrodes and neurons [20, 28].

In one of the first studies dealing with the issue of neuroanatomical gap, Shepherd et al. [28] observed the relationship between the position of the electrodes within the cat's scala tympani and the level of evoked auditory brainstem responses (EABR) as a method of confirming the transmitted signal from the electrodes to the primary auditory neurons in the cochlea. The study showed significant differences in the amount of EABR for different electrode positions (Figure 1.17).

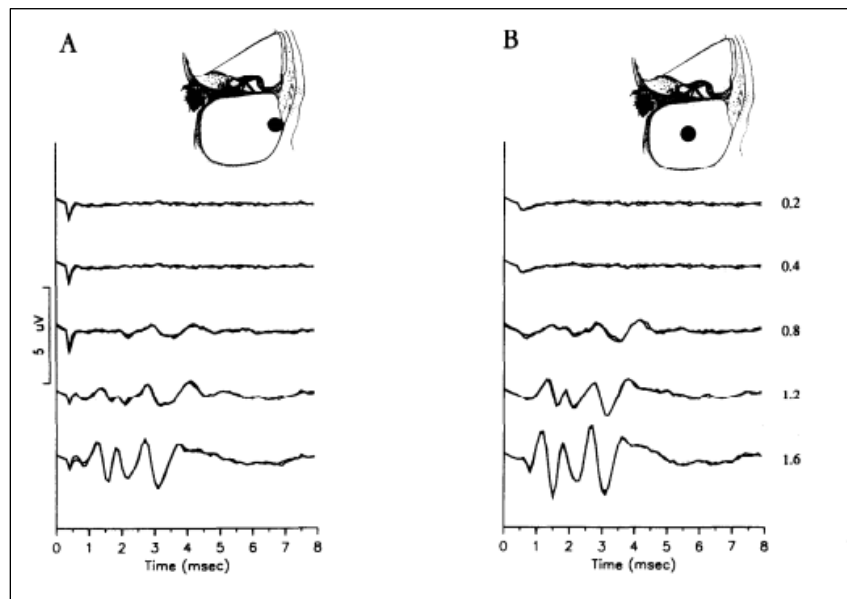


Figure 1.17 EABR with respect to electrode position [28]

Gstoettner et al. [29] obtained a clear and realistic representation of the position of the electrodes in the cross-section of the cochlea based on X-rays of the scala tympani for 8 different cases and 3 types of electrodes on human cadavers with implants inserted up to the point of resistance.

Hahnewald et al. [30] investigated the direct effect of neuroanatomical gap on the excitability of primary auditory neurons in mice. The results showed significantly weaker neuronal responses with increasing distance from the electrodes (Figure 1.18).

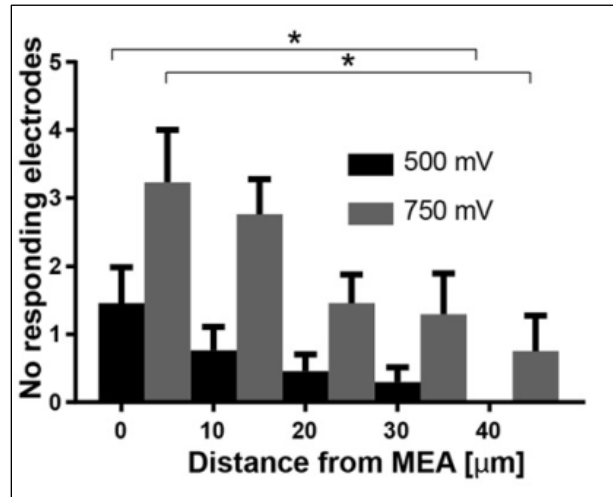


Figure 1.18 Relationship between NAG and neuronal excitability; Adapted from [30]

O'Leary et al. [31] approached the problem of neuroanatomical gap by proposing the regeneration of dendrites of primary auditory neurons towards the electrode using neurotrophin 3 and brain-derived neurotrophic factor, which is shown in Figure 1.19.

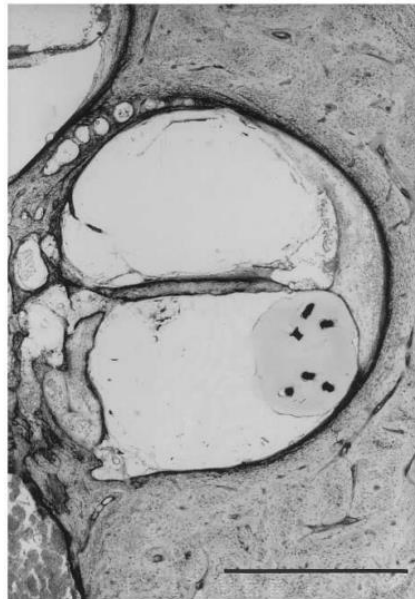


Figure 1.19 X-ray of a section of an implant with electrodes in the cochlea [32]

The basic characteristics of electrodes in terms of performance in cochlear implants are spatial and temporal resolution. Spatial resolution increases inversely with the electrode area. The limiting factor of this problem is the fact that impedance also increases inversely with the electrode area. This means that for each system, depending on the target signals, technical design and materials, there is a limit at which the impedance becomes so large that it raises the root mean square (RMS) noise thus reducing the signal-to-noise ratio (SNR) to a level that makes it difficult to read the target signal as shown in Figure 1.20.

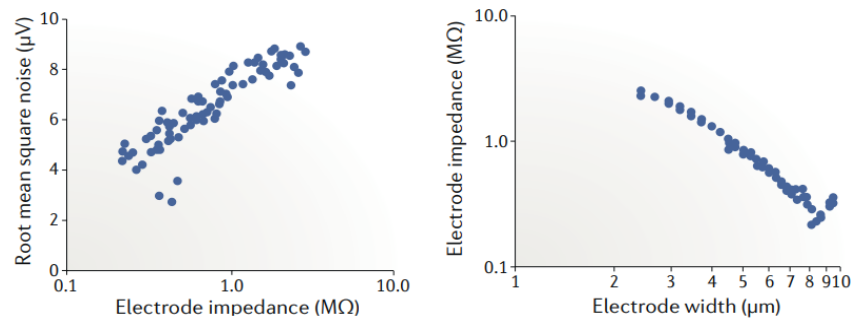


Figure 1.20 Relationship between electrode width, impedance and RMS [32]

From the above, it follows that, with existing materials and technologies, it is not possible to produce electrodes small enough and sufficiently robust to noise to overcome the neuroanatomical gap and thus achieve better auditory performance for users. Therefore, research approaches to this issue are comprehensive and multidisciplinary. Wilson and Dorman [33] propose that further advances in cochlear implant performance should focus on the following strategies:

- Development of systems with a larger number of electrodes
- Development of new modes for more precise spatial control of stimulation
- Better modulation of the fundamental frequency (the lowest frequency of a periodic waveform; e.g., for a male voice 85-180 Hz, and for a female voice 165-255 Hz)
- Application of the electric and acoustic stimulation principle for users with partial hearing loss
- Preservation of existing healthy structures of the inner ear (primarily neurons and sensory auditory cells) through stimulation methods and pharmacological preparations

- Development of strategies to mimic complex processes and interactions in the healthy cochlea
- New design of electrodes and supports to get as close to neurons as possible
- Promoting the guidance, movement and growth of neurons towards the electrodes

Following the last of these strategies, there is a need to investigate mechanisms for promoting the guidance, movement and growth of neurons towards the electrodes, and their potential application in cochlear implant technology. Among them, mechanotaxis and electrotaxis are of particular importance, as they have been shown to be suitable for the stated purpose. These mechanisms rely on mechanical and electrical guidance cues, respectively, and will be described in greater detail in Chapter 2. To investigate the impact of the above mechanisms on neuronal cultures, it is necessary to implement them in a system that will enable the analysis of their influence on neuronal morphology as well as on electrophysiological properties, which serve as indicators of preserved cell functionality. Among these systems, microelectrode arrays (MEAs) stand out, as they have been widely used to study general extracellular electrophysiological properties of neurons in vitro for decades and which will also be discussed in more detail in Chapter 2.

In this context, the motivation for this research stems from the need to develop a more efficient neuroelectronic interface for recording and stimulating neurons in vitro, in order to understand the effects of mechanotaxis and electrotaxis on the interaction between neurons and electrodes in MEA systems, with the aim of:

- Designing a neuroelectronic interface with microstructured substrates optimized to support the growth and development of primary auditory neurons
- Establishing an experimental methodology for characterizing the electrophysiological behavior of primary auditory neurons in vitro under the influence of mechanotaxis and electrotaxis induced by the neuroelectronic interface stimulation and an externally applied electric field (EF)
- Evaluating the potential of this technology in the context of improving future neuroelectronic interfaces and its potential application in cochlear implants

1.2 Hypothesis

Microstructured substrates that exploit the mechanisms of mechanotaxis and electrotaxis provide conditions that support the growth and development of primary auditory neurons *in vitro* while preserving their electrophysiological properties.

1.3 Research methodology

The research methodology is designed in such a way that first the design of the substrate and the experimental interface and their mutual integration are presented. Then the preparation and cultivation of cell cultures are presented, followed by a description of the experimental protocols used, sampling of the results, and statistical methods for analyzing the obtained data. Subsequently, the effects of the substrate with three-dimensional surface microtopography and electric field stimulation on the morphological parameters of neurons are analyzed. Finally, the spontaneous electrophysiological activity of neurons under the influence of validated mechanisms is analyzed. A detailed description of the substrate and the experimental interface, as well as the experimental protocols and statistical methods used for analyzing the results are presented in Chapters 3 and 4.

The research methodology is divided into two mutually complementary parts:

- A) Investigation of the effects of three-dimensional micropatterned substrates optimized for mechanotaxis on the electrophysiological activity of spiral ganglion neurons using the neuroelectronic interface for extracellular stimulation and recording.
- Design and characterization of three-dimensional micropatterned substrates
 - Design and development of chips with SiO₂ micropillars divided into four zones with different micropillar dimensions, based on previous studies of the influence of mechanotaxis on neuromorphology and incorporating 192 TiN electrodes
 - Geometrical and qualitative compositional characterization of the chip SEM and energy-dispersive X-ray spectroscopy (EDS)
- Design and development of the neuroelectronic interface for extracellular stimulation and recording of spiral ganglion neuron neurophysiological activity and integration of substrates into the system

- Design and assembly of the neuroelectronic interface, including design and fabrication of printed circuit boards (PCBs) for connecting chips and the system
- Connecting the connector PCBs to RHS2000 stimulation/recording controller
- Mounting the chip on the chip carrier PCB and connecting the pads using wire bonding
- Sealing the contact area and ensuring retention of the culture medium
- Connecting the PCBs with vertical spring pins and integrating the chip into the system
- Isolation and cultivation of neuronal cultures
 - Extraction of spiral ganglion neurons from the cochleae of Sprague–Dawley rat pups, ranging from postnatal day 6 to postnatal day 8 (P6–P8).
 - Cultivation of spiral ganglion neurons in vitro on the chips for 5-7 days
- Analysis of neurophysiological activities of spiral ganglion neurons
 - Characterization of parameters of system
 - Recording of spontaneous action potentials and neuronal responses to electrical stimulation
 - Filtering and sorting of electrophysiological signals with an application programmed in MATLAB according to parameters such as amplitude, width and polarity of the signal
 - Statistical analysis of electrophysiological signals: descriptive analysis, spatial distribution and source identification by correlation
- Fluorescence microscopy and analysis of morphological parameters
 - Fixation and staining of cell cultures
 - Neuron imaging and mapping with a fluorescence microscope
 - Morphological analysis of neurite length and orientation with image processing software

- B) Investigation of the influence of mechanotaxis and electrotaxis mechanisms on primary auditory neurons cultured on three-dimensional micropatterned substrates exposed to an electric field induced by the magnetic field stimulator (MFS) coil
- Isolation and cultivation of neuronal cultures
 - Extraction of spiral ganglion neurons from the cochleae of 6-days old (P6) Sprague-Dawley rat pups
 - Cultivation of spiral ganglion neurons in vitro on the chips for 6 days
 - Experimental setup and stimulation protocol
 - Placement of neuronal cultures in the magnetic field stimulator with a sawtooth-driven coil that generates a time-varying magnetic field and the corresponding induced electric field in the culture medium
 - Application of electric field of defined amplitude, frequency and duration according to a predefined stimulation protocol
 - Analysis of results
 - Fixation and staining of cell cultures
 - Neuron imaging and mapping with a fluorescence microscope
 - Quantitative analysis of soma area (SA), neurite length (NL), and neurite alignment (NA) with image processing software to assess the effects of electrotaxis and mechanotaxis on neuronal growth and spatial organization
 - Comparison of four experimental conditions:
 - Glass substrate without EF stimulation
 - Chip substrate without EF stimulation
 - Glass substrate with EF stimulation
 - Chip substrate with EF stimulation

1.4 Scientific contribution

The expected scientific contributions of this doctoral dissertation are as follows:

The development of three-dimensional microstructured substrates through the construction, characterization, and application of microtopographic structures optimized for neuronal growth and alignment, along with an analysis of the influence of the mechanism of mechanotaxis between cells and substrates. Special emphasis is placed on the development of a neuroelectronic interface for the electrophysiological characterization of spiral ganglion neurons, which is crucial for assessing their functionality.

The influence of electric fields on neuronal cultures: statistical determination of the influence of electric field stimulation on the modulation of growth and spatial organization of neurons on microtopographic substrates, with an analysis of the combined effects of mechanotaxis and electrotaxis.

1.5 Structure of the dissertation

The first chapter of the doctoral dissertation provides an introduction to the subject and research issues, as well as the motivation for the research work. The hypotheses of the scientific research, the methodology of the scientific research, and the original scientific contributions are presented.

The second chapter provides an overview of the relevant scientific literature. An overview of basic electrophysiological methods for recording cellular activity is presented, with an emphasis on systems for extracellular recording and stimulation of neuronal cultures. The mechanisms of mechanotaxis and electrotaxis and the influence of substrates based on them on the growth and development of neuronal cultures are described.

The third chapter describes the design of the experimental interface. The design of the MEA, the neuroelectronic interface and the magnetic field stimulator is presented with diagrams, basic principles of functioning, and fabrication and assembly procedures.

The fourth chapter defines the experimental methods of scientific research. Sample preparation and protocols for conducting experiments are described. Metrics and statistical quantities obtained as a product of the experiment are defined. An application for signal review and analysis is described.

The fifth chapter characterizes the microstructured substrate. SEM images of the chips were acquired to present the topography of the substrate. Qualitative analysis of the composition by EDS with the aim of checking the uniformity of the geometry and composition of the substrate by zones within the chip and between chips was performed. The interaction of the substrate with the culture medium was also analyzed.

In the sixth chapter, the individual and combined influence of mechanotaxis and electrotaxis on cell cultures of spiral ganglion neurons was analyzed. Analysis of morphological parameters under the influence of microtopography without electric field stimulation was performed, along with the influence of electric field stimulation on the morphological parameters of spiral ganglion neurons induced by a magnetic field stimulator. The last part of the chapter presents the results of the combined effect analysis.

In the seventh chapter, the neurophysiological activity of spiral ganglion neurons on microsubstrates was analyzed under the influence of mechanotaxis using the neuroelectronic interface for extracellular recording and stimulation.

At the end of the doctoral dissertation, the conclusions of the entire research are given, along with guidelines for future scientific research work.

2 LITERATURE REVIEW

The introductory chapter of the dissertation presents the research problem, research motivation and methodology used to address the described problem. To provide the theoretical basis for the research, the second chapter gives an overview of the relevant literature related to the main areas of interest in this work: the mechanisms of mechanotaxis and electrotaxis, and electrophysiological methods for recording cellular activity.

2.1 Mechanotaxis

The need to improve the interaction between neurons and electrodes in cochlear implants has led to the development of new approaches to this problem. As previously mentioned, one of the guidelines of Wilson and Dorman [33] emphasizes the design of interfaces to support the movement and growth of neurons towards the electrodes in order to reduce neuroanatomical gap. Although this approach is relatively new, the phenomenon of cell–environment interaction in the context of cell movement and growth has been considered since 1934, when three basic mechanisms of action were defined: mechanotaxis, electrotaxis and chemotaxis [34]. These mechanisms represent the phenomena of directed movement, growth and development of cells under the action of mechanical guides, electrical impulses or chemical substances. The development of artificial cochlea technology and the recognition of the need to overcome neuroanatomical gap have made these mechanisms a subject of interest in neurophysiological and electrophysiological research, with special attention being paid to the development of substrates adapted to microtopography and the phenomenon of mechanotaxis.

After early pioneering observations of the phenomenon of mechanotaxis [35, 36], the first serious study dates back to 1964 when Curtis and Varde [37] managed to control the growth and development of chick-heart fibroblasts from 9-day old embryos by varying the topography of the substrate. Ridged and furrowed substrates influenced cell orientation and overlap within dense cultures.

Advancements in material science in the following decades enabled the development of microstructured substrates that influenced the morphology and behavior of cell cultures imitating the extracellular matrix [38], creating extracellular micro and nanoenvironments using specially adapted surface topography to control cellular functions [39]. Many studies have shown how the

dimensions and shape of topographic substrates on the micro and nano scale can affect cell adhesion, spreading, alignment, morphology and gene expression of various cell cultures, including neurons, for which the influence of the dimensions and shape of the substrate is of particular importance [40]. This phenomenon has aroused special interest in the field of tissue engineering and regenerative medicine [41].

In one of the first modern studies on mechanotaxis in the CNS, Webb et al. [42] cultured adult mouse oligodendrocytes in vitro on lithographically patterned microchannels with a spacing of 260 nm and a depth of 100 nm. The cells showed a tendency for directional growth with their processes extending along the microchannels compared to a control surface. Fozdar et al. [43] cultured rat embryonic hippocampal neurons in vitro on substrates with 2 μm wide channels and 300 nm diameter holes. Neurons on the substrates showed a significant tendency for morphological polarity and greater neurite elongation compared to control samples.

Ferrari et al. [44] examined the mechanical properties of the lattice structure and the influence of structure dimensions on the morphological characteristics of PC12 cell differentiation with emphasis on polarity. The widths of the lattice segments of 500, 750, 1 000, 1 250, 1 500 and 2 000 nm were used in the experiment. With an increase in the width of the segments, an increase in the proportion of multipolar neurons after differentiation from stem cells was recorded. In addition to substrates with vertical orientation of topography and channel surface structures, the propensity of topographic features to support contact guidance has also been demonstrated. Seo et al. [45], in an experiment with h-PDMS (polydimethylsiloxane) substrates with irregularly distributed nanopillars < 500 nm in diameter, showed a tendency of rat hippocampal neurons to develop axon branches from the main axons. Leclech et al. [46] proved the influence of topography on the migration of cortical neurons in mice.

The influence of substrates with multidirectional topography to better mimic the extracellular matrix was investigated by Dowell-Mesfin et al. [47] with a focus on the orientation and growth of hippocampal neurons of rat embryos. The structure consisted of square micropillars with a side length of 0.5 and 2 μm and a distance between them in the interval from 1 to 5 μm with a step of 0.5 μm . The highest orientation and elongation of neurites was recorded on the sample with 1.5 μm spacing as shown in Figure 2.1.

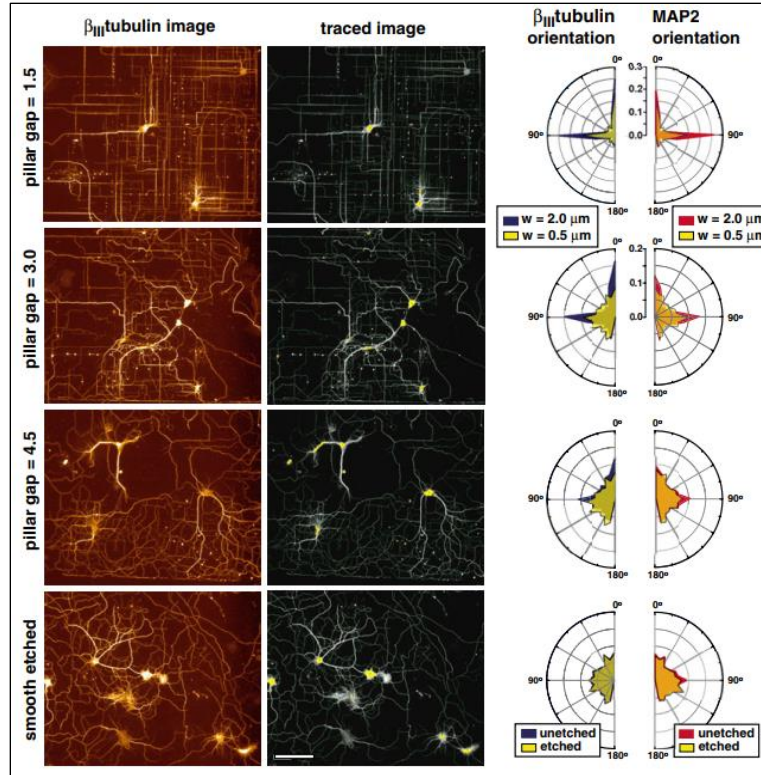


Figure 2.1 Neurite orientation and elongation of rat embryonic hippocampal neurons on square micropillar arrays with different spacings [47]

Kundu et al. [48] combined contact guidance by the mechanism of mechanotaxis with micropillars and chemotaxis using Netrin-1 with the hypothesis of eliminating the negative influence of the chemorepellent Semaphorin3A on the growth and direction of hippocampal neurons of mice, demonstrating the synergistic influence of mechanotaxis and chemotaxis, i.e., the possibility of superimposing the effects of several different types of contact guidance mechanisms. Johansson et al. [49] demonstrated the ability to orient axons of peripheral neurons on nanopatterns in a PMMA (polymethyl methacrylate) layer on parallel grooves of silicon chips. Grooves 100 to 400 nm wide and 300 nm deep showed an effect on axon growth in such a way that neurons preferred to grow along edges and raised grooves, with a threshold value of lateral structure dimensions greater than 100 nm. Bugincourt et al. [50] demonstrated a strong effect of silicon nanopillars on axon growth and differentiation in primary hippocampal neurons that attach to the tips of the pillars and, with the formation of a smaller neurite, show a tendency to further than on a control surface. The importance of the dimensions of microstructured substrates has been demonstrated on neurites of primary hippocampal neurons with the possibility of guidance and directionality [51]. Chua et al. [52] examined the influence of groove dimensions on neurite elongation of murine neural

progenitor cells after neuronal differentiation. It has been proven that the dimensions of the substrate can influence the process and degree of differentiation, whereby filopodial adhesion in the growth cone promotes elongation, which is opposed by the stiffness of the neurite cytoskeleton. The influence of substrate topography on differentiation was also shown by Micholt et al. [53]. Micropillars have shown the ability to direct polarization markers, which results in the elongation of axons along the pillar, with the influence of pillar dimensions.

The more detailed influence of topography with micropillars on the morphology of primary rat auditory neurons after 7 days in vitro (DIV) was examined by Mattotti et al. [54] and Radotić et al. [55, 56]. A clear positive connection between the geometry of the SiO₂ substrate surface and morphological characteristics such as neurite elongation, soma area and neuron polarity has been demonstrated. As a substrate, a complementary metal-oxide semiconductor (CMOS) chip was used without the use of stimulation.

2.2 Electrotaxis

Electric fields are naturally present in developing tissues and in the process of regeneration, and as such represent a biophysical signal capable of directing the migration, growth and differentiation of cells. Therefore, their study and interaction with cell cultures is of particular importance in the context of electrotaxis research [57].

Patel and Poo [58] in 1984 conducted the first significant study that demonstrated an electrotactic effect on neuronal cultures from frog embryos. In the study, a DC threshold field of 0.2–2 $\mu\text{A}/\mu\text{m}^2$ and a pulsed threshold electric field of 4 $\mu\text{A}/\mu\text{m}^2$ were applied; at a frequency of 10 Hz, lasting 15 minutes. Electric fields of negative polarity caused attraction and electric fields of positive polarity caused neurite repulsion. The field was generated with a micropipette.

Nishimura et al. [59] demonstrated a tendency of human keratinocytes (epidermal cells) to respond to a DC field of 100 mV/mm by migrating half of the cells within 14 minutes towards the cathode. The field strengths in the experiment correspond to those naturally occurring during wound healing.

In a 1998 study, Araki et al. [60] reported the effect of electric field on the spiral ganglion neuron size in vivo in kittens pharmacologically deafened immediately after birth. Stimulation with a 4-electrode implant for 60 days resulted in a smaller reduction in size after prolonged auditory

deprivation compared to the control group, demonstrating the ability of the electric field to affect the morphological parameters of neurons.

Brushart et al. [61] achieved a significantly higher rate of axon regeneration in the rat femoral nerve by stimulating dorsal root ganglion neurons (DRG). After cutting and suturing the femoral trunk, DRG neurons after 1 hour of stimulation (20 Hz) showed a significantly higher proportion of neurons directed to the target tissue compared to the control group.

Yao et al. [62] demonstrated that neuronal division, differentiation and migration depend on endogenous electric fields. In *in vivo* studies, it was observed that applied electric fields can stimulate the growth of damaged spinal cord axons, which opens the perspective of using a combination of endogenous and applied electric fields to target transplanted stem cells after injury. The same research group [63] was able to direct the migration of rat hippocampal neurons *in vitro* using the applied electric field. It was observed that at a field strength of 120 mV/mm neurons move towards the cathode, while changing the polarity also changes the direction of migration, suggesting the possibility of the electric field affecting the regeneration of neurons in the CNS.

Ye et al. [64] have documented a bidirectional interaction between neurons and the applied electric field. In addition to the fact that electric field induces an additional transmembrane potential of neurons when acting on it, the cell itself simultaneously locally redistributes the field around itself and thus influences neighboring cells by changing the local geometry of the field, creating an additional electrotactic effect.

Li et al. [65] studied the orientation of explant neurites of rat pup spiral ganglion neurons *in vitro* with stimulation similar to that present in cochlear implants. In the experiment, the bending angle of neurites was measured under the influence of different electric fields, generated by two parallel Pt-Ir wires 22 mm apart or by two Pt-Ir electrode rings. In DC fields, the field distribution was approximately uniform in the central region, while charge-balanced biphasic pulse fields produced a nonuniform distribution of current density and voltage gradient around the electrode rings, as shown in Figure 2.2. With constant and pulsating DC fields, neurites on laminin-coated substrates turned toward the cathode for 4 hours, and on poly-D-lysine (PDL)-coated substrates they turned toward the anode, which shows the dependence of the direction of electrotaxis on the composition of the substrate. In charge-balanced biphasic pulse fields, neurites tended to deflect from the electrode rings, whereby this effect weakened with distance and followed the inhomogeneous field

distribution, thus demonstrating that spiral ganglion neuron neurites are sensitive to the type of electric field and the chemical composition of the substrate, which may have key implications for the design of the experimental neuroelectronic interfaces. In Figure 2.2, panels a and b refer to the DC electric field, while panels c and d refer to the charge-balanced biphasic pulsed electric field.

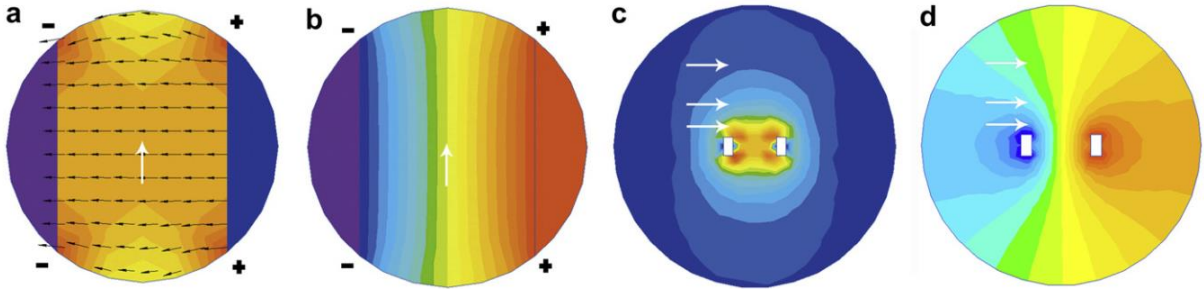


Figure 2.2 Finite element analysis of current-density and voltage-gradient distributions in DC and charge-balanced biphasic pulsed electric fields [65]

2.3 Electrophysiological recording methods

According to the generally accepted definition, electrophysiology is the branch of physiology that studies the electrical properties of cells and tissues by measuring and stimulating changes in voltage or current. In neuroscience, the main subject of interest of electrophysiology is the electrical activity of neurons, with an emphasis on AP, which can be observed at the single-cell and network scale [66]. The historical development of electrophysiology should be viewed in the context of the parallel development of natural and medical sciences on the one hand, and technical sciences on the other. The first application in clinical trials is considered to be the experiment from 1967 in which Durrer and Wellens achieved arrhythmia control in a patient with Parkinson-White syndrome [67]. In parallel, applications are developing in other branches of medicine and biotechnology, including in the field of neuroscience. This chapter briefly presents the most commonly used methods, with an emphasis on MEA systems for extracellular recording. The main electrophysiological recording techniques are defined by Spira and Hai [68] and schematically shown in Figure 2.3. Blue shows the intercellular medium, orange shows the electrodes, and yellow shows the substrate on which the cell culture is grown.

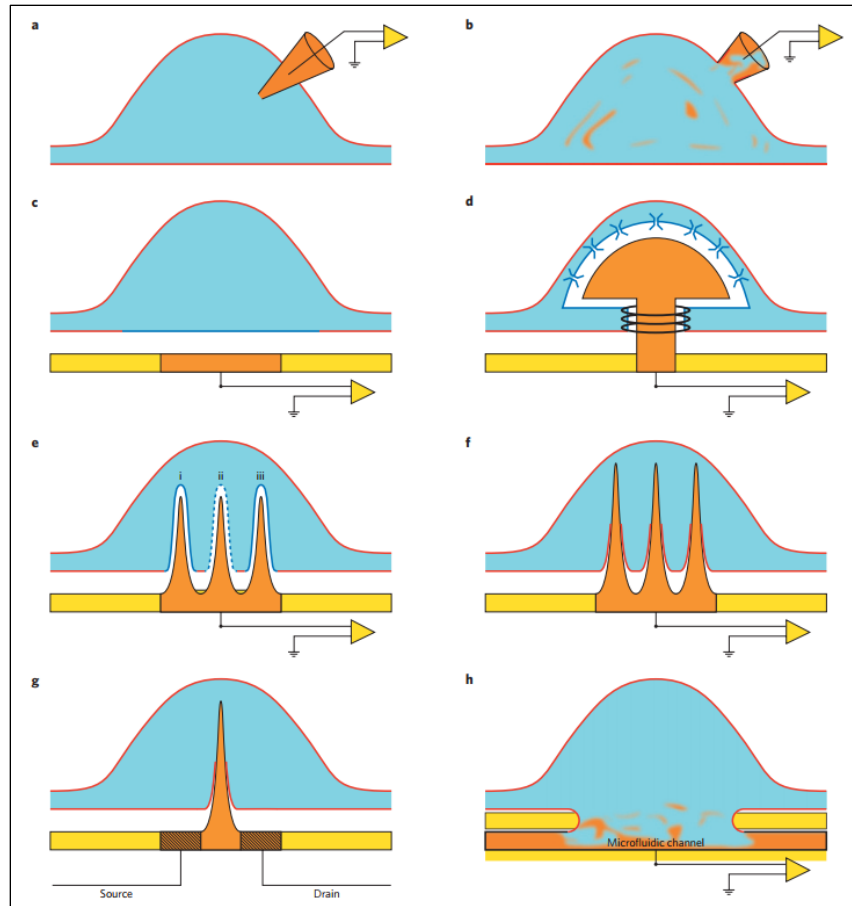


Figure 2.3 Electrophysiological recording methods [68]

The following recording techniques are distinguished:

- a) A sharp glass intracellular microelectrode
- b) Whole-cell patch-electrode configuration
- c) Substrate-integrated planar extracellular electrode
- d) Mushroom-shaped protruding microelectrode
- e) Recording with nanopillar electrodes without membrane penetration
- f) Recording with nanopillar electrodes with membrane penetration
- g) A nanopillar that serves as the gate for a nano-FET penetrates the cell's membrane
- h) Microfluidic system

Methods for recording neurophysiological activity are generally divided into intracellular and extracellular methods according to the position of the recording site. In intracellular methods, the recording electrode, regardless of the technical design, is in direct contact with the intracellular medium. Depending on the design, some methods allow mixing between the intracellular medium and the solution inside the electrode, while others only involve contact between the electrode and the intracellular medium. In intracellular recording, the direct effect of the action of ionic currents is observed.

In extracellular recording, there is no direct contact between the intracellular medium and the electrode. The recorded signals are the result of the interaction of transmembrane ionic currents with the surrounding medium collectively called local field potentials. The recorded medium may be the culture environment at the recording site under *in vitro* conditions, or the intervening tissue between the electrode and the target cells in *in vivo* recordings.

According to Buzsaki et al. [69], the following neurophysiological activities can be recorded using extracellular recording methods:

- a) Action potentials
- b) Synaptic and postsynaptic activities
- c) Activities induced by calcium
- d) Intrinsic currents and resonances
- e) Spike afterhyperpolarizations and down state
- f) Interactions between neurons and glial cells
- g) Ephaptic effect

When recording total activity, it is important to take into account the individual impact of each of these activities and, if necessary, separate them from the target activity, most often AP. Each of the listed activities has its own specific characteristics such as amplitude, duration, shape and frequency of occurrence. The methods also differ in the principle of operation, temporal and spatial resolution of recording, recording duration, shape, material and arrangement of electrodes, etc.

With the development of recording technology and software support, great attention is paid to filtering and sorting signals of different origins.

In a classic 1972 study, Thomas et al. [70] presented a pioneering MEA system that enabled successful stimulation of chicken cardiomyocytes in vitro. A 200 nm gold-plated nickel layer was deposited on a glass substrate by photo etching. The electrode pattern consisted of 30 electrodes with an area of $50 \mu\text{m}^2$ in 2 rows, with a distance between rows of $50 \mu\text{m}$ and a distance between electrodes of $100 \mu\text{m}$.

Gross et al. [71] presented a MEA system for long-term multichannel monitoring of neural networks of murine spinal neurons in vitro. Electrodes made of gold-plated indium-tin oxide (ITO) were applied by the photo etching technique in 4 rows of 16 electrodes, with a distance between electrodes of $40 \mu\text{m}$ and a distance between rows of $200 \mu\text{m}$. Cell culture showed spontaneous neurophysiological activity in the form of bursts.

Although MEA systems have been known for decades, they have only recently become a focus of broader research [68]. Modern systems enable simultaneous recording and stimulation of a large number of neurons with advanced sorting, filtering and visualization methods, thus providing a more detailed insight into neuronal behavior and understanding of fundamental electrophysiological mechanisms. However, the subject of most research remains the neurons of the CNS [72, 73], and in particular cortical neurons [74–76].

Modern MEA systems, such as the one from the study by Ronchi et al. [76], feature a large number of bidirectional electrodes (26 400) densely distributed at $17.5 \mu\text{m}$ spacing, enabling very precise stimulation (as low as 100 nA, with pulse durations as short as $18 \mu\text{s}$) and high-resolution visualization of the activity of embryonic rat cortical neurons, as shown in Figure 2.4. Stimulation electrodes are marked with a red box, while the electrical footprints are shown in white.

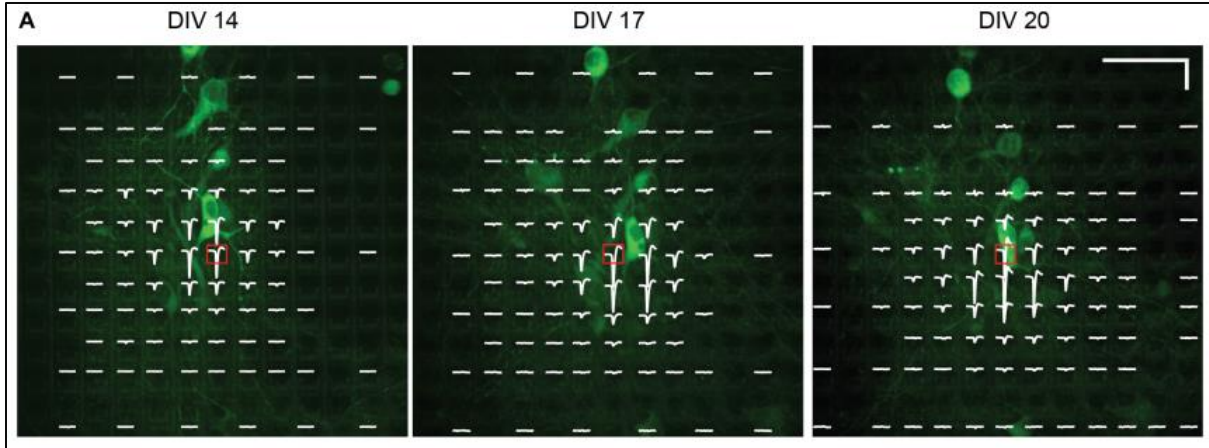


Figure 2.4 Superimposed fluorescence image and electrical footprint of the same neuron at DIV 14, 17 and 20; Adapted from [76]

Despite the increasing technical capabilities and growing interest in MEA systems, studies involving spiral ganglion neurons are still very rare.

Hahnewald et al. [30, 77] in their studies coupled an MEA system with spiral ganglion neurons with the aim of optimizing the interaction between neurons and electrodes in neuroelectronic interfaces and of deepening the understanding of the steps necessary to bridge the neuroanatomical gap in cochlear implants. For this purpose, an in vitro platform was developed with 68 Pt electrodes with a surface of $40\ \mu\text{m} \times 40\ \mu\text{m}$, spaced $200\ \mu\text{m}$ apart, on which explant cultures of murine spiral ganglion neurons (P5-P8) were grown in order to examine how the parameters of the stimulation pulse and the distance of the electrodes from the neuron affect the excitation threshold and the required stimulation energy, as shown partially earlier in Figure 1.18. The ability of the MEA system to serve as an experimental model for cochlear implant and optimization of interaction with neurons was demonstrated.

Finally, and following on from Hahnewald's studies, Senn et al. [78] demonstrated a mechanism of guiding spiral ganglion neurons by chemotaxis to integrate into the neuroelectronic interface using neurotrophic growth factors with a nanostructured gel, injected directly into the cochlea and shaped in a manner that mimics the extracellular matrix.

2.4 Literature review: summary

The above presented studies demonstrated the ability of microstructured substrates to cause the occurrence of mechanotaxis and directly affect the growth, development, alignment and

differentiation of neuronal cultures. Studies related to electrotaxis have shown the property of electric fields for neural guidance and neurite extension and alignment, as well as the influence on cell regeneration, including spiral ganglion neurons. Systems for extracellular recording of neurophysiological activity based on MEA technology have proven to be effective and efficient in stimulating and recording the activity of neuronal cultures with the aim of better understanding their properties and behavior.

However, these approaches have so far been mostly investigated separately, and studies involving spiral ganglion neuron cultures are especially rare. Furthermore, so far, no study has been presented that integrates all three mentioned approaches in one system, which limits the progress in the knowledge crucial for improving the performance of cochlear implants. Therefore, there is a clear need for an *in vitro* platform that will integrate the mechanisms of mechanotaxis, electrotaxis and systems for electrophysiology based on MEA technology into a neuroelectronic interface and enable experimental testing of the interdependence of the aforementioned mechanisms, in order to reduce the influence of neuroanatomical gap in the future and enable the design of more efficient cochlear implants.

Based on this identified need, the following chapter presents the design of the experimental interface developed to integrate the MEA substrate, the neuroelectronic interface and the magnetic field stimulator into an integrated experimental platform.

3 EXPERIMENTAL INTERFACE DESIGN

Based on the research gap identified in the previous chapter, the experimental platform was designed to combine microtopographic guidance, electric field stimulation and extracellular electrophysiological recording within a single in vitro system. It consists of three mutually complementary components:

- MEA substrate: microchip with three-dimensional microtopography optimized to induce mechanotactic effect equipped with electrodes for recording and stimulation of neuronal cultures
- NEI: system for simultaneous recording and stimulation of extracellular neurophysiological activity of cell cultures
- MFS: coil-based magnetic field stimulator

The listed components together enable the application of controlled mechanical cues via substrate microtopography, induced electric fields via a coil, and recording and stimulation in extracellular conditions, thus providing insight into the action of mechanotactic and electrotactic mechanisms on neuronal cultures, and enabling analysis of their electrical activity. This chapter describes the design and the operating principles of the MEA substrate and the NEI and MFS systems. The coupling of the components is shown in Figure 3.1.

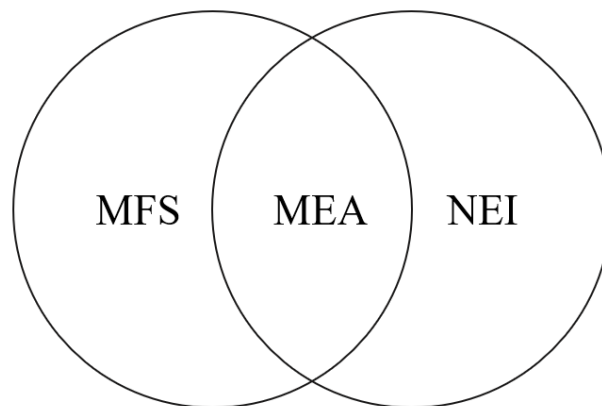


Figure 3.1 Schematic relation between MFS, NEI and MEA as their common substrate

3.1 Microelectrode array substrate

The central component of the experimental interface is the MEA chip, which serves as a substrate for growing spiral ganglion neuron cultures. The geometry of the chips was defined based on the conclusions of the previously mentioned works of our research group [54–56], and the fabrication procedure itself is based on the technology originally described by Huys [79]. A partial description and initial validation of this design in spiral ganglion neuron cultures have been previously published in our works [80–83].

Each chip contains 384 titanium nitride (TiN)-based electrodes with a diameter of 20 μm . The electrodes are evenly distributed into four zones, each containing 96 electrodes arranged in four rows of 24 electrodes. The distance between the electrodes across rows and columns is 100 μm . Due to technological limitations of production, it was not possible to connect every electrode to a corresponding pad, therefore every other row was connected, resulting in a total of 192 connected electrodes. Each zone features a separate microtopography consisting of cylindrical micropillars with the following diameters:

- Zone 1: 1.0 μm
- Zone 2: 1.8 μm
- Zone 3: 2.8 μm
- Zone 4: 4.0 μm

Micropillars can be arranged with either 1.2 μm or 2 μm spacing. Each chip is fabricated with only one spacing size. The height of micropillars and electrodes is 1 μm .

Figure 3.2 (a) shows a schematic representation of the chip by zone. The active area of the chip is depicted as a 4 mm \times 4 mm magenta square, with zones labeled by their micropillar dimensions. The connections between the electrodes and the pads on the edge of the chip, which are located in the area marked in gray, are marked with green lines. The total dimension of the chip is 11 mm \times 11 mm.

Figure 3.2 (b) shows an enlarged schematic view of the zone 4 segment with the electrode and the micropillars surrounding it. The corresponding dimensions of the diameter of the electrode, pillar and distance between the micropillars are indicated.

Figure 3.2 (c) shows a side cross-sectional schematic of the active part of the chip based on the tungsten micro-nail fabrication process described in [79]. The chip is built on a silicon wafer, with aluminum conductors located below the active surface and connected to the upper electrode through tungsten micro-nails. The tungsten micro-nails are formed through the insulating SiO_2/SiC stack and enable contact with the aluminum conductor. The surrounding SiO_2 layer forms the three-dimensional microtopography with micropillars around the electrode, while the final electrode surface is completed by the TaN/Ti/TiN metallization layer. The schematic is not drawn to scale, but it shows the principle of vertical connection between the bottom metal layer and the electrode surface.

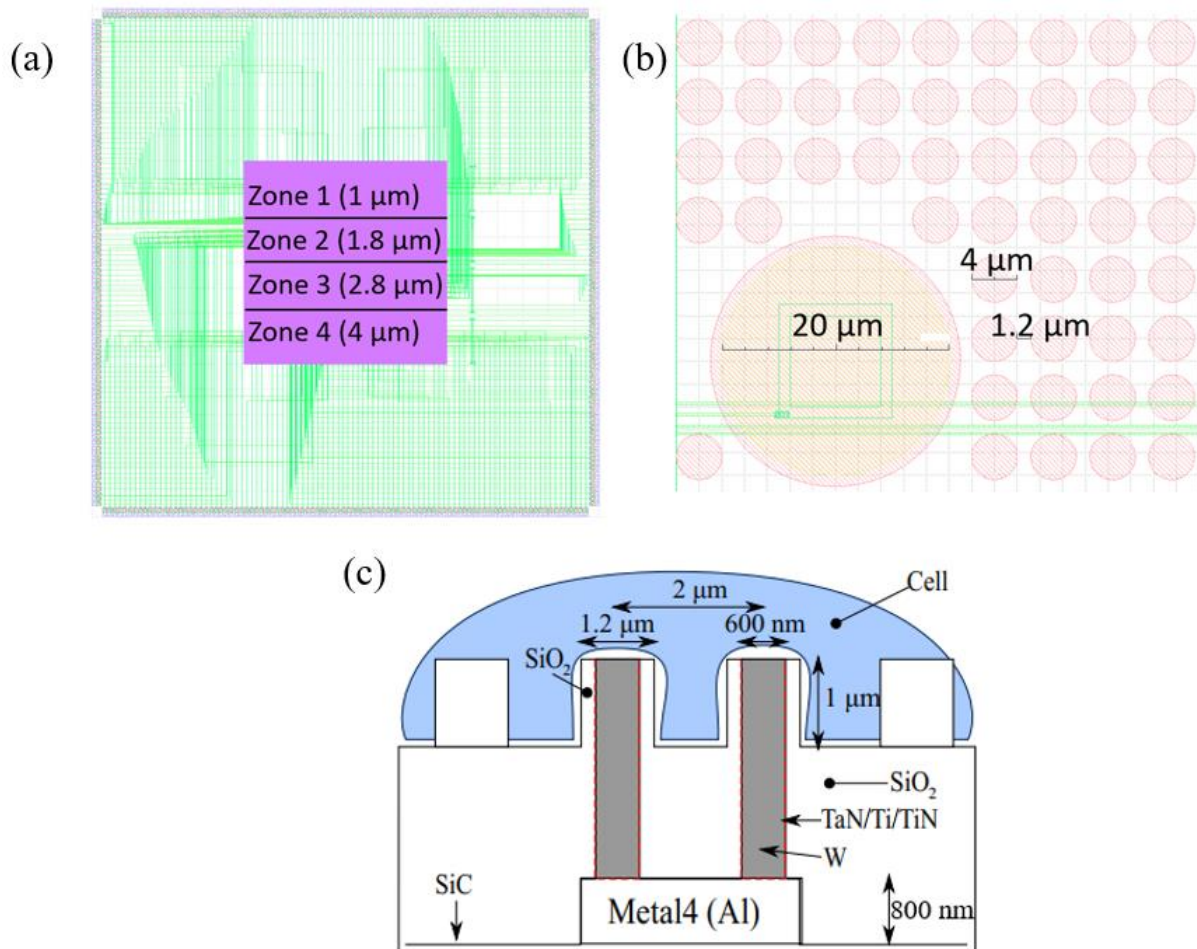


Figure 3.2 Schematic view of the MEA substrate with: (a) zone layout, (b) electrode top view and (c) electrode cross-section; panels (a, b) adapted from [83], panel (c) adapted from [79]

Figure 3.3 (a) shows a magnified view of the electrode and the surrounding micropillars captured using SEM. The image shows the electrode and micropillars at zone 4, with a micropillar spacing

of 1.2 μm . The image was captured using JSM-7610F (JEOL, Tokyo, Japan) at an angle of 35° with $3000\times$ magnification. Figure 3.3 (b) shows the EDS image of the same area, where the turquoise color is an indicator of the presence of titanium. The EDS analysis was carried out using Oxford Instruments X-MaxN 80 mm² EDS module (Oxford Instruments, Abingdon, UK), which was operated with Aztec software (version: 5.1; Oxford Instruments, Abingdon, UK) and paired with a SEM device. The scale bar applies to both panels. A more detailed characterization of the consistency of chip geometry and composition is given in Chapter 5.

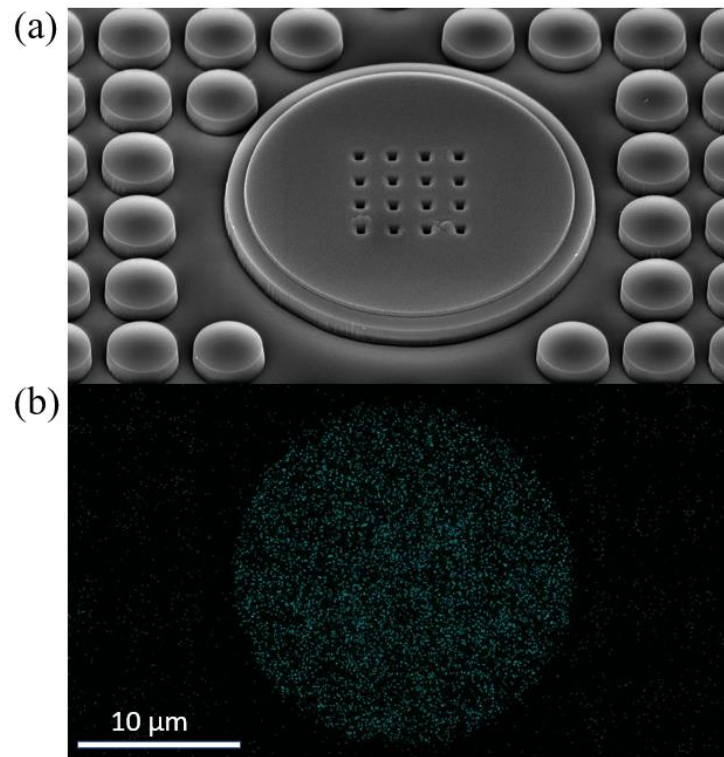


Figure 3.3 Structure and composition of the chip: (a) SEM image of the chip surface (b) EDS image of the chip surface [83]

3.2 Neuroelectronic interface

Figure 3.4 illustrates the overall architecture and operating principle of the neuroelectronic interface used for extracellular recording and stimulation. Neuroelectronic interface is based on a 32-channel Intan RHS stimulation/recording headstage connected to the MEA with a set of two PCBs. According to the Intan Stimulation/Recording Controller User Guide and the RHS Stim SPI Interface Cable/Connector Specification [84, 85], the headstage features two RHS2116 digital stimulator–amplifier integrated circuits, providing 32 channels that can each be configured for

extracellular recording or stimulation with constant current. The headstage communicates with an Intan RHS2000 128-channel stimulation/recording controller via a digital serial peripheral interface cable. During experiments, the controller is operated from a computer connected via a USB 2.0 cable. Signal monitoring and system adjustments are performed using a graphical user interface (GUI) and the recorded data are saved in RHS format. The controller has a separate power supply.

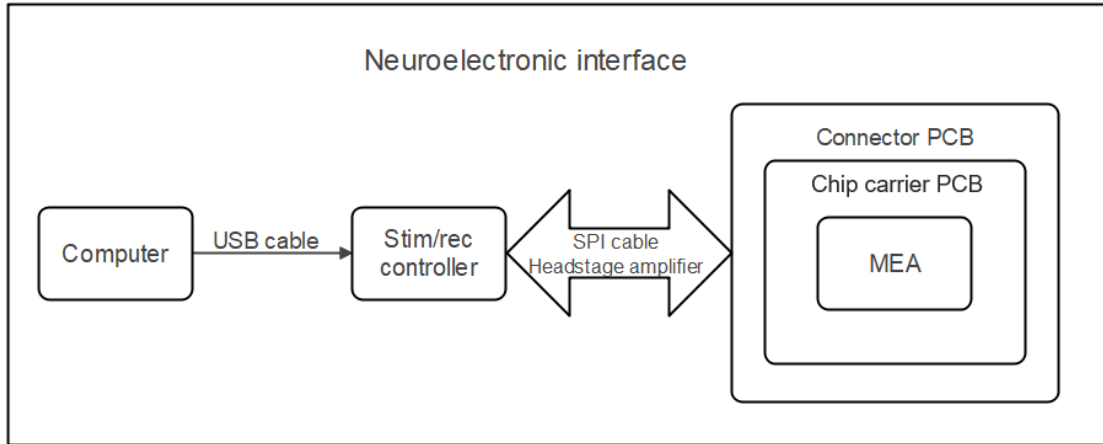


Figure 3.4 Schematic view of the NEI; Adapted from [83]

The MEA communicates with the controller via a two-level PCB (connector PCB + chip carrier PCB) set shown in Figure 3.5. The upper-level PCB, i.e., the connector PCB, measuring 110 mm \times 110 mm, contains 8 Nano-Miniature Connector adapters (NPD-36-AA-GS from Omnetics Connector Corp., Minneapolis, MN, USA) that represent the connection between the controller and the PCBs. There are two adapters on each side of the connector PCB, and each side represents the connections of one zone of the chip. The connector PCB, shown in panel c (left), has a 55 mm \times 55 mm square cut out in the middle to allow access to the chip. The connector PCB connects to the lower-level PCB, i.e., the chip carrier PCB, shown in panel c (right), via 192 vertical spring pins. Each pin represents the connection of the controller with one electrode on the chip. The chip carrier PCB measures 78 mm \times 78 mm and is separated from the system and placed in an incubator during cell culturing. The chip carrier PCB sits on a 120 mm \times 120 mm steel plate that serves as the base of the system. It is attached to the plate with four M4 nuts and screws that also serve as mechanical supports for the assembly. Both PCBs were designed using KiCad (version 5.0.2; KiCad Development Team, open-source software).

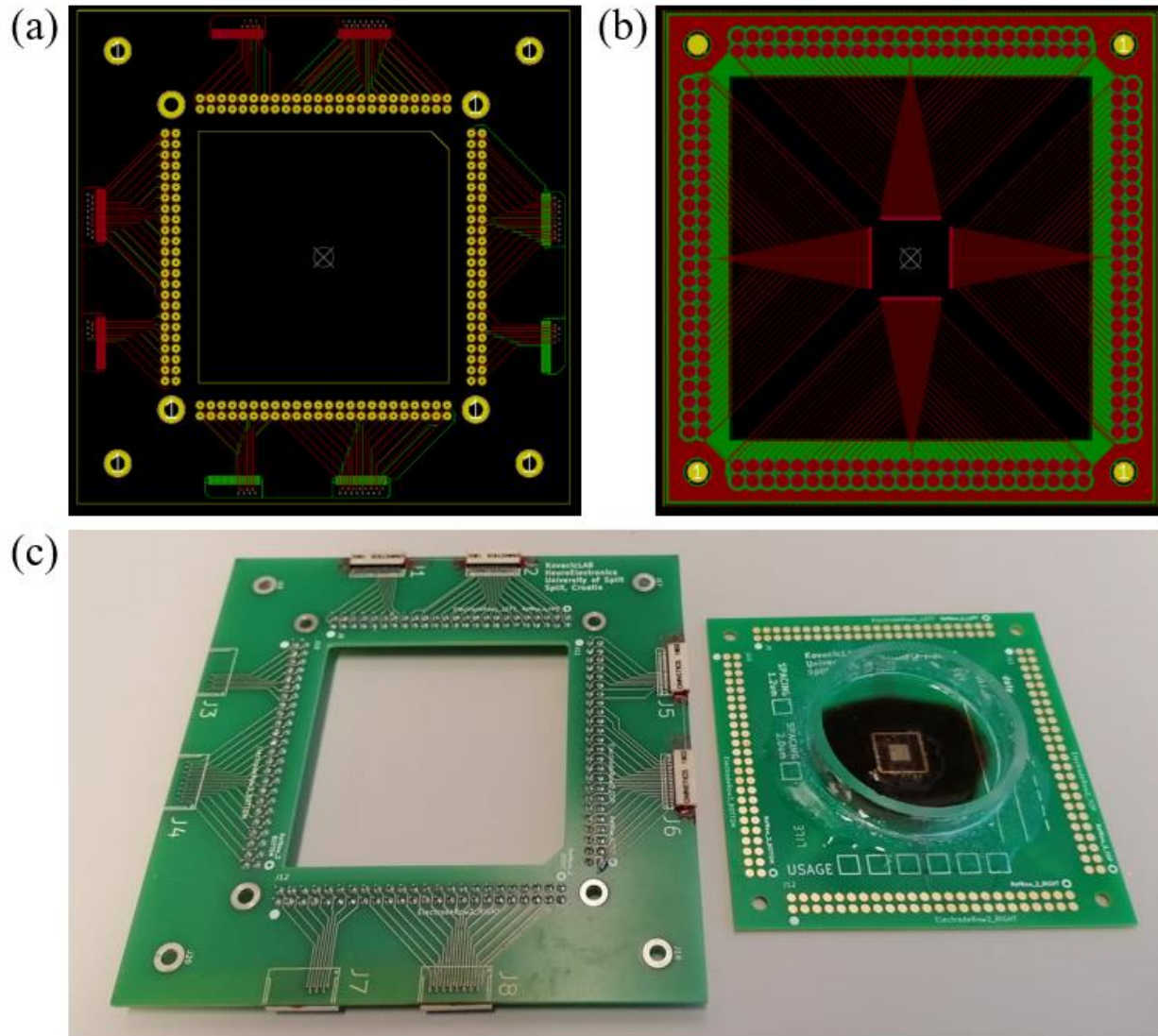


Figure 3.5 Two-level PCB architecture: (a) KiCad layout of the connector PCB (b) KiCad layout of the chip carrier PCB (c) Connector PCB (left) and chip carrier PCB (right) [83]

After designing the PCB layout in KiCad, the process parameters were set in the user interface of the manufacturer (Eurocircuits N.V., Mechelen, Belgium). Some of the PCBs were manufactured according to the same designs and parameters in the manufacturing companies Ever Star Electronics Pte., Singapore and Markovac d.o.o., Zagreb, Croatia. Table 3.1 shows the data for the chip carrier PCB. All values except board size are the same for the connector PCB.

Table 3.1 Fabrication parameters of the chip carrier PCB

Fabrication parameters of the chip carrier PCB	
Number of layers	2
Board size (X × Y)	78 mm × 78 mm
Board thickness	1.55 mm
Base material	FR4-Improved, Tg 145–150 °C
Outer layer copper thickness	12 μm base Cu
Surface finish	chemical Ni/Au
Minimum outer layer track width	0.10 mm
Minimum outer layer clearance	0.10 mm
Minimum outer layer annular ring	0.10 mm
Soldermask / legend	top & bottom soldermask: green; top

The chip was connected to the chip carrier PCB using a wedge wire bonding process with 25 μm gold wire on 192 gold pads, 48 on each side. Each golden pad was bonded using a manually operated bench-top thermosonic wire bonding machine HB05 (TPT, Karlsfeld, Germany), equipped with a 63 kHz ultrasonic system (0–10 W) [86]. The optimal bonding parameters obtained after extensive experimentation are shown in Table 3.2. US denotes a dimensionless setting defined as the relative strength of the ultrasonic signal applied to the bonding tool, which is a key parameter for bond quality.

Table 3.2 Wire bonding process parameters for the chip carrier

Wire bonding process parameters for the chip carrier		
Bond number	Bond 1	Bond 2
US	80	90
Time (ms)	200	200
Force (g; mN)	20 (196 mN)	20 (196 mN)
Tail (μm)	170	
Feed ±	10	
Bonding stage	58	

Wire bonds were encapsulated using a two-component high-temperature epoxy EPO-TEK 353ND (Epoxy Technology, Billerica, MA, USA), mixed 10:1 by weight and cured at 120 °C for 30 min. A glass ring with a diameter of 40 mm was attached to the chip carrier PCB using two-component biomedical grade elastomer Silastic MDX4-4210 (Dow Chemical Company, Midland, MI, USA), forming a circular culture well that effectively acted as a small Petri dish for the cell culture medium during experiments. Figure 3.6 shows the chip carrier PCB before and after epoxy coating and attaching the glass ring.

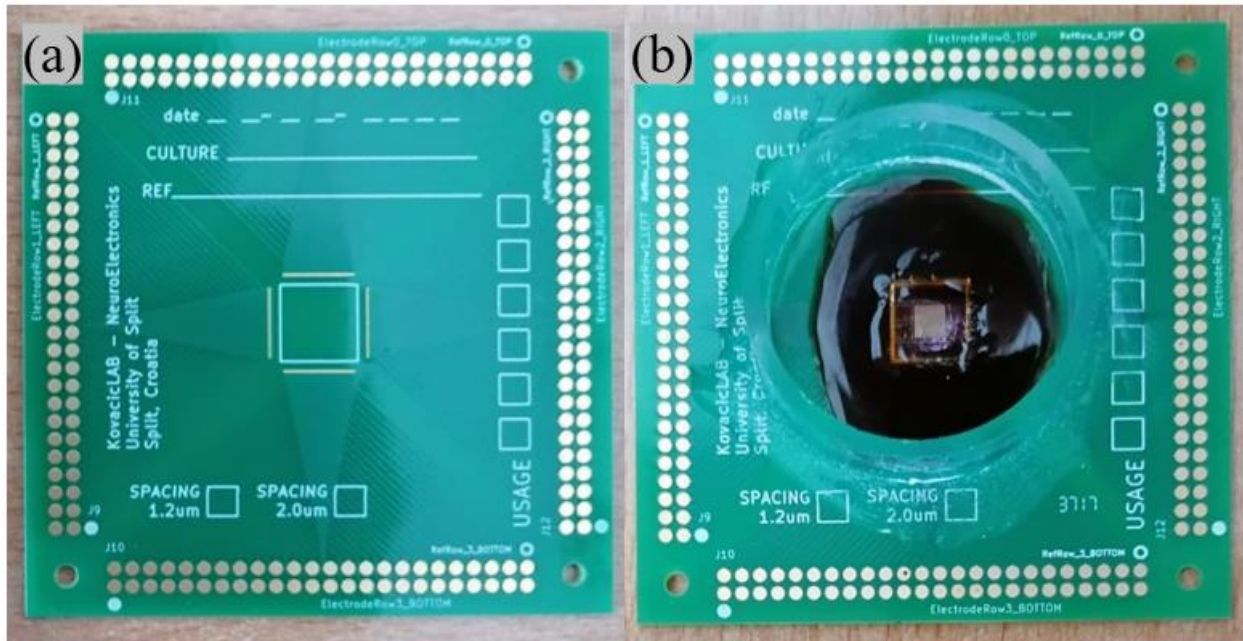


Figure 3.6 Chip carrier PCB before (a) and after (b) epoxy coating and attachment of the glass ring

During the measurements, the MEA system with cell cultures was placed in a metal box lined with aluminum foil that acted as a Faraday cage, thus reducing the influence of electromagnetic interference from the environment. Finally, the connected system with its associated components is shown in Figure 3.7. The components shown in Figure 3.7 are: computer with GUI (1), USB 2.0 cable (2), Intan RHS2000 Stimulation/Recording Controller (3), serial peripheral interface cables (4), Intan RHS 32-channel Stimulation/Recording headstages (5), PCBs with mounted MEA (6) and aluminum foil-lined metal box (7).

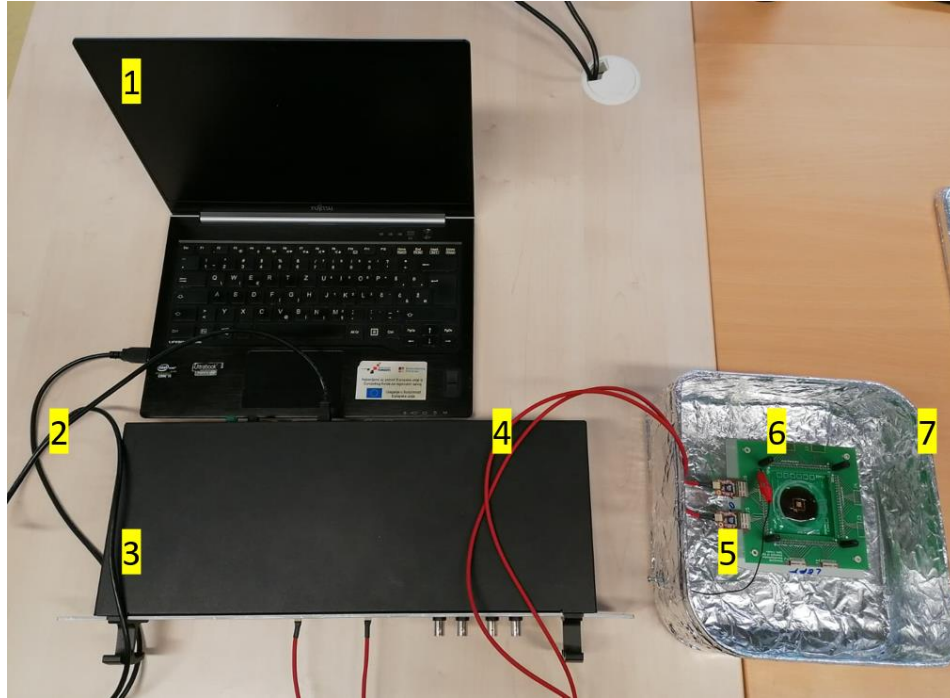


Figure 3.7 Fully assembled experimental setup for NEI/MEA combination

3.3 Magnetic field stimulator

The magnetic field stimulator used in this thesis was originally developed and characterized within our research group as part of a diploma thesis by Borić [81], and later applied in a conference paper on the effect of the electric field on spiral ganglion neurons [82]. In the following, we summarize its design and operating principles. A schematic representation of the magnetic field stimulator in relation to the MEA during the experiment is shown in Figure 3.8.

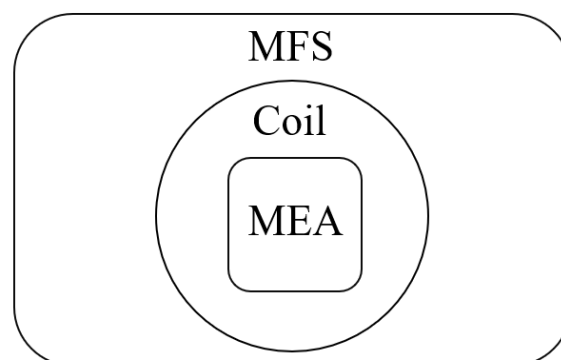


Figure 3.8 Schematic representation of the relationship between the position of the MEA and the MFS coil

The magnetic field stimulator is a self-contained battery-powered circuit for stimulating a coil that induces an electric field in the medium above the MEA chip. The electronics are implemented on a prototype PCB and powered by a pack of four Ni-MH AA 1.2 V batteries connected in series, providing a nominal voltage of 4.8 V and sufficient operating capacity for several hours of stimulation. The PCB houses an integrated circuit that generates a periodic excitation signal, discrete resistors and capacitors for signal shaping, and an output stage with a transistor in a TO-220 package, attached to a small heat sink that takes over the power dissipation at higher currents through the coil. The coil is designed without a ferromagnetic core (so-called air core coil), with a diameter of 41 mm, with 80 turns of copper wire, and is electrically connected to the PCB via a double screw terminal. The amplitude of the current through the coil is adjusted by a trimmer potentiometer which, together with a series-connected 1 Ω sense resistor, defines the output current. The voltage drop across this resistor directly corresponds to the current value (e.g., 210 mV \approx 210 mA), for easier calibration and repeatability of parameters. The values listed were defined after multiple iterations on test samples.

When a time-varying current defined in this way flows through the coil, a time-varying magnetic field generated by the coil induces an electric field with closed field lines in the medium above the MEA, as described by Faraday's law given in Eq. 3.1, where the left side of the equation represents the circulation of the induced electric field along a closed contour and the right side of the equation the negative time derivative of the magnetic flux through the surface bounded by that contour [87].

$$\oint \vec{E} d\vec{l} = - \frac{d\Phi_B}{dt} \quad (3.1)$$

where:

E – electric field / V/m

dl – line element / m

Φ_B – magnetic flux / Wb

t – time / s

Since the active area of the MEA (4 \times 4 mm) on which the neurons are monitored during the experiment is significantly smaller than the coil diameter (\approx 41 mm), the spatial change in the

intensity of the induced field within this area is relatively small, so it can be viewed in further analysis as a reproducible stimulation condition.

A simplified numerical estimate of the induced electric field was calculated from the coil geometry and the applied current waveform [87]. The MFS coil had ($N = 80$) turns, a mean radius of ($R = 20.5$) mm and an approximate axial thickness of ($l = 5$) mm. For the peak current of ($I_{max} = 210$) mA, the peak magnetic flux density at the centre of the coil was estimated from the Eq. 3.2 as:

$$B_{max} = \frac{\mu_0 N I_{max}}{2 \sqrt{R^2 + (\frac{l}{2})^2}} \quad (3.2)$$

where:

B_{max} – peak magnetic flux density / T

μ_0 – vacuum permeability / H/m

N – number of coil turns

I_{max} – peak coil current / A

R – mean coil radius / m

l – axial thickness of the coil / m

which gives $B_{max} \approx 0.51$ mT. During the 80 ms ramp phase of the sawtooth signal, the magnetic flux density increases approximately linearly from 0 to B_{max} . Assuming that the magnetic field is approximately uniform over the active 4 mm × 4 mm MEA area, the induced electric field along a circular contour can be estimated from Faraday's law (Eq. 3.1) as:

$$E(r) = \frac{r}{2} \frac{B_{MAX}}{t_p} \quad (3.3)$$

where:

$E(r)$ – induced electric field magnitude at radial distance (r) / V/m

r – radial distance from the centre of the coil / m

B_{max} – peak magnetic flux density / T

t_p – duration of the current ramp phase / s

For the active MEA area, the maximum distance from the centre to the corner is ($r = 2.83$) mm. This gives an estimated induced electric field of approximately $E \approx 9.0 \cdot 10^{-6}$ V/m. This calculation represents a simplified order-of-magnitude estimate and does not include local perturbations caused by the medium, substrate or surrounding structures.

The stimulation protocol is visualized in Chapter 4. Figure 3.9 shows magnetic field stimulator with its main components: stimulation coil (1), driver PCB with control electronics (2) and battery pack connector (3).

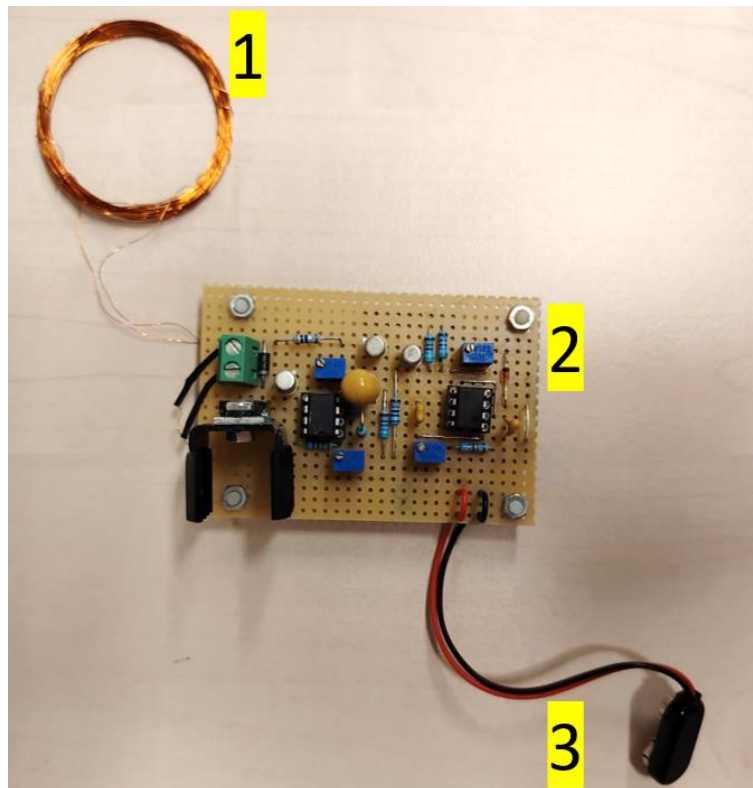


Figure 3.9 Magnetic field stimulator: main components

The description of the MEA substrate, the neuroelectronic interface and the magnetic field stimulator defines the complete experimental platform used in this dissertation. Building on the described platform, the next chapter presents experimental methods used in this dissertation, including preparation of cell cultures, stimulation protocols, acquisition and analysis of morphometric parameters, and methods for statistical processing of the obtained data.

4 EXPERIMENTAL METHODS

After defining the experimental platform in Chapter 3, this chapter presents the experimental methods used in this dissertation. Sample preparation protocols are described, including preparation of substrates and neuronal cultures *in vitro*. Data acquisition tools and procedures are defined, along with statistical methods for data processing for both research branches (MEA + magnetic field stimulator and MEA + neuroelectronic interface). Figure 4.1 shows a flow chart of the experiment, which includes the preparation of cultures, the implementation of measurements, and further processing and statistical analysis of the data.

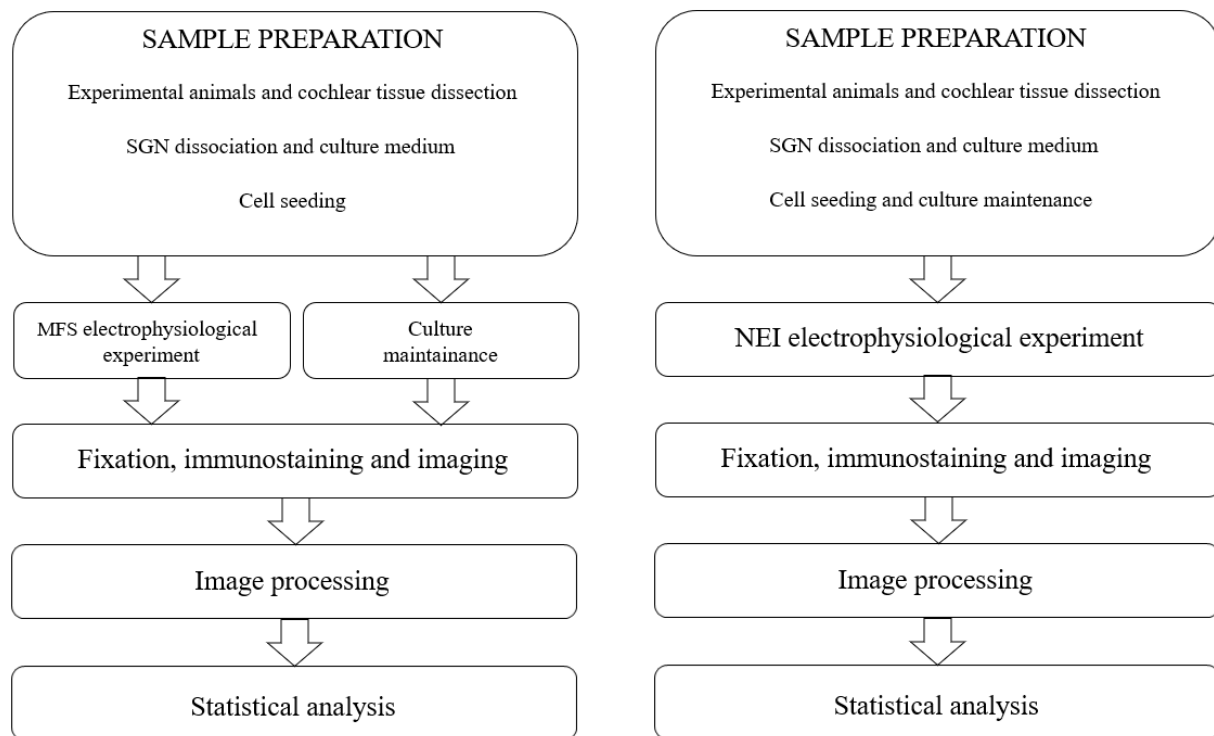


Figure 4.1 Flow chart of the experiment

4.1 Sample preparation

The sample preparation procedures described in the following sections were previously presented in our studies [80–83], and individual steps of the procedures are originally based on the established protocols referenced in the text [88 – 91]. The general protocol for working with cell cultures is identical in both research branches, and the differences in specific steps are clearly indicated. The procedure for working with laboratory animals and cell cultures was approved by the Veterinary and Food Safety Office of the Croatian Ministry of Agriculture (approvals: HR-

POK-022, registered as 525-10/0255-17-4 on 8 September 2017, and as 525-09/589-23-7 on 2 November 2023) and was carried out following the Code of Practice of Animal Care at the University of Split, School of Medicine, as stated in [83].

4.1.1 Experimental animals and cochlear tissue dissection

Dissection and culturing of spiral ganglion neurons were carried out following the established protocols previously described in Szabó et al. [88] and Vieira et al. [89]. Spiral ganglion neuron tissue was dissected from the cochleae of Sprague–Dawley rat pups at P6–P8. The animals were initially anesthetized with ice and decapitated, after which their heads were placed in dissecting buffer consisting of phosphate-buffered saline (PBS) with 0.6 % glucose (Sigma-Aldrich, St. Louis, MO, USA) and 0.3 % bovine serum albumin (BSA; Sigma-Aldrich, USA), following the protocol from Mattotti et al. [90]. Under a microscope, after opening the skull along the mid-sagittal plane, the brain was removed. The temporal bone was placed in fresh dissecting buffer, in which dissection of the otic capsule and isolation of the cochlea were performed, after which the modiolar cartilage and the organ of Corti were removed.

4.1.2 Spiral ganglion neurons dissociation and culture medium

Enzymatic dissociation of spiral ganglion neurons was conducted in 0.25 % trypsin-EDTA (Sigma-Aldrich, USA) for 25 min at 37 °C. After the dissociation, the digestion was terminated by adding an equal volume of DMEM/F12 medium (Gibco, Thermo Fisher Scientific, Waltham, MA, USA) supplemented with 10 % fetal bovine serum (FBS; Biochem, Karlsruhe, Germany) and 38 U/mL DNase (Sigma-Aldrich, USA). The tissue suspension was centrifuged for 10 min at 2 000 rpm, after which the pellet was triturated, and a single-cell suspension was obtained. Following the protocol for the promotion of the spiral ganglion neuron neurite outgrowth, according to Euteneuer et al. [91], the cells were resuspended in a Neurobasal-A-based culture medium (Gibco, Thermo Fisher Scientific, USA) containing 1 % Pen–Strep (Lonza, Basel, Switzerland), 0.5 mM L-glutamine (Gibco, Thermo Fisher Scientific, USA), B27 supplement (Gibco, Thermo Fisher Scientific, USA) and 30 ng/mL GDNF (Merck Millipore, Darmstadt, Germany). Cell concentration was determined using a Bürker–Türk counting chamber.

4.1.3 Cell seeding and culture maintenance

Cultures for the neuroelectronic interface experiments were seeded at a density of 20 000 cells per substrate in a 100 μ L volume and settled for 1–2 h in an incubator (37 °C, 5 % CO₂, 85 % humidity). For magnetic field stimulator experiments a higher seeding density of 40 000 cells per MEA chip was used, while the remaining steps of the protocol were identical. A portion of the medium (approximately 50 %) was replaced every 2–3 days with fresh, pre-warmed culture medium in the neuroelectronic interface experiment, and every day for six DIV in the magnetic field stimulator experiment. Depending on the experiment, cultures were maintained for 6–7 DIV. Electrophysiological recordings with the neuroelectronic interface were performed on DIV 7, whereas magnetic field stimulator stimulation protocols were applied for DIV 6.

4.1.4 Fixation, immunostaining and imaging

The cell culture treatment protocol in the following paragraph was performed after electrophysiological experiments. Cells were fixed in 4 % paraformaldehyde (Thermo Fisher Scientific, Waltham, MA, USA) for 30 min, and washed three times with 1X PBS after 6 to 7 DIV, depending on the experiment. Permeabilization was conducted with 0.1 % Triton X-100 (Millipore, Merck, Germany) for 5 min. Samples were rinsed three additional times with 1X PBS. Incubation was carried out to block non-specific binding. The samples were incubated for 90 min at room temperature in PBS containing 1 % normal goat serum (Dako, Santa Clara, CA, USA). Immunostaining was performed with a mouse monoclonal anti- β III tubulin antibody (1:500, Millipore, Merck, Germany) for neuron labeling (Tuj-1) and a rabbit polyclonal anti-S100 antibody (1:500, Sigma-Aldrich, USA) for labeling of the glial cells (S100+). Primary antibodies were applied overnight at 4 °C. The next day, samples were washed three times in PBS and incubated for 90 min with secondary antibodies: Alexa 488 goat anti-mouse and Alexa 568 goat anti-rabbit (Thermo Fisher Scientific, Waltham, MA, USA), each diluted 1:500 in PBS with 1 % normal goat serum. DAPI (5 μ g/mL, 1:500 dilution; Molecular Probes, Thermo Fisher Scientific, USA) was used for the nuclear counterstaining for 5 min. Additionally, samples were rinsed five times with PBS. Immu-Mount (Thermo Scientific, Waltham, MA, USA) was used for mounting the samples and preparation for imaging. Fluorescence images were acquired using a fluorescent microscope BX61 (Olympus, Tokyo, Japan), paired with a monochromatic CCD Retiga R6 camera (Teledyne, Thousand Oaks, CA, USA). Sample positioning was controlled with a motorized scanning stage from Prior Scientific (Prior Scientific, Cambridge, UK), driven by μ Manager

software (version 2.0.2, Vale Lab, UCSF, San Francisco, CA, USA). Machine learning-based KARMENscience image analysis platform (Bedalov d.o.o., Kaštel Sucurac, Croatia) was implemented to overlap images and map them into a single composite image. The chip surface with P6, 7 DIV rat pup spiral ganglion neurons stained with Tuj-1 is shown in Figure 4.2. Whole-chip image was reconstructed from a 6×6 grid of images acquired at $40\times$ magnification. Neurons are labeled with β III-tubulin and nuclei with DAPI.

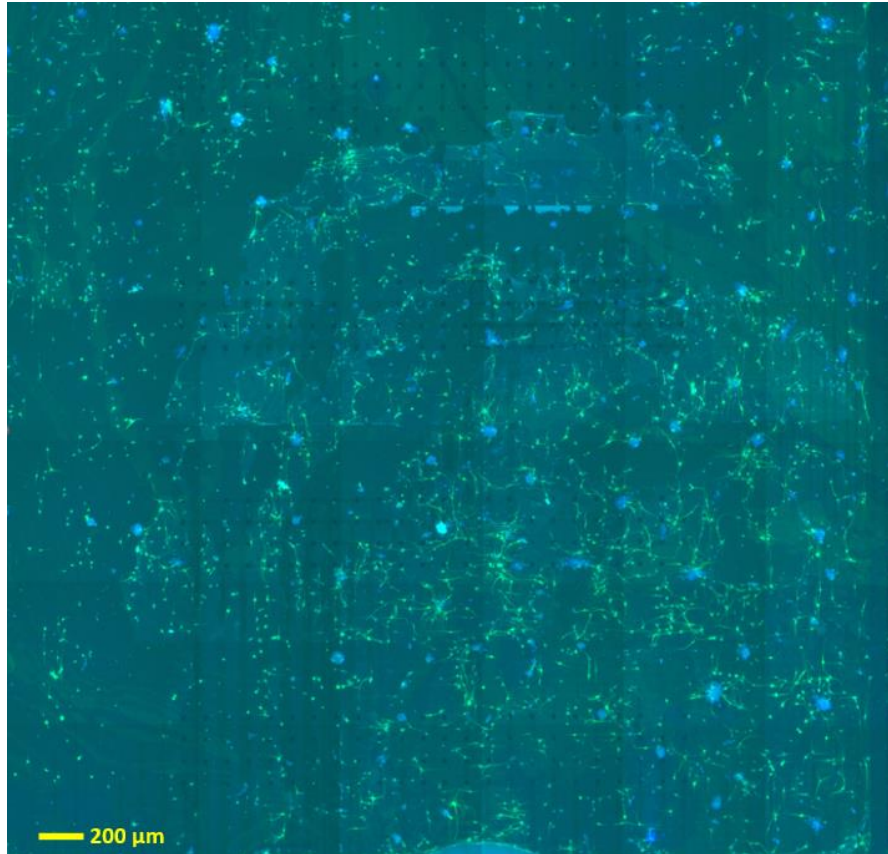


Figure 4.2 Whole-chip composite fluorescence image of SGN cultures on the MEA [83]

4.2 Magnetic field stimulator experiment

In this section, the methods of conducting the experiment with magnetic field stimulator are described, complementing the hardware description in Section 3.3, and following the flow chart in Figure 4.1. The design of the experiment is presented, the procedure of morphometry and data processing with image processing software is described, and the statistical methods used in Chapter 6 are defined and explained. The analyses presented in this section are based on the same experimental groups and imaging datasets previously described in our studies [81, 82]. Here, we

re-analyze these cultures using an extended set of morphometric and orientation metrics, together with new statistical methods and application of different image processing software, in order to obtain a more detailed quantitative description of mechanotactic and electrotactic effects.

The aim of this experiment is to examine the effects of mechanotactic mechanisms from substrate microtopography and electrotactic mechanisms from electric field stimulation on spiral ganglion neuron morphology. The effects of the aforementioned mechanisms are observed separately and in combination. A control group without the presence of substrate microtopography and electric field is also analyzed. Table 4.1 shows the four experimental groups.

Table 4.1 Experimental groups used in the MFS mechanotaxis and electrotaxis experiments; Adapted from [81]

Experimental groups		Substrate	
		Glass	MEA
Stimulation	No stimulation	Glass control	Chip control
	EF	Glass EF	Chip EF

4.2.1 Magnetic field stimulator: stimulation protocol

Stimulation with magnetic field stimulator was performed using a 41 mm diameter, 80-turn air core copper coil, described in Section 3.3. The magnetic field stimulator generated a sawtooth signal with a period of 100 ms ($f = 10$ Hz), shown in Figure 4.3. Each period $T = 100$ ms consisted of an 80 ms ramp phase (t_p) during which the current increased linearly to the peak value I , followed by a 20 ms low interval (t_L) at zero current. The voltage on the trimmer potentiometer was adjusted to 210 mV using a 1Ω series resistor, resulting in a peak coil current of 210 mA, and a reproducible induced electric field in the culture medium. The stability of the signal shape, amplitude and period was checked manually with a TENMA 72-8725 oscilloscope (TENMA, Farnell, UK) every 60 minutes during 13 hours of operation. In order to maintain a stable stimulation configuration due to voltage drop in the circuit, the batteries were changed every 12 hours throughout the experiment. During stimulation, the coil was positioned in such a way that its plane was parallel to the plane of the MEA substrate, and its central axis was perpendicular to the plane of the substrate. The total exposure of the samples to electric field stimulation was 6 days, and the control groups (Glass control and Chip control) were kept under the same conditions without stimulation, described in Section 4.1.2.

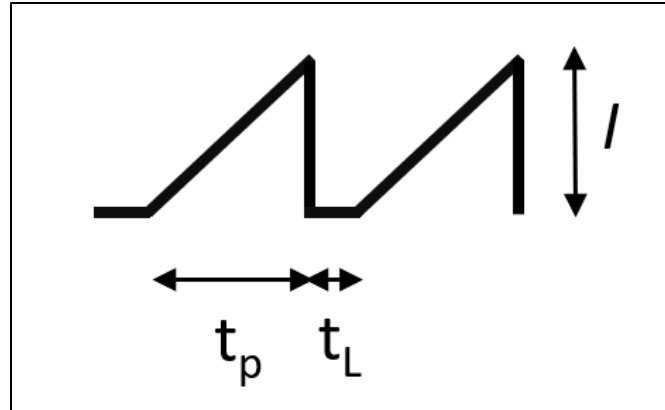


Figure 4.3 Schematic of the MFS stimulation waveform; Adapted from [81]

4.2.2 Morphometrics and image processing

The following morphological parameters were observed in this experiment:

- Soma area (μm^2)
 - Only neurons where it is possible to visually identify the soma were observed.
 - Clumps of multiple somas into a single larger structure are ignored.
- Neurite length (μm)
 - The longest neuron neurites were observed, except in cases where they could not be discerned.
 - Only one neurite per neuron was observed, except in cases where there were not enough neurites in the observed area from which the statistical sample was taken.
 - Neurites in clumps that could not be clearly differentiated were ignored.
- Orientation of neurites relative to the 0° and 90° axes ($^\circ$)
 - Only one neurite per neuron was observed, except in cases where there were not enough neurites in the observed area from which the statistical sample was taken.
 - Neurites in clumps that could not be clearly differentiated were ignored.

ImageJ software (version 1.54 g; National Institutes of Health, Wayne Rasband, MD, USA) was used for image processing. The processing steps consisted of loading and scaling the image,

marking the soma or neurite with appropriate tools, measuring the required parameters, and saving and exporting them in a format suitable for further statistical processing. After uploading the image, the first step was to adjust the scale of the image in order to obtain the appropriate measured dimensions. The default distance in pixels was set at 2.2 for unit distance at pixel aspect ratio 1.0, and the unit length of μm was set. This resulted in a scale of 2.2 pixels/ μm , which was used in the measurements. For each of the mentioned parameters, a separate tool was used to manually mark the elements on the image. The soma area was measured with the tool "Elliptical selection" with stroke color cyan, width 3. The length of the neurites was measured with the tool "Segmented line" with stroke color magenta, width 3. The orientation of the neurites was measured with the tool "Rotated rectangle" with stroke color white, width 3. Each of these measurements was performed separately and, if possible, on different neurons.

Each measured item was saved with the command "m" in the table of measurements in comma separated value (CSV) format and with the command "t" in a separate region of interest (ROI) in order to preserve the data on the measurement and the position of the marks. The commands in the checkboxes "Show All" and "Labels" were used to label the marks, and the command "Flatten" enabled saving these labels to the image in full format. Each parameter was measured on 270 different ROIs per sample, 30 in each of the 9 segmented images from which the entire image was composed. The CSV files were named according to the principle "Chapter number in which the metric is used_Sample name_Abbreviation of the measured parameter_Measure". For example, the name "6_Glass_Control_NL_Measure" was used for the file with the measured neurite length on a glass substrate without stimulation, where NL denoted neurite length. Analogously, the labels for soma area (SA) and neurite alignment (NA) were used. The ROI files were also named according to the same principle, except that "ROI" was added at the end instead of "Measure". The CSV files were imported into MS Excel (version: 2021 LTSC) with the number of the measured parameter (1–270), the name of the set, and the values "Area", "Length" and "Angle" for the corresponding parameters. In some cases, the coordinates of the position of the measured parameter x and y and the coordinates of the center of the entire sample x_0 and y_0 were also used.

A representative view of ROI measurements is shown in Figure 4.4 for the morphological parameters: soma area (a), neurite length (b) and neurite alignment (c). For each measured

parameter, an image crop with multiple neurons is shown, with only some structures suitable for measurement, i.e., included in the analysis.

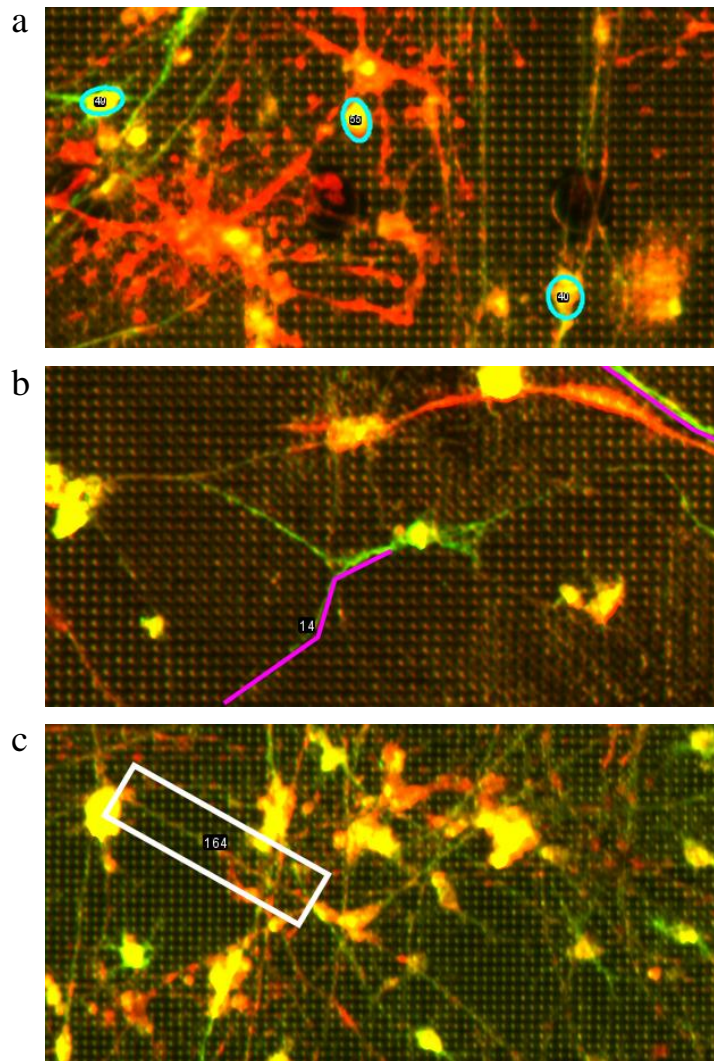


Figure 4.4 Representative ImageJ morphometric measurements: (a) soma area, (b) neurite length and (c) neurite alignment; Adapted from [81]

In panel a, cyan ellipses mark the suitable somata that were measured and included in the statistical analysis. Clusters of neuronal somata are visible in the image, but they were not measured due to large overlaps and unclear boundaries, which prevent reliable area measurement.

In panel b, the measurement of neurite length is shown. The segment that was taken into account, marked with a magenta dashed line, is clean and can be clearly distinguished. The other neurites are also clean and the image quality is good, but due to mutual overlap it is not possible to

determine where their boundaries are and which neurite belongs to which cell, therefore no measurement was performed on them.

Panel c shows the measurement of neurite alignment, indicated by the white rectangle. In the example from the picture, a large number of neurites overlap and it is not possible to reliably determine their boundaries and which neuron they belong to.

In future experiments, the cell culture density, i.e., the number of neurons per chips, should be taken into account. The high density of 40 000 cells per sample (used in Chapter 6) made clear reading difficult, but it was still possible to reliably measure a sufficient number of ROIs. On the samples paired with the neuroelectronic interface in Chapter 7, half the density of cell cultures on the chips was used, which made the measurement easier and increased its reliability.

4.2.3 Statistical methods and data processing

This section describes the statistical methods and data processing used to analyze the impact of mechanotaxis on spiral ganglion neuron cultures, carried out in Chapter 6. The procedure is almost identical to the analysis of the impact of electrotaxis in the second section of the same chapter, and the difference is stated in the appropriate place in the text. The same methods are used in the third section of the chapter, which deals with the combination of the effects of the mentioned mechanisms. Analyses using all individual neurites/cells were interpreted purely descriptively and were not used to calculate inferential p-values to avoid pseudoreplication. A comparison of the following samples is used for the analysis:

- Mechanotaxis: Glass control and Chip control
- Electrotaxis: Glass control and Glass EF
- Combined effect:
 - Glass control and Chip EF
 - Chip control and Chip EF
 - Glass EF and Chip EF

After importing data from CSV tables and transforming it into XLSX format, the data is grouped by main tables, namely for soma area (μm^2), neurite length (μm) and neurite alignment ($^\circ$).

4.2.3.1 Soma area and neurite length: methods and processing

A description of the data distribution was obtained using classical methods of descriptive statistics. The table of descriptive statistics for both samples (Glass control and Chip control) contains the following values, marked in the tables with the indicated symbols:

- Sample size: n
- Mean
- Median
- Standard deviation
- Standard error: SE
- 95 % confidence interval: CI (95 %)
- The smallest value within the sample: MIN
- The largest value within the sample: MAX
- First quartile: Q1
- Third quartile: Q3
- Interquartile range: IQR
- Value of the bottom 10 %: Percentile_10 (P10)
- Value of the top 10 %: Percentile_90 (P90)
- Mean without the bottom and the top 10 %: Trimmed mean (10 %)
- Skewness
- Kurtosis

The above measures are calculated using standard MS Excel formulas. Based on the obtained data, box-and-whisker plot graphs are drawn for soma area and neurite length for both samples. The "Histogram" tool from the "Data analysis" toolpack provides bins for soma area and neurite length, which are used to create comparative histograms for both samples. Tukey fences were calculated

for both samples to estimate the proportion of extreme values within the set [92]. The lower limit is calculated by formula 4.1, and the lower limit by formula 4.2 and indicate the whiskers of the boxplots. The Tukey fences, Q1, Q3 and IQR are expressed in the same unit as the analyzed variable.

$$\text{Lower} = Q1 - \text{IQR} \cdot 1,5 \quad (4.1)$$

$$\text{Upper} = Q3 + \text{IQR} \cdot 1,5 \quad (4.2)$$

Cliff's δ was used to measure the difference between the proportion of pairs (Glass control, Chip control) with Glass control > Chip control and the proportion of pairs with Chip control > Glass control [93]. Probability of superiority (PS) was defined as $PS = P(\text{Glass control} > \text{Chip control})$, with the relationship $\delta = 2 \cdot PS - 1$ [94]. Mann–Whitney U was used as an auxiliary step in this calculation [95]. The purpose of this use of the method is to measure how likely it is that a value from one set will be greater than a value from the other set when all possible pairs are compared, i.e., it does not depend on the difference between mean or median values. The method does not require the assumption of normality of the distributions and is robust to differences in the shape of the distributions. In principle, the value of Cliff's δ is interpreted as follows regarding the superiority of the members of the two sets: $|\delta| \approx 0.15$ small effect, ≈ 0.33 medium effect, ≈ 0.47 high effect [93, 94].

A non-parametric permutation approach based on the median difference was used to estimate the location difference between the two groups [96]. Given that only one sample was available for each experimental setup, and the number of analyzed objects (soma, neurite, orientation) was large, classical parametric inferential tests based on independent experimental replicates were not applied. Instead, the observed median difference, Δ_{median} , was calculated and the empirical null distribution Δ_{perm} was constructed by randomly permuting the group labels.

In each permutation, the condition labels (A/B) were randomly permuted, after which the median difference Δ_{perm} was recalculated. The procedure was repeated $N = 5\,000$ times or $N = 1\,000$ times, depending on the case, yielding the distribution of values that would be expected under the null hypothesis that there is no systematic difference between conditions (i.e., that the group labels are interchangeable). The two-tailed Monte Carlo p-like value is defined by formula 4.3, where k is the number of permutations for which $|\Delta_{\text{perm}}| \geq |\Delta_{\text{median}}|$:

$$p_{like} = \frac{k+1}{N+1} \quad (4.3)$$

Due to $n = 1$ culture/chip per condition, $p_{like_two_sided}$ is not interpreted as a classical inferential p-value, but as a descriptive measure of the compatibility of the observed difference with the null hypothesis within the framework of the particular experiment. In addition to $p_{like_two_sided}$, the effect size (Cliff's δ) and the median difference itself were reported for each comparison.

Finally, the permutation of the null distribution of Δ_{med} is shown by a histogram.

4.2.3.2 Neurite alignment: methods and processing

Two metrics indirectly obtained from the measured neurite angle were used to analyze NA:

- Biaxial alignment index: AI_{bi}
- Angle to the nearest substrate axis: $\delta\theta_{ax}$

Biaxial alignment index (AI_{bi}) indicates how close the measured values of neurite angles are in relation to the reference 0° and 90° axes. It is calculated by formula 4.4, where θ is the measured angle. The calculated values of AI_{bi} range from 0 to 1, where 0 means the greatest possible distance from the reference axes, and 1 the complete coincidence with them. In this way, the influence of the topography of the substrate on NA is checked.

$$AI_{bi} = \text{AVERAGE} (\text{ABS} (\text{COS} (2 \cdot \text{RADIANS} (\theta)))) \quad (4.4)$$

Angle to the nearest substrate axis ($\delta\theta_{ax}$) denotes the distance from the reference axes in absolute value and is calculated using formula 4.5.

$$\delta\theta_{ax} = \text{MIN} (\text{MOD} (\theta; 90); 90 - \text{MOD} (\theta; 90)) \quad (4.5)$$

Descriptive statistics (main table of descriptive statistics) and box-and-whisker plot diagrams are calculated and plotted in the same way as in the case of soma area and neurite length. The Monte Carlo procedure is used for AI_{bi} in the same way as for soma area and neurite length. The comparison of the neurite orientation angles θ of the observed groups is shown graphically with a polar graph.

When analyzing NA in electroaxis, alignment values are used in relation to the circular electric field lines induced by the coil and read:

- Circular alignment index (AI_circ)
- Angle to local field tangent ($\delta\theta_{\text{circ}}$)

To obtain the above values, it is necessary to know the coordinates of each measured ROI (x, y) and its position relative to the center of the sample (x_0, y_0). AI_circ is calculated using formulas 4.6 – 4.11.

$$\text{AI}_{\text{circ}} = \text{COS} (\text{RADIANS} (\Delta\theta [0^\circ, 180^\circ]))^2 \quad (4.6)$$

$$\Delta\theta [0^\circ, 180^\circ] = \text{MOD} (\theta - (\text{phi}_{\text{rad}_{180}} (\text{set_name})) + 180; 180) \quad (4.7)$$

$$\text{phi}_{\text{rad}_{180}} (\text{set_name}) = \text{DEGREES} (\text{ACOS} ((\Delta x(\text{set_name})) / (r(\text{set_name})))) \quad (4.8)$$

$$\Delta x(\text{set_name}) = x - x_0 \quad (4.9)$$

$$r(\text{set_name}) = \text{SQRT} (\Delta x(\text{set_name})^2 + \Delta y_{\text{math}} (\text{set_name})^2) \quad (4.10)$$

$$\Delta y_{\text{math}} (\text{set_name}) = y - y_0 \quad (4.11)$$

$\delta\theta_{\text{circ}}$ is calculated using formula 4.12:

$$\delta\theta_{\text{circ}} = \text{IF} ((\Delta\theta [0^\circ, 180^\circ]) > 90; 180 - (\Delta\theta [0^\circ, 180^\circ]); (\Delta\theta [0^\circ, 180^\circ])) \quad (4.12)$$

All alignment indicators in equations 4.4 to 4.12 are dimensionless quantities, and all angles are expressed in degrees. The longitudinal coordinates x, y, x_0 and y_0 are expressed in the same units.

The rest of the procedure is the same as for the mechanotaxis analysis case. The combined cases in Section 6.3 are compared analogously to the cases in Sections 6.1 and 6.2, using the metrics and methods that were used in those cases.

4.3 Neuroelectronic interface experiment

In this section, building on Section 3.2, the experimental procedures and statistical methods used in Chapter 7 are described. An overview of mechanotaxis testing on MEA samples of spiral ganglion neuron cultures grown according to the protocol from Section 4.1 is presented. Analyses were performed on the experimental group of samples partially processed in [83].

The aim of the experiment is to examine whether spiral ganglion neuron cell cultures grown in vitro on MEA substrates directly affect their morphological parameters, i.e., neurite length and orientation along the substrate axis, through the action of mechanotaxis.

4.3.1 Validation of mechanotaxis on microelectrode array substrates

Before electrophysiological analysis of spiral ganglion neuron cultures, the validation experiment was performed on 5 chips with 20 000 neurons seeded per chip, in contrast to the samples from Chapter 6, which contained 40 000 neurons per chip. Considering a set of 5 identical chips with the same density of neurons, in addition to basic descriptive statistics, an inferential statistical analysis was performed using two-factor analysis of variance (ANOVA) with replication [97] in MS Excel in order to examine the uniformity of the influence of mechanotaxis in the observed population.

Morphometric measurements were taken and organized using the same methods described in Section 4.2.2, with the exception that the soma area was not taken into account during the analysis in this chapter. 30 ROIs per zone were measured on each sample, i.e., a total of 120 ROIs per chip, which gives a total of 600 ROIs for neurite length and the same number for neurite orientation. The samples were selected according to the same rules as in Chapter 6, i.e., the longest neurite per neuron for the neurite length. Given the half-smaller density of the neuronal population, the occurrence of clusters of neurons with unclear neurite boundaries was significantly lower, therefore the measurement process itself was significantly easier. The sampling plan is shown in Table 4.2. The same plan applies to both metrics (neurite length and neurite alignment).

Table 4.2 Measurement plan for mechanotaxis parameters for the NEI experiment

Chip	Zone				
	Zone 1	Zone 2	Zone 3	Zone 4	ROIs/chip
Sample 1	30	30	30	30	120
Sample 2	30	30	30	30	120
Sample 3	30	30	30	30	120
Sample 4	30	30	30	30	120
Sample 5	30	30	30	30	120
				Total	600

The descriptive part of the analysis was carried out using part of the methods described in Section 4.2.3. In MS Excel, the basic descriptive values were tabulated (listed in the entries in Section 4.2.3.1. Neurite lengths (μm) and neurite alignment (AI_bi) for the neuronal population by zone were compared graphically with box-and-whisker plots.

The influence of mechanotaxis on the parameters of neurite length and AI_bi was tested with a two-factor ANOVA test with replication (5 chips \times 4 zones) in MS Excel (Data / Data Analysis / ANOVA: Two-Factor With Replication / Alpha = 0.05 / Labels included). In the experimental design, the rows of the ANOVA table represent the chip factor, i.e., the biological replicate, and the columns represent the zone factor, i.e., the substrate microtopography dimension. Each cell of the 5 \times 4 data table for the ANOVA test contained the weighted average of 30 ROIs for the corresponding metric. In addition to the variability between chips (Rows) and between zones (Columns), the final table also gives the residual error component (Error). For each source of variation, the sum of squares (SS), the degrees of freedom (df), the mean square (MS = SS/df), the F statistic (MS_factor / MS_error), the associated p-value and the critical F value (F_crit) for $\alpha = 0.05$. The null hypothesis is that the averages for the observed metric, neurite length or AI_bi, are the same across all chips and zones, i.e., that there is no effect of either chip or zone). A factor is considered to have a statistically significant effect if $F > F_{\text{crit}}$ and $p < 0.05$. In this way, the two-factor ANOVA tests whether mechanotactic readouts (neurite length and alignment) show systematic differences between micropillar zones and whether these effects are reproducible across MEA chips.

4.3.2 Acquisition and stimulation of extracellular neuronal activity

This section describes the settings of the system for recording and stimulation of neurons, as well as the procedures and protocols of recording and stimulation during the electrophysiological experiment. An overview of the application programmed in MATLAB for browsing, sorting and analyzing the recorded data is also given. The manufacturer's GUI (Intan Technologies) has the ability to simultaneously monitor 32 channels on each of the four ports (A-D). Each channel corresponds to one electrode on the chip, and the pairing is determined by the architecture of the chip and the derived bonds. The layout of the electrodes on the chip zone is shown in Figure 4.5.

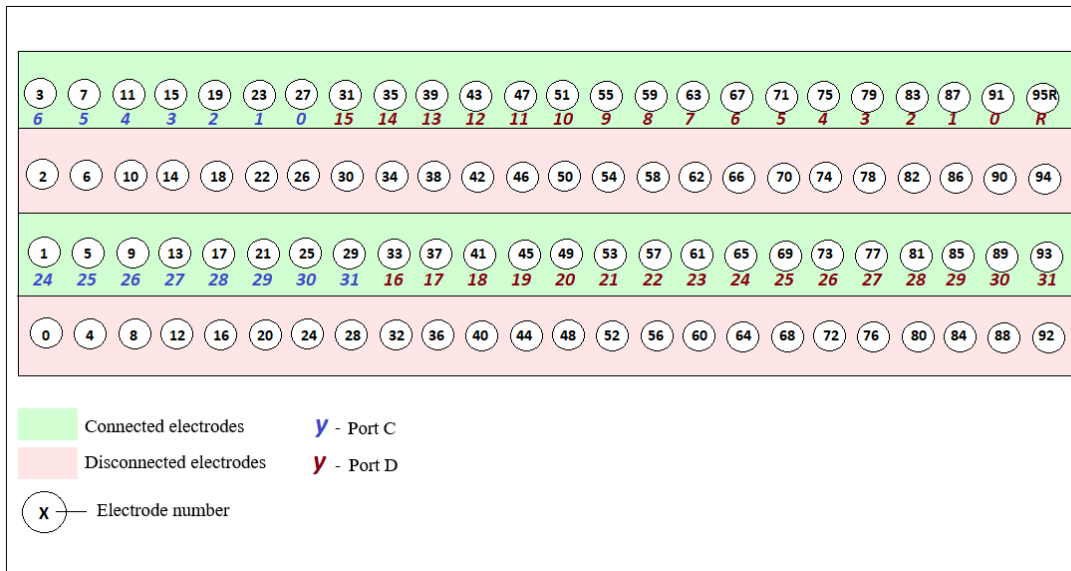


Figure 4.5 Electrode arrangement per chip zone

During recording, with our hardware settings, it is possible to observe one zone at a time, i.e., 47 active electrodes, arranged every other row (highlighted in green as in Figure 4.5), and a reference electrode (top row on the right) that is connected to the ground of the aluminum box (Figure 3.7) to significantly reduce noise. In all recordings, the highest available resolution signal acquisition sampling rate was used ($33.3 \mu\text{s}$ for 30 kS/s). When recording extracellular signals, as stated in [69], readings of a wide range of different neurophysiological activities are possible, therefore it is important to perform initial filtration to remove unwanted signals and noise without negatively affecting the system's ability to read APs. After experimenting with different values on several samples, a lower cutoff frequency of 750 Hz and an upper cutoff frequency of 7500 Hz were determined for the basic band-pass filter settings. During recording, for easier data management in post-processing, the recordings are cut to 60 seconds, after which the system saves the existing one and starts a new RHS file. The manufacturer's GUI enables monophasic, biphasic and triphasic stimulation pulses, individual or in a pulse train with a set frequency in the range of $\pm 10 \text{ nA}$ up to $\pm 2.55 \text{ mA}$. In our experiments, we used predominantly monophasic negative pulses of the order of tens and hundreds of μA , which approximately corresponds to the sizes used in [76]. Because electrical stimulation of one electrode creates artifacts on adjacent microelectrodes due to capacitive crosstalk between pins ($\approx 0.15 \text{ pF}$ between adjacent pins). In order to reduce this, the "Amplifier settling" function was activated during stimulation on all headstage channels.

4.3.3 Postprocessing in a MATLAB application

RHS files recorded as in the previous section are viewed, searched, processed and prepared for further processing in MS Excel using a custom-made application programmed in MATLAB. The application is adapted to the architecture of the experimental hardware interface described in the previous chapters. The application consists of 31 functions and approximately 5 000 lines of code. Only those functions that were used in the creation of this dissertation are described below.

The home page is shown in Figure 4.6. The main buttons for loading the RHS file (Open .rhs File) and the plot signal (Plot) are displayed on the home page. Loaded files with their parameters (A: stimulation amplitude, D: phase duration, Left: zone, equivalent to zone 2) are visible in the "Loaded RHS data" window, and the moments of stimulation triggers, if any, are visible in the "Triggers" window. The system allows manual selection of channels to be plotted using checkbox buttons at the bottom of the screen that correspond to the arrangement of electrodes on the chip zone, or automatic selection of channels according to the parameters set in the "Automatic channel selection" menu. With automatic selection, the application independently searches for signal parameters such as the minimum distance between signal peaks, minimum prominence, minimum and maximum value of the peak. The system can also load multiple files simultaneously (checkbox "Multiple RHS"), align signals to the same starting time point (checkbox "Relative time") and plot signals in separate windows (checkbox "Multiple plots").

The signal is viewed on the main plot shown in Figure 4.7. The upper graph shows the signal of the selected channel or more (y shows the amplitude in μV), and the lower graph on the same time scale shows the stimulation pulse expressed in μA . The color of the selected channels, the name of the channel, the zone in which it is located and the stimulation parameters, if stimulation is present, are indicated in the image legend. The two main functions of the application, in addition to the visual review of recordings; signal search by default parameters with export of statistical data in XLSX format (button "Signal analysis") and Pearson correlation coefficient calculation with visual display for selected channels (button "Compare sig.").

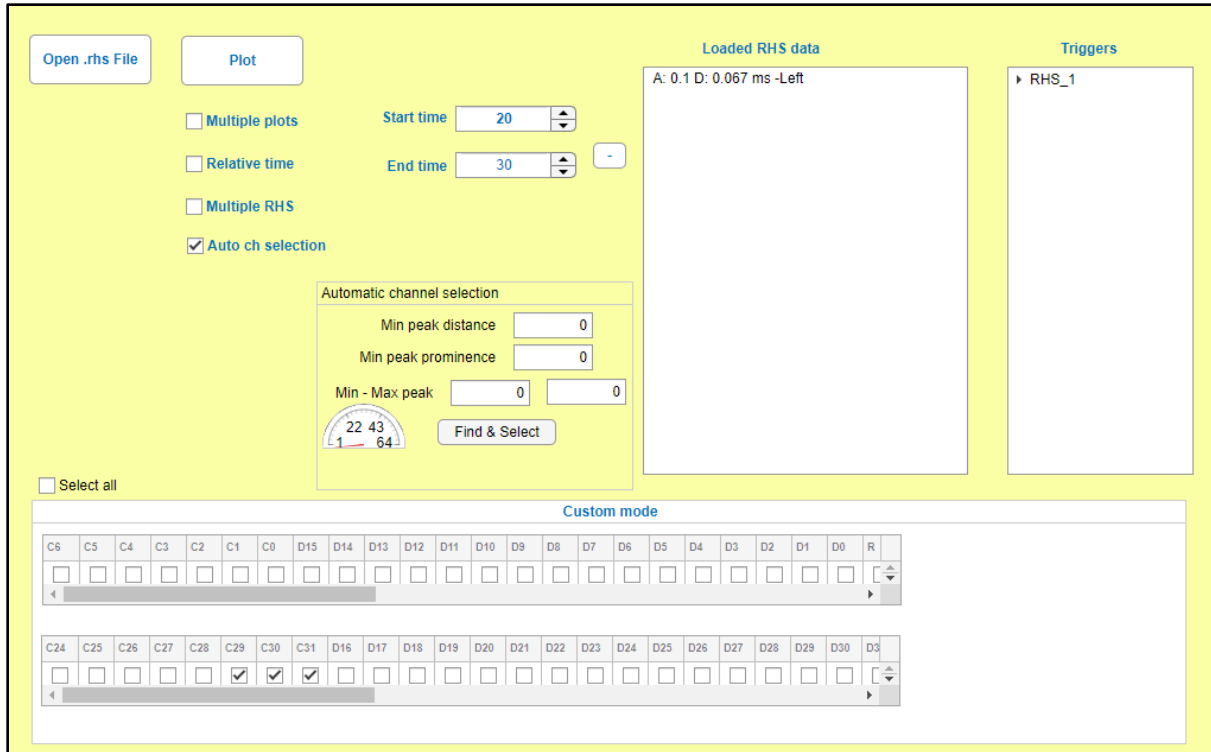


Figure 4.6 The home page of the MATLAB application interface

The signal detection function enables finding signal peaks according to the given signal values, namely: minimum and maximum signal amplitude, minimum prominence, and peak distance, which also represents a detection step. Based on the peaks found in this way, a table is created in XLSX format with the following sizes:

- Total number of peaks
- Amplitudes of positive, negative and all peaks (μV)
- Width of positive, negative and all peaks at half-height of the signal (ms)
- Distances between positive, negative and all peaks (ms); essential for constructing interspike intervals (ISI); (ms)
- Mean, standard deviation and standard error for all listed quantities

The origin of the signal source is determined using the Pearson correlation coefficient (R) for the selected electrodes and represents a linear correlation of the compared data sets. The value of the coefficient ranges from -1 to 1, with a higher absolute value representing a higher probability that

the signals originate from the same source. In Chapter 7, the values of the dominant electrodes, i.e., the electrodes on which the highest signal reading was recorded, were compared with other neighboring electrodes and the search window and correlogram are shown.

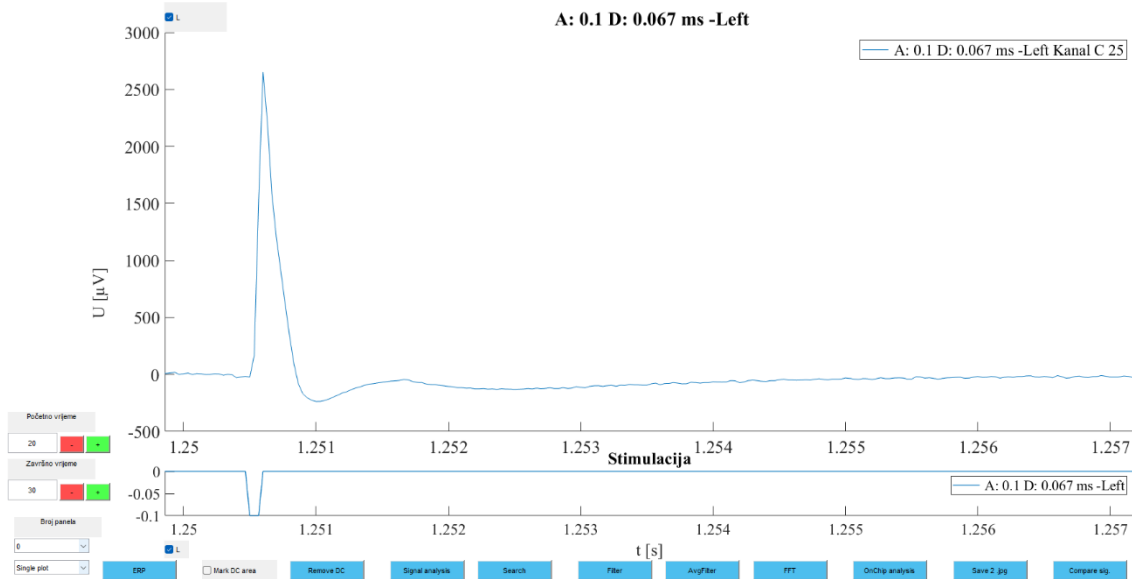


Figure 4.7 Main plot window with basic functions

This chapter described the experimental methods used in this dissertation. The preparation and cultivation of cell cultures were presented, together with neuronal stimulation protocols, data acquisition procedures and statistical methods. Before the biological effects of the developed platform can be interpreted, it is necessary to evaluate the quality and uniformity of the substrate itself, since substrate irregularities could directly affect the measured parameters. Therefore, the following chapter presents the characterization of the MEA substrate, including the analysis of its material composition and the interaction with the culture medium.

5 SUBSTRATE CHARACTERIZATION

Before the interpretation of the biological experiments, this chapter presents the characterization of the substrate, originally published in Delipetar et al. [98]. A quantitative analysis of the composition of the chip surface and the interaction with Neurobasal-A-based culture medium, hereafter NB-A, which is the main component of the culture medium, was performed. Figure 5.1 shows SEM images for each of the four chip zones (panel a - panel d), with the corresponding micropillars as previously defined in Section 3.1, and one electrode. The following settings were used for acquisition: magnification 1600 \times , 15 kV, tilt 0 $^\circ$, working distance (WD) 6.4–6.5 mm.

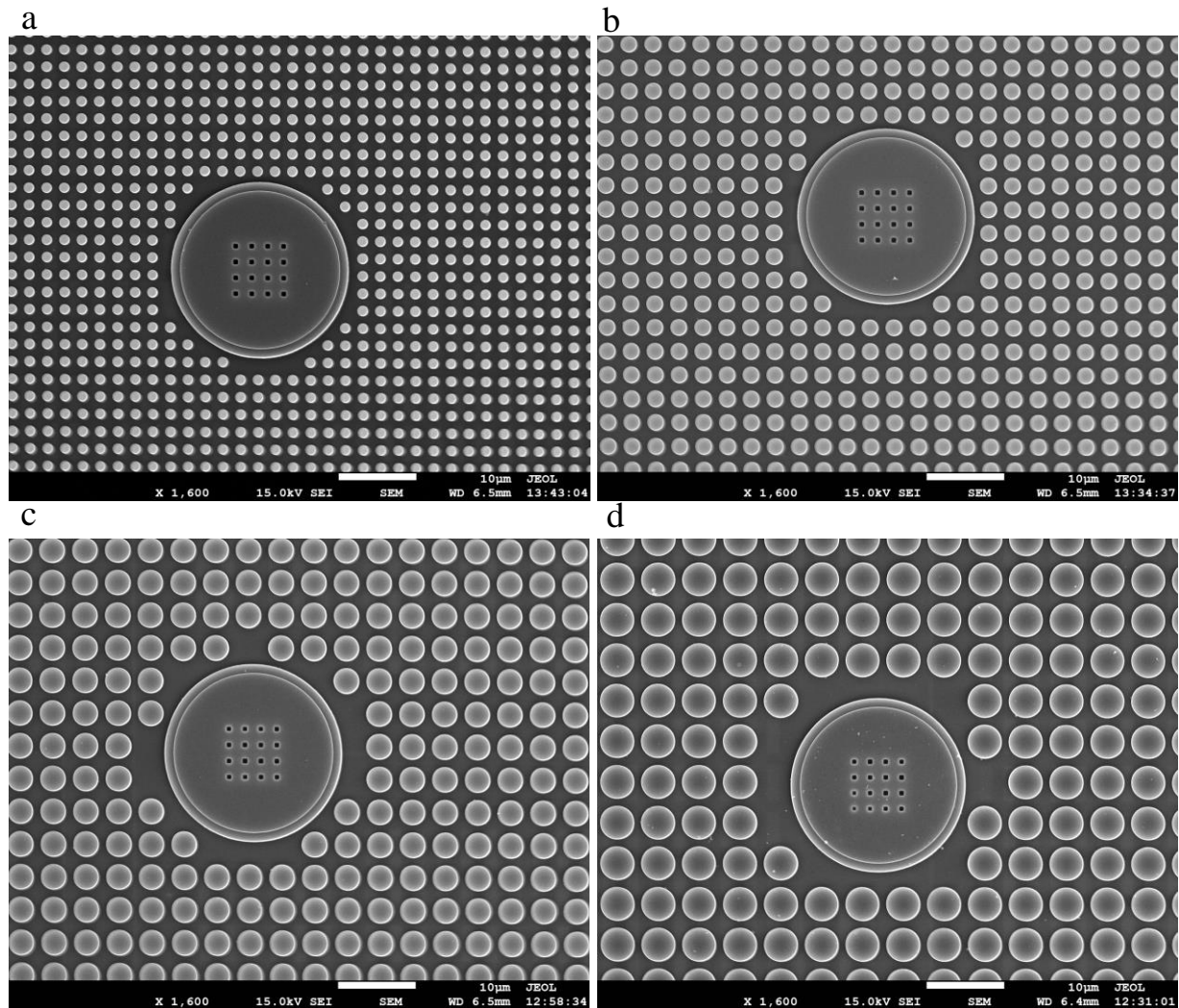


Figure 5.1 SEM view of chip zones with micropillar diameters: (a) zone 1: 1.0 μm (b) zone 2: 1.8 μm (c) zone 3: 2.8 μm (d) zone 4: 4.0 μm [98]

Before imaging, 1–2 nm Pt was sputter coated on the samples with a Q 150T ES (Quorum Technologies, Lewes, UK) to suppress charging and maximize resolution. The aim of the test is to check the uniformity of the material by zones and chips and to evaluate traces of the NaCl mixture as an indirect indicator of substrate surface coverage after drying. The SEM device JSM-7610F (JEOL, Tokyo, Japan) was used for image acquisition, and the Oxford Instruments X-MaxN 80 mm² EDS module (Oxford Instruments, Abingdon, UK), controlled with Aztec software (version: 5.1; Oxford Instruments, Abingdon, UK) was used for EDS acquisition, as previously mentioned in Section 3.1. The primary metrics used in the recordings are Ti_index as an indicator of material uniformity and NaCl_index as an indicator of chip surface coverage with NB-A. Both quantities are derived from the atomic fraction of elements (at %) and are robust to absolute intensity and minor differences in imaging conditions.

5.1 Quantitative analysis of chip composition

This section describes the quantitative analysis of the surface composition of the empty chip by zones (Zone 1–Zone 4) and by chips (D1–D3). Three locations (points) were recorded for each zone, which gives us 12 spectra per chip, a total of 36, as shown in Table 5.1. The acquisition settings were chosen with the aim of exciting the lines key to the analysis (O, Al, Si, Ti) with sufficient energy range and resolution. The main acquisition parameters (magnification, energy range, energy per channel, accelerating voltage, process time and live time) are listed in Table 5.2. Process time denotes a dimensionless AZtec EDS pulse-processing setting related to X-ray signal noise reduction and energy resolution, rather than acquisition time expressed in seconds. The same settings were used for all recordings in this section.

The following elements were used in the analysis:

- Si: the main building element of micropillars (SiO₂)
- O: oxide in the substrate (SiO₂)
- Ti: the main building material of electrodes (TiN).

The elements that are excluded are:

- Al: metal interconnections → geometrically not consistently present → excluded from the Ti_index denominator

- C: present in contaminating particles from the environment
- Pt: sputter coating
- N: low energy line ($K\alpha_N = 0.392$ keV) \rightarrow strong absorption \rightarrow unstable quantification.

We observed K-lines rather than low-energy L-lines due to less overlap and absorption sensitivity at 15 kV.

Table 5.1 EDS sampling plan (empty chip) [98]

Chip	Zone				
	Zone 1	Zone 2	Zone 3	Zone 4	Spectra/chip
D1	3	3	3	3	12
D2	3	3	3	3	12
D3	3	3	3	3	12
				Total	36

Table 5.2 SEM/EDS acquisition settings (empty chip) [98]

Magnification	1600
Energy range (keV)	20
Energy per channel (eV)	10
Accelerating voltage (kV)	15
Working distance (mm)	6.4
Process time	6
Livetime (s)	30

Figure 5.2 shows a demonstrative visual example of EDS measurements for Si, O and Ti for (Sample D1, Zone 4, Point 2) to assess the ability of the system to adequately measure the mentioned elements. The resulting visual representation corresponds to the expected distribution of elements over the chip surface, as shown in Figure 5.1 (d). The same field of view (FOV) was applied to all frames. Table 5.3 lists the elemental proportions, including Al (not used in the subsequent statistical analysis) for the same FOV as in Figure 5.2. Each recording is marked with a pattern designation (D or Ch in next section), zone (Z), point (P) and NB-A volume (V) if present.

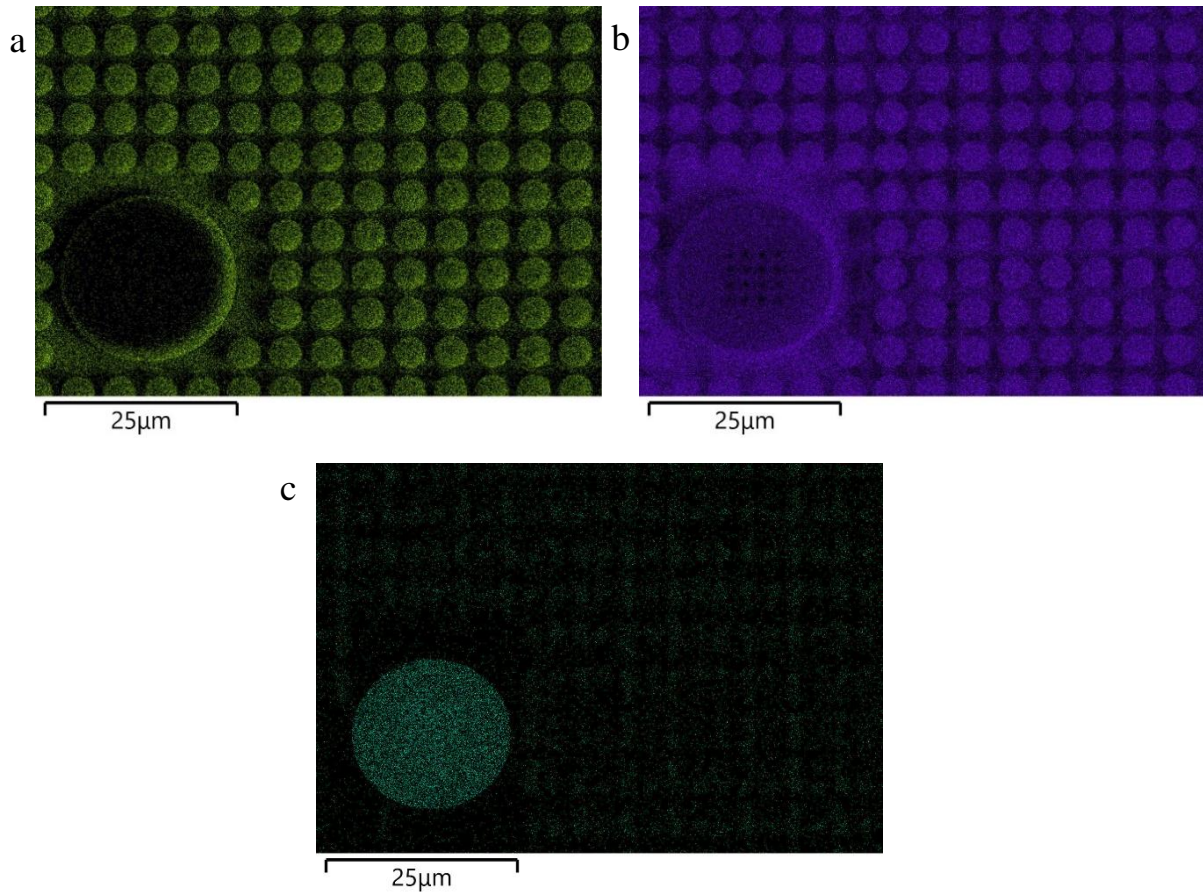


Figure 5.2 EDS elemental maps of O (a), Si (b) and Ti (c) for D1-Z4-P2 [98]

Table 5.3 Atomic percentage for empty chip (D1-Z4-P2) [98]

Spectrum 12 (D1-Z4-P2)		
Element	Line Type	Atomic percentage (at %)
O	K series	55.43
Al	K series	9.25
Si	K series	33.41
Ti	K series	1.92
Total		100.00

Ti_index was used as the main metric for analyzing the chip composition. It is the relative proportion of titanium atoms in relation to other consistent and dominant elements of the surface

matrix (Si and O). The atomic fraction of each element is expressed as at %. Ti_index , defined by Eq. 5.1, is a dimensionless ratio. The same applies to $NaCl_index$, defined later by Eq. 5.2.

$$Ti_index = \frac{Ti_{at\%}}{Ti_{at\%} + Si_{at\%} + O_{at\%}} \quad (5.1)$$

The EDS spectra of the blank chip were quantified at % (O, Si, Ti), and then for each chip \times zone combination $Ti_index = Ti / (Ti + Si + O)$ was calculated as a ratio metric less sensitive to absolute count-rate and small differences in WD. The first table (Chip, Zone, Mean_ Ti_idx , SD_ Ti_idx , CoV) shows per chip and zone the average index (Mean), standard deviation (SD) and coefficient of variation (CoV = SD / Mean) obtained from three measurement points per zone. A higher value indicates a relatively higher contribution of Ti (electrodes) compared to the substrate (SiO₂). The second table is a two-factor ANOVA test with replication where the factors are chip and zone; the columns SS (sum of squares), df (degrees of freedom), MS (mean square), F (ratio of MSs), P-value, F crit (critical F-value for $\alpha = 0.05$) and η^2 (= SS_effect / SS_total) as the effect size are shown. Row Within represents the within-group variance (residual). The analysis was performed in MS Excel (ANOVA: Two-Factor With Replication) on the zonal means per chip, with the assumptions of independence of observations, approximate normality and approximately equal variances. The results of the analyses are presented in Tables 5.4 and 5.5.

Table 5.4 Ti_index per chip and zone on empty chip [98]

Chip	Zone	Mean_Ti_idx	SD_Ti_idx	CoV = SD / Mean
D1	Z1	0.0307	0.0030	0.0974
D1	Z2	0.0259	0.0030	0.1168
D1	Z3	0.0234	0.0032	0.1380
D1	Z4	0.0219	0.0024	0.1092
D2	Z1	0.0223	0.0033	0.1461
D2	Z2	0.0238	0.0007	0.0297
D2	Z3	0.0256	0.0009	0.0361
D2	Z4	0.0221	0.0028	0.1281
D3	Z1	0.0255	0.0027	0.1073
D3	Z2	0.0300	0.0022	0.0738
D3	Z3	0.0219	0.0019	0.0880
D3	Z4	0.0189	0.0010	0.0521

Table 5.5 Two-factor ANOVA with replication for Ti_index on empty chip [98]

Source of variation	SS	df	MS	F	P-value	F crit	η^2
Chip	0.000026	2	0.000013	2.2219	0.1302	3.4028	0.04946
Zone (Z1–Z4)	0.000181	3	0.00006	10.1706	0.0002	3.0088	0.339607
Chip \times zone	0.000183	6	0.000031	5.1482	0.0016	2.5082	0.343805
Within	0.000143	24	0.000006				0.267128
Total	0.000533						

As shown in Table 5.4, Ti_index values cover a range of approximately 0.019–0.031 (e.g., D3–Z4 \approx 0.019; D1–Z1 \approx 0.031). Within individual chip \times zone combinations, the reproducibility is good: typical CoV is around 3–15 % (e.g., D2–Z2 \approx 3 %, D2–Z1 \approx 15 %). Two-factor ANOVA with replication in Table 5.5 shows that zone is a significant source of variability ($F = 10.17$; $p = 0.0002$; $\eta^2 = 0.340$), while the main effect of chip is modest ($F = 2.22$; $p = 0.130$; $\eta^2 = 0.049$). There is also a chip \times zone interaction effect ($F = 5.15$; $p = 0.0016$; $\eta^2 = 0.344$), indicating that the zonal profile of Ti_index differs between chips. The residual (within-group) variance is small ($SS_{within} = 0.000143$; $df = 24$). The significant zone effect is consistent with the expected change in the ratio of electrode (Ti) to substrate (SiO_2) in the FOV: zones with a higher proportion of visible substrate give a lower Ti_index , and zones with a higher proportion of electrode give a higher Ti_index . The small main effect of chip suggests good process uniformity between samples, while the chip \times zone interaction most likely reflects small differences in framing (position relative to the edge of the electrode/pillar) and microrelief between chips, rather than real compositional changes.

Part of the observed decrease in Ti_index with increasing pillar dimensions can also be attributed to the metrology of EDS on relief surfaces. As pillars grow, the space between them becomes geometrically simpler (shallow, with less sharp transitions), and EDS, due to electron reach, X-ray emission angle, and self-absorption in the “valleys”, collects relatively weaker signal from inter-pillar regions. Although both pillars and “valleys” are made of the same material (Si and O), this topographic bias changes the effective weighting of the substrate contribution versus flat parts of the frame (e.g., electrode faces/edges), which further lowers Ti_index in zones with larger pillars. Importantly, this component does not compromise the assessment of process uniformity. All measurements in this section were recorded with the same settings (15 kV, Process time = 6, WD

= 6.4–6.5 mm) and a consistent protocol within each zone, so any bias is canceled out in “chip-within-zone” comparisons. Therefore, the zone effect is partly physical-geometric and partly metric, while the chip effect is still a valid indicator of the reliability of the fabrication process.

5.2 Chip coverage with culture medium

This section describes the quantitative analysis of chip surface coverage with NB-A for two different volumes dropped onto the sample: 30 μL and 3 μL , two chips each. Each chip was recorded in three points for all four zones, as in Section 5.1, with the fact that in this case, three spectrum acquisitions were made for each point for better measurement reliability, as shown in Table 5.6. Also, in this case, precise and consistent shifts per chip were taken (step along the x axis = 1 mm, step along the y axis = 1 mm) because in some cases, due to the NB-A layer, it was not possible to precisely determine the location of the recording, and thus the zone, which could harm the consistency of the results. Acquisition settings are shown in Table 5.7.

Table 5.6 Data acquisition plan for NB-A coverage assessment [98]

Chip	Volume (μL)	Zone (points \times replications)				
		Zone 1	Zone 2	Zone 3	Zone 4	Spectra/chip
Ch1	3	3 \times 3 = 9	3 \times 3 = 9	3 \times 3 = 9	3 \times 3 = 9	36
Ch2	3	3 \times 3 = 9	3 \times 3 = 9	3 \times 3 = 9	3 \times 3 = 9	36
Ch3	30	3 \times 3 = 9	3 \times 3 = 9	3 \times 3 = 9	3 \times 3 = 9	36
Ch4	30	3 \times 3 = 9	3 \times 3 = 9	3 \times 3 = 9	3 \times 3 = 9	36
					Total	144

Table 5.7 EDS acquisition settings for NB-A coverage assessment [98]

Magnification	700
Energy range (keV)	20
Energy per channel (eV)	10
Accelerating voltage (kV)	15
Process time	6
Livetime (s)	20

NaCl_index was used as the main metric for analyzing the coverage of the chip. It is the relative proportion of Na and Cl atoms in relation to Si and Al. Due to its presence in both the NB-A and the surface composition, O was excluded from the measurements, and Al was included. Analogously to equation 5.1, NaCl_index is defined by the formula 5.2:

$$\text{NaCl_index} = \frac{Na_{at\%} + Cl_{at\%}}{Na_{at\%} + Cl_{at\%} + Si_{at\%} + Al_{at\%}} \quad (5.2)$$

The compositional analysis of oxygen and silicon on a substrate (Zone 3) partially covered with dried NB-A is shown in Figure 5.3 and Table 5.8. Panel a shows the EDS intensity map of Si–K α , and panel b shows the EDS map of O–K α . The figure shows the presence of oxygen on the covered and uncovered part of the substrate, which makes it unsuitable for the analysis of the coverage ratio. Silicon was used as a control element. Panel c shows an SEM image of the same segment of the chip. All three panels refer to the same FOV.

Table 5.8 Atomic percentage for covered chip (Z3-V5) [98]

Test sample (Z3-V5)		
Element	Line Type	Atomic percentage (at %)
Na	K series	8.22
Al	K series	0.29
Si	K series	19.80
Cl	K series	3.17
Ti	K series	0.01
O	K series	68.51
Total		100.00

In the example from Figure 5.3, a magnification of 950 \times was used for a clearer visual representation, and 5 μ L of NB-A was applied to the surface. In addition to oxygen, titanium was also included in the calculation. It was excluded in further measurements because it was impossible to estimate how many electrodes are in the FOV due to the NB-A surface coverage. Unlike in Section 5.1, WD was maintained in the range of 6–8 mm throughout all measurements to achieve adequate image focus. Since we use normalized ratios (NaCl / (NaCl + Si + Al)), minimal sensitivity to small changes in WD is expected.

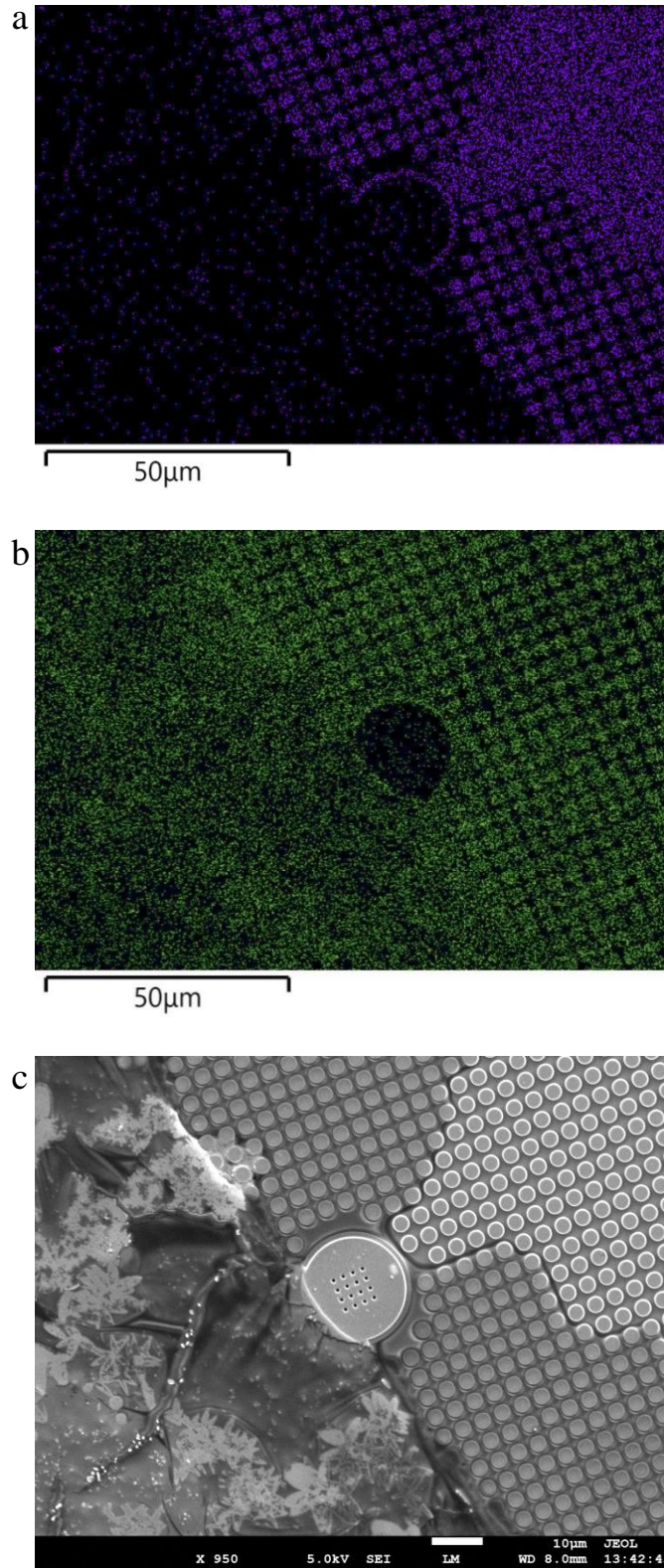


Figure 5.3 View of the chip surface partially covered with NB-A [98]

Figure 5.4 shows a demonstrative SEM image (Ch1-Z2-V3) and a spectrum of acquired elements for the same FOV. Panel a shows SEM view of the surface partially covered with NB-A, while panel b shows spectra of Na, Cl, Si and Al, labeled as Spectrum 89. Cps/eV (counts per second per electronvolt) on the y-axis indicates the differential count rate per energy. The image confirms the presence of previously defined elements and their suitability for measurements. Data on acquisition settings are given in Table 5.7. The composition analysis is given in Table 5.8.

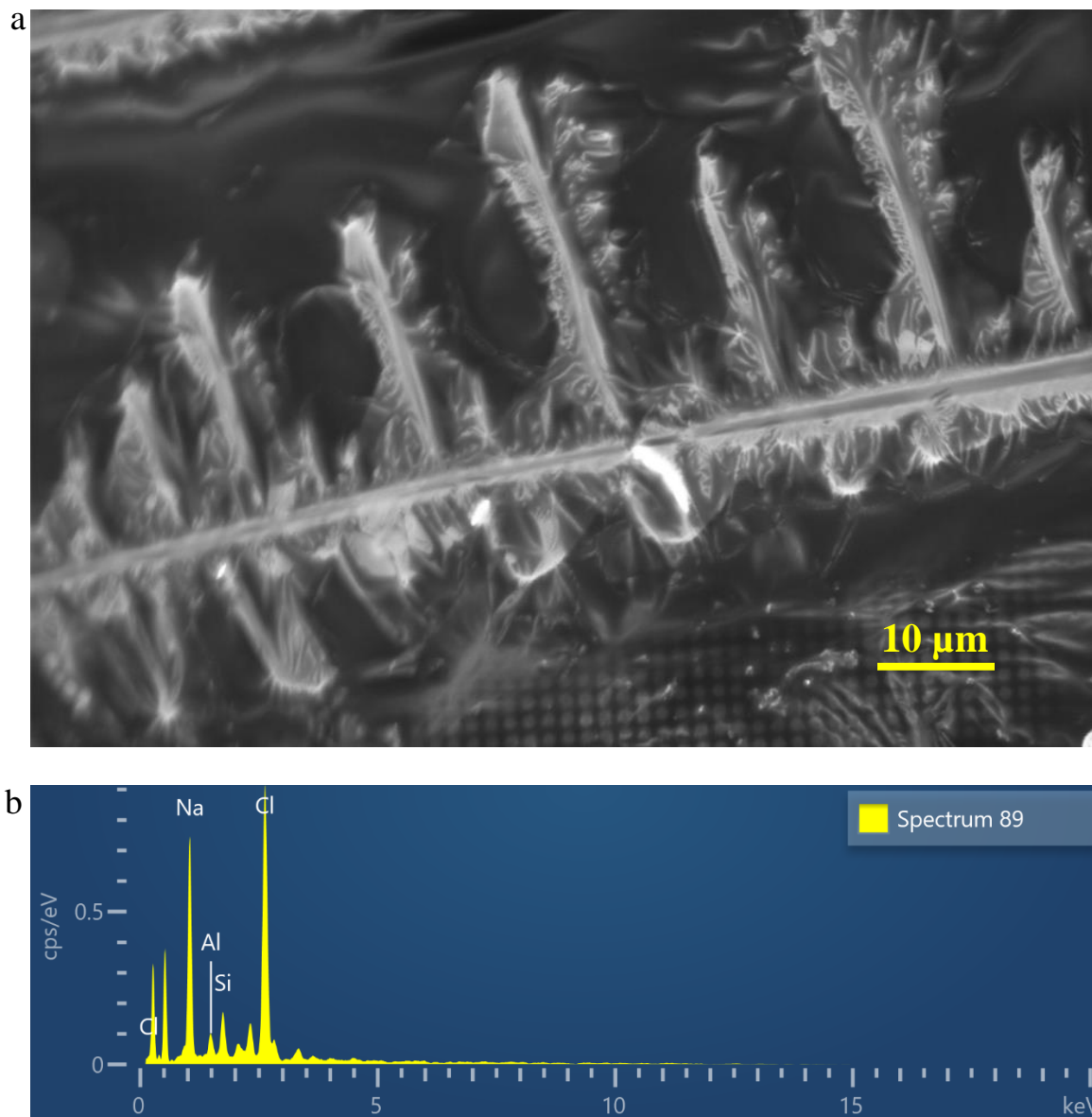


Figure 5.4 Sample (Ch1-Z2-V3): (a) SEM view (b) Spectra of Na, Cl, Si and Al [98]

Table 5.8: Atomic percentage for covered chip (Ch1-Z2-P3-V3) [98]

Spectrum 89 (Ch1-Z2-P2-V3)		
Element	Line Type	Atomic percentage (at %)
Na	K series	38.49
Al	K series	3.6
Si	K series	6.85
Cl	K series	51.06
Total		100.00

NaCl_index was calculated using the same descriptive and inferential statistical methods as in Section 5.1. Higher NaCl_index indicates greater NB-A residue coverage (lower substrate visibility). The results are shown in Tables 5.9 and 5.10.

Table 5.9 NaCl_index per chip (Ch1–Ch4) and zone (Z1–Z4) [98]

Chip	Volume (μL)	Zone	Mean_NaCl_idx	SD_NaCl_idx	CoV = SD / Mean
Ch1	3	Z1	0.908	0.011	0.0125
Ch1	3	Z2	0.918	0.028	0.0301
Ch1	3	Z3	0.956	0.011	0.0111
Ch1	3	Z4	0.904	0.092	0.1021
Ch2	3	Z1	0.984	0.009	0.0088
Ch2	3	Z2	0.959	0.046	0.0479
Ch2	3	Z3	0.971	0.013	0.0133
Ch2	3	Z4	0.981	0.005	0.0052
Ch3	30	Z1	0.994	0.000	0.0004
Ch3	30	Z2	0.987	0.006	0.0061
Ch3	30	Z3	0.982	0.006	0.0059
Ch3	30	Z4	0.995	0.005	0.0050
Ch4	30	Z1	0.992	0.015	0.0148
Ch4	30	Z2	0.979	0.036	0.0371
Ch4	30	Z3	1.000	0.000	0.0000
Ch4	30	Z4	0.990	0.017	0.0168

Table 5.10 Two-factor ANOVA with replication for NaCl_index [98]

Source of Variation	SS	df	MS	F	P-value	F crit	η^2
Volume	0.0072	1	0.0072	8.1948	0.0211	5.3177	0.4773
Zone (Z1–Z4)	0.0006	3	0.0002	0.2088	0.8875	4.0662	0.0365
Volume \times zone	0.0003	3	0.0001	0.1162	0.9481	4.0662	0.0203
Within	0.0071	8	0.0009				
Total	0.015133						

As shown in Table 5.9 NaCl_index spans roughly 0.904–1.000 (e.g., Ch1–Z4 \approx 0.904; Ch4–Z3 = 1.000). Reproducibility within chip \times zone is good: typical CoV is on the order of 0.5–5 % for 30 μ L chips (e.g., Ch3–Z2 \approx 0.006; Ch4–Z1 \approx 0.015) and \sim 1–10 % for 3 μ L chips (e.g., Ch2–Z4 \approx 0.005; Ch1–Z4 \approx 0.102). Mean values are systematically higher for 30 μ L (\approx 0.98–1.00 across zones) than for 3 μ L (\approx 0.90–0.98), indicating greater residue coverage after drying at higher initial volume.

In Table 5.10 Volume (3 vs 30 μ L), Zone (1-4) and volume \times zone interaction were used as factors. Reported are SS (sum of squares), df (degrees of freedom), MS (SS / df), F, P-value, F_crit ($\alpha = 0.05$), and η^2 (= SS_effect / SS_total) as effect size. The row Within denotes the residual (within-cell) variance. Chips served as replicates within each volume level and results were computed as per-zone means of point-level means. The volume main effect is significant (F = 8.19, p = 0.021, $\eta^2 = 0.477$), whereas zone is not (F = 0.21, p = 0.888, $\eta^2 = 0.037$), and the volume \times zone interaction is also not significant (F = 0.12, p = 0.948, $\eta^2 = 0.020$). The residual (within-cell) variance is given by SS_within = 0.0071 with df = 8. We come to conclusion that increasing the droplet volume from 3 to 30 μ L consistently raises NaCl_index across all zones, while the micropillar dimensions do not systematically change coverage, nor do they modulate the volume effect. (Note: Ti is excluded from the NaCl_index denominator to avoid confounding by unknown electrode fraction in the FOV.)

A graphic representation of the comparison of NaCl_index for V = 3 μ L and V = 30 μ L by zones is given in Figure 5.5. The difference in the amounts of NaCl_index for the mentioned volumes by zone is shown in Figure 5.6.

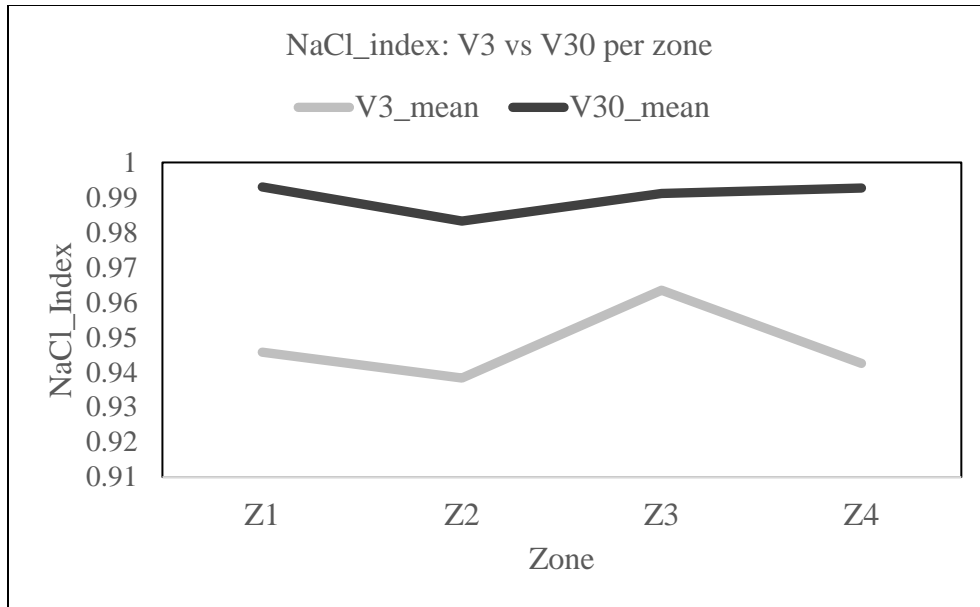


Figure 5.5 NaCl_index: V3 vs V30 per zone [98]

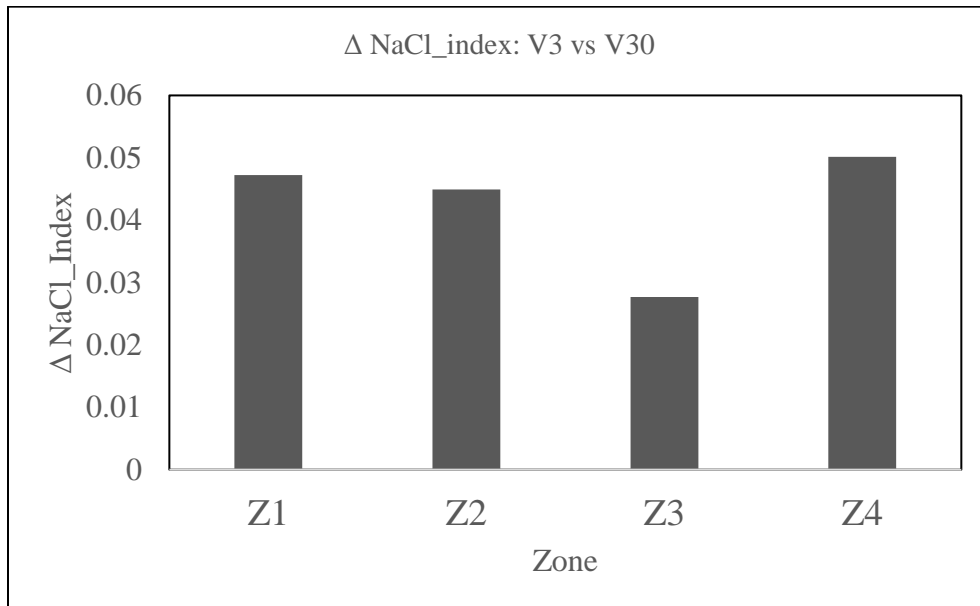


Figure 5.6 Δ NaCl_index; V3 vs V30 per zone

5.3 Summary

In this chapter, the uniformity of the fabrication process of the MEA chip as a substrate with a three-dimensional microstructured surface and the interaction of the substrate with the culture medium, NB-A, with respect to the surface coverage properties are quantitatively analyzed.

Composition analysis on an empty chip (sample set 1) based on 36 EDS spectra showed high uniformity between different chips, which directly implies a high quality of the fabrication process. The observed differences in zones are attributed to the influence of the dimensions of the micropillar structures as the main factors defining the topography, i.e., the ratio of valleys to ridges, and the influence of such geometry on the electron-beam induced charging during SEM/EDS imaging.

Interaction with the culture medium showed a clear positive relationship between the volume of the NB-A droplet and the coverage of the chip surface with crystallized NaCl residues, regardless of chip zone, i.e., the surface geometry.

From the obtained results, it can be concluded that the uniformity of the chip surface composition is at the level necessary for carrying out the experimental methods described in Chapters 3 and 4 and that the quality of the fabrication process should not affect the occurrence of mechanotaxis and electrotaxis in the analyzed experiments. This provides a reliable technical basis for the interpretation of the morphometric and electrophysiological results presented in the following chapters.

6 INDIVIDUAL AND COMBINED EFFECTS OF MECHANOTAXIS AND ELECTROTAXIS ON MICROSTRUCTURED SUBSTRATES

In this chapter, a unified analysis of the influence of mechanotaxis and electrotaxis on spiral ganglion neuron cultures under in vitro conditions is presented. Following the substrate characterization presented in Chapter 5, the obtained morphometric results can be interpreted with greater confidence, since the substrate composition and fabrication quality were previously shown to be sufficiently uniform. An overview of data acquisition, their statistical processing and interpretation in the context of the significance of this work is given. The experimental interface from Section 3.3 was used paired with the substrate from Section 3.1. Spiral ganglion neuron cultures were grown according to the protocols from Section 4.1 and the analysis was performed according to the methods from Section 4.2. The experimental design is defined in Table 4.1, originally presented by Borić et al. [81], with new tools for extended analysis and robust statistical methods. The influence of mechanotaxis, electrotaxis and their combined effects on cultures, i.e., on their previously defined soma area (SA), neurite length (NL), and neurite alignment (NA), was analyzed respectively. Given the number of substrates in this phase of the research, in this chapter, in order to avoid pseudoreplication, exclusively descriptive statistics were used. Their reliability was ensured by the sample size, the number of measurements, and the use of robust statistical measures. Confirmation of the influence of the described mechanisms is of crucial importance and a basic prerequisite for the application of extracellular recording methods and using the neuroelectronic interface, in the following chapter of the doctoral thesis.

6.1 Mechanotaxis on microstructured substrates

In this section, the effect of microtopography (Chip) versus smooth glass (Glass) on the morphology and orientation of spiral ganglion neurons without electrical stimulation was quantified. The analysis is based on measurements described in Chapter 4 (N = 270 measurements per metric and group), standard descriptive statistics, robust measures (median, trimmed mean 10 %), Tukey fences for identifying outliers, Cliff's δ/PS for effect size, and the permutation (Monte Carlo) test Δ_{median} (N = 5 000 / 1 000) which does not assume normality. Quality control was performed through equal ROI selection criteria, identical bin settings on histograms, reporting both outliers and trimmed measures and checking the stability of p-values over 5 000 or 1 000 permutations. Note on pseudoreplication: units of analysis in this chapter are neurons/neurites from

the same sample per group. The conclusions therefore relate to within-sample effects of microtopography, with reporting of effect sizes and robust p-like indicators.

Figures 6.1 and 6.2 show ROI measurement slices for soma area (ROI marked with cyan ellipse), neurite length (ROI marked with magenta segmented line) and neurite alignment (ROI marked with white rectangle) for the Glass control sample in Figure 6.1 and for the Chip control sample in Figure 6.2. The same marking principle was applied to all samples in Chapter 6. Also, the FOV of $200\ \mu\text{m} \times 100\ \mu\text{m}$ shown in Figures 6.1 and 6.2 applies to all samples in Chapter 6.

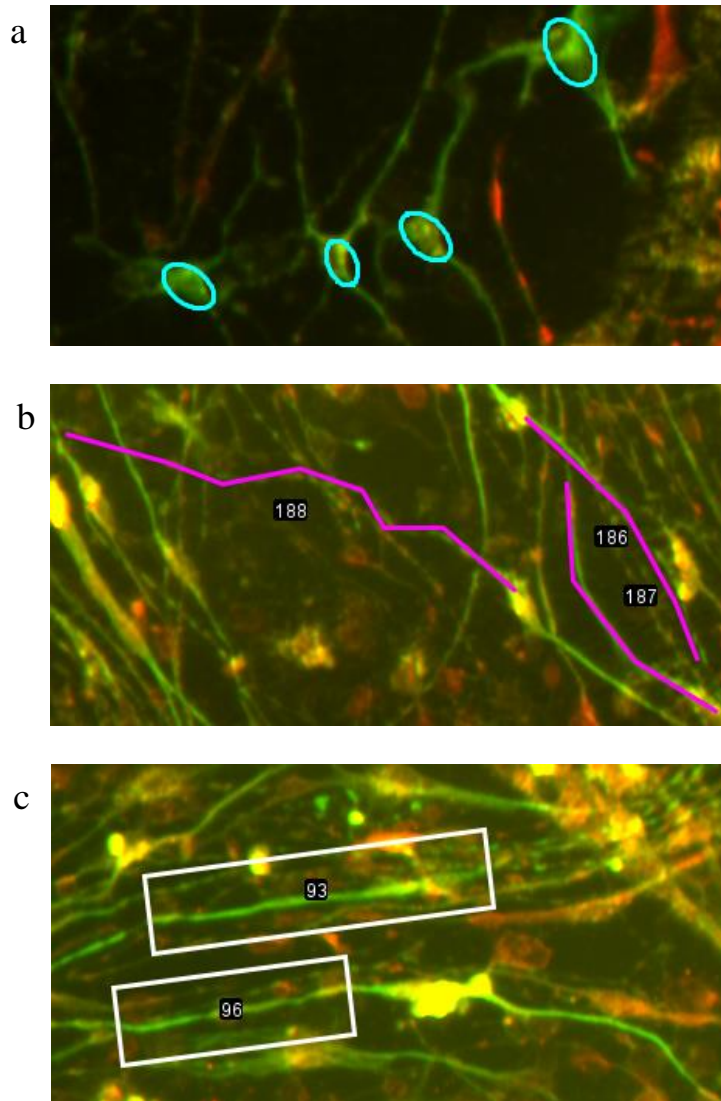


Figure 6.1 Representative ROI measurements on Glass control: (a) SA (b) NL (c) NA; Adapted from [81]

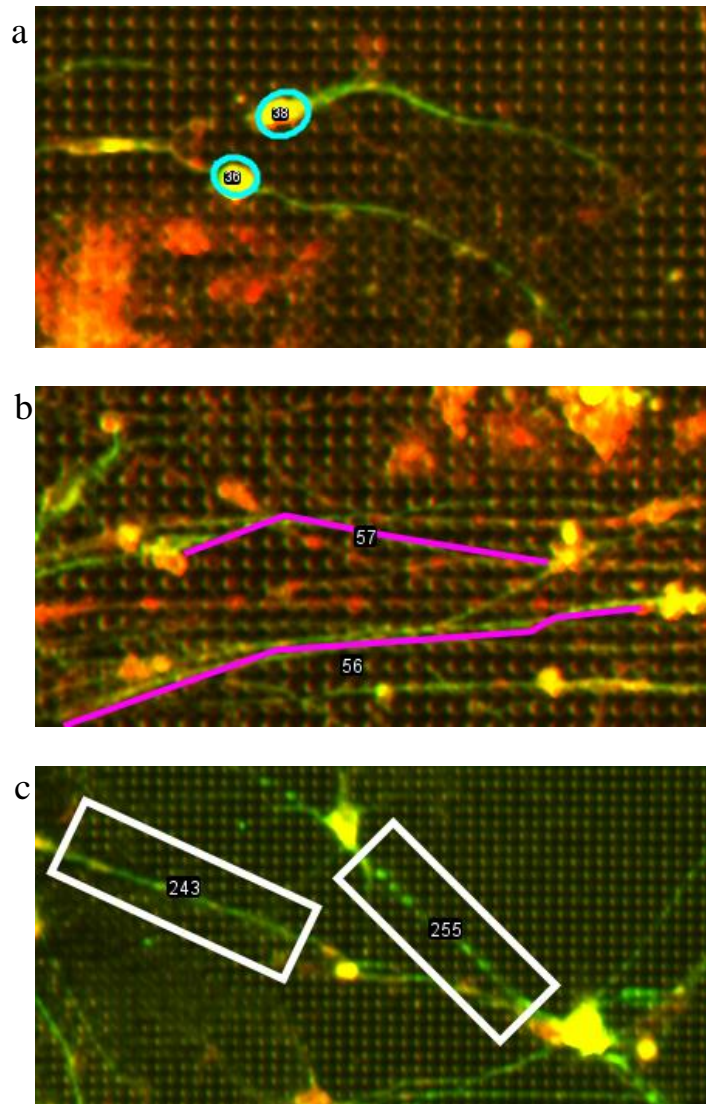


Figure 6.2 Representative ROI measurements on Chip control: (a) SA (b) NL (c) NA; Adapted from [81]

6.1.1 Soma area

By comparing Glass control vs Chip control (without EF stimulation), we obtain a morphometric signature of mechanotaxis: neurons on substrate with microtopography show larger and more variable somatic areas than on smooth glass as shown in Figure 6.3. In the box-and-whisker plots, the whiskers denote the most extreme data points within Tukey's limits ($Q1 - 1.5 \cdot IQR$ and $Q3 + 1.5 \cdot IQR$), while values beyond these limits are treated as outliers, as previously defined in 4.1 and 4.2. The central line indicates the median, the \times indicates the mean, and the box encompasses

the interval Q1-Q3. The same applies to the measurements of neurite length and neurite alignment throughout Chapter 6.

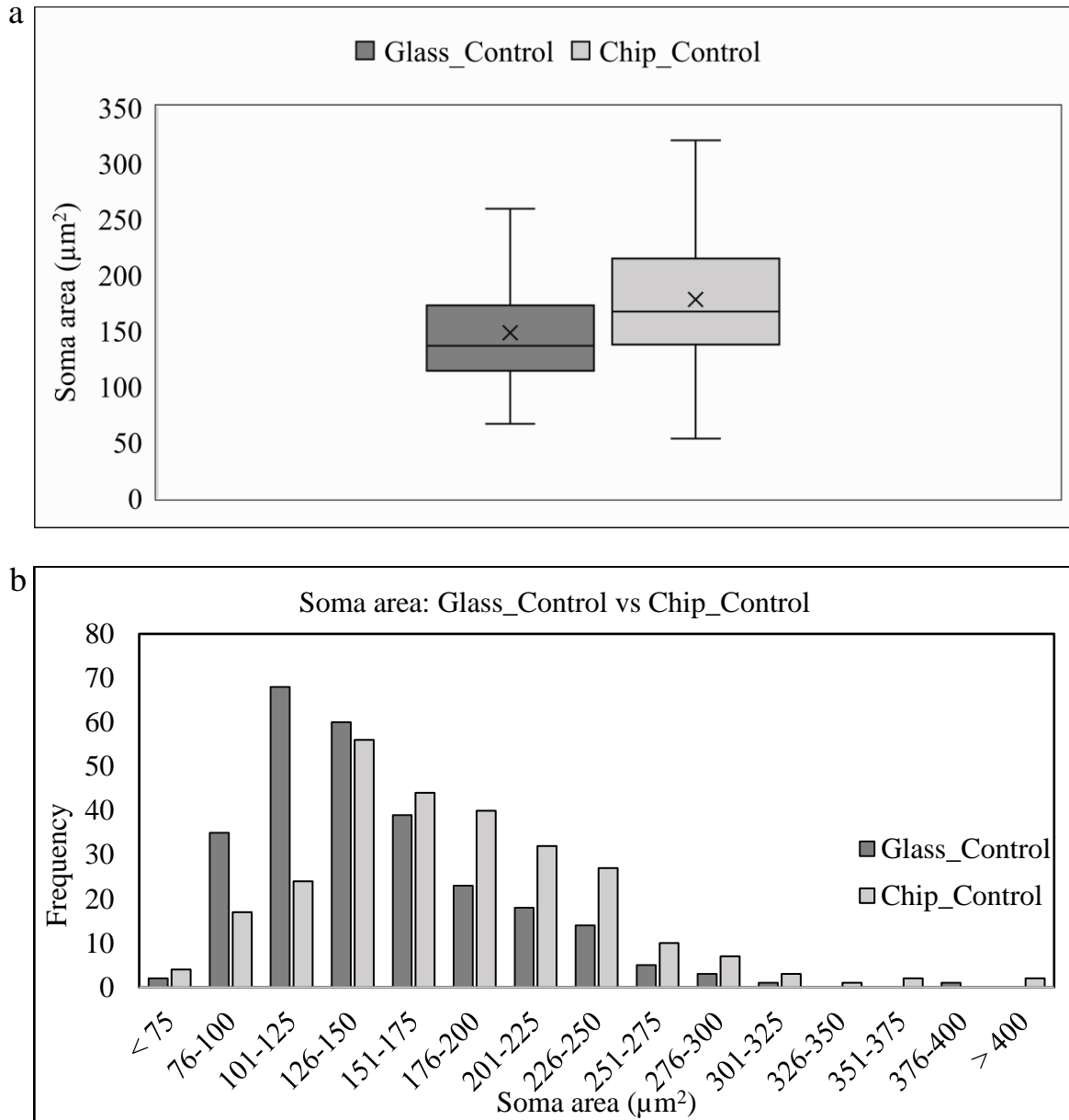


Figure 6.3 SA (Glass control vs Chip control): (a) Box-and-whisker plot (b) Histogram

The soma area distribution on a sample of 270 neurons per group shows a bias towards higher values on the chip. The median of the control sample (Glass control) is $\sim 30.6 \mu\text{m}^2$ or about 22–23 % less compared to the median of $166.74 \mu\text{m}^2$ on the chip (Chip control). This is supported by the trimmed mean (10 %) value: $142.00 \mu\text{m}^2$ vs $172.89 \mu\text{m}^2$. The entire distribution on the chip shifts towards higher values. Q1 increases from $113.64 \mu\text{m}^2$ vs $137.29 \mu\text{m}^2$, and Q3 from 172.31

μm^2 vs $214.47 \mu\text{m}^2$, which results in a widening of the interquartile range ($58.67 \mu\text{m}^2$ vs $77.17 \mu\text{m}^2$) and greater dispersion. Considering the difference in SE (3.01 vs 3.87), the 95 % confidence interval around the average for the control group (Glass control) is $\sim 147.89 \mu\text{m}^2 \pm 5.90 \mu\text{m}^2$, and $\sim 177.77 \pm 7.59 \mu\text{m}^2$ for the Chip control, the separation remains consistent even at the confidence interval level, with the expected higher maximum value in the sample ($571.90 \mu\text{m}^2$ vs $378.51 \mu\text{m}^2$). In this case, a consistent tendency of the microtopographic substrate to increase the soma area values and widen the distribution values was observed.

The share of outliers in both groups is low and comparable. On the glass it is 2.96 %, i.e., 8/270, and on the chip 1.85 %, i.e., 5/270. On the chip, the upper fences are larger than on the glass ($330.22 \mu\text{m}^2$ vs $260.32 \mu\text{m}^2$), which is expected considering the inclination of the chip distribution to the right and the higher values of the upper quartiles compared to the Glass control. The values of the lower brackets (25.64 vs $21.53 \mu\text{m}^2$) suggest that the rare extremely small values have no significant impact on the analysis. It is clear from the above that the values of Tukey's quality control support the thesis that the difference in the distributions of the groups is their real characteristic, and not a consequence of a smaller number of extreme values.

Higher values of soma area on the chip compared to those on the glass were also confirmed by the non-parametric Mann-Whitney U test. The values for the glass surface are $U = 24\,789$ (with both samples of size 270 units), which gives $PS = P(\text{Glass} > \text{Chip}) = U / (n_1 \cdot n_2) = 0.34$. This result can be interpreted so that the probability that the soma area of a randomly selected Glass control neuron will be higher than the soma area randomly selected from the Chip control group is approximately 34 %, from which in the opposite direction $P(\text{Chip} > \text{Glass}) \approx 66$ % follows. Such values are consistent with the obtained medians and quartiles descriptively given in the previous paragraphs.

Looking at the comparison of the values of individual ordered pairs in both distributions (Glass–Chip pairs), the values of Cliff's δ are $\delta(\text{Glass}) = -0.32$ and $\delta(\text{Chip}) = +0.32$, respectively. This suggests that the interrelationship of the distributions is constant throughout the entire distribution, and not just through its central part, which is especially relevant for distributions that do not follow a normal distribution, as in the present case.

By permutation test for 5 000 random label distributions, the difference in medians between the glass surface and the chip is $\Delta_{\text{median}} = 30.59 \mu\text{m}^2$. It is approximately $3.5 \times$ higher than the value

assumed by the null hypothesis (95 % $|\Delta_{perm}|$ does not exceed $8.68 \mu\text{m}^2$), according to which there are no systematic differences between the two groups. As a consequence, the minimum value of p-like for a sample of 5 000 permutations (0.0002) results, from which it can be concluded that the differences in the central values of the distributions are independent of the shape of the distributions. The null distribution of the permutation of the median differences (Δ_{perm}) of the observed samples (Glass control vs Chip control) for the measured soma area values at $N_{perm} = 5\ 000$ is shown in Figure 6.4. 95 % of the absolute differences do not exceed $8.68 \mu\text{m}^2$. The observed median difference of $\Delta_{median} = 30.59 \mu\text{m}^2$ is far outside the null-range.

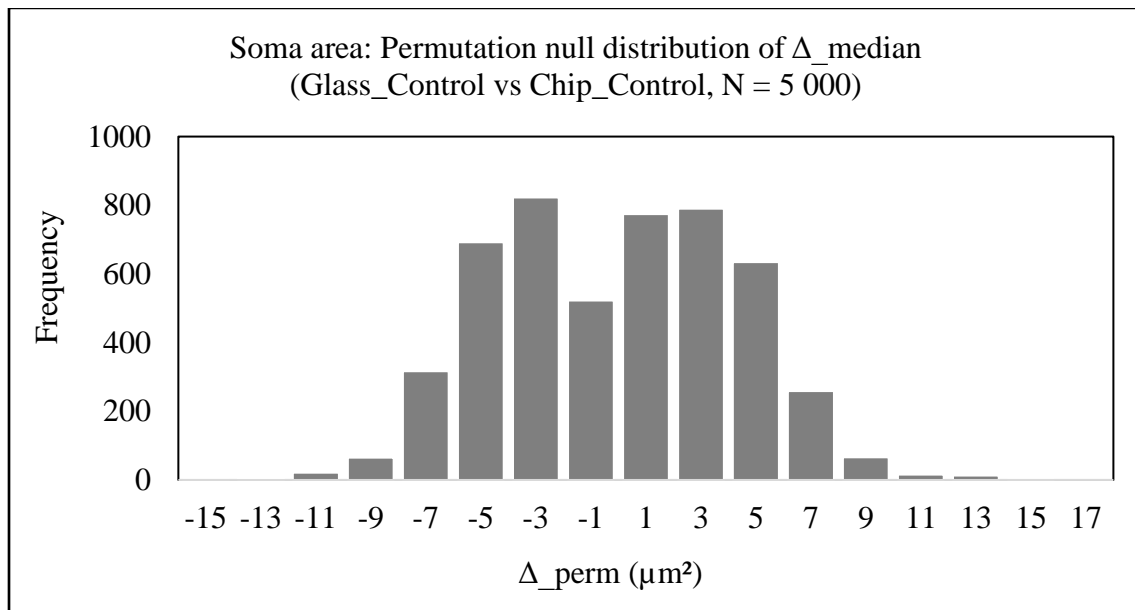


Figure 6.4 SA: Permutation null distribution of Δ_{median} (Glass control vs Chip control)

The results of three independent metrics, descriptive, effect size, and permutation test, support the claim that the microtopography of the chip increases soma area compared to samples on a smooth glass surface. The obtained results can be considered as a morphometric signature of mechanotaxis in conditions without electric field stimulation.

6.1.2 Neurite length

For both observed cases, at a sample size of 270, the average neurite length on the chip shows a 54 % higher value compared to that on the glass surface ($156.10 \mu\text{m}$ vs $101.18 \mu\text{m}$). The same comparison for the median gives similar values, i.e., 48 % difference in favor of the values on the chip ($138.35 \mu\text{m}$ vs $93.23 \mu\text{m}$). The distribution of neurite length on the chip (IQR $76.85 \mu\text{m}$) is

wider than on the glass (IQR 56.60 μm). The upper tail of the distribution is more pronounced on the chip ($P_{90} = 236.14 \mu\text{m}$) than on the glass ($P_{90} = 155.05 \mu\text{m}$), with positive asymmetry of both distributions (skewness ≈ 1.5). Both sets of data are leptokurtic, although such a shape is somewhat more pronounced with the glass substrate than with the chip (4.37 vs 3.09). A comparison is given in Figure 6.5.

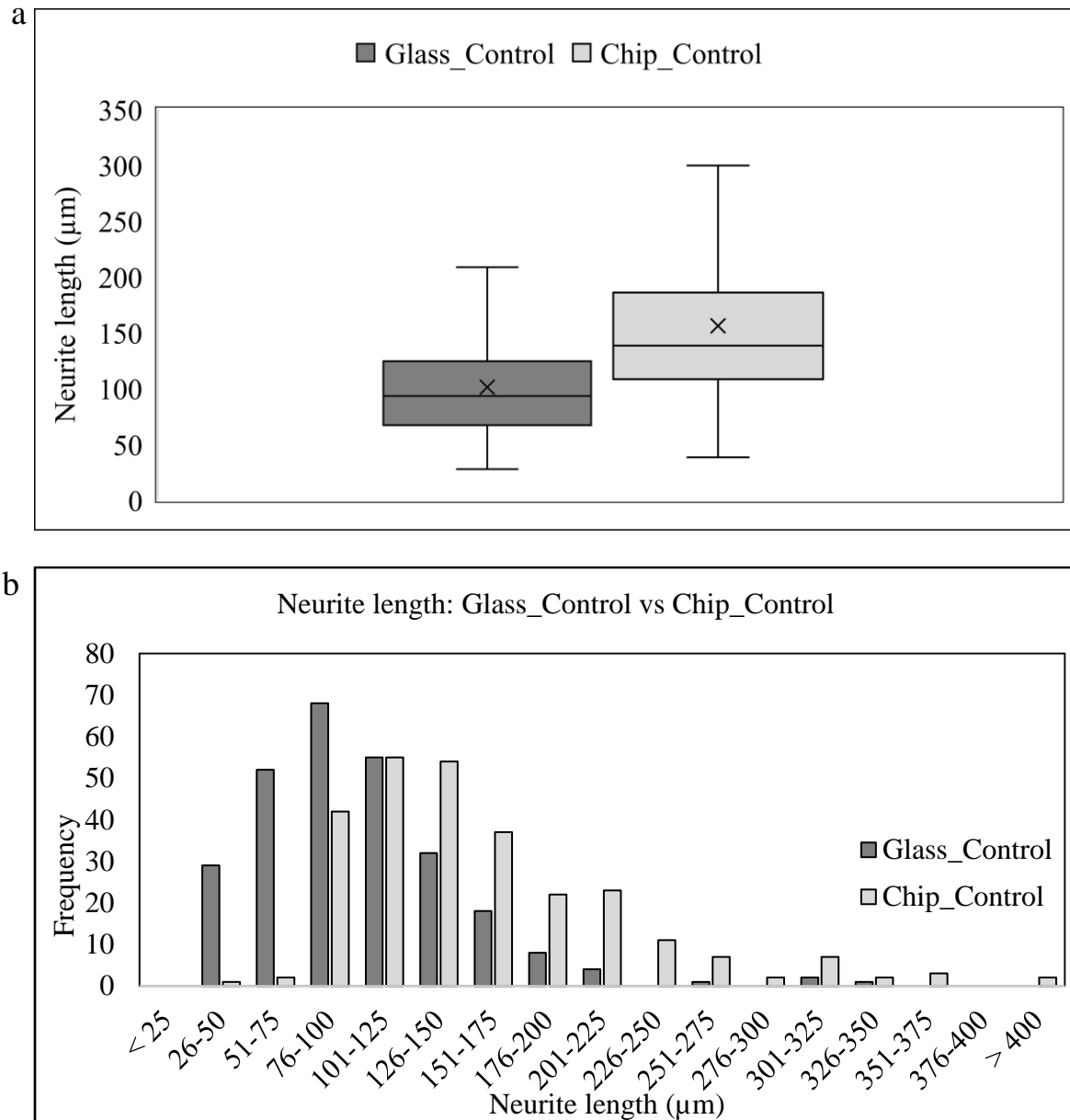


Figure 6.5 NL (Glass control vs Chip control): (a) Box-and-whisker plot (b) Histogram Differences in neurite length values are also evident in the lower percentiles (P_{10} : 91.97 μm on chip vs 49.41 μm on glass), suggesting that the differences in the main descriptive parameters do

not come only from the right tails. Neurites on the chip are longer in all parameters and show greater variability, consistent with the expected occurrence of mechanotaxis.

The upper Tukey's fence on the chip (300.39 μm) is expectedly larger than that on the glass (208.63 μm). The outlier fraction on the chip of 5.19 % (14/270) is higher than on the glass, where it is 2.59 % (7/270), which is consistent with the broader distribution and longer upper tail of the distribution on the chip.

The systematic difference in favor of the length of neurites on the chip is also confirmed by rank-based metrics. With the sum of the chip (93 289) and glass (52 781) ranks, Mann-Whitney $U = 16\ 196$ was calculated, for both samples of 270 units. Analogous to the interpretation of the soma area, from PS (Glass > Chip) = 0.22 it follows that in 78 % of randomly selected pairs from both samples, the one from the chip would show a longer neurite length. Measured values Cliff's $\delta = -0.56$ (for glass; or +0.56 for the chip), indicates a medium to larger effect in favor of the chip. As in the case of the comparison for soma area, non-parametric measures are also robust to distribution asymmetry and outliers, and are consistent with the results from the previous paragraph.

5 000 random permutations in the permutation test gave the observed chip-to-glass median difference $\Delta_{\text{median}} = 45.12\ \mu\text{m}$., which is several times higher than expected by the null hypothesis because the null distribution of median differences for the 95 percent interval is $|\Delta_{\text{perm}}| = 0.49\text{--}12.64\ \mu\text{m}$. The two-sided p-like value of 0.0002 at $N_{\text{perm}} = 5\ 000$, supports the thesis that even random shuffling of data almost never gives differences comparable to those observed in measurement.

These results unequivocally support the conclusion that the microtopography of the substrate has a significant positive effect on neurite length compared to those on a flat glass surface. This difference is noticeable both practically and statistically, and is robust with respect to the shape of the distribution and the rare extreme values.

The histogram in Figure 6.6 shows the described null distribution of the permutation of the median neurite length difference (Δ_{median}) for glass and chip. The distribution is narrow and centered around 0 μm , with 95 % of the results in the $\pm 12\text{--}13\ \mu\text{m}$ range. The previously mentioned

$\Delta_median = 45.12 \mu\text{m}$ is not shown because its amount significantly falls out of the range of the null distribution, which is in accordance with the also previously mentioned p-like of 0.0002.

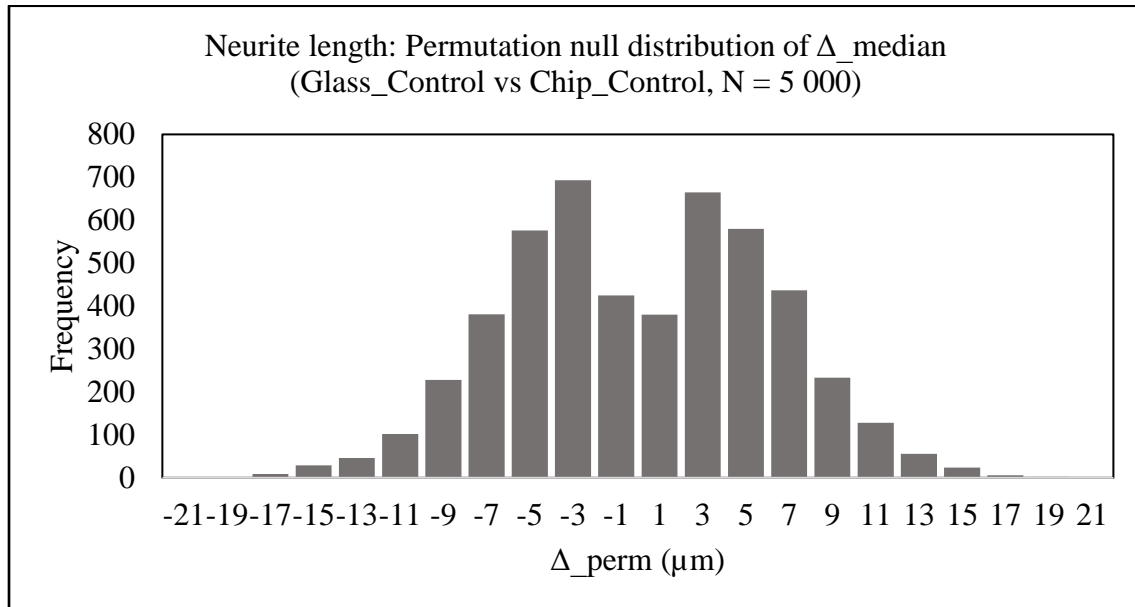


Figure 6.6 NL: Permutation null distribution of Δ_median (Glass control vs Chip control)

6.1.3 Neurite alignment

In this subsection, we analyze neurite alignment through two metrics, previously defined in Chapter 4: Biaxial alignment index (AI_{bi}) and Angle to nearest axis ($\delta\theta_ax$). The measured neurite orientation density is shown on half-polar plot (0–180°) in Figure 6.7.

6.1.3.1 Biaxial alignment index

Neurites on the chip are more aligned than on glass. The mean value differs by 0.17 (0.72 vs 0.59), and an even larger difference is observed for the median (0.82 vs 0.62). The lower 95 % confidence interval values are 0.68 for the chip and 0.55 for glass, which is a consistent difference in addition to the difference in the mean values. The difference is further emphasized by comparing the trimmed mean (10 %), where 0.76 is on the chip and 0.61 on glass, so the influence of extreme values is not large. The difference in distributions is also evident through their dispersions. The interquartile range on the chip is smaller than on the glass (0.30 vs 0.50), which indicates that the AI_{bi} on the chip are more concentrated around high values, while on the glass they are, as expected, wider and more heterogeneous. This trend is also supported by the quartile values. The

lower quartiles are 0.52 for chip and 0.36 for glass, while the upper quartiles are 0.82 for chip and 0.86 for glass.

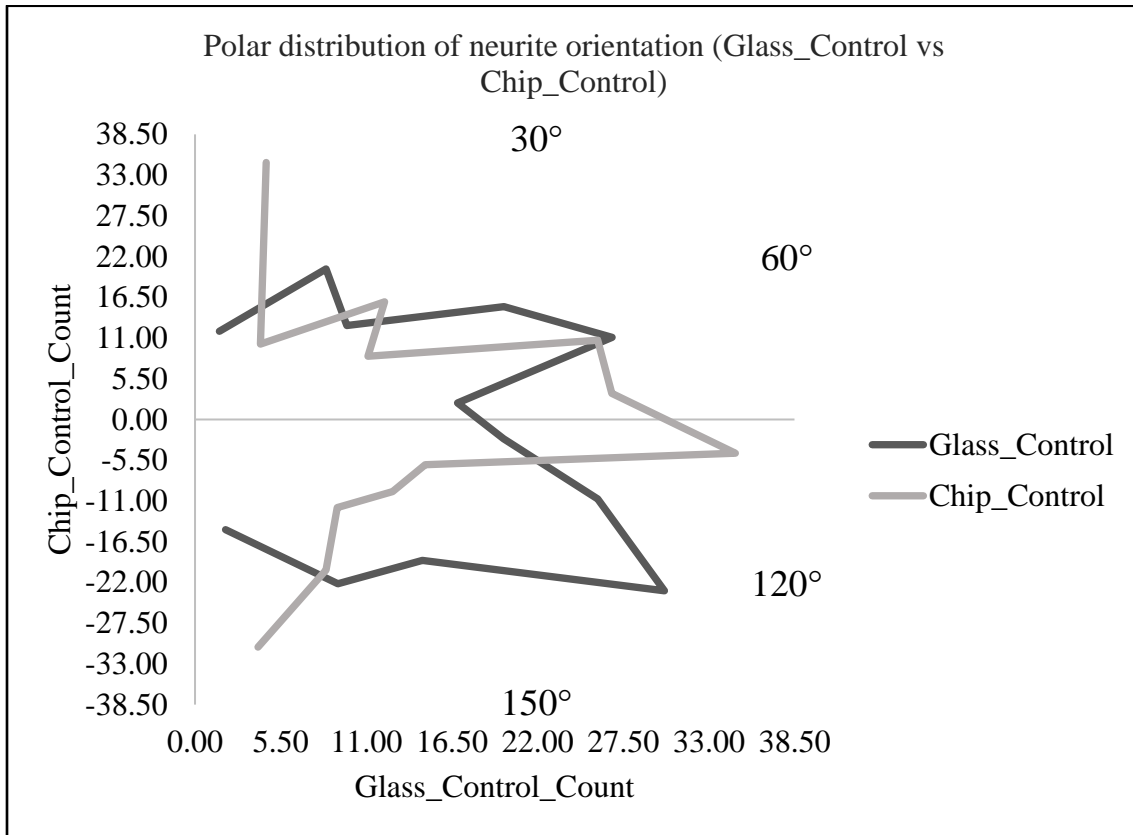


Figure 6.7 NA (Glass control vs Chip control): Half-polar plot (0–180°)

Both observed groups have a negatively symmetrical distribution, which, however, is more pronounced on the chip (skewness -0.78 on chip vs -0.30 on glass). This is typical when using metrics where there is a possibility of grouping with an upper limit. Many values are close to 1.0, which is the maximum index value given the defined range from 0.00 to 1.00. The kurtosis in both groups is negative, which indicates a somewhat flatter distribution than that of a normal distribution. These results suggest that the chip as a substrate has a significant influence on the biaxial alignment of neurites. A visual representation for the glass and chip is given in Figure 6.8. Given the nature of the metric, the whiskers span the min-max interval, with no outliers. As in other measurements, the sample size is 270 ROIs per group.

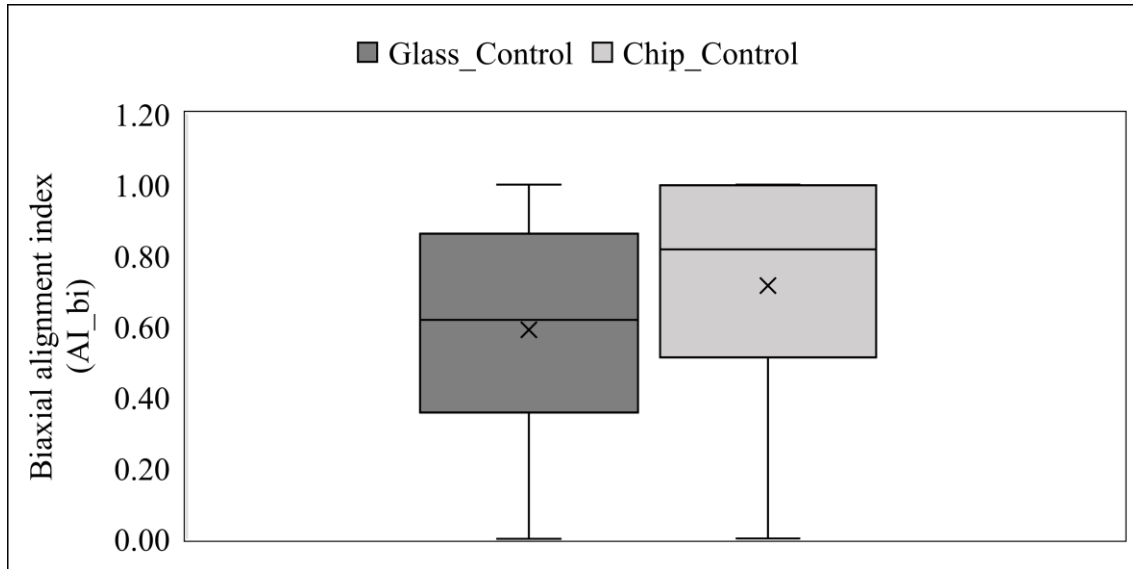


Figure 6.8 Biaxial alignment index (AI_{bi}): Glass control vs Chip control

Permutational analysis of biaxial alignment at 1 000 permutations also suggests the presence of directional alignment of neurites on the chip. The noted difference of the median on the chip and the control glass in the amount of $\Delta_{\text{median}} = 0.20$ at the value of p-like in the amount of 0.0002 is an indicator of the low probability of the outcome from the null hypothesis, since 95 % of the permutations under the null hypothesis are located in the interval from 0.00 to 0.11. Given that the index is defined in the interval from 0 to 1, Δ_{median} of +0.20 represents a large value of the differences of the compared medians in this context.

All the described metrics with their values, and especially the accumulation of AI_{bi} near the theoretical maximum value of 1, consistently indicate a clear influence of the topographic substrate on biaxial alignment compared to a flat glass surface without microtopographical structures.

6.1.3.2 Angle to nearest substrate axis

As for the second metric value ($\delta\theta_{\text{ax}}$) of neurite orientation, the distances of the observed neurite orientation angles from the axes of the microtopographic substrate are smaller compared to the flat glass surface without microtopography. This is reflected in the median, which is smaller on the chip than on the glass (25.90° vs 17.60°), and the mean follows the same trend (24.76° vs 17.27°). Their differences are especially pronounced in the lower quartiles, which on the chip has a value of only 1.45° with the tenth percentile P10 = 0.00°, indicating an almost complete alignment of a significant number of neurites with the edges of the substrate. The distribution on glass is wider

and shows no tendency to cluster around the axis, with a lower quartile of 15.26° and the tenth percentile $P_{10} = 6.84^\circ$. The values of the upper quartiles (29.48° on the chip vs. 34.55° on the glass) also indicate that on the glass a smaller proportion of neurites align around the axis of the substrate. A comparison between the substrates is given in Figure 6.9.

In the case of differences in the interquartile range (28.03° on the chip vs 19.29° on the glass), it is important to take into account the very definition of the metric size, where some of the minimum values can stretch the interquartile range, so these differences should be interpreted with caution. Trimmed mean (10 %) confirms the consistency of median differences (25.16° vs 16.30°). The skewness distribution has the opposite sign, but relatively smaller amounts compared to some previously described morphological parameters (-0.27 on the glass vs $+0.27$ on the chip).

In general, it can be stated that in the observed experiment, the average and median angle to the nearest axis ($\delta\theta_{ax}$) decreases by 7° to 8° , whereby numerous neurites are completely collinear with the edges of the chip, which favors the emergence of mechanotactic effects.

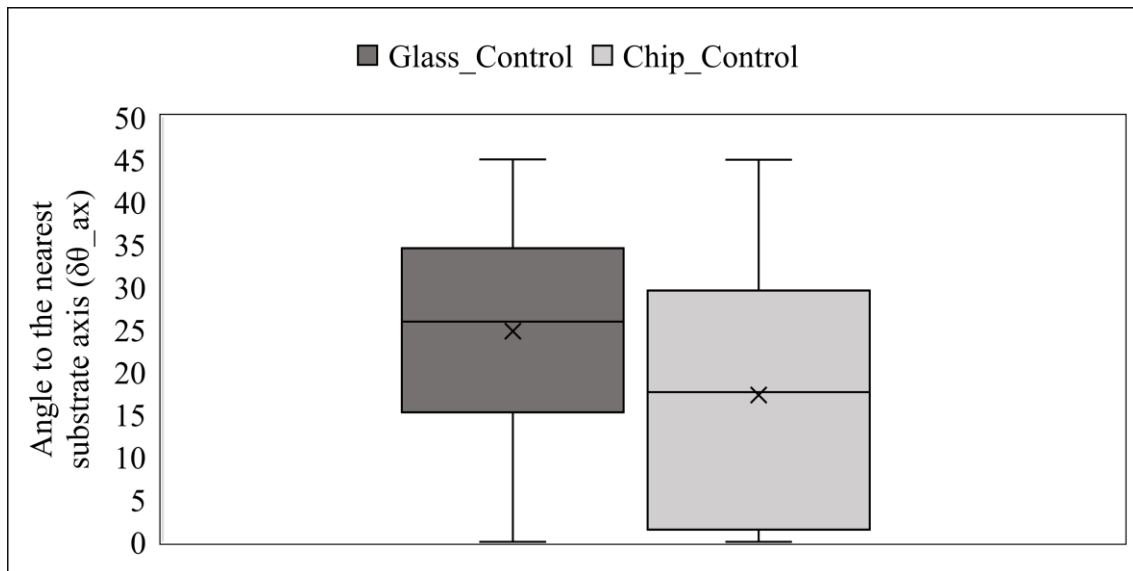


Figure 6.9 Angle to the nearest substrate axis ($\delta\theta_{ax}$): Glass control vs Chip control

6.1.4 Summary

Statistical analysis showed a consistent effect of the MEA substrate on all observed morphological parameters without electric field stimulation. The chip, with its microtopography, moderately but stably affects soma area ($166.7 \mu\text{m}^2$ on the chip vs. $136.2 \mu\text{m}^2$ on glass), with a relatively small proportion of Tukey outliers of 2 to 3 %. The permutation test resulted in a very low p-like value

of the theoretically minimal 0.0002, and this is supported by the Cliff's δ value of approximately +0.32 in favor of the chip. In neurite length, the effect of the substrate is even more pronounced. The differences in medians are larger than in soma area (138.4 μm on the chip vs. 93.2 μm on glass), the Cliff's δ value is +0.56, also in favor of the chip, and the permutation test gave the same, theoretically minimal values. Neurites showed a great tendency to align with the edges of three-dimensional substrates. In support of this conclusion, the higher biaxial alignment index (AI_bi) on the chip with the smaller angle to the nearest axis ($\delta\theta_{\text{ax}}$) stands out. Mann–Whitney, Cliff's δ and permutations ensured the reliability of the interpretation regardless of distribution asymmetry and extreme values, and bypassing inferential population methods avoided pseudoreplication.

The above results show a noticeable influence of the microstructures on the morphological parameters, above all on the alignment of the neurites, which showed a clear tendency to be oriented along the edges of the substrate. Regardless of the suboptimal conditions for the acquisition of morphometric parameters due to the high density and neurites overlapping, it can be stated that the MEA substrates have a distinct mechanotactic effect on spiral ganglion neurons. Based on this confirmed contact guidance effect, the following section examines whether electric field stimulation can additionally influence neuronal morphology through electrotaxis.

6.2 Electrotaxis on glass substrates

In this section, the influence of electrotaxis on flat glass substrates is analyzed. A sample of neuronal culture on flat glass without the presence of electric field (Glass control) and with the presence of electric field (Glass EF), i.e., without the influence of topographical effects, was compared. The same set of analytical methods as in Section 6.1 was used. Soma area and neurite length values were analyzed using previously demonstrated descriptive methods, with special emphasis on robustness with respect to distribution symmetry. The difference from the previous section lies in the metric used for neurite alignment. Instead of biaxial alignment index, circular alignment index (AI_circ) was used, and instead of angle to the nearest axis, angle to the local field tangent ($\delta\theta_{\text{circ}}$) was used. The new metric was introduced because, unlike the previous case where the neurite alignment was observed in relation to the vertical x and y axes of the substrate, in this case the influence on the neurites was exerted by a circular electric field. Therefore, for each ROI, its coordinates relative to the center of the chip (x_0, y_0) were recorded so that the angle it makes with the electric field tangent at the observed point could be determined from the

measured neurite orientation angle. The main indicator of the occurrence of electrotaxis is a lower value of $\delta\theta_{\text{circ}}$, which suggests a smaller deviation from the field tangent, and at the same time a higher value of AI_{circ} , which indicates a stronger alignment along the field tangent. In this way, a clear measure of the influence of electrotaxis on neurite alignment is ensured, while maintaining comparability with the previous unit on mechanotaxis. An example of the measured ROIs for soma area, neurite length and neurite alignment for the Glass_EF sample is shown in Figure 6.10.

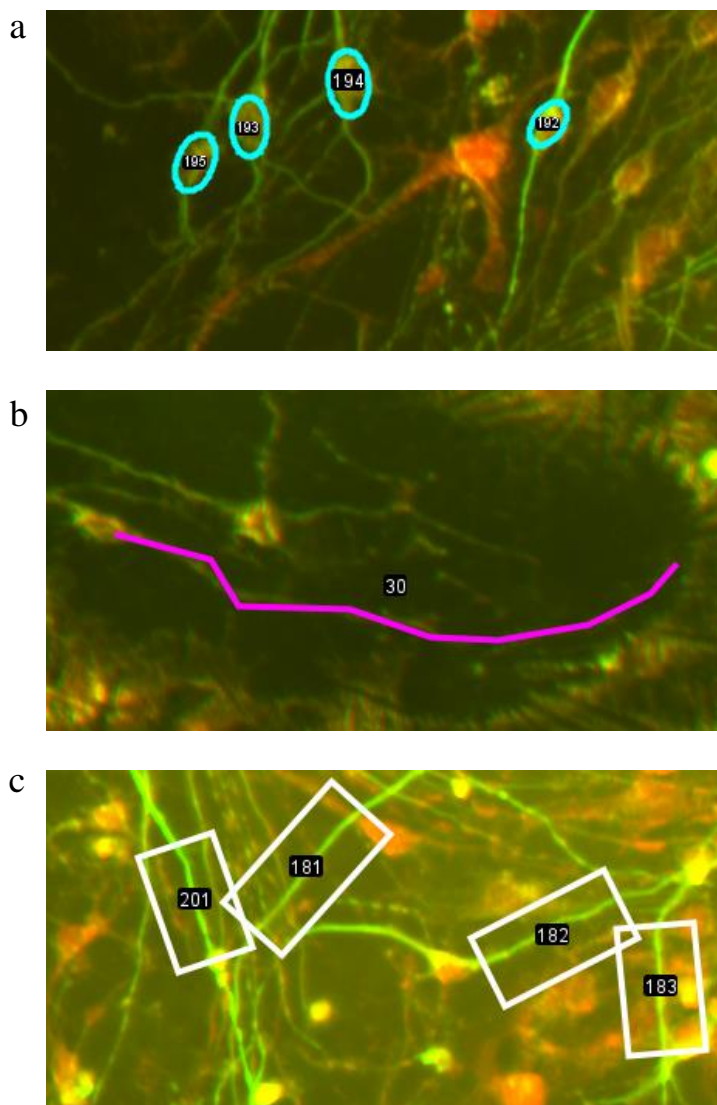


Figure 6.10 Representative ROI measurements on Glass EF: (a) SA (b) NL (c) NA; Adapted from [81]

6.2.1 Soma area

Figure 6.11 shows that the average soma area values in the stimulated sample are practically the same as in the control sample ($147.89 \mu\text{m}^2$ vs $149.11 \mu\text{m}^2$), with slightly larger differences in the median ($136.16 \mu\text{m}^2$ vs $145.04 \mu\text{m}^2$). A smaller dispersion was observed in the stimulated sample: standard deviation is $40.14 \mu\text{m}^2$ in the sample with electric field, and $49.42 \mu\text{m}^2$ in the sample without electric field.

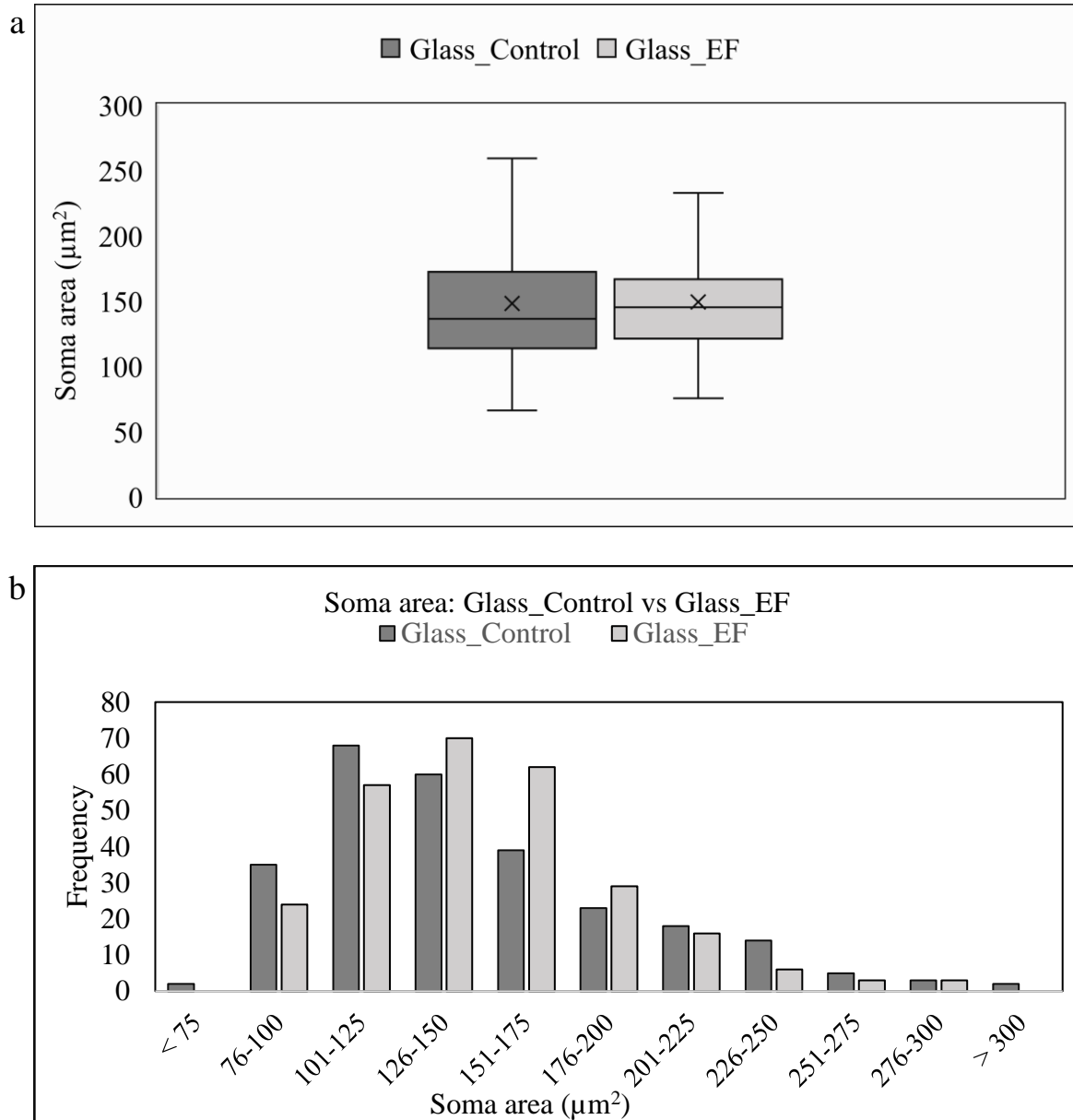


Figure 6.11 SA (Glass control vs Glass EF): (a) Box-and-whisker plot (b) Histogram

Accordingly, the interquartile range of the unstimulated sample ($58.67 \mu\text{m}^2$) is larger than that of the sample under electric field ($45.46 \mu\text{m}^2$). The trimmed mean (10 %) is slightly larger in the stimulated sample ($142.00 \mu\text{m}^2$ vs $145.79 \mu\text{m}^2$). The tenth and ninetieth percentiles confirm the effect of narrowing the distribution under the influence of electric field. P10 of the surface of the soma on the sample without stimulation is $96.16 \mu\text{m}^2$ compared to $102.07 \mu\text{m}^2$ on the sample with stimulation. P90 follows the same logic. Its amount on the sample without stimulation is $212.64 \mu\text{m}^2$ compared to $200.62 \mu\text{m}^2$ on the sample with electric field. The stimulated sample shows less asymmetry (skewness 1.22 vs 0.85), and kurtosis is much closer to the normal distribution (1.88 vs 0.90). It follows from the above that electric field has a barely noticeable effect on the soma area.

The narrower distribution of the sample with stimulation is also reflected in the values of Tukey's fences. In the control sample, the lower limit is $25.64 \mu\text{m}^2$, and the upper limit is $260.32 \mu\text{m}^2$, while in the stimulated sample, the lower limit is $52.88 \mu\text{m}^2$, and the lower limit is $234.72 \mu\text{m}^2$. Both analyzed groups have a small number of outliers: 8/270 in the Glass control group and 9/270 in the Glass EF group. Following on from the previous paragraph, it follows from the above that electric field had a slight influence on the stabilization of the size of the soma. The results of the permutation test also suggest a statistically significant but very weak difference. On 5 000 permutations, $\Delta_{\text{med}} = +8.88 \mu\text{m}^2$ was observed in favor of the stimulated sample, with p-like in the amount of 0.043, which means that the mentioned difference is present in 4.3 % of random permutations. This is supported by 95 % permutations with absolute differences in the interval from 0.00 to $10.54 \mu\text{m}^2$, where the median difference falls into the range of the null distribution.

The permutation null distribution of the median difference is shown in Figure 6.12 and takes the shape of a bell. Permuted distributions have overlaps, so it can be concluded that this effect, although present, is several orders of magnitude weaker than that of isolated mechanotaxis.

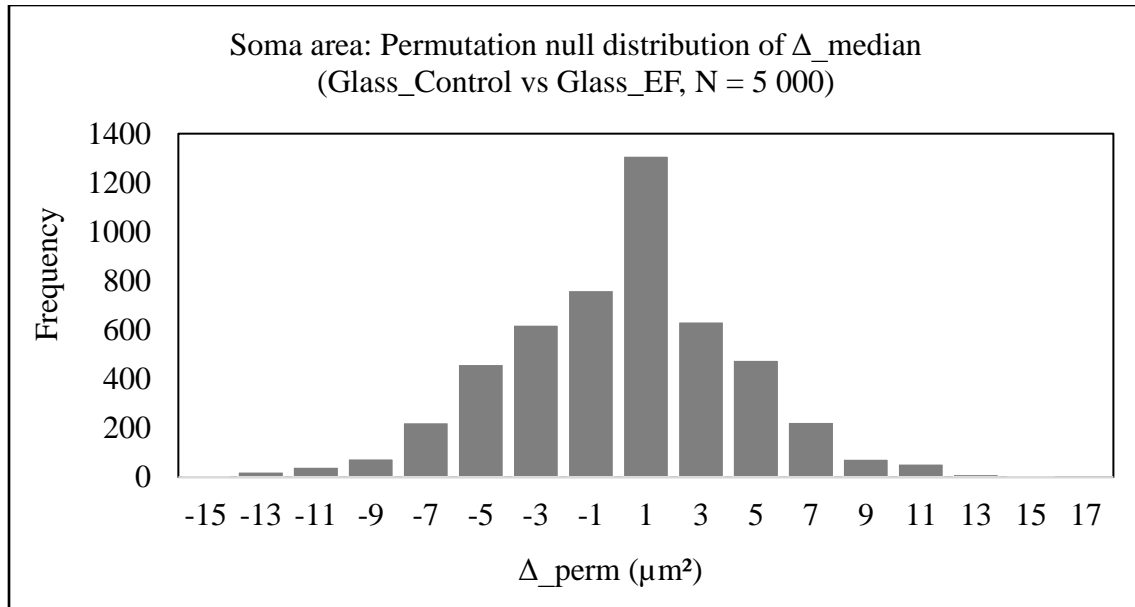


Figure 6.12 SA: Permutation null distribution of Δ_median (Glass control vs Glass EF)

6.2.2 Neurite length

Descriptive statistics of neurite length on a sample of 270 ROIs on Figure 6.13 shows a positive influence of electric field stimulation. The average neurite length on the stimulated sample is higher than that on the non-stimulated sample (115.90 μm vs. 101.18 μm). The median follows the same trend (112.23 μm vs. 93.23 μm). In accordance with the median and average, P10 in the stimulated group is higher (73.63 μm vs. 49.41 μm), as is P90, but with a slightly smaller difference (164.15 μm vs. 155.05 μm). Similar to soma area, the stimulated sample shows a smaller dispersion, which is reflected in a smaller interquartile range (45.15 μm vs 56.60 μm) and a smaller standard deviation (35.17 μm vs 46.47 μm).

Also, the stimulated sample takes on a more symmetrical shape (skewness 0.64 vs 1.54). In the stimulated sample, the trimmed mean (10 %) has a value similar to the average of all measured ROIs (115.90 μm vs 113.49 μm), so the effect of extreme values can be excluded. The lower Tukey's fences for Glass control are -17.77 μm , and the upper 208.63 μm . For the stimulated sample, the values are 23.24 μm and 203.84 μm . Both distributions have a small proportion of extreme values: Glass control 2.59 % (7/270), and 1.85 % (5/270) for the Glass EF sample.

Statistics based on ranks point to similar conclusions. 37 % (PS = 0.37) of all 270 \times 270 pairs have longer neurites on the glass compared to neurites under stimulation, from which it follows that

63 % of them are longer on the stimulated sample. The Cliff's δ value for the Glass control sample is -0.27 and analogously +0.27 for the Glass EF, which is considered a small to medium effect in favor of the stimulated sample. From the rank sum (63 328 vs 82 742) and the corresponding Mann–Whitney U for Glass control = 26 743, a conclusion follows from the previous ones: Neurites are longer on the stimulated sample.

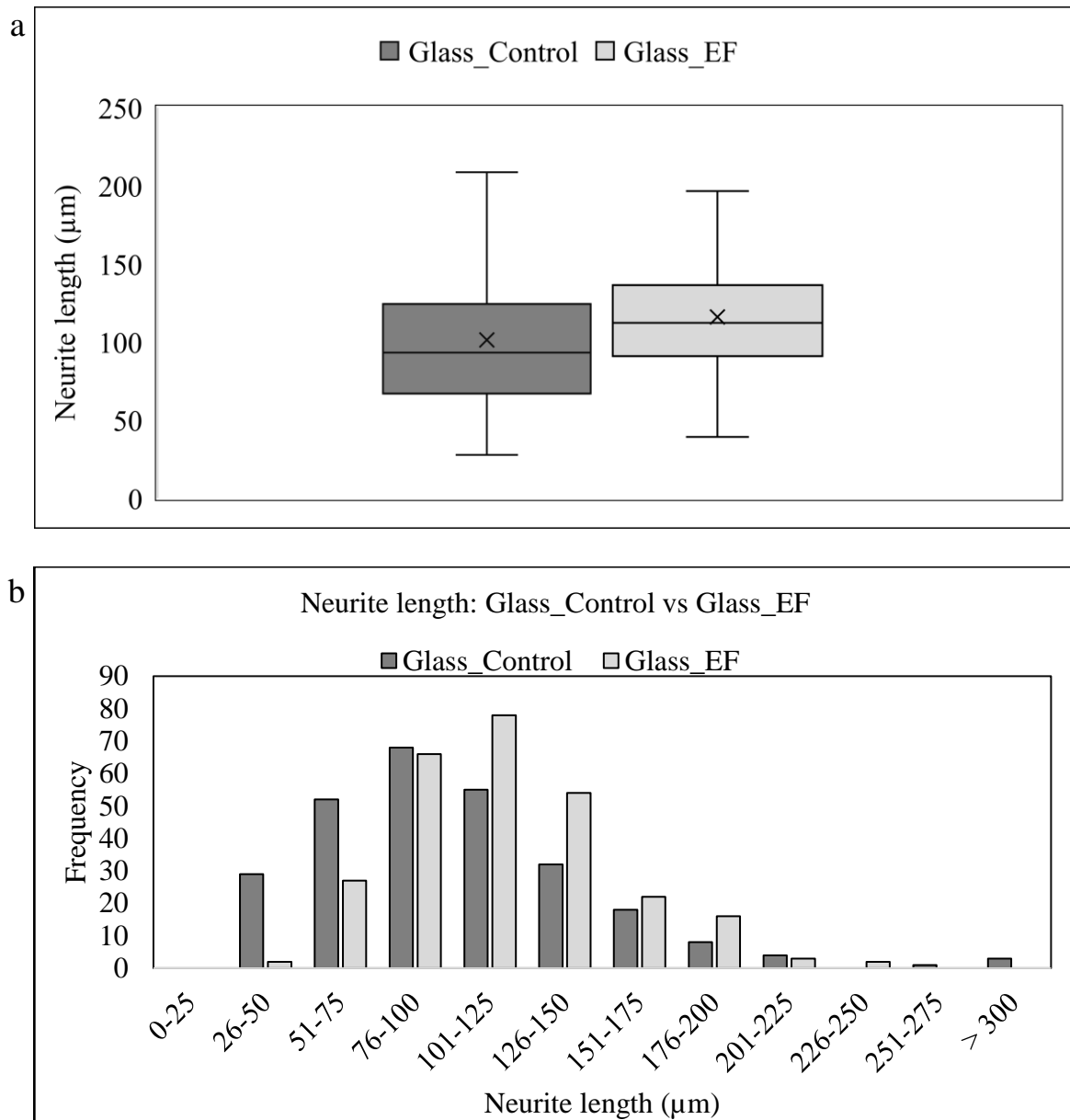


Figure 6.13 NL (Glass control vs Glass EF): (a) Box-and-whisker plot (b) Histogram

For 5 000 permutations the measured median difference is $\Delta_{\text{median}} = 19.00 \mu\text{m}$, again in favor of the Glass EF sample. Typical random differences of permutations are small ($\text{CI}_{95 \text{ perm}} \approx$

0.13–8.02 μm), which is consistent with the minimum p-like value of 0.0002. In other words, such a difference in the median is significantly larger than expected from a random shuffling of ROIs.

The permutation histogram of the null distribution of the median neurite length differences is shown in Figure 6.14. It can be seen from the figure that Δ_{median} in the amount of 19.00 μm is significantly outside the 95 % permutation interval, and that the tail of the null distribution contains only 0.02 % of permutations, making the conclusion about the increase in neurite length under the influence of the electric field robust and reliable.

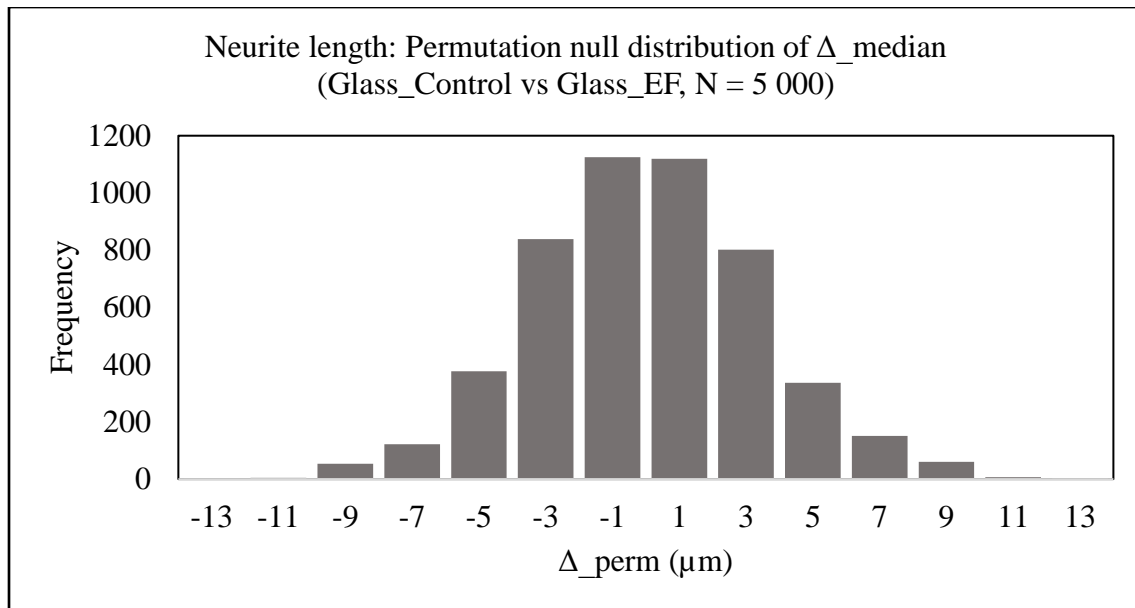


Figure 6.14 NL: Permutation null distribution of Δ_{median} (Glass control vs Glass EF)

6.2.3 Neurite alignment

In this subsection, the influence of electric field stimulation on neurite alignment is analyzed using the metrics defined in Chapter 4, as stated at the beginning of the chapter. Figure 6.15 shows the distribution of the measured neurite orientations for the glass substrate without stimulation and the glass substrate with electric field stimulation. The glass control sample covered in this subsection is the same as the sample covered in Section 6.1.

6.2.3.1 Circular alignment index

Looking at the circular alignment index (AI_circ), it is obvious that both groups show a wide distribution in the allowed interval from 0.00 to 1.00 with minor differences in favor of the Glass EF sample, as shown in Figure 6.16. In the stimulated group, a slightly higher median (0.58 vs

0.51) and a slightly higher mean (0.54 vs 0.51) were observed. The difference is also accompanied by the 95 % confidence interval for the mean (0.47 vs 0.50). The interquartile ranges show a small advantage in favor of the stimulated group (0.73 vs 0.70), as do the standard deviations (0.36 vs 0.35). The lower quartile of the stimulated group is higher than the lower quartile of the non-stimulated group (0.20 vs 0.15), and the same applies to the upper quartile with a slightly smaller difference (0.87 vs 0.89).

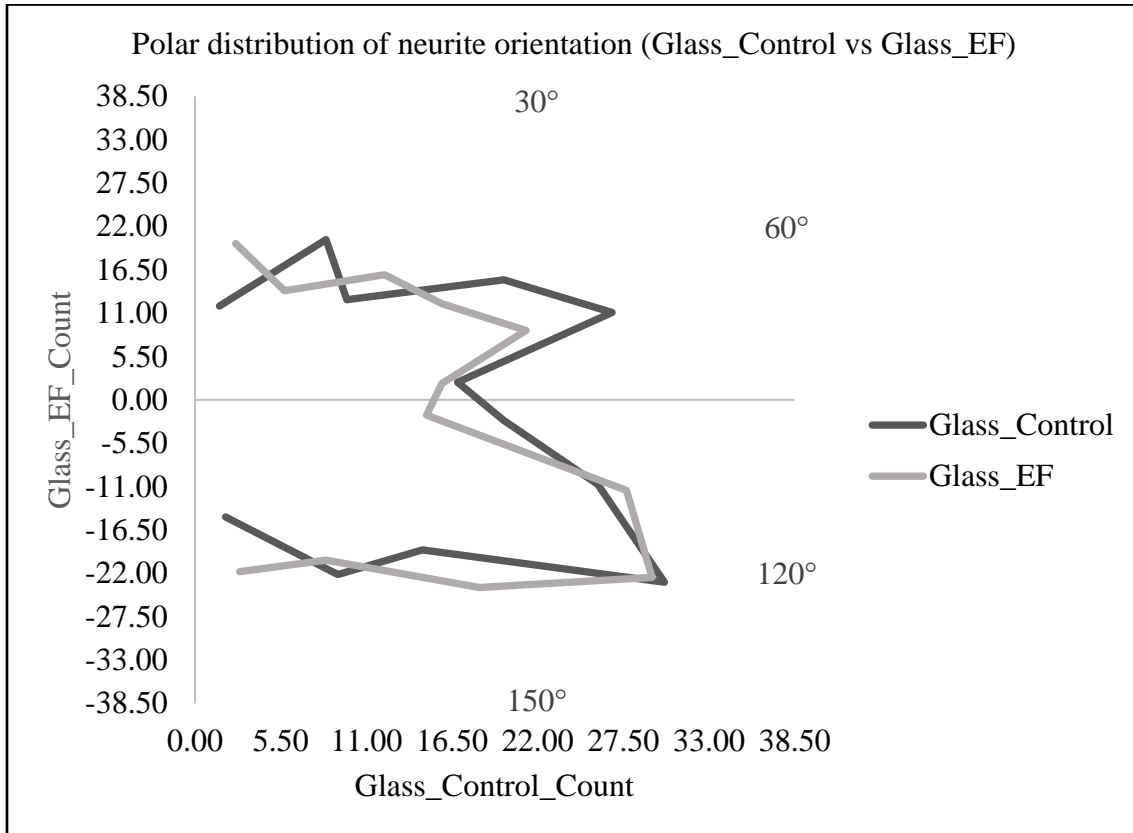


Figure 6.15 NA (Glass control vs Glass EF): Half-polar plot (0–180°)

The 90th percentile of the unstimulated sample is 0.98, and 0.99 for the stimulated sample. Although small, this difference suggests a non-negligibly larger number of highly aligned ROIs. The similarity of the distributions is reflected in close values of skewness (-0.02 vs -0.15) and platykurticity (kurtosis -1.49 vs -1.44). Taken together, these results support the thesis that the stimulation causes a slightly greater alignment along the local electric field tangent, with a similar distribution of the measured alignment angle values.

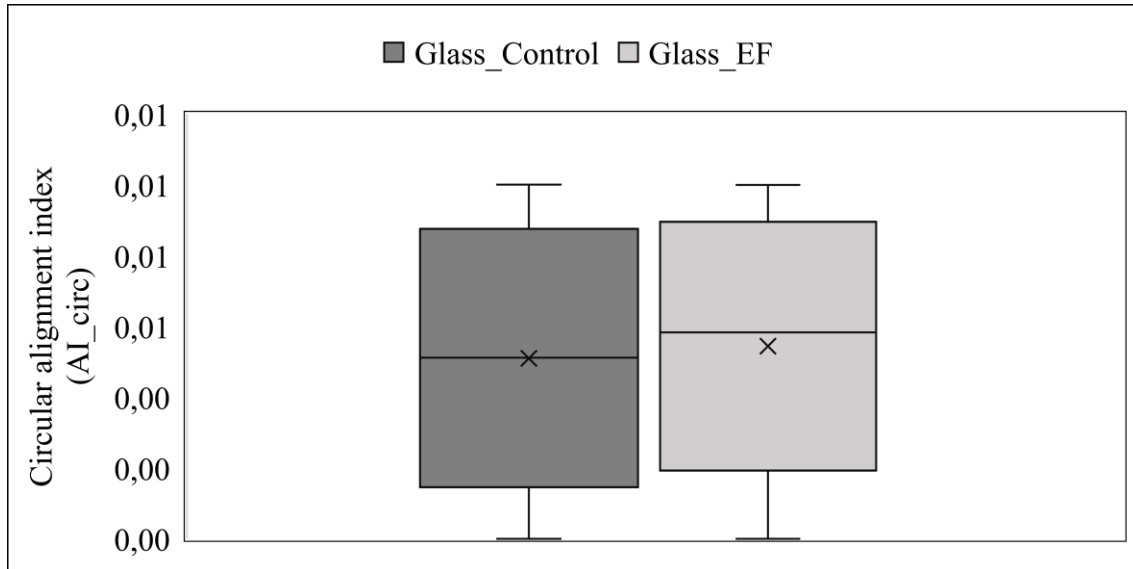


Figure 6.16 Circular alignment index (AI_circ): Glass control vs Glass EF

The observed difference in medians for AI_circ per 1 000 permutations is +0.07 in favor of the stimulated sample. The permutation probability measure shown (p-like = 0.036) suggests that a difference of at least +0.07 occurs in approximately 3.6 % of random permutations, and the estimated 95 percent permutation interval for the median difference is in the range of 0.00 to 0.10, and shows that there is a small but consistent effect in accordance with the results shown in the box-and-whisker plot. Given that the AI_circ measure is limited to a defined interval from 0.00 to 1.00 and that the interquartile range is 0.70, the median difference of 0.07 represents a tenth of the range. Such an effect can be described as modest, but it supports the existence of electric field's influence on the alignment of neurites along the local field tangent.

6.2.3.2 Angle to local field tangent

The angle to the local field tangent distribution for both groups is wide and almost symmetrical, and the skewness tends to zero. Small differences in median and mean values were recorded in the two observed samples, shown in Figure 6.17. The median of the sample without stimulation is 44.34°, and the median of the sample with stimulation is 40.20°, which is 4.1° less. A similar trend with a slightly smaller difference is also recorded in the means, with 44.22° for the unstimulated sample and 41.64° for the stimulated sample. A similar trend is present in other descriptive measures. Lower quartile 20.81° vs 18.98°, upper quartile 67.52° vs 63.59° and trimmed mean (10 %) 44.02° vs 41.05°.

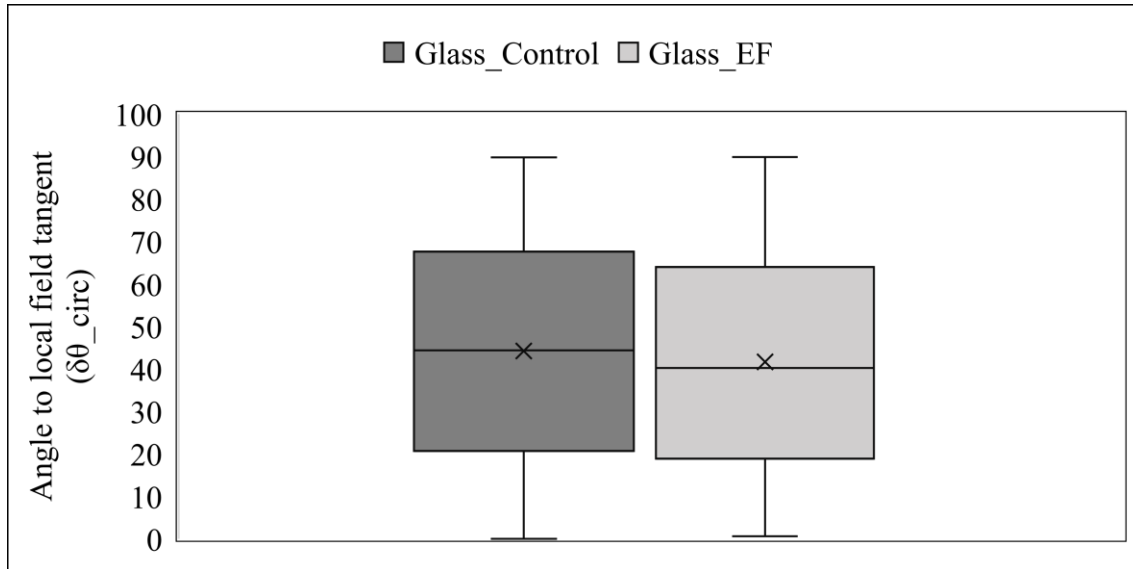


Figure 6.17 Angle to local field tangent ($\delta\theta_{circ}$): Glass control vs Glass EF

6.2.4 Summary

Overall, the effect of electrotaxis, although not negligible, is noticeably weaker than that of mechanotaxis. The electric field showed a weak effect on the area of the soma, with smaller differences in medians and means and a weaker permutation result (p-like ≈ 0.043) and Cliff's $\delta \approx 0.07$ than in the case of mechanotaxis. The effect of the electric field is somewhat stronger on neurite length, with noticeably significantly stronger results in permutations (p-like = 0.0002) and a stronger effect Cliff's $\delta \approx 0.27$. A tendency to align neurites was also observed, but to a lesser extent than in Section 6.1. The consistency of the results, but also their small amount, suggest the existence of an effect, but also indicate the further possibility and even the need for optimization of parameters and the experimental interface in general. Based on the separately confirmed effects of mechanotaxis and electrotaxis, although with different intensities, the following section analyzes their combined influence on spiral ganglion neuron morphology.

6.3 Mechanotaxis and electrotaxis: combined effect

In this section, the combined effect of substrate microtopography and EF stimulation is analyzed. The previously presented samples (Glass control, Chip control, and Glass EF) are compared with a sample with electric field stimulation on a substrate with microtopography (Chip EF) using the same metrics as in the previous cases. Figure 6.18 shows the ROI measurement snippets for Chip EF.

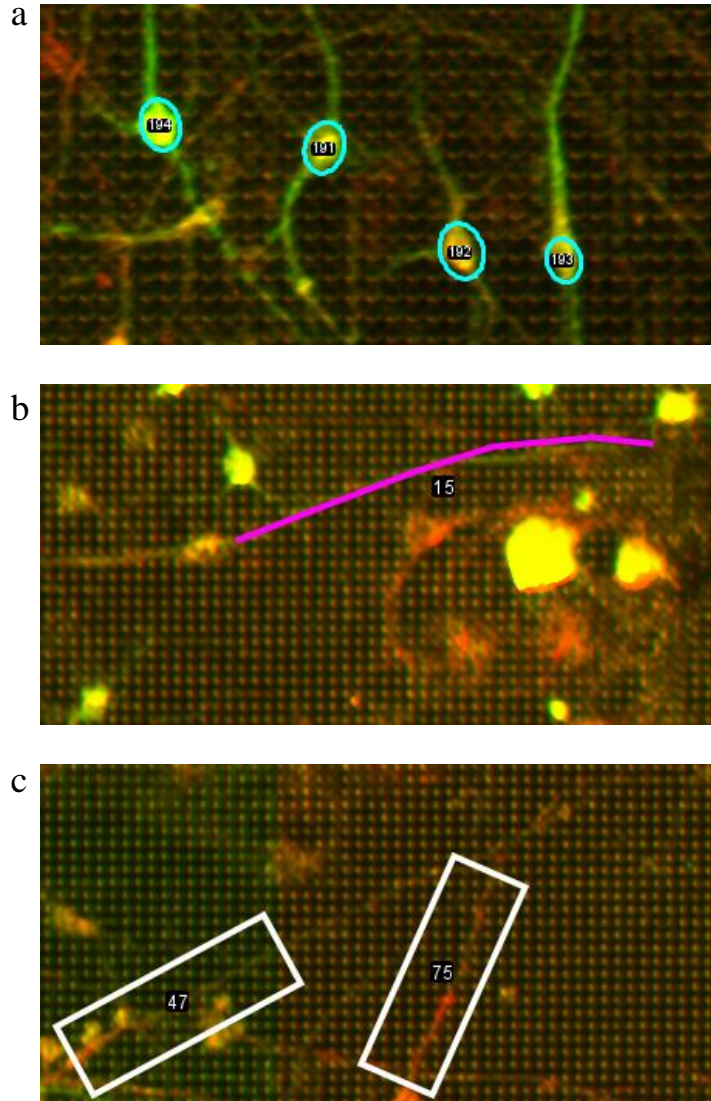


Figure 6.18 Representative ROI measurements on Chip EF: (a) SA (b) NL (c) NA; Adapted from [81]

6.3.1 Soma area

The comparison for the difference in soma area is given for the samples:

- Glass control vs Chip EF: No cues vs combined effect (mechanotaxis + electrotaxis)
- Chip control vs Chip EF: Mechanotaxis vs combined effect (mechanotaxis + electrotaxis)
- Glass EF vs Chip EF: Electrotaxis vs combined effect (mechanotaxis + electrotaxis)

The comparison for neurite length and neurite alignment is given in the same way.

6.3.1.1 No cues vs combined effect

The mean values of the control sample, as shown in Figure 6.19, are very similar to those of the sample with both cues, which is also reflected in the means ($147.89 \mu\text{m}^2$ on Glass control vs $150.78 \mu\text{m}^2$ on Chip EF) and somewhat less in the median ($136.16 \mu\text{m}^2$ on Glass control vs $150.78 \mu\text{m}^2$ on Chip EF). The same trend is followed by the values of the upper quartiles ($172.31 \mu\text{m}^2$ on Glass control vs $174.59 \mu\text{m}^2$ on Chip EF), while a slightly larger difference can be observed in the lower quartile ($113.64 \mu\text{m}^2$ on Glass control vs $125.83 \mu\text{m}^2$ for Chip EF).

As for the variation within the samples themselves, the dispersion is somewhat smaller in the Chip electric field sample, which is reflected in the standard deviation of $38.60 \mu\text{m}^2$ compared to $49.42 \mu\text{m}^2$ in the control sample. Furthermore, Tukey's fences on the chip with stimulation show fewer outliers (1.11 % vs 2.96 %). There are also noticeable differences in the interquartile range from $58.67 \mu\text{m}^2$, which is in the control sample, to $48.76 \mu\text{m}^2$, which is in the sample with both cues. In the observed case, the microtopography in combination with the electric field did not significantly increase the surface of the soma, but narrowed the distribution.

The comparison of ranks showed a consistent, but very small difference in favor of the sample with both cues. On the control glass for the same sample sizes as in the previous cases ($N = 270$) $U = 32\,232$ was calculated with a probability of superiority of 0.44 in the condition (Glass control $>$ Chip EF), from which it follows that in 56 % of randomly selected pairs soma area is higher for the Chip EF sample. The effect is admittedly weak, since Cliff's δ (Glass control) = -0.12 , which gives $+0.12$ for Chip EF.

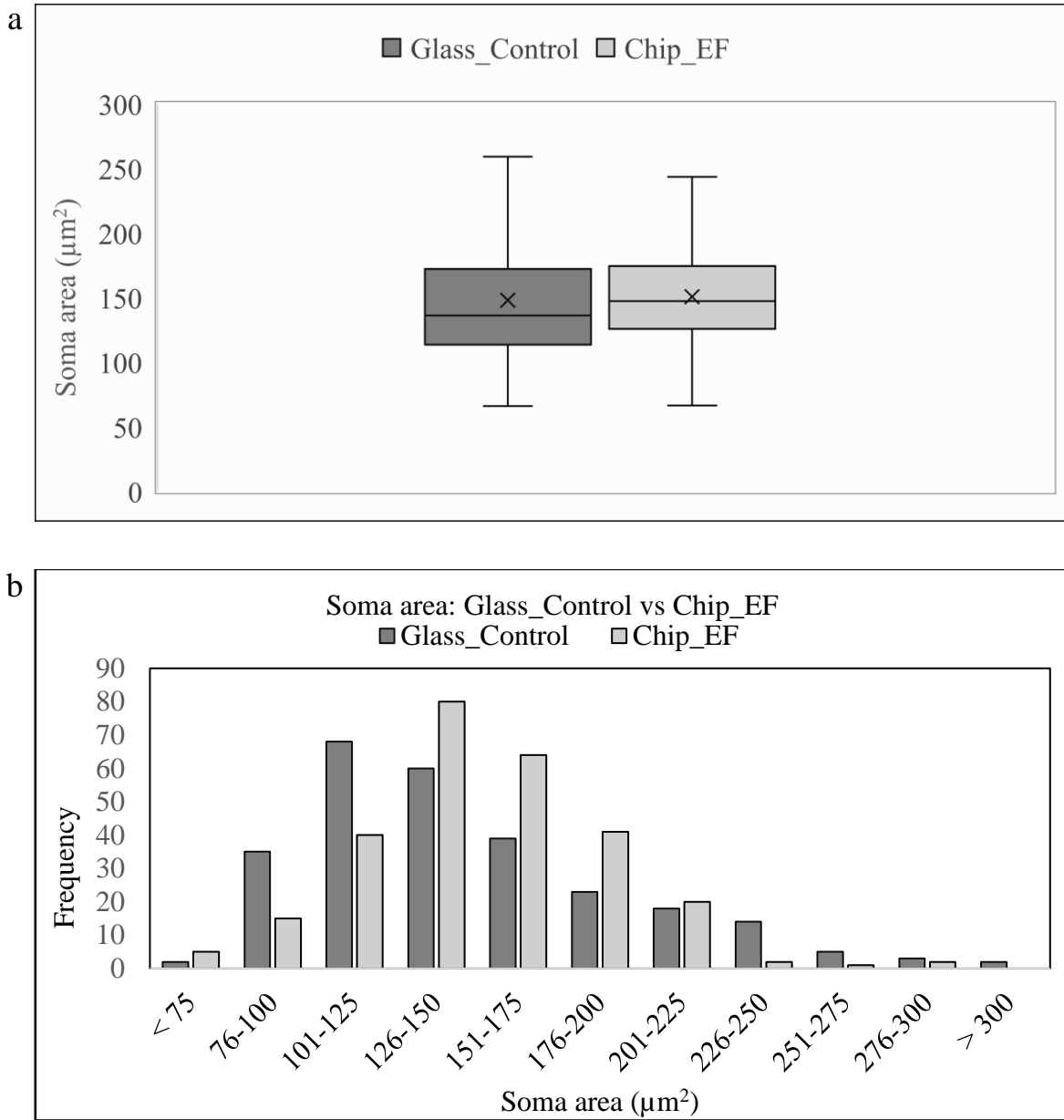


Figure 6.19 SA (Glass control vs Chip EF): (a) Box-and-whisker plot (b) Histogram

In 1 000 permutations, a difference in medians of $11.16 \mu\text{m}^2$ was observed, with a p-like value of 0.0036 and a 95 % null hypothesis interval ranging from $0.21 \mu\text{m}^2$ to $10.95 \mu\text{m}^2$. Therefore, $|\Delta_median|$ slightly falls out of that interval, from which a similar conclusion emerges as with the descriptive indicators, according to which both cues combined have a small but consistent effect on soma area.

This case is shown by the histogram in Figure 6.20 for 1 000 permutations. The distribution is centered around zero and approximately symmetrical in shape, and Δ_{median} in the amount of $11.16 \mu\text{m}^2$ is located on the far right edge of the null distribution, in accordance with the p-like value.

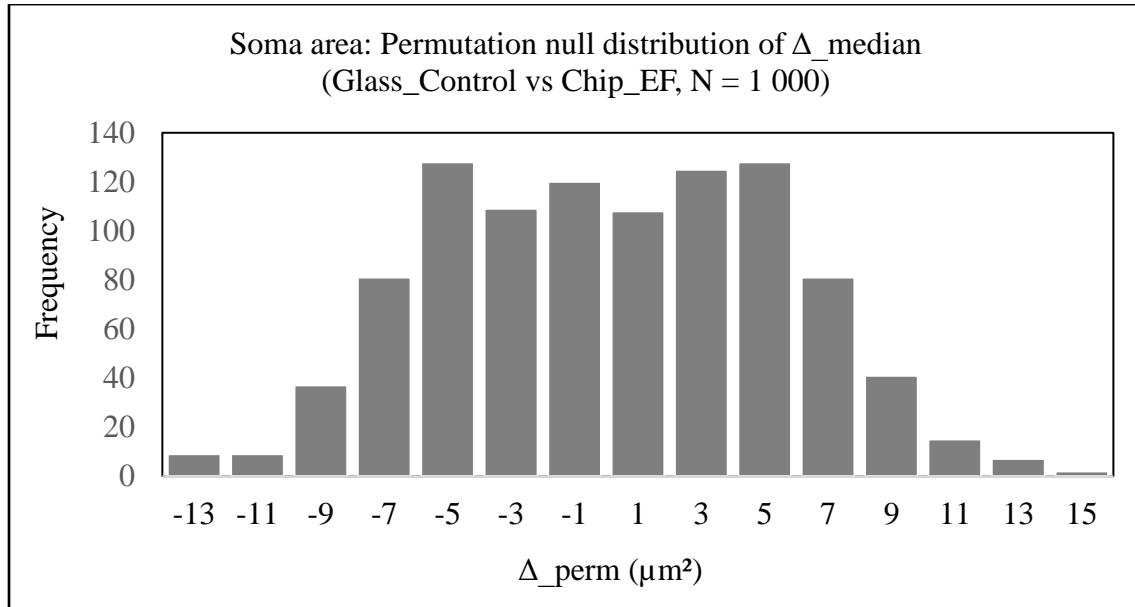


Figure 6.20 SA: Permutation null distribution of Δ_{median} (Glass control vs Chip EF)

6.3.1.2 Mechanotaxis vs combined effect

Comparing the effects of mechanotaxis with the effects of the pattern with both cues, a systematic difference in favor of isolated mechanotaxis can be observed, as shown in Figure 6.21. The differences in the means ($177.77 \mu\text{m}^2$ for Chip control vs $150.78 \mu\text{m}^2$ for Chip EF) are obvious, as are the differences in the medians ($166.74 \mu\text{m}^2$ for Chip control vs $147.32 \mu\text{m}^2$ for Chip EF). The tenth percentile shows a slightly smaller difference ($110.21 \mu\text{m}^2$ for Chip control vs $102.07 \mu\text{m}^2$ for Chip EF), while the ninetieth percentile shows a very pronounced difference ($247.02 \mu\text{m}^2$ for Chip control vs $199.21 \mu\text{m}^2$ for Chip EF). The sample with both cues shows lower variability, which is reflected in both standard deviations ($38.60 \mu\text{m}^2$ vs $63.66 \mu\text{m}^2$) and interquartile ranges ($48.76 \mu\text{m}^2$ vs $77.17 \mu\text{m}^2$), which, as in the previous section, shows that soma area variability decreases in the presence of electric field. This is also supported by the difference in the maximum measured value ($571.90 \mu\text{m}^2$ vs $299.79 \mu\text{m}^2$).

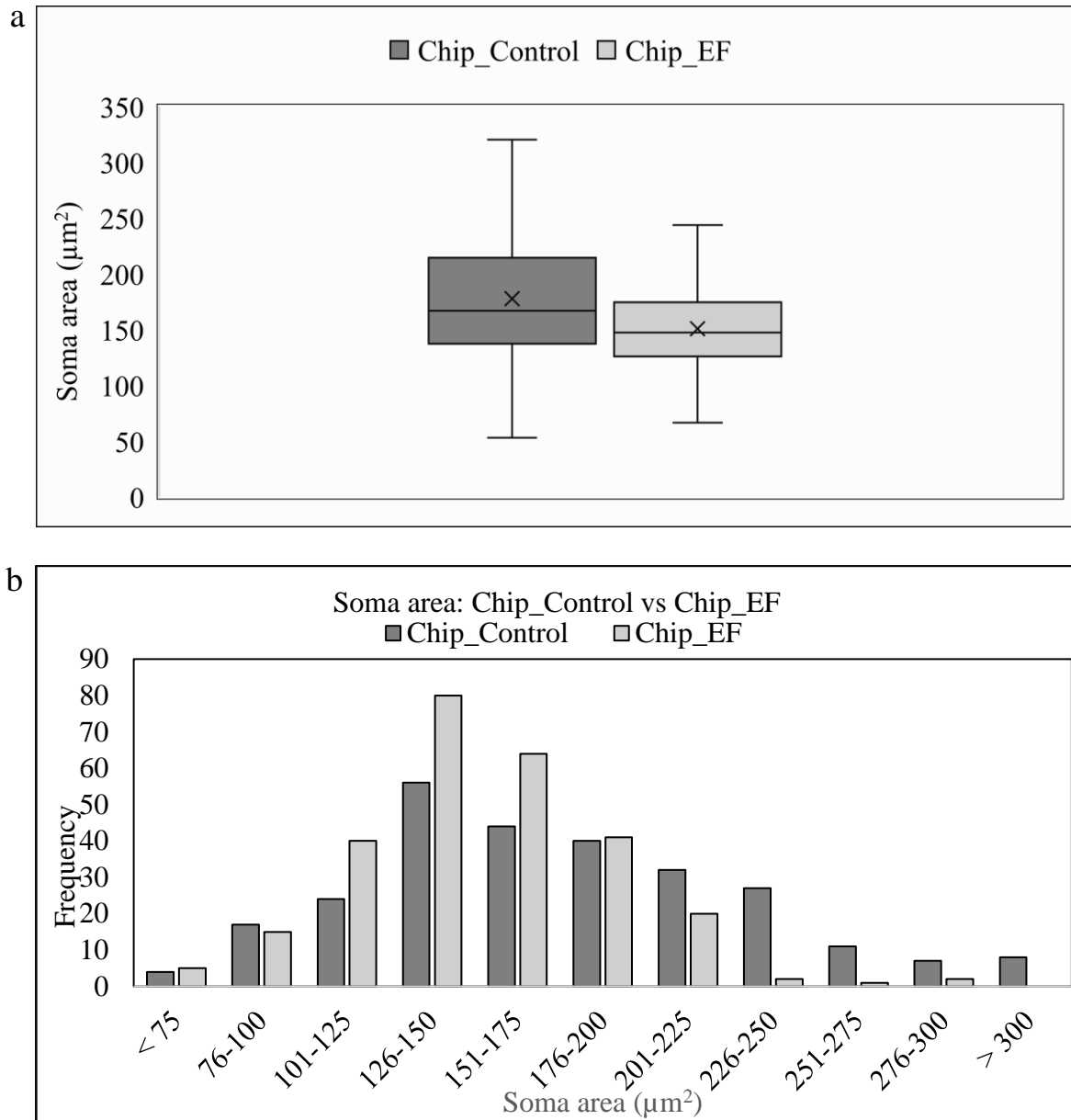


Figure 6.21 SA (Chip control vs Chip EF): (a) Box-and-whisker plot (b) Histogram

Tukey's fences also confirm the differences in dispersion. In the conditions of mechanotaxis, the limits are in the interval from 21.53 µm² to 330.22 µm², and in the combined effect the interval is in the range from 52.69 µm² to 247.73 µm². Both samples have a very small number of outliers: 1.85 % for the Chip control, and 1.11 % for the Chip electric field sample. These results are consistent with the results of descriptive statistics, according to which also electric field stimulation on three-dimensional surfaces makes the surface distribution of soma narrower.

The comparison of the rank sums for the samples of 270 ROIs gives the value of the U parameter in the amount of 46 025, with a probability of superiority of 0.63, which implies that in 63 % of the randomly selected somas, the one with both cues has a smaller area. This is supported by the values of Cliff's $\delta = +0.26$ (Chip control) and -0.26 (Chip EF), which give a small to medium advantage to the sample without stimulation.

As for the permutation test, it showed on 1 000 labels a median difference of $19.43 \mu\text{m}^2$, and that for the null distribution, which is located in the 95 percent range from $0.21 \mu\text{m}^2$ to $11.38 \mu\text{m}^2$. This is visually shown in Figure 6.22, from which it is obvious that $|\Delta_{\text{median}}|$ is located far outside the interval of the null distribution, which is normally the case for such a small p-like, as in some previously described examples.

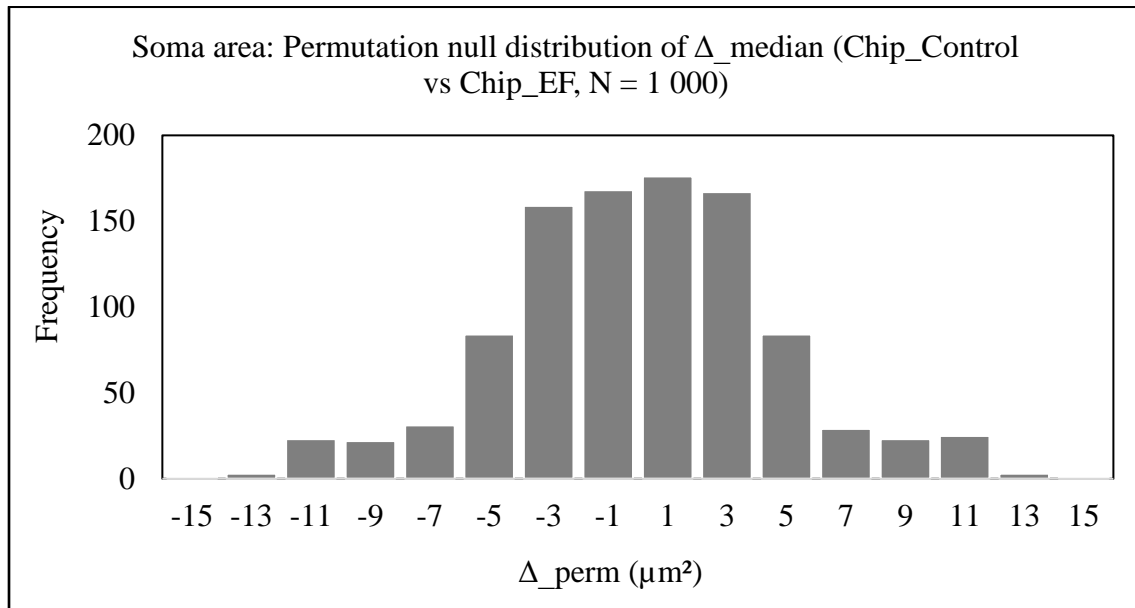


Figure 6.22 SA: Permutation null distribution of Δ_{median} (Chip control vs Chip EF)

For this case, the p-like is again theoretically minimal 0.0002, from which it can be concluded that the random permutation is greater than or equal to $|\Delta_{\text{median}}|$ in only 0.02 % of cases. The distribution itself is almost symmetrical and is clustered around zero. These results are consistent with the results of descriptive statistics that suggest a slight but consistent decrease in soma area on samples with both cues, compared to those where only mechanotaxis is present.

6.3.1.3 Electrotaxis vs combined effect

As far as the soma area is concerned, for both observed substrates under the conditions of electric field stimulation, the central values record very similar amounts, as shown in Figure 6.23. Mean on Glass EF is $149.11 \mu\text{m}^2$, and on Chip EF its value is $150.78 \mu\text{m}^2$. The situation is similar with the median, where the median on the glass is $145.04 \mu\text{m}^2$ while on the chip it is $147.32 \mu\text{m}^2$. In this case, there are no big differences in the dispersion of the distribution. The standard deviations are $40.14 \mu\text{m}^2$ on glass vs $38.60 \mu\text{m}^2$ on chip, while the interquartile ranges are also not much different: $45.46 \mu\text{m}^2$ on glass vs $48.76 \mu\text{m}^2$ on chip. In accordance with the above, the 95 % confidence intervals of the mean also overlap ($144.30 \mu\text{m}^2$ on glass vs $146.15 \mu\text{m}^2$ on chip). The lower and upper quartile values are slightly higher on the chip (Q1: $121.07 \mu\text{m}^2$ vs $125.83 \mu\text{m}^2$ and Q3: $166.53 \mu\text{m}^2$ vs $174.59 \mu\text{m}^2$). Both distributions lean to the right (skewness is 0.85 and 0.42), and both distributions also have slightly thicker tails, i.e., less clustering around the average (kurtosis 0.90 and 0.74). The described quantities suggest that in the presence of electric field there is no great influence on soma area depending on the substrate.

Tukey's fences values for these samples are almost identical. In the glass sample, the lower soma area limit is $52.88 \mu\text{m}^2$, and the upper limit is $234.72 \mu\text{m}^2$. The sample on the chip gives the lower limit at $52.69 \mu\text{m}^2$ while the upper limit is $247.73 \mu\text{m}^2$. In both observed groups, the share of outliers is low. On the glass it is 3.33 % (9/270), and on the chip 1.11 % (3/270). The conclusion rests on the previous paragraph. The distributions are stable and similar in shape. Following on from previous results, microtopography shows less influence on soma area in the presence of electric field compared to the case without electric field.

The rank test yielded a value of $U = 34\ 354$ with a probability of superiority (Glass EF > Chip EF) of 0.47, which is almost 50 %, so the advantage of the chip under stimulation conditions for this metric is very small. In line with these results, the Cliff's δ value is 0.06, which represents a negligibly strong effect compared to the usual threshold of $|\delta| < 0.147$.

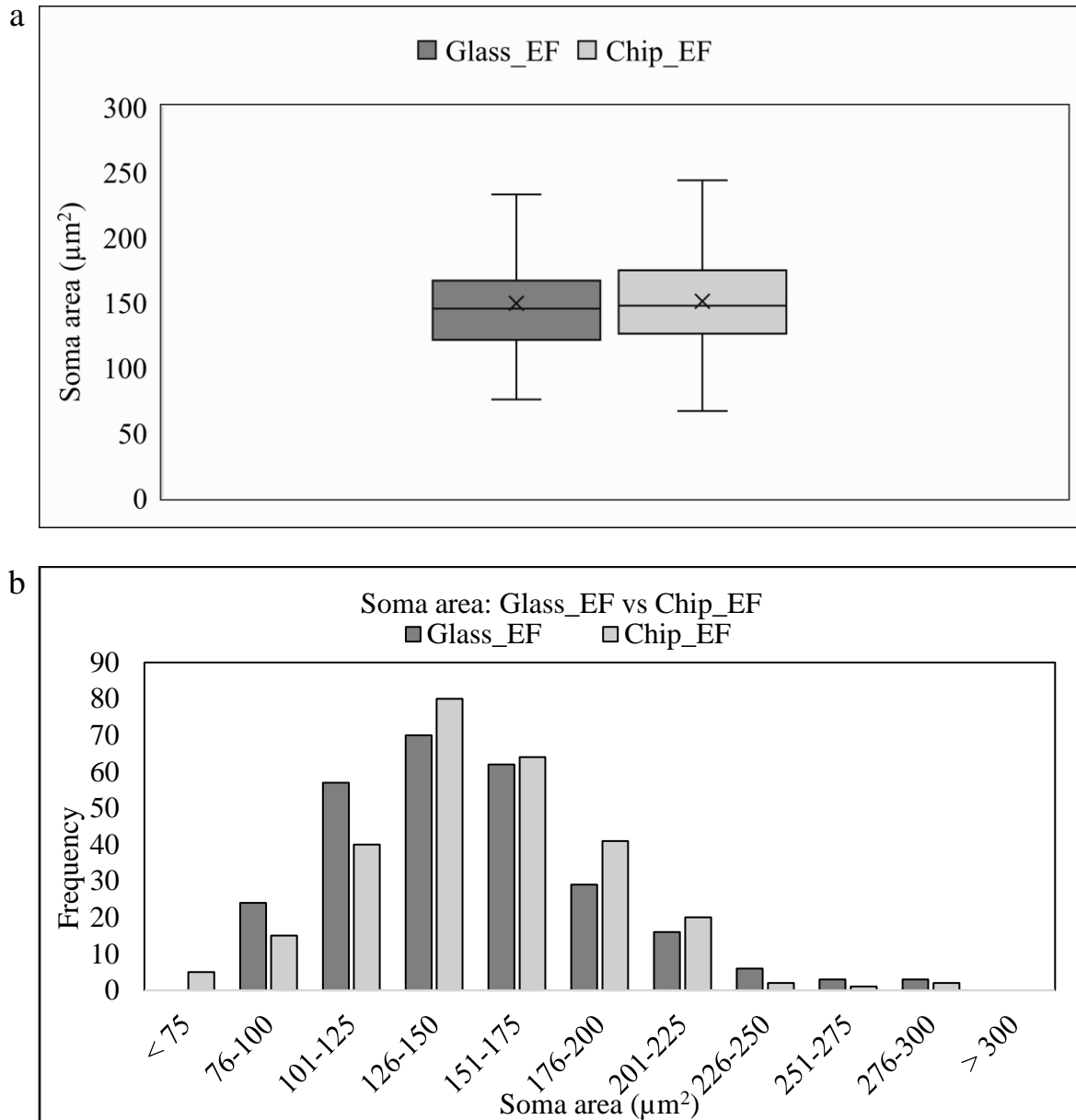


Figure 6.23 SA: Glass EF vs Chip EF: (a) Box-and-whisker plots (b) Histogram

The results of the permutation test, presented in Figure 6.24, show the same. On a group of 1 000 labels, the median difference is only 2.28 μm^2 in favor of the sample with both cues. The two-sided p-like value of 0.0898 is on the same trace. The 95 percent confidence interval ranges from 0.21 μm^2 to 8.69 μm^2 . The histogram shows a relatively symmetric null distribution clustered around zero, into which confidence interval range Δ_{median} falls. These results statistically support the claim from the descriptive quantities, according to which the difference in the soma

area on the chip and glass under the conditions of electric field stimulation is very small and statistically uncertain.

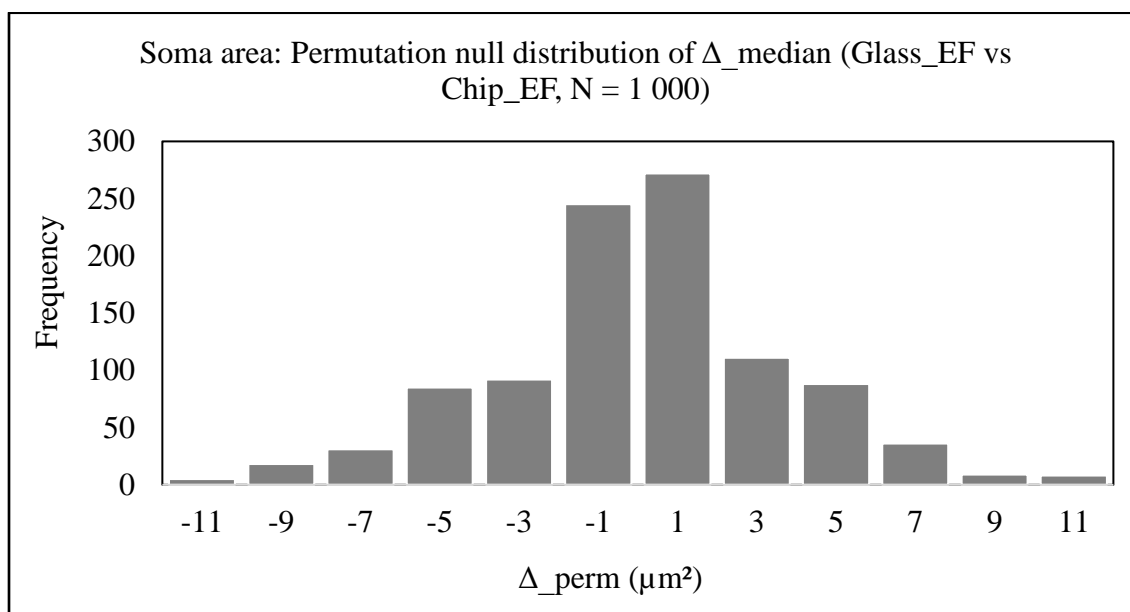


Figure 6.24 SA: Permutation null distribution of Δ_{median} (Glass EF vs Chip EF)

6.3.2 Neurite length

6.3.2.1 No cues vs combined effect

As for the length of the neurites, the sequence of the observed conditions is the same as for the surface of the soma. A comparison of the observed groups is given in Figure 6.25. In the first group, the combined effect (Chip EF) was observed in comparison with the sample without cues, i.e., with the control group (Glass control). For a sample of 270 neurites, the Chip EF showed a noticeable difference. The mean was measured to be 160.11 μm , while on the flat glass without stimulation the value was 101.18 μm . The median is also similar. In the combined effect it is 156.84 μm , and in the control group it is 93.23 μm . The quartiles continue with their values in the same direction. The first quartile of the control sample is 67.13 μm compared to 117.41 μm on the chip with stimulation. The third quartile of the control sample takes on a value of 123.73 μm , and in the Chip EF sample it is 194.29 μm . The differences in lengths are also evident in the values of the tenth and ninetieth percentiles. P10 (Chip EF) is 89.09 μm , while the same percentile for the control sample is 49.41 μm . On the other hand, the P90 (Chip EF) distribution takes on a value of 234.02 μm , and for the control sample it is 155.05 μm . The difference is also confirmed by the trimmed mean (10 %) with values of 156.25 μm and 96.35 μm . The stimulated sample showed

slightly greater variability (standard deviation: 58.47 μm vs 46.47 μm . Both groups are clustered around the mean, but the sample with both cues is less clustered around the mean (kurtosis 1.91 vs 4.37).

Tukey's bars show that the sample with on-chip stimulation has a wider range. The lower limit is 2.97 μm , and the upper limit is 309.62 μm . In the control sample with no cues, the lower limit is 17.77 μm , and the upper limit is 208.63 μm . Accordingly, the interquartile range of the chip with stimulation is greater than that of the control sample (76.89 μm vs 56.60 μm). Both groups have only a smaller share of outliers. In the control group, this share is 2.59 % (7/270), and in the stimulated chip 1.85 % (5/270), therefore their effect on the results is not great.

The Mann-Whitney U (Glass control) is 14 281 with PS (Glass control) = 0.20, implying that in 80 % of random pairs, the sample takes on a higher value under the influence of mechanotaxis and electric field stimulation with a relatively strong effect (Cliff's delta $|\delta| = 0.61$). The rank sum in this comparison for the control sample is 50 866, and for the Chip EF 95 205. The rank test clearly shows that the neurites are longer under stimulation conditions on the chip compared to the substrate with no cues.

On 1 000 permutations, Δ_{median} was recorded in the amount of 63.61 μm . Since the null distribution is relatively narrow, with the 95 percent interval lying in the range from 0.79 μm to 19.50 μm , the Δ_{median} is several times larger than the value within it. In accordance with this, the theoretical minimum value of the two-sided p-like in the amount of 0.0002, as well as with other samples where the descriptive measures showed a big difference.

The null distribution, relatively symmetric and centered around zero, for 1 000 permutations is shown in the histogram in Figure 6.26. It is obvious that $\Delta_{\text{median}} \approx +63.61$ lies far outside the range of the null distribution at the very right edge. From all the above measured values, it can be safely concluded that in the combined microtopographical conditions under electric field stimulation, the neurites take on noticeably longer lengths compared to those from the control group.

INDIVIDUAL AND COMBINED EFFECTS OF MECHANOTAXIS AND ELECTROTAXIS ON MICROSTRUCTURED SUBSTRATES

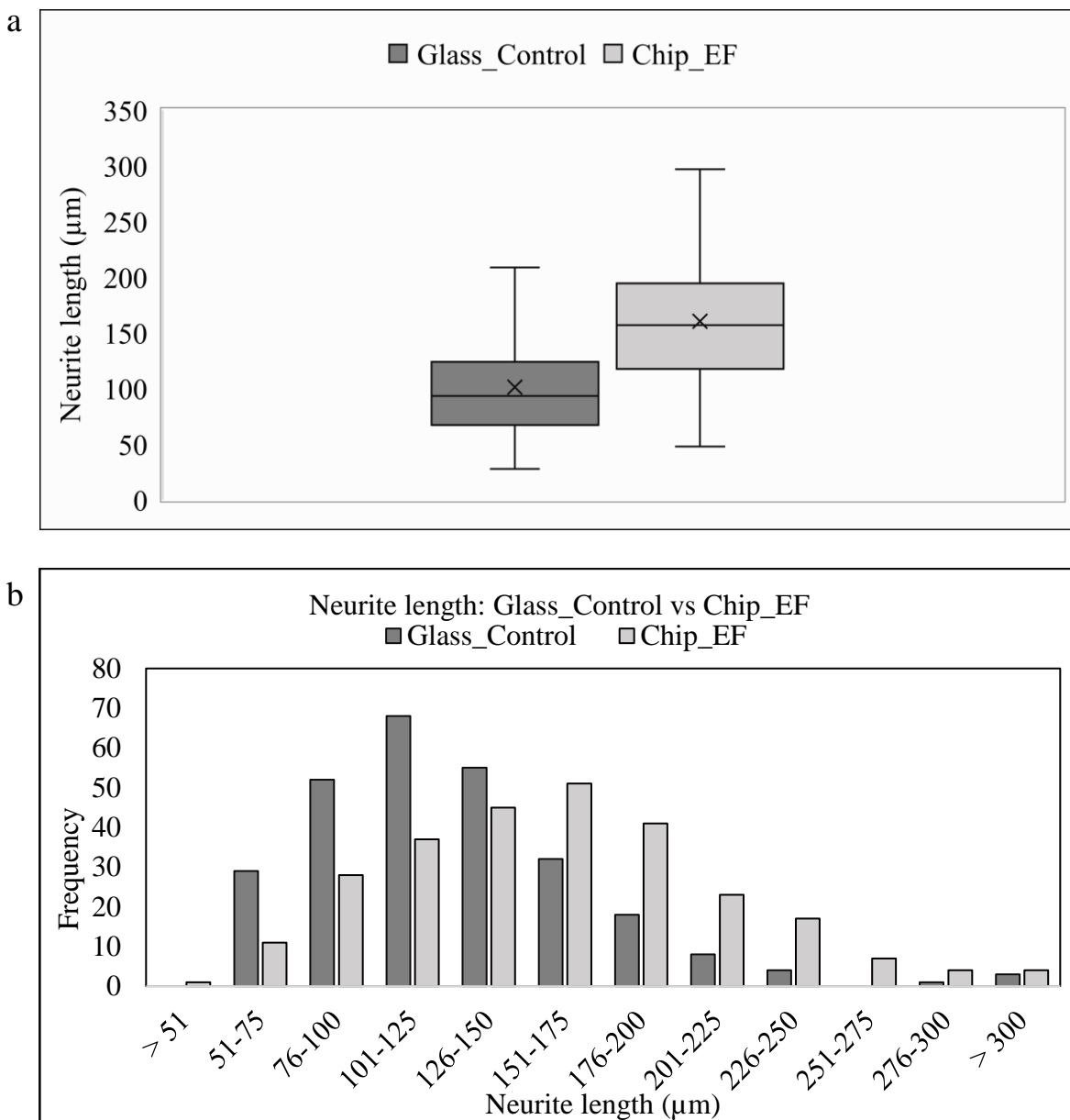


Figure 6.25 NL (Glass control vs Chip EF): (a) Box-and-whisker plots (b) Histogram

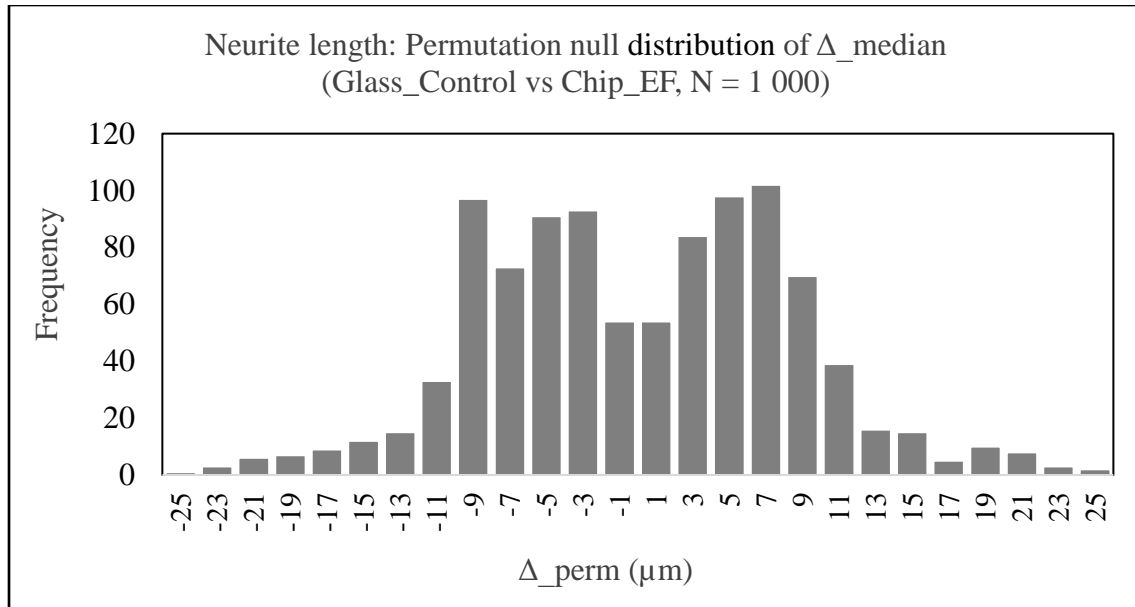


Figure 6.26 NL: Permutation null distribution of Δ_{median} (Glass control vs Chip EF)

6.3.2.2 Mechanotaxis vs combined effect

Comparison of basic descriptive parameters of neurite length on the chip without and with electric field stimulation is shown by box-and-whisker plot and histogram in Figure 6.27. The chip with stimulation showed a slightly higher average length (160.11 μm vs 156.10 μm), while the median difference was noticeably larger (156.84 μm vs 138.35 μm). Similar to the previous cases under stimulation conditions, here too the dispersion is somewhat smaller, which was manifested in a smaller standard deviation (58.47 μm vs 65.86 μm). The lower quartile of the stimulated chip is 117.41 μm , and the upper quartile is 194.29 μm . With the chip itself without stimulation, these quartiles are 108.27 μm and 185.12 μm . Interestingly, the interquartile range of both groups is almost identical, at approximately 76.9 μm . Both the longest (474.60 μm vs 398.22 μm) and shortest neurites (38.21 μm vs 47.73 μm) were recorded in the unstimulated sample.

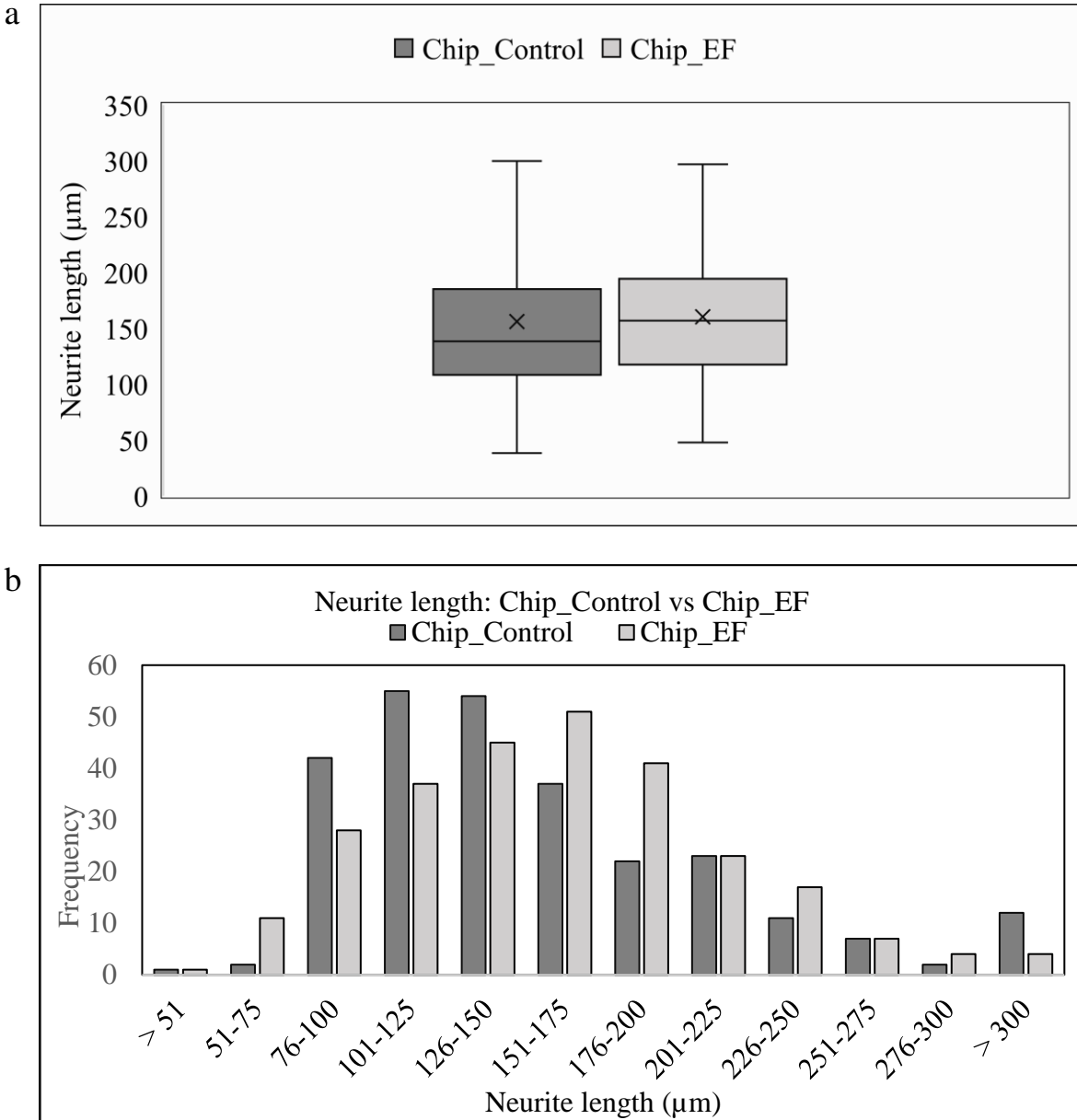


Figure 6.27 NL (Chip control vs Chip EF): (a) Box-and-whisker plots (b) Histogram

The upper Tukey's fence for the chip without stimulation is at 300.39 μm and 309.62 μm for the chip under stimulation conditions. In the control sample, there are 5.19 % outliers (14/270), which is slightly more than most of the previously described samples. In the sample with stimulation, this share is 1.85 %, i.e., 5/270. These results continue to demonstrate the higher variability of the distribution without the presence of an electric field, with slight but consistently longer neurites.

The effect size of these two samples also shows a small but consistent stimulation effect. The Mann–Whitney rank-sum test gave a parameter U in the amount of 33 114 with a probability of

superiority of the unstimulated sample of 0.45, which implies that in 55 % of the pairs the higher value belonged to the stimulated chip. However, one should be careful when interpreting, considering the very low value of Cliff's δ in the amount of $= -0.09$ for the chip without stimulation, or $+0.09$ for the stimulated chip. Therefore, it is safer to conclude that there is a large overlap of distribution pairs with longer neurites in favor of the Chip EF pattern.

Permutation analysis on a sample of 1 000 labels for a chip with stimulation and a chip without stimulation gave results following the previous paragraphs. The median difference Δ_median was $18.50 \mu\text{m}$, and as such was positioned outside the 95 percent interval of the null distribution, which was from $0.12 \mu\text{m}$ to $14.44 \mu\text{m}$. Despite the distance of the median difference from the upper limit of the interval of the null distribution, which was not as pronounced as in some previously observed cases, the two-sided p-like amounted to a theoretical minimum of 0.0002, which means that even in this case a median difference of less than $18.50 \mu\text{m}$ would occur very rarely. According to the permutation test, the differences are more robust and stable than in the measurement of the measurement effect size, whose δ showed a very small value. All the more, these results call for caution. The histogram in Figure 6.28 shows the permutations of the null distribution for the median neurite length differences with Δ_median falling out of the range of the distribution.

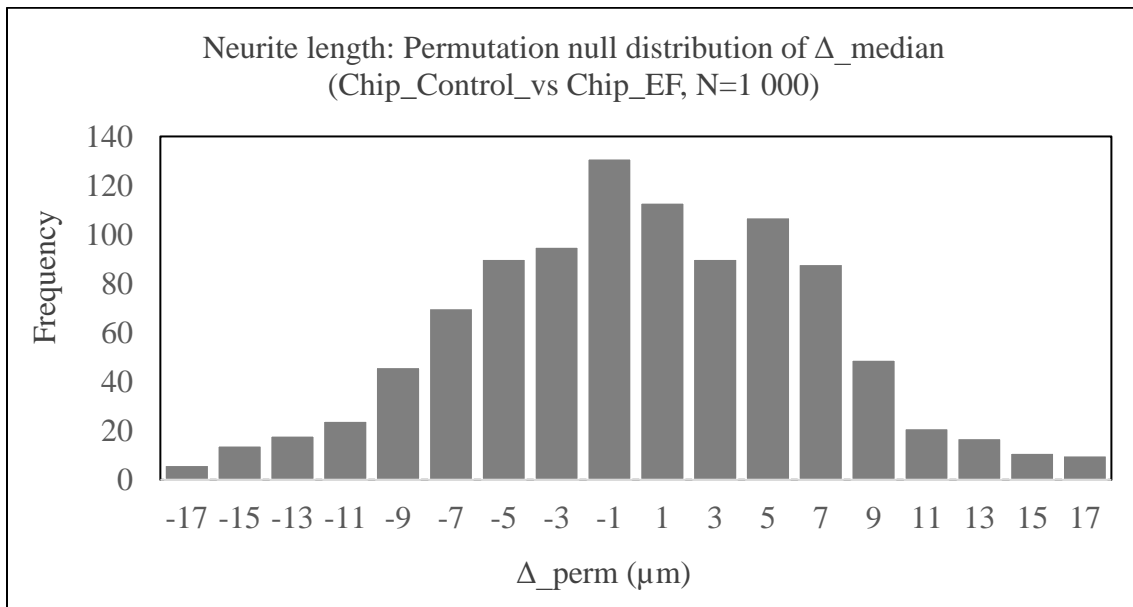


Figure 6.28 NL: Permutation null distribution of Δ_median (Chip control vs Chip EF)

6.3.2.3 Electrotaxis vs combined effect

Figure 6.29 shows a comparison of descriptive measures of neurite lengths under stimulation conditions on glass (Glass EF) and on chip (Chip EF). The average length of neurites stimulated on chip was 160.11 μm with a 95 % confidence interval ranging from 153.1 μm to 167.1 μm , while on glass an average of 115.90 μm was recorded with a confidence interval ranging from 111.7 μm to 120.1. The measured median on the glass sample was 112.23 μm , and on chip it was 156.84 μm .

Neurons on chip also showed greater variability in the lengths of their neurites. The standard deviation measured on the chip was 58.47 μm , and on the glass 35.17 μm , which is consistent with the differences in the interquartile ranges, which are 76.89 μm on the chip compared to 45.15 μm on the glass. The lower quartile of the chip is still higher than the lower one, but the difference is smaller than in the medians, (117.41 μm vs 90.97 μm). The difference in the upper quartiles is still significantly larger: 194.29 μm on the chip vs 136.12 μm on the glass. A small number of outliers were recorded on both substrates, namely 1.85 %, i.e., 5/270. The lower Tukey's fences of the sample on the glass are 23.24 μm , and on the chip 2.07 μm . The upper fences are 203.84 μm on the glass and 309.62 μm on the chip.

The rank test showed results in favor of the chip as a substrate. The sum of the ranks for the Glass EF sample was 55 596 compared to 90 474 calculated for the Chip EF sample. The Mann-Whitney U is 19 011 for the Glass EF sample, with a probability of superiority $PS = 0.26$, giving only a 26 % chance that a random neurite from a cell culture grown on glass will be longer than a neurite from the chip, which gives a longer length in 74 % of the cases. Cliff's δ for the glass substrate is -0.48, which analogously gives +0.48 for the on-chip sample. Such an effect is medium to large and represents a clear indication of a systematic difference in the values of the two observed distributions.

The permutation test on 1 000 permutations confirms the results of the previous paragraphs. For the calculated difference in the medians in the amount of 44.62 μm in favor of the sample on the chip, a two-sided p-like was calculated in the amount of the theoretically minimal 0.0002, which gives only a 0.02 % chance of fulfilling the null hypothesis. Accordingly, 95 % of the differences in the permutation test lie in the range of 0.20 μm to 11.39 μm , which leaves Δ_{median} well

outside the range. The null distribution of permutation differences is shown on the histogram in Figure 6.30. The distribution itself has an almost symmetrical shape and is centered around zero.

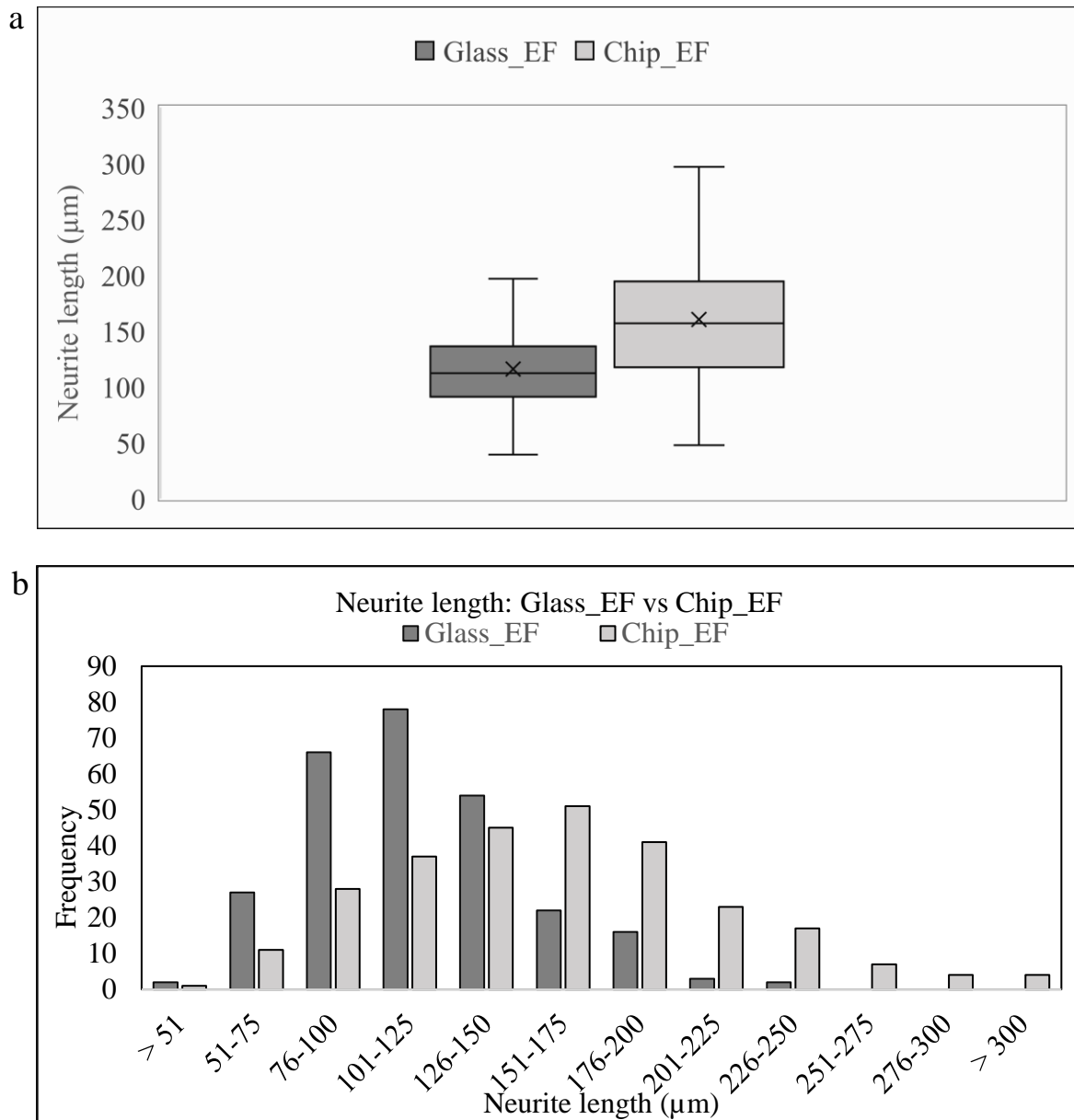


Figure 6.29 NL (Glass EF vs Chip EF): (a) Box-and-whisker plots (b) Histogram

As in the previously observed cases, here too it was shown that the mechanical cues of the chip as a substrate have a strong influence on the morphological parameters, i.e., the length of the neurites, more obvious than for the soma area. The stimulated samples showed different variability, but one should be cautious in drawing conclusions about the cause of these differences. What can be

asserted with greater certainty is the undeniable presence of mechanotaxis caused by the microtopography of the substrate.

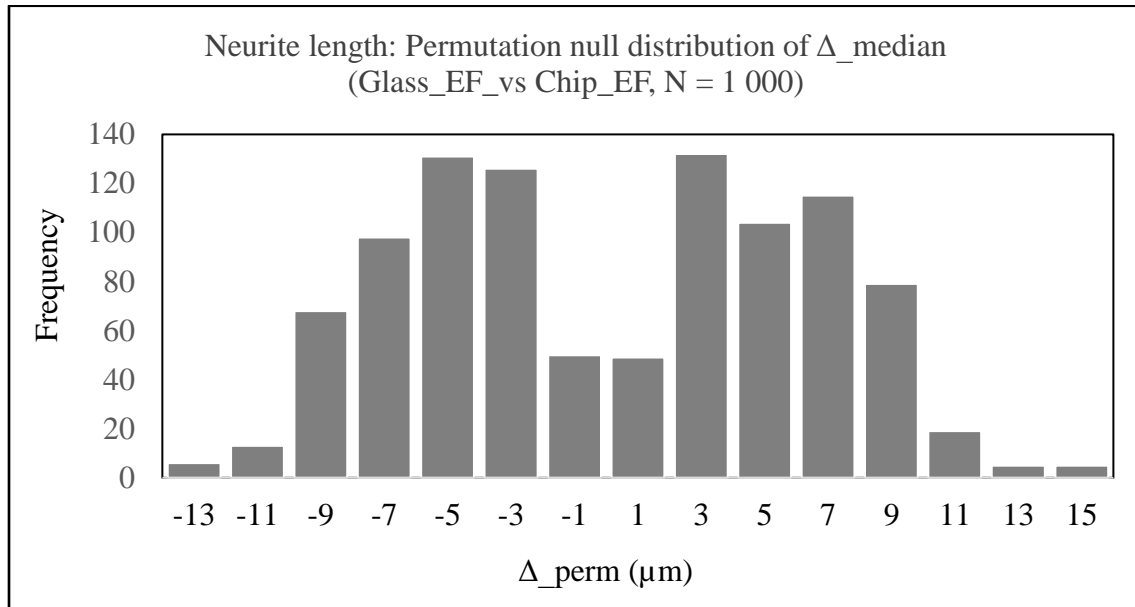


Figure 6.30 NL: Permutation null distribution of Δ_{median} (Glass EF vs Chip EF)

6.3.3 Neurite alignment

6.3.3.1 No cues vs combined effect

The distribution of measured neurite angles for the Glass control vs Chip EF sample is given in Figure 6.31.

6.3.3.1.1 Circular alignment index

As for the circular alignment index (AI_circ), which can take a value from 0 to 1, the values on both samples are similar. A comparison for Glass control and Chip EF is given in Figure 6.32. The median on the glass substrate is 0.51, and on the chip it is slightly lower, 0.47. The arithmetic mean values are almost identical to the medians: 0.51 for the control group and 0.48 for the Chip EF group. The standard deviations are 0.36 for the control sample and 0.34 for the chip. The difference between the interquartile ranges is slightly larger. 0.73 was recorded for the control sample, and 0.68 for the Chip EF sample. The reason lies in the upper quartiles, which differ (0.87 vs 0.83), while the lower ones are the same.

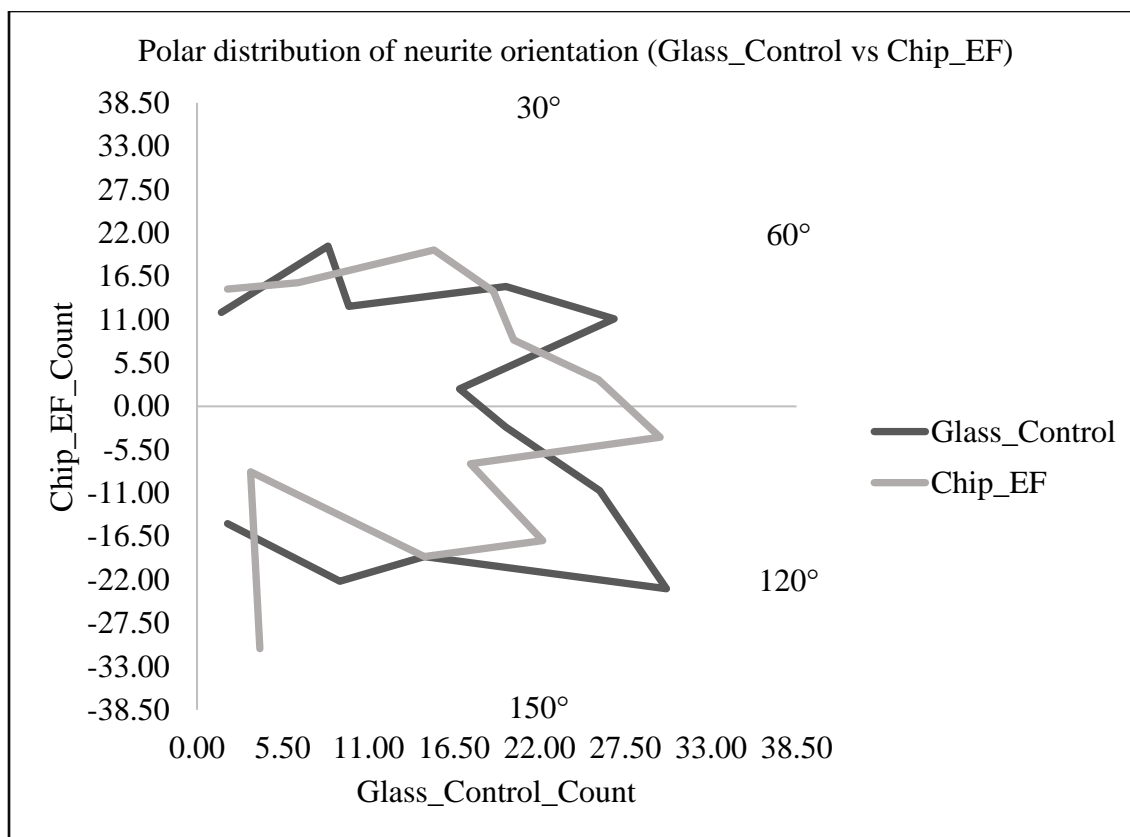


Figure 6.31 NA (Glass control vs Chip EF): Half-polar plot (0–180°)

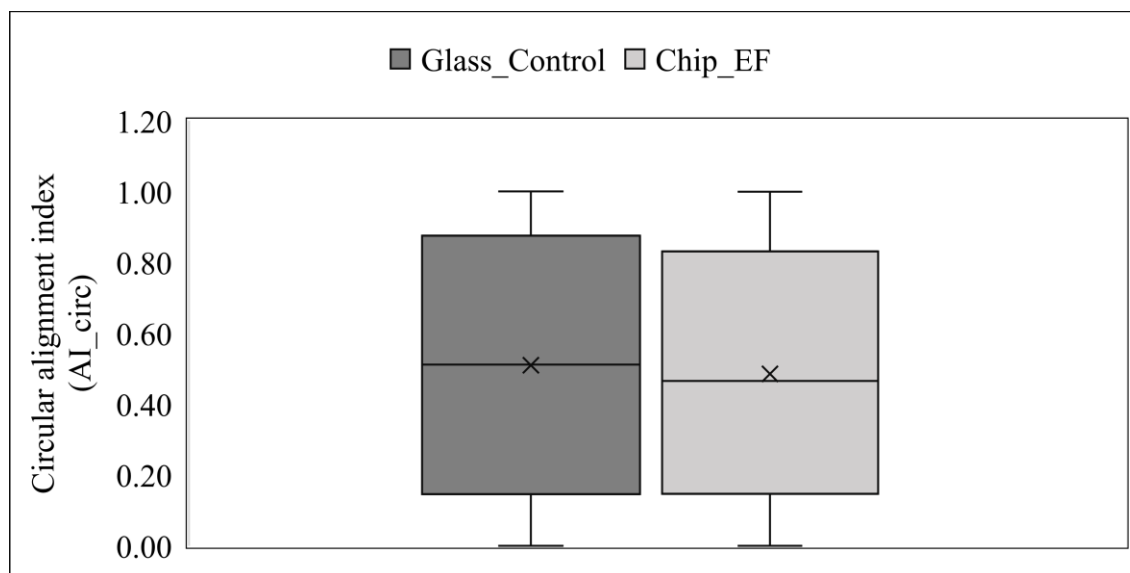


Figure 6.32 Circular alignment index (AI_circ): Glass control vs Chip EF

At 1 000 permutations with $\Delta_{\text{median}} = -0.04$, a two-sided p-like of 0.0914 was obtained. The 95 % permutation interval is in the range from 0.00 to 0.12, therefore the observed difference is

consistent with the null hypothesis and the difference in the distributions is small and cannot be statistically confirmed with the permutation test.

6.3.3.1.2 Angle to local field tangent

Figure 6.33 shows a comparison of the angle to the local field tangent for the control sample (Glass control) and the sample on the chip with stimulation (Chip EF). The results are consistent with the results for the circular alignment index. The median on the chip with stimulation was measured with a value of 46.98° , and on the control sample it was 44.34° . Means are 46.13° on the chip and 44.22° on the glass. Both distributions have very similar variability with standard deviations of 26.45° for the control sample and 25.13° for the chip. The interquartile ranges differ slightly more, with the distribution narrower on the chip, 42.95° vs 46.71° . The difference in the interquartile range is attributed to the difference in the lower quartiles, where it is higher on the chip (24.49° vs 20.81°), and the upper quartiles are the same and amount to 67.5° . Both distributions are almost completely symmetrical (skewness on glass is 0.02 and on chip is -0.04), and the clustering around the center is weaker and also equal for both distributions, with a kurtosis value of -1.2 . It can be concluded that for the parameters used, mechanical and electrical cues do not give a combination of neurite alignment compared to the case with no cues.

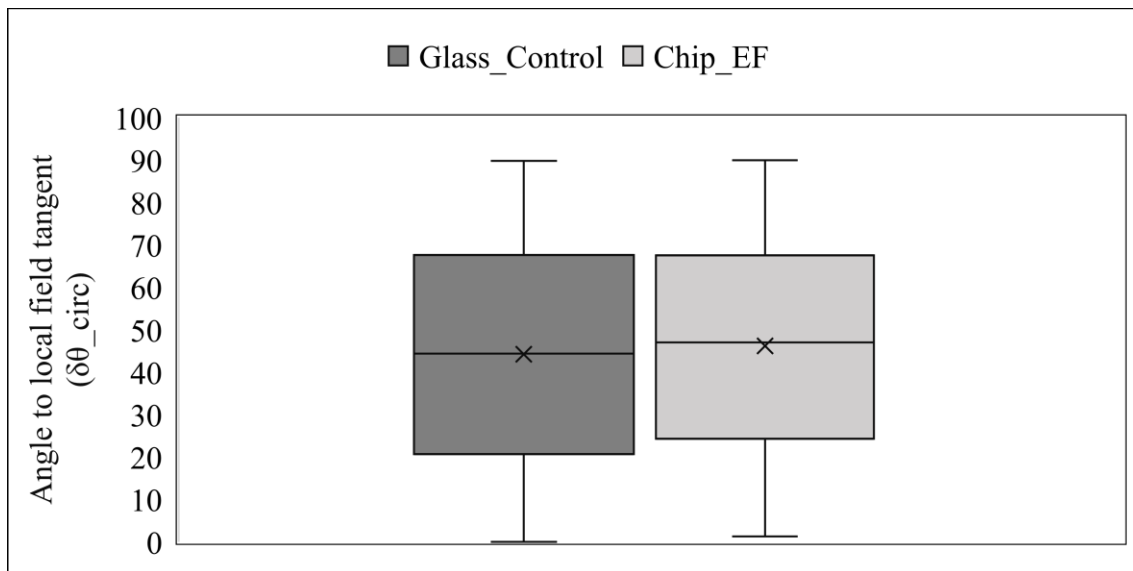


Figure 6.33 Angle to local field tangent ($\delta\theta_{circ}$): Glass control vs Chip EF

6.3.3.2 Mechanotaxis vs combined effect

Comparison of distributions of neurite orientation angles for Chip control and Chip EF sample is given in Figure 6.34.

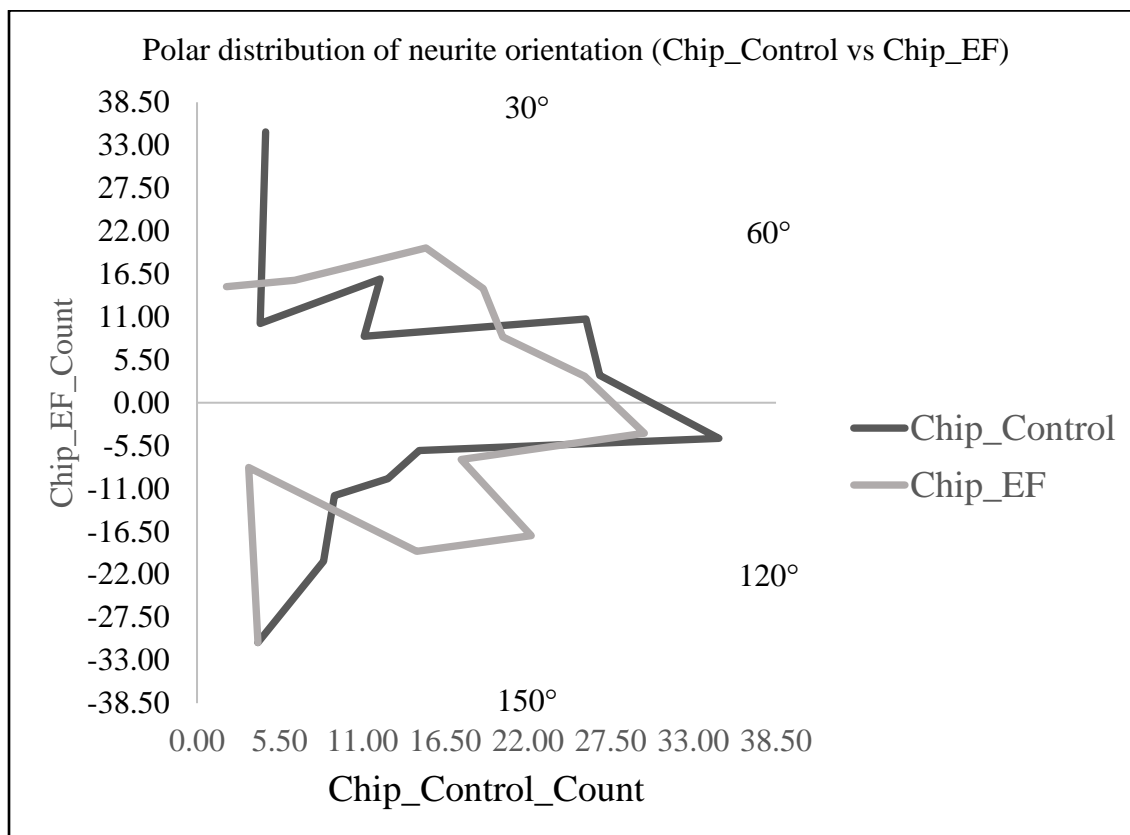


Figure 6.34 NA (Chip control vs Chip EF): Half-polar plot (0–180°)

6.3.3.2.1 Circular alignment index

A comparison of isolated mechanotaxis and the combination of both mechanisms is shown in Figure 6.35 for AI_circ. Average neurite alignment is similar, with 0.51 on the Chip control sample and 0.48 on the Chip EF sample, with 95 % confidence intervals of 0.47 to 0.55 on the unstimulated chip and 0.44 to 0.52 on the stimulated chip. The medians of both samples are 0.01 lower than the means and are 0.50 and 0.47. The differences in the quartiles are also not large. The lower quartiles are almost identical (0.15 for Chip EF and 0.16 for Chip control), and there is a smaller difference in the upper quartiles (0.83 vs 0.87). Both distributions are symmetric (skewness is almost zero), and as in the previous case, both distributions have the same kurtosis of -1.5, which implies less clustering around the mean, but does not say whether this is a consequence of alignment or random distribution of neurites. To get a complete picture, it is necessary to look at the values of the tenth

and ninetieth percentiles, where P10 is 0.03 for Chip control and 0.04 for Chip EF, and P90 is 0.98 for Chip control and 0.97 for Chip EF, implicating a high level of alignment in some neurites.

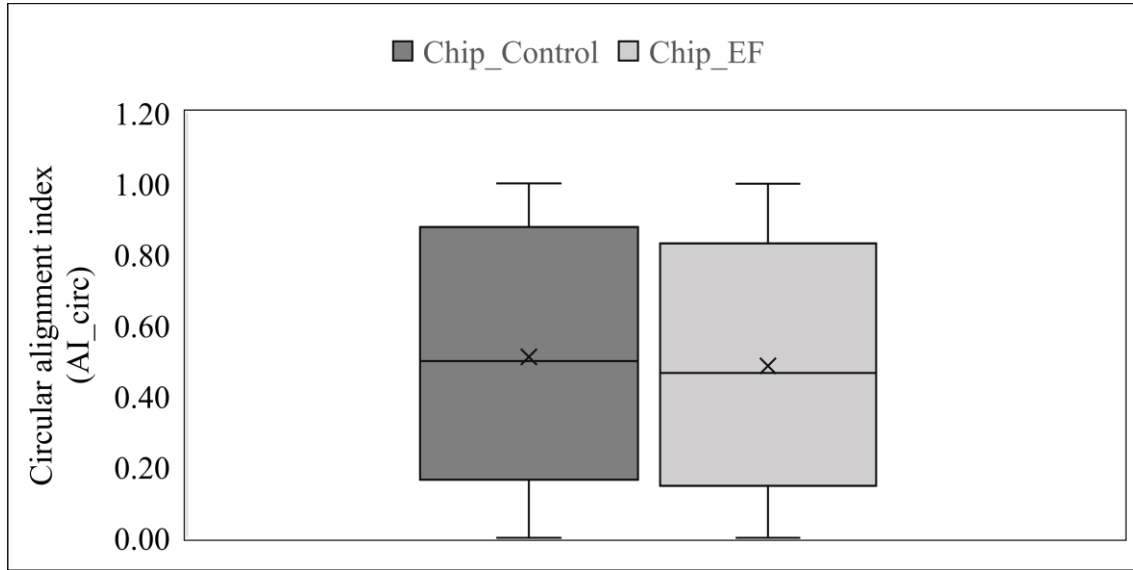


Figure 6.35 Circular alignment index (AI_circ): Chip control vs Chip EF

On 1 000 permutations with a median difference of $\Delta_{\text{median}} = -0.03$ in favor of the Chip control sample, a two-sided p-like was obtained in the amount of 0.096. Such a result implies 9.6 % of permutations with an absolute difference greater than or equal to 0.03, which with a 95 % permutation interval of the null distribution ranging from 0.00 to 0.11 suggests that the differences in alignment are small.

6.3.3.2.2 Angle to local field tangent

For the angle to the local field tangent, the medians are 45.10° on the Chip control sample and 46.98° on the Chip EF sample, as shown in Figure 6.36. Means are 43.96° in conditions without stimulation and 46.13° in conditions with stimulation with very comparable variability and symmetry of distribution. The standard deviations are 26° without stimulation and 25° with stimulation, and the differences are slightly more noticeable in the interquartile ranges, which are 45.33° for Chip control and 42.95° for Chip EF. P10 for Chip control is 8° and for Chip EF 10° , indicating that there are no major differences in alignments between these two cases.

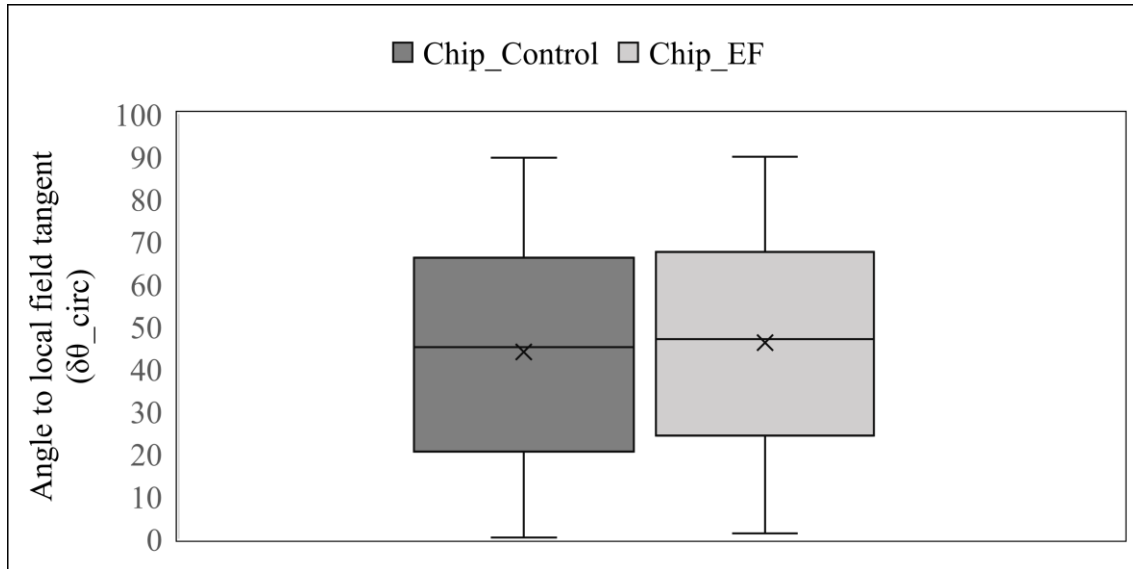


Figure 6.36 Angle to local field tangent ($\delta\theta_{circ}$): Chip control vs Chip EF

Both distributions are highly symmetric (skewness for Chip control -0.01, and for Chip EF -0.04) and are not centered around the mean values (kurtosis for Chip control -1.19 and -1.11 for Chip EF), which is expected given the definition of the $\delta\theta_{circ}$ metric used.

6.3.3.3 Electrotaxis vs combined effect

A comparison of the distributions of measured neurites for the Glass EF vs Chip EF sample is given in Figure 6.37.

6.3.3.3.1 Circular alignment index

The circular alignment index (AI_circ) for the sample on the glass with stimulation (Glass EF) and the sample on the chip with stimulation (Chip EF) showed a slightly higher median on the chip (0.42 vs 0.47) and a smaller difference in means (0.46 vs 0.48). Statistical comparison of samples is visually given in Figure 6.38. Variations are similar, with standard deviations of 0.35 for Glass EF and 0.34 for Chip EF. The same is true for the interquartile ranges, namely 0.70 for the glass substrate and 0.68 for the Chip EF. Skewness for Glass EF is 0.15 and 0.07 for Chip EF, so both samples are almost completely symmetrical. The kurtosis of -1.4 in both samples is consistent with the previous cases and expected for the metric defined in this way.

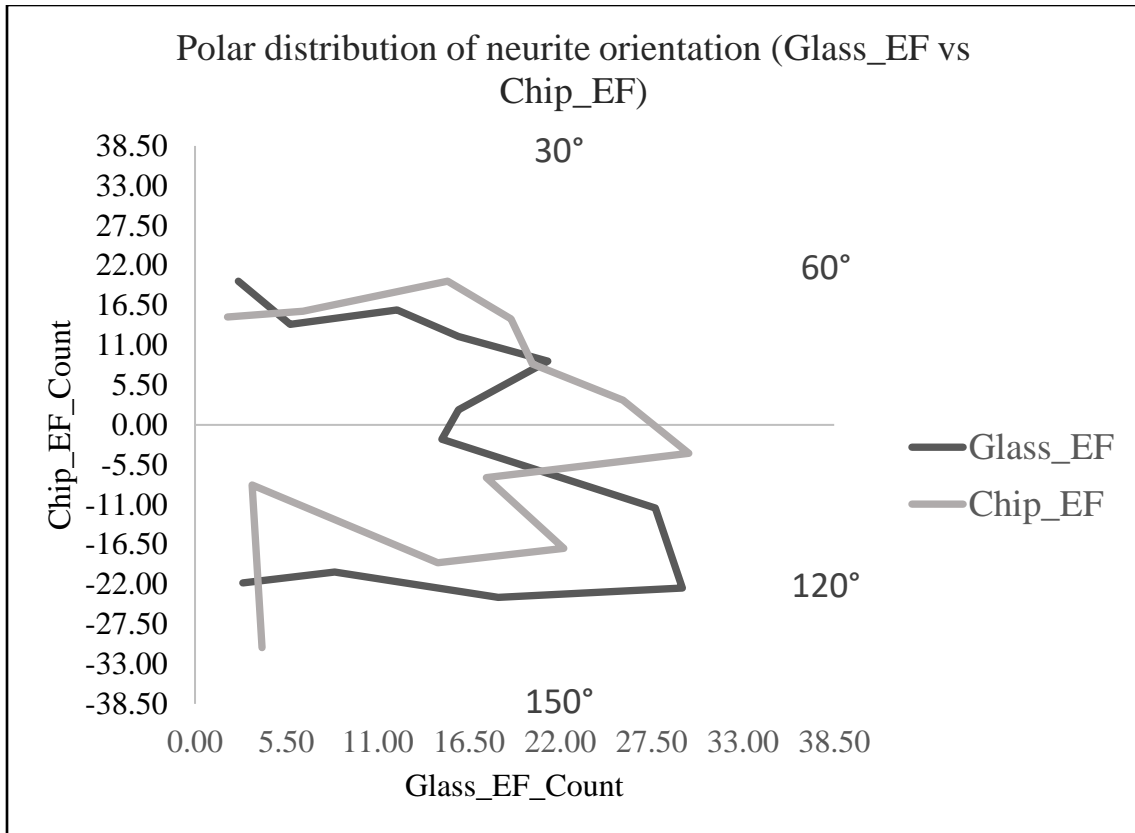


Figure 6.37 NA (Glass EF vs Chip EF): Half-polar plot (0–180°)

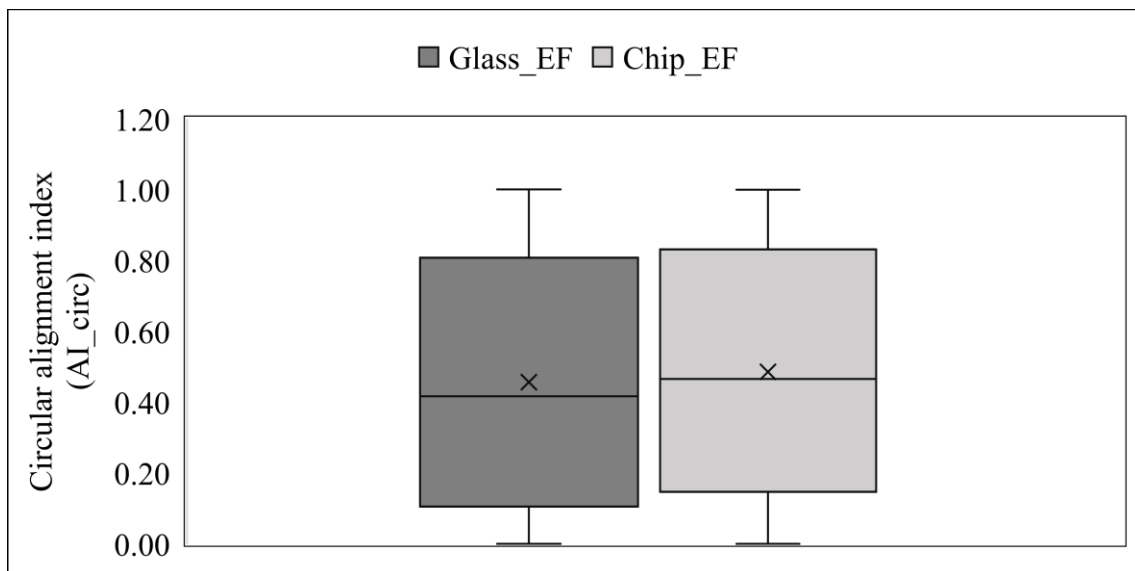


Figure 6.38 Circular alignment index (AI_circ) for Glass EF vs Chip EF

At 1 000 permutations and with a Δ_{median} of 0.05, a two-tailed p-like value of 0.0578 was obtained with a 95 % confidence interval of the null distribution ranging from 0.00 to 0.12, which can be interpreted as the existence of a minor difference in neurite alignment.

6.3.3.3.2 Angle to local field tangent

The results of the angle to the local field tangent, shown in Figure 6.39, are on the same track. On the Glass EF sample, the median is 49.80° , and on the Chip EF sample it is 46.98° . The smaller tenth percentile on the chip (12.17° vs 10.40°) suggests a slightly higher proportion of aligned neurites, since for this metric, a smaller angle means more alignment. The standard deviations are almost identical (25.50° on Glass EF vs 25.13° on Chip EF), as is the shape of the distribution: Skewness on glass is -0.12, and on chip -0.04, while kurtosis for both substrates is -1.1.

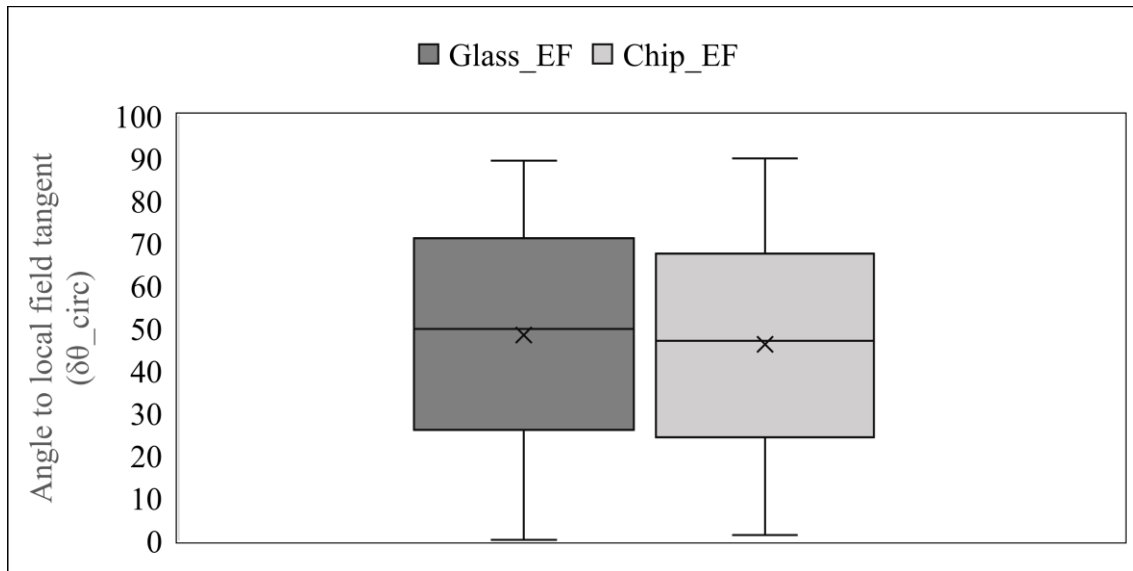


Figure 6.39 Angle to local field tangent ($\delta\theta_{\text{circ}}$): Glass EF vs Chip EF

6.3.4 Summary

In this section, by comparing three cases (Glass control vs Chip EF, Chip control vs Chip EF and Glass EF vs Chip EF), results were obtained that suggest that mechanotaxis has a noticeably stronger influence on the morphological properties of neurons and their neurites, while the influence of electric field stimulation is weaker and less consistent. For each of the observed parameters, the following can be summarized:

1. Soma area: The differences are noticeable, but of a smaller amount. The area is only slightly larger on the chip with stimulation compared to the control sample ($\Delta = \sim 11 \mu\text{m}^2$;

p-like ≈ 0.004), but it is smaller than on the chip without stimulation ($\Delta \approx -19 \mu\text{m}^2$; p-like ≈ 0.0002). The addition of stimulation did not result in a systematic greater increase in soma area.

2. Neurite length: The difference in neurite length is the most obvious. The lengths in the presence of both mechanisms are significantly longer than in the control sample (Δ median $\approx 64 \mu\text{m}$; p-like ≈ 0.0002). The difference is smaller when observing samples on chips with and without stimulation ($\Delta \approx 18.5 \mu\text{m}$; p-like ≈ 0.0002 , but small effect). Mechanotaxis assumes the role of the dominant mechanism in terms of influencing neurite length.
3. Alignment of neurites: Changes in orientations are small and inconsistent. Considering the different directions of action of the mechanical and electrical field cues, it is possible that to some extent there is a mutual cancellation of these mechanisms.

6.4 Discussion and summary

The results presented in Chapter 6 clearly indicate a noticeable influence of the microtopography of the substrate surface on the growth and development of spiral ganglion neuron cultures under in vitro conditions. All measured morphological parameters, soma area, neurite length and neurite alignment support the interpretation of a positive effect of mechanotaxis, consistent with the findings from previous studies [54-56, 80, 81]. The mentioned morphological parameters were adequately selected and in themselves provide a good overview of the interaction of neurons and the substrate.

From the perspective of the quality and reliability of the results for the purpose of obtaining a valid scientific conclusion, it is necessary to take into account the morphometrics and statistical methods used in the experiment for this chapter. Given that manual measurement of all parameters through the selection of ROIs always carries the risk of selection bias, it was important to ensure a sufficiently large number of measurements per population for each parameter ($N = 270$), in order to reduce the probability of bias and random deviations to the lowest possible level. Also, measurement reliability was further supported by the separate measurement of neurite length and neurite alignment, which made the number of total ROIs even larger. A total of 3 240 ROIs were manually selected for the purposes of this chapter, i.e., 810 for each of the four processed samples (Glass control, Chip control, Glass EF and Chip EF). During each measurement in one data set of

270 ROIs, the measurement was performed in such a way that 30 ROIs were selected from each of 9 smaller images that were assembled into one large image of the sample. A particular challenge in the ROI selection procedure was the local density of neuronal structures, which in some cases made it more difficult to select adequate ROIs on a particular part of the sample. A minor difficulty in the measurement was the accumulation of cell somas in clusters, which in some cases made it more difficult to select ROIs for the soma area, which is why it was necessary to avoid such structural clusters. A greater difficulty was the overlapping of neurites in some segments, which required the careful and time-consuming selection of ROIs. The cause of both of these problems lies in the high density of seeded neurons of 40 000 per culture, which caused fluorescence signal saturation due to high neuronal marker intensity in some places. In further experiments in Chapter 7, for the purpose of validating the obtained conclusions, the density was reduced to 20 000 neurons per culture for better clarity and more reliable measurement. Also, one of the reasons for the larger number of processed ROIs is the fact that in this part of the study, one sample was used for each experimental case (Table 4.1), which made it impossible to apply inferential statistical methods, as otherwise pseudoreplication would occur. In order to compensate for the impossibility of using inferential statistics, enhanced parameters and methods of descriptive statistics were added to increase the reliability of the obtained result, which was especially contributed to by the use of the effect size metric and the Monte Carlo permutation test with 1 000 and 5 000 permutations. Special attention was paid to the measurement of neurite alignment, considering the sensitivity and potential inaccuracy of the measurement. For this purpose, two metrics (biaxial alignment and angle to the nearest substrate axis) were defined in order to further enhance the quality of the results.

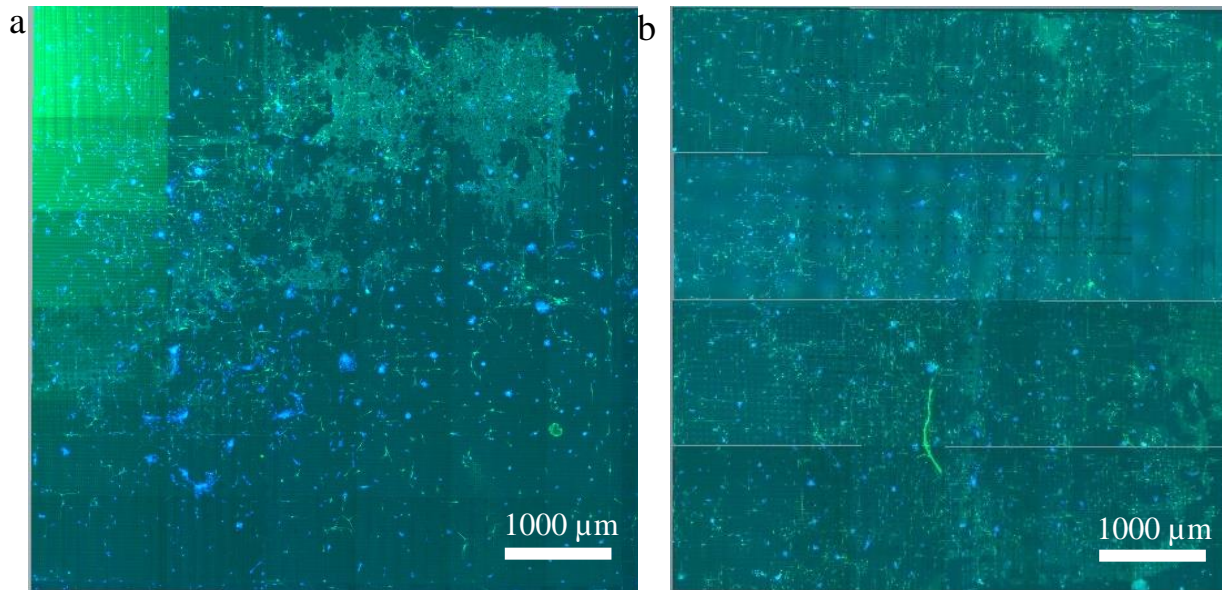
As far as the measurement of neurite alignment is concerned, for the case of mechanotaxis, a more conservative approach of measuring the alignment exclusively in relation to the x and y axis of the substrate was chosen, in order to obtain the cleanest possible results with less possibility of error. For the measurement of more complex directional geometries, a very high quality and clarity of the sample image is primarily required, regardless of whether the selection of ROIs was carried out manually or automatically. Certainly, in these circumstances mechanotaxis showed a consistent and noticeable effect on neurite alignment. Electrotaxis showed a measurable, but still significantly smaller effect than mechanotaxis. The reasons for this in the observed case may lie in the choice of stimulation parameters, the size of the substrate in relation to the circular electric

field lines, and the metric itself, where the tangential alignment of neurites to the circular lines is more difficult to measure precisely and reliably, especially at the densities used in the observed cultures. In this case, manual selection of ROIs even has an advantage over automatic selection, although it does not bring a completely satisfactory effect either. The combined effect of mechanotaxis and electrotaxis exists, but it does not appear to be strongly synergistic. One reason for this may be the very difference in the direction of action of these mechanisms, whereby the observed effect of substrate mechanotaxis is easier and more reliably measurable. Also, given the direction of action of the electric field, it is possible that in certain segments there is an action directed in the same direction as the action of the substrate geometry, but in order to determine this, it is necessary to establish a more complex and precise metric. Another reason may lie in the fact that mechanotaxis may simply exert a stronger effect on spiral ganglion neuron cultures in these *in vitro* conditions.

In the continuation of the research, and for the purpose of analyzing the electrical activity of neurons under the influence of mechanotaxis, it is necessary to validate mechanotaxis with more reliable methods at, as already mentioned earlier in this section, a lower density of neuronal culture sample. To increase the statistical reliability of the results, it is primarily recommended to use a larger number of samples so that inferential statistical methods can be applied and to ensure that any recorded electrical activity is observed under conditions of mechanotaxis.

7 EXTRACELLULAR RECORDING WITH NEUROELECTRONIC INTERFACE

In this chapter, an overview of the validation of the neurophysiological activity of spiral ganglion neuron cultures on three-dimensional microstructured MEA substrates with the application of the neuroelectronic interface for extracellular recording, presented in Chapter 3, is given. The purpose of the experiment is to examine whether spiral ganglion neuron cultures grown on substrates that promote mechanotaxis, described in Chapter 6, have a tendency to spontaneous and evoked electrical activity, and to give a perspective for application in hearing prosthetics. The experiment was conducted on 5 samples under the conditions described in Chapter 4.1 and recorded and mapped according to the protocol described in Section 4.1.4, shown in Figure 7.1. Each image of a sample of spiral ganglion neuron cultures on a MEA substrate represents a composite 6×6 grid with a magnification of $40\times$ for each smaller image. Neuronal marker β -tubulin III (green) and cell bodies marker DAPI (blue) were used. Scale bars are shown in the bottom right. The samples are labeled: Sample 1 (a), Sample 2 (b), Sample 3 (c), Sample 4 (d) and Sample 5 (e). In the following text, each sample is abbreviated with the letter S and the sample number.



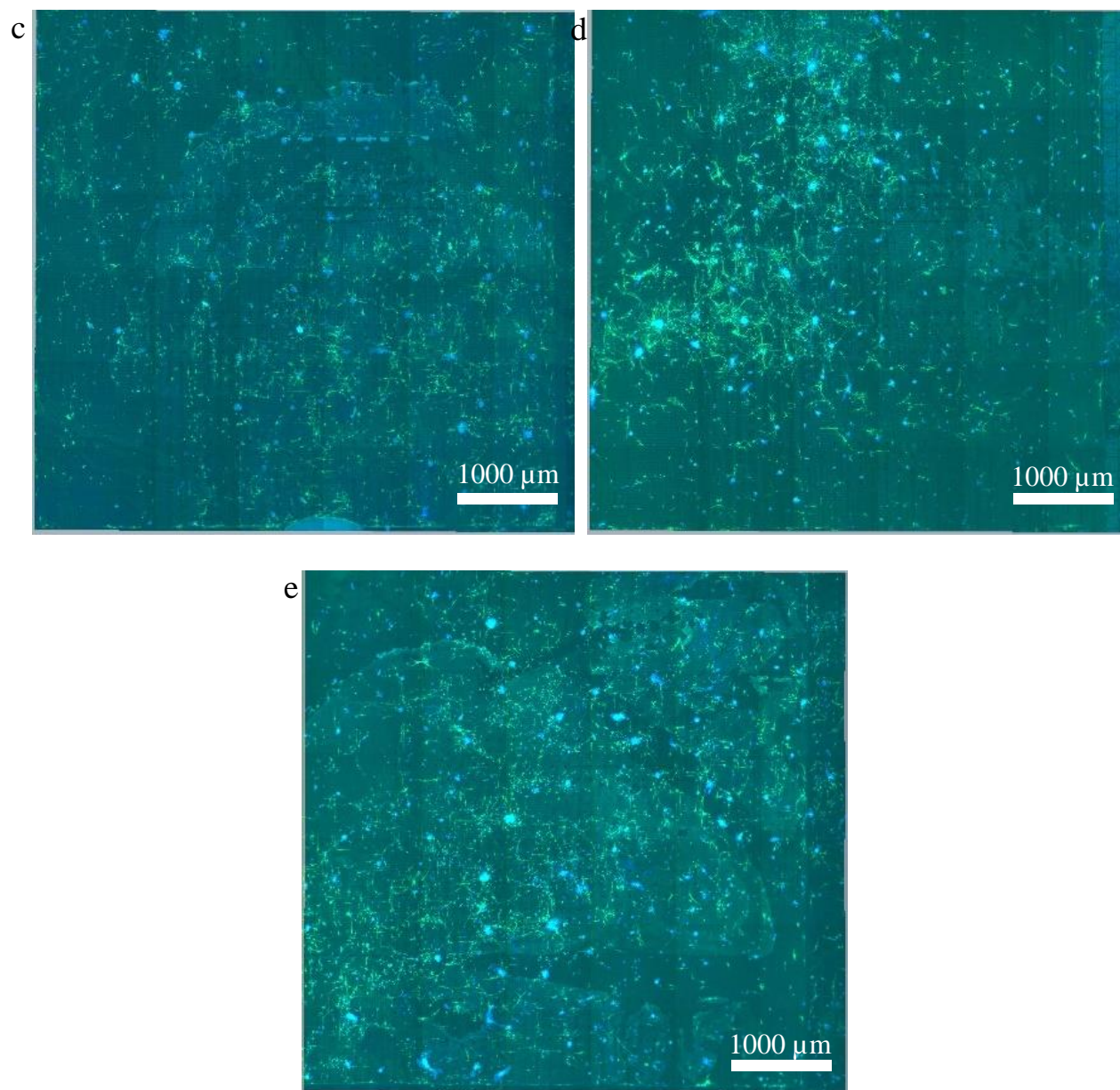


Figure 7.1 Experimental samples: SGN cultures on MEA substrates (b) adapted from [81] (c) adapted from [83]

7.1 Validation of mechanotaxis on microelectrode array

Validation of the occurrence of mechanotaxis on MEA substrates was carried out following the conclusions of Chapter 6, in which the influence of substrate topography on spiral ganglion neuron cultures was demonstrated. Validation of mechanotaxis is a key requirement for a reliable approach to recording neurophysiological activities in the context of this dissertation. The methods used in this section are based on those used in Chapter 6, with the addition of the sampling pattern

and inferential statistical analysis described in Section 4.3 due to the presence of multiple samples. Analysis was performed for neurite length and neurite alignment. Figure 7.2 shows sections from S3 and S4, which clearly demonstrates the property of neurites to align along the 0° and 90° substrate axes. Examples of corresponding ROI measurements in image processing software for neurite length and neurite alignment are also presented. Panel a shows neurite alignment along the 0° and 90° substrate axes on raw image (S3), panel b shows neurite length measurement on two ROIs (S3) and panel c shows neurite alignment measurement on one ROI (S4).

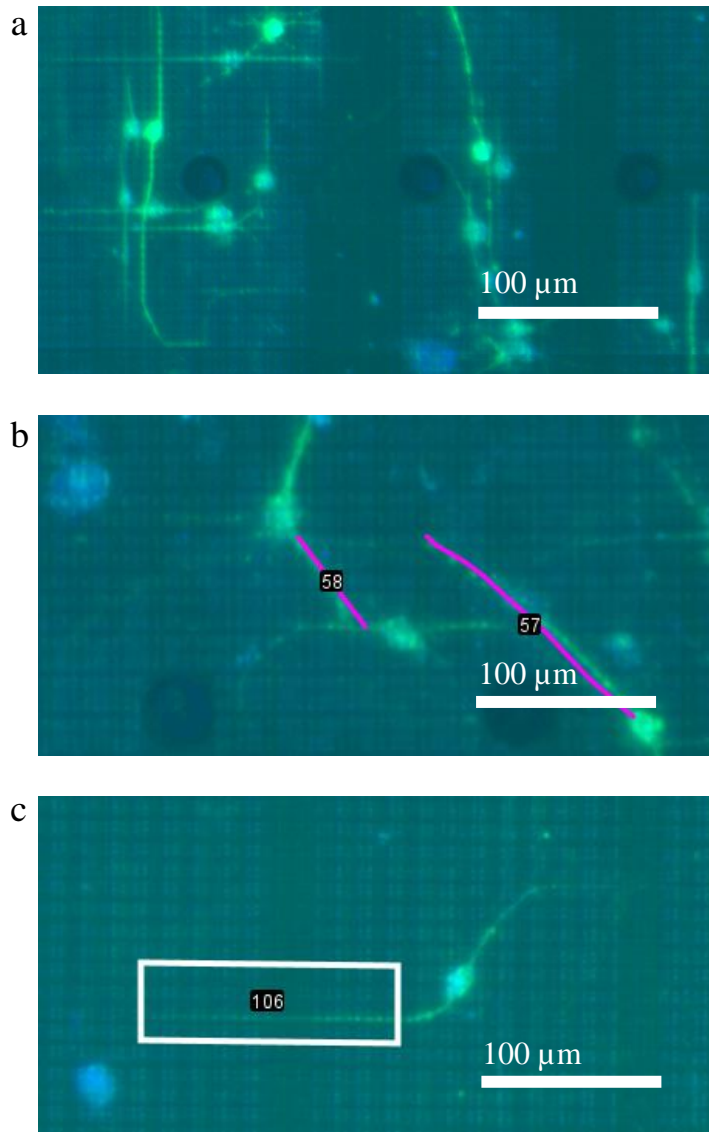


Figure 7.2 Cropped examples of ROI-based measurements: (a) Raw image (b) NL measurement (c) NA measurement

7.1.1 The effect of mechanotaxis on neurite length on microelectrode array

An overview of the results of neurite length measurements in four zones for all five samples (S1-S5) is given descriptively in Table 7.1.

Table 7.1 Descriptive statistics of neurite length across 4 zones for S1-S5

NL (S1-S5): descriptive statistics				
	Zone 1	Zone 2	Zone 3	Zone 4
N	150	150	150	150
Mean	99.65	106.75	109.08	95.75
Median	89.72	102.10	104.07	89.26
SD	40.81	35.28	39.64	32.79
SE	3.332	2.880	3.237	2.677
CI (95 %)	93.07	101.06	102.69	90.46
MIN	39.55	33.19	32.45	42.77
MAX	244.98	224.16	221.30	255.57
Q1	68.36	81.05	80.34	72.08
Q3	119.99	127.65	132.25	114.52
IQR	51.63	46.60	51.91	42.44
Percentile_10	55.56	64.57	62.13	60.37
Percentile_90	161.90	155.74	163.31	134.66
Trimmed mean (10 %)	95.24	104.48	106.54	92.95
Skewness	1.03	0.68	0.59	1.28
Kurtosis	0.81	0.57	0.03	3.44

Compared to zones 1 and 4, neurite lengths in zones 2 and 3 take on higher values. The medians in zone 1 are $89.72 \mu\text{m} \pm 3.33$, in zone 2: $102.10 \mu\text{m} \pm 2.88$, in zone 3: $104.07 \mu\text{m} \pm 3.23$ and in zone 4: $89.26 \mu\text{m} \pm 2.67$, with similar distribution dispersions (IQR: $42.44\text{--}51.91 \mu\text{m}$). The trimmed mean values (10 %) follow the same trend: zone 1: $95.24 \mu\text{m}$, zone 2: $104.48 \mu\text{m}$, zone 3: $106.54 \mu\text{m}$ and zone 4: $92.95 \mu\text{m}$. It follows from the above that the differences are not caused by extreme values, but rather by a shift of the distribution from the center. The trend of high uniformity is followed by extreme values in the interval of $32.45\text{--}42.77 \mu\text{m}$ for the minimum and of $221.30\text{--}255.57 \mu\text{m}$ for the maximum values. The only major difference was observed in the

kurtosis of the distribution. For zone 3 it is 0.03, and for zone 4 it is 3.44. More moderate values for zone 1 are 0.81 and for zone 2, 0.57. The difference in neurite length distributions by zone is shown on the box-and-whisker plot in Figure 7.3.

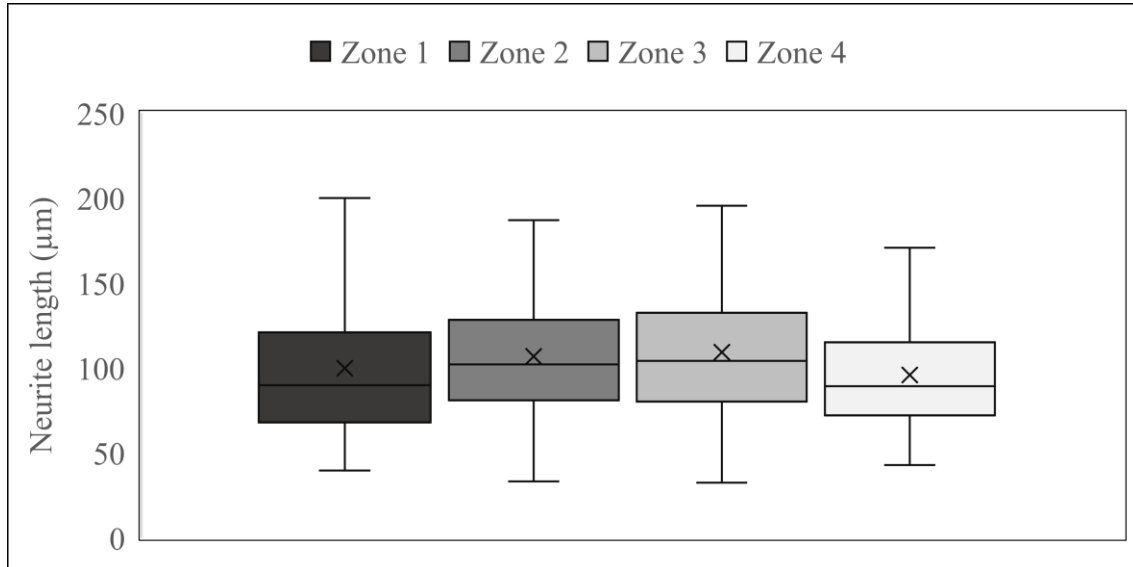


Figure 7.3 Distribution of neurite length for Zone 1-Zone 4

Table 7.2 shows the results of a two-factor ANOVA test with replication for 5 chips and 4 zones for the average neurite length. No statistical significance was observed for either zone or chip. The analysis showed that for the chip factor (Rows), $SS = 1573.08$ with 4 degrees of freedom, giving $MS = 393.27$. Compared with the residual mean square of $MS_{error} = 158.41$ with 12 degrees of freedom, this results in $F(4,12) = 2.48$, at $p = 0.10$, which is below the critical F value of 3.26. Therefore, although there are variations in neurite length between chips, their values do not reach the 5 % significance threshold. As for the variance, the chip factor is responsible for 39 % of the total sum of squares ($\eta^2 \approx 0.39$), or roughly 45 % of the variance after removing residual error (partial $\eta^2 \approx 0.45$), suggesting a moderate but not statistically significant effect.

The zone factor (Columns) with a 3-degree-of-freedom condition gives a sum of squares of $SS = 573.59$ and $MS = 191.20$. The values of $F(3, 12) = 1.21$ compared to $F_{crit} = 3.49$ suggest insignificance, with the zone factor explaining about 14 % of the variation in mean neurite length ($\eta^2 \approx 0.14$), implying that the average neurite length is homogeneous across all four topographic zones when chip variability is taken into account. The residual between cells remains significant, amounting to $SS_{error} = 1900.90$, i.e., approximately 47 % of the total variance, meaning that the

difference in biological variability is not caused by chip and zone factors. These results indicate that neurite length in this measurement does not show a robust and systematic dependence on either the individual substrate or the substrate zone, but rather fluctuates within a moderate range for all conditions.

Table 7.2 Two-factor ANOVA test: Neurite length

Two-factor ANOVA test: NL						
Source of Variation	SS	df	MS	F	P-value	F crit
Rows	1573.08	4	393.27	2.48	0.10	3.26
Columns	573.59	3	191.20	1.21	0.35	3.49
Error	1900.90	12	158.41			
Total	4047.57	19				

7.1.2 The effect of mechanotaxis on neurite alignment on microelectrode array

Table 7.3 gives a descriptive presentation of measurements for neurite alignment in four zones for all 5 samples. Biaxial index of neural alignment (AI_{bi}) showed high values in all four zones with small differences in averages. On a sample of 150 neurites per zone, the averages showed a very narrow distribution, all in the range of 0.77 to 0.78. Very high median values in the range from 0.94 to 0.98 suggest a large number of extreme values, i.e., neurites with maximum alignment along the edges of the substrate. A similar conclusion follows after removing 10 % of extreme values, whereby the trimmed means is still in the high range of 0.82 to 0.84. Standard deviations (0.29-0.31) indicate moderate and similar dispersion by zone with interquartile range ranging from 0.35 to 0.41 and 10th and 90th percentiles from 0.20-0.28 and 1.00. In all zones, the minimums were zero, and the maximums were 1.00, indicating the existence of very strongly aligned, but also completely unaligned neurites, with a clear advantage to the former. This is supported by the skewness distribution (-1.10 to -1.21) with a very small kurtosis (-0.16 to 0.03). All descriptive values consistently indicate a robust biaxial alignment of neurites in all zones with only minor differences in the shape of the distributions, implying a very clear pattern of mechanotactic effect. The measured results are consistent with a large number of neurites aligned at 0° and 90°, which is evident by visual inspection of the images. The box-and-whisker plot in Figure 7.4 shows the values of neurite alignment by zone.

Table 7.3 Descriptive statistics of NA across 4 zones for S1-S5

Biaxial index of NA (AI_bi): descriptive statistics				
	Zone 1	Zone 2	Zone 3	Zone 4
N	150	150	150	150
Mean	0.77	0.78	0.78	0.77
Median	0.96	0.98	0.94	0.95
SD	0.30	0.31	0.29	0.31
SE	0.025	0.025	0.024	0.025
CI (95 %)	0.72	0.73	0.73	0.72
MIN	0.03	0.02	0.02	0.00
MAX	1.00	1.00	1.00	1.00
Q1	0.58	0.65	0.60	0.65
Q3	1.00	1.00	1.00	1.00
IQR	0.41	0.35	0.40	0.35
Percentile_ 25	0.20	0.20	0.28	0.21
Percentile_ 75	1.00	1.00	1.00	1.00
Trimmed Mean	0.82	0.84	0.83	0.82
Skewness	-1.10	-1.21	-1.17	-1.17
Kurtosis	-0.16	0.01	0.03	0.03

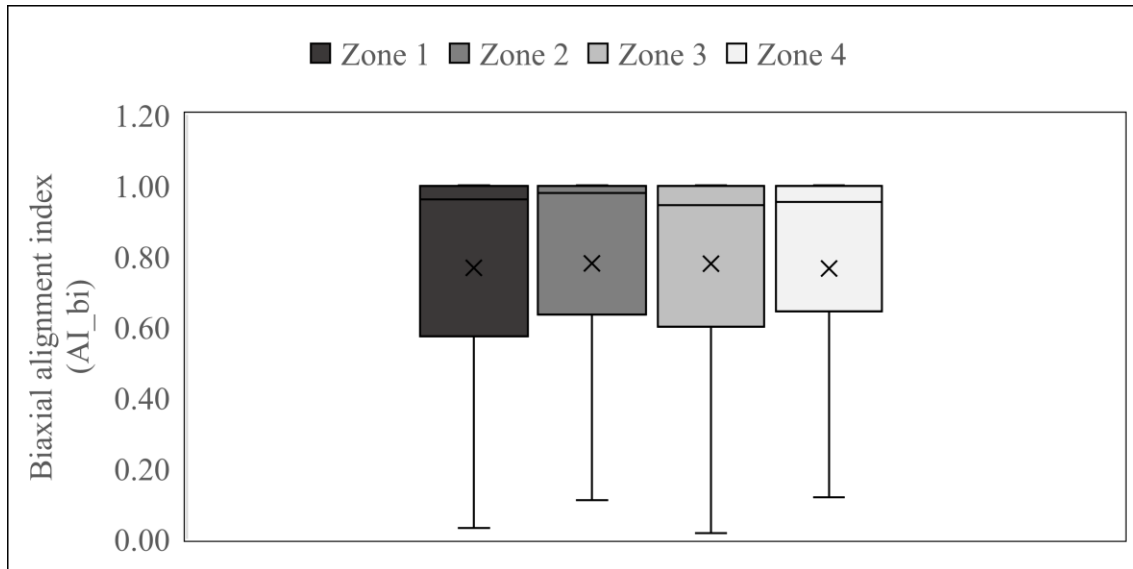


Figure 7.4 Distribution of NA for Zone 1-Zone 4

In contrast to the case of neurite length, the two-factor ANOVA test showed a significant chip effect without a significant zone effect. The results are given in Table 7.4. For the chip factor (Rows), the sum of squares at four degrees of freedom is $SS = 0.07$, with $MS_{error} = 0.002$. The

F ratio takes the values $F(4,12) = 7.27$, thus significantly above the critical F crit 3.26 with a highly significant $p = 0.003$. The chip is responsible for about 70 % of the total variance of the alignment index ($\eta^2 \approx 0.70$) and about 71 % of the non-residual variance (partial $\eta^2 \approx 0.71$), which corresponds to a large effect size. From the above results, it follows that different chips show different degrees of neurite alignment, even after averaging over zones.

The sum of squares for the zone factor (Columns) is minimal with three degrees of freedom and is $SS = 0.001$ with $MS = 0.0003$. The value $F(3,12) = 0.11$ in relation to $F \text{ crit} = 3.49$ at $p = 0.95$, indicates an insignificant influence of the zone on neurite alignment. Zones as a factor contribute almost negligibly to the total variance of the alignment index ($\eta^2 \approx 0.01$). Residual variance ($SS_{\text{error}} = 0.029$) indicates heterogeneity among chips and measurement noise. From all of the above, it follows that the biaxial alignment of neurites along the edge of the substrate does not depend on the chip zone on the observed population, i.e., differences in topography, but that all topographies have a similar strong effect.

Table 7.4 Two-factor ANOVA test: Biaxial index of neural alignment

Two-factor ANOVA test: Neurite alignment						
Source of Variation	SS	df	MS	F	P-value	F crit
Rows	0.070	4	0.018	7.274	0.003	3.259
Columns	0.001	3	0.0003	0.114	0.950	3.490
Error	0.029	12	0.002			
Total	0.100	19				

These results show that neurite alignment is highly consistent across zones but varies substantially from chip to chip, whereas neurite length is comparatively uniform and does not display a strong dependence on either factor in this dataset. Overall, the measured values of neurite lengths are consistently smaller than those measured in Chapter 6, while the measured biaxial index of neural alignment are consistently larger. This discrepancy can be explained by differences in sample density (20 000 in Chapter 7 vs 40 000 in Chapter 6), different populations of experimental animals, and differences in microconditions of culturing. Considering the high propensity of spiral ganglion neuron culture to clearly align with the edges of the substrate in these samples, it can be concluded that there is a strong influence of mechanotaxis on neurites.

Since the cases of recorded neurophysiological activity were recorded on different chips and with different detection settings, we avoid direct quantitative comparisons between cases. Instead, we analyze each case within-case: we display descriptive distributions (amplitude, width, ISI), check spatial consistency (correlations of neighboring electrodes), and, where applicable, source separation. This preserves the methodological purity and informativeness of the obtained results.

7.2 Recording of spontaneous neurophysiological activity from a single source

In this section, the recording and basic descriptive analysis of signals observed on Sample 4, Zone 3, dominant electrode D18, designated for short as (S4-Z3-D18), are presented in the mapped image section of S4 at magnification of 40 \times , in Figure 7.5. The signals were recorded for an observation time of 60 seconds and, in addition to the signals on the dominant electrode D18, the signals on the neighboring electrodes separated on both sides by 100 μm (D17 and D19) and 200 μm (D16 and D20), are also included. The row containing the listed electrodes is active. The row above and the row below are not connected. The detection parameters, shown in Table 7.5, are applied to all marked electrodes, but due to significantly smaller amplitudes, their visibility is significantly lower, and thus their statistical record.

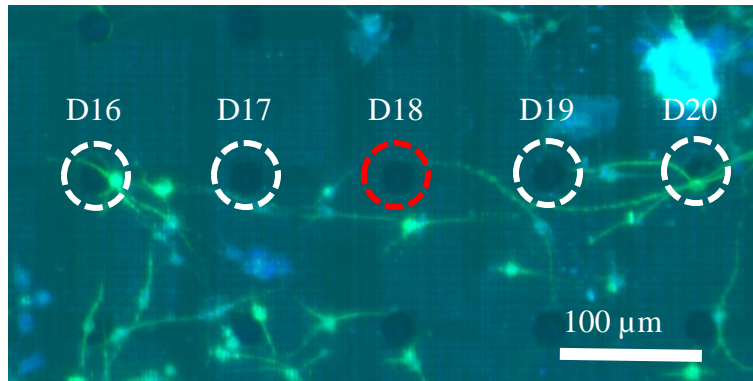


Figure 7.5 Single signal source (S4-Z3): cropped view of an electrode array on an MEA substrate with SGN cultures

Table 7.5 Single signal source (S4-Z3): detection parameter settings

Detection parameters (S4-Z3-D18)	
Min. prominence (μV)	50
Min height (μV)	100
Peak distance (s)	0.001

Figure 7.6 partially shows the recorded signal on the marked electrodes (D16-D20). The dominant electrode D18 is shown in yellow. Peaks detected by the MATLAB application based on the parameters from Table 7.5 are marked with yellow \times marks. In this time window, 5 positive peaks are visible on the dominant electrode.

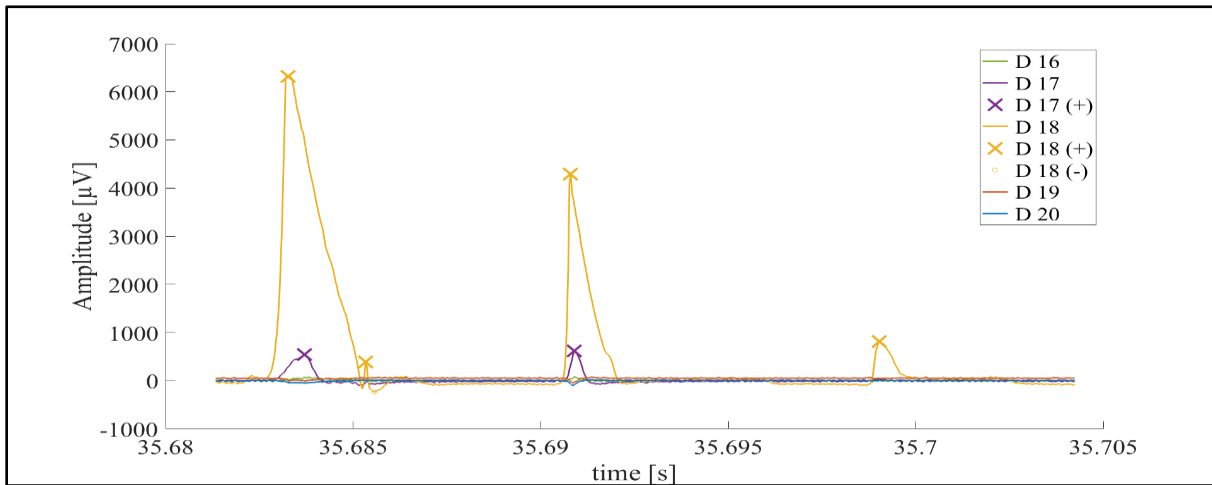


Figure 7.6 Single signal source (S4-Z3): search time window

Figure 7.7 shows a histogram of the distribution of recorded amplitudes for a single source (S4-Z3-D18). On the sample of 401 signals, an asymmetric distribution towards the ends is visible, with an even decrease from the minimal towards the middle and extreme values at the maximum. This is also confirmed by the average amplitude of $1357.5 \mu\text{V}$ with a median of only $348.5 \mu\text{V}$. This difference is the result of a smaller number of very large values compared to other histogram bins. This is confirmed by strong positive asymmetry (skewness = 1.70) and kurtosis = 1.48. On the same track, the standard deviation ($1961.8 \mu\text{V}$) is very high compared to the median. Amplitudes vary in the range from $100.1 \mu\text{V}$ to $6273.6 \mu\text{V}$. The lower limit is limited by noise, and the upper limit by the voltage saturation of the amplifier. The same pattern of amplitude distributions appeared in all other cases not shown in this paper. Extreme values were not removed but they should be interpreted with caution. Except for extreme values, which can be attributed to system imperfections and the aggregation of a larger voltage range into one large bin (2000-ca. $6300 \mu\text{V}$), the amplitude distribution is expected for spontaneous action potentials.

The value of the lower quartile ($Q1 = 158.3 \mu\text{V}$) and the upper quartile ($Q3 = 1685.6 \mu\text{V}$) indicates that most of the signals take a value closer to the lower part of the distribution. Interquartile range in the amount of $1527.3 \mu\text{V}$ suggests that the value of half of the amplitudes of all signals is in the

range from 0.16 to 1.68 mV. Even more pronounced is the difference between the 10th and 90th percentiles ($P_{10} = 112.6 \mu\text{V}$, $P_{90} = 6208.9 \mu\text{V}$), from which it can be read that a relatively large number of amplitude values are very close to the minimum and maximum, as can be seen on the histogram. By removing 10 % of the extreme values, the mean drops to $900.9 \mu\text{V}$ compared to $1357.5 \mu\text{V}$, which is the untrimmed mean, which is consistent with a relatively large number of extremely large values, i.e., the occurrence of system saturation. The standard error of the mean of $98.0 \mu\text{V}$ with a corresponding 95 % confidence interval ($= 1357.5 \pm 192.6 \mu\text{V}$) implies a relatively precise estimate of the mean amplitude despite the high variability of individual results. Overall, the recorded signals, except for extreme values, assume a stable distribution with a consistent decreasing trend. The reliability of the observed results, as previously stated, is contributed by the large number of recorded signals, and part of the variation in amplitude can be attributed to local conditions in the extracellular environment.

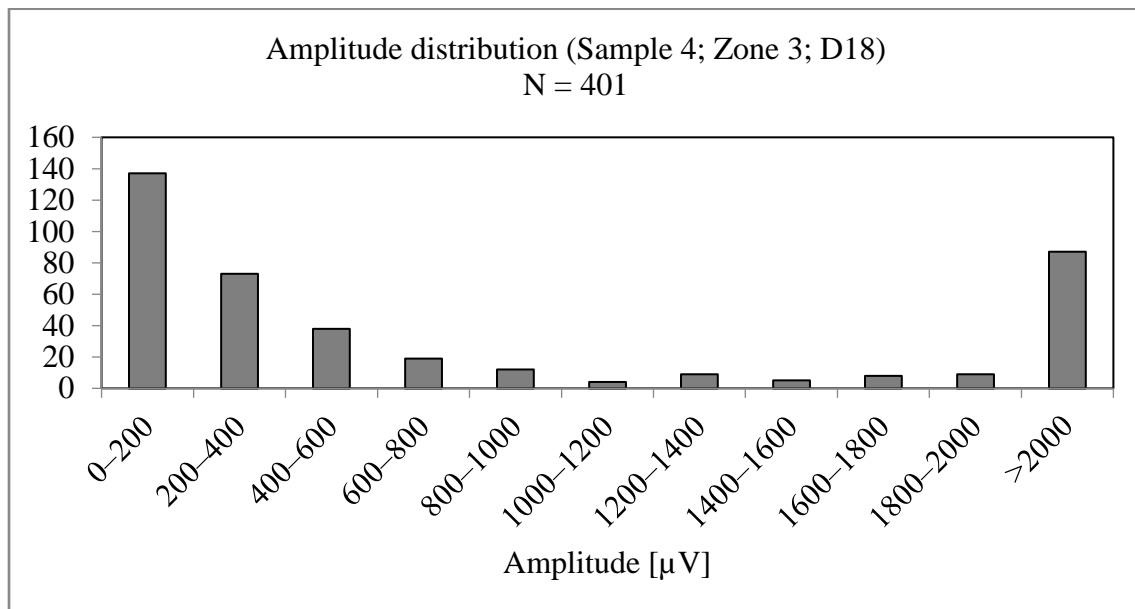


Figure 7.7 Single signal source (S4-Z3-D18): amplitude distribution histogram

The distribution of the signal width for the observed case on the dominant electrode D18 is shown by a histogram in Figure 7.8. On a sample of 401 recorded signals, the arithmetic mean is 0.71 ms, and the median is 0.43 ms. As in the case of amplitudes, also with signal widths, a smaller number of extremely large values are responsible for the difference between the average and the median, but in this case the difference is still more moderate, because the signal widths grow proportionally less in relation to the amplitude. The values for skewness (14.89) and kurtosis (263.19) behave

accordingly. Despite the fact that the distribution has so-called long tail, most signals are in the range of a few milliseconds, which corresponds to the footprint of action potentials. The standard deviation (1.63 ms) is several times higher than the median, in accordance with the accumulation of the largest number of signals around smaller values. Signal widths range from 0.03 ms to 30.10 ms.

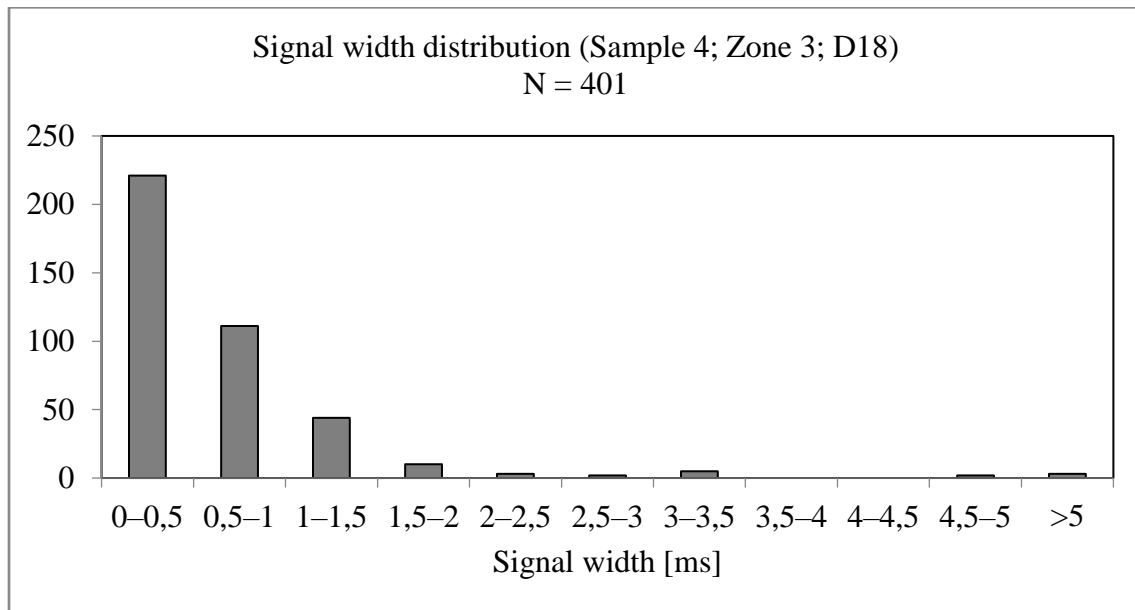


Figure 7.8 Single signal source (S4-Z3-D18): width distribution histogram

The interquartile range (IQR = 0.57 ms), with the lower quartile (Q1 = 0.23 ms) and the upper quartile (Q3 = 0.80 ms) shows that half of the signals are in a relatively narrow range of approximately 0.2-0.8 ms, which is again in accordance with the conditions of extracellular recording, in which the signal widths should not vary more than the amplitudes of these same action potential signals. The 10th percentile (P10 = 0.13) and the 90th percentile (P90 = 1.29) imply that 80 % of the signal is within a range of approximately one millisecond and that the large total range of approximately 30 ms is caused by extreme values, further to the amplitude distribution data. By removing 10 % of the extreme values, the trimmed mean (10 %) drops to 0.51 ms, approaching the median approximately closer than the untrimmed mean, which is consistent with previous results. The standard error (SE = 0.08) and the 95 % confidence interval ($\approx 0.71 \pm 0.16$ ms) indicate a stable reliability of the average estimate, despite outliers. Based on the previously demonstrated results, it is clear that the majority of signals fall into the

submillisecond range, as expected for this type of signal, while the longer tail of the distribution is caused by a smaller number of large values.

The ISI distribution at electrode D18 shows a clear bursting pattern of activity, with a large number of short intervals between spikes and rare longer intervals that can be attributed to the interburst intervals. In a sample of 400 measured ISIs, an arithmetic mean of 104.9 ms was recorded with a median of 6.87 ms. As in the previous two cases, for amplitude and width, in the case of ISIs, a small number of extreme values causes the difference between the median and the average. These data are confirmed by the values of skewness = 15.26 and kurtosis = 256.87. The standard deviation (862.5 ms) exceeds the median by several orders of magnitude, and the interval of the total range ranges from 1.03 ms to as much as 15401.10 ms. The lower limit is limited by the detection parameters (peak distance from Table 7.5), and the upper limit indicates the largest interval between bursts, i.e., the longest period without recorded electrical activity of neurons. The distribution is shown in the histogram in Figure 7.9.

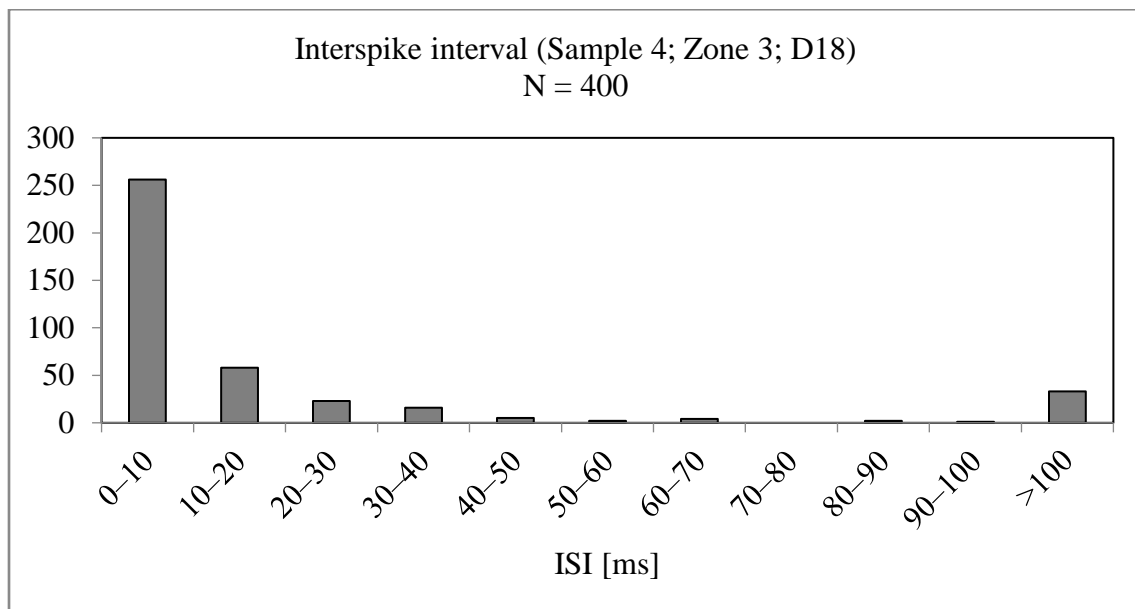


Figure 7.9 Single signal source (S4-Z3-D18): ISI histogram

By removing the 10 % of the shortest and longest intervals, the trimmed mean (10 %) drops to 10.16 ms, approaching the median and interquartile range compared to the untrimmed mean of 104.9 ms. It is obvious from the above that the largest number of spikes is found within short and medium ISIs, ranging from approximately 5 to 20 ms, while, as stated earlier, a smaller number of extremely long intervals represent periods of inactivity between bursts of spontaneous action

potentials. The standard error of 43.12 with a wide 95 % confidence interval ($\approx 104.9 \pm 84.8$ ms) proves that the arithmetic mean is not a precise descriptor when describing the distribution. Overall, the descriptive statistics for ISI clearly point to a bursting pattern of activity. Most of the time the neuron fires a series of pulses separated by short intervals, occasionally interrupted by long periods of silence that dominate the global average and variability.

The observed signal amplitude pattern shows that a small number of signals deviate significantly from the majority, which follows the expected values for spontaneous action potential of spiral ganglion neurons. The ISI shows the footprint expected for spontaneous action potentials of spiral ganglion neurons, with extremely large values (> 100 ms) representing the interburst spacing on the time scale and as such can be taken as an approximate measure of the number of bursts on the whole recording level.

7.3 Recording of spontaneous neurophysiological activity from different independent sources

This section presents signals from different sources, 200-250 μm apart, recorded on S3-Z4-D19/21/22. The correlation of the observed series of electrodes (D19-D23) with the aim of distinguishing the signal source is presented. A descriptive description of the signal amplitudes and widths and ISI for both electrodes is given, and the distribution of the mentioned parameters is described. As in Section 7.2, the total length of the observed recording was 60 seconds. Detection parameters are shown in Table 7.6.

Table 7.6 Multiple signal sources (S3-Z4-D19/22): detection parameter settings

Detection parameters (S3-Z4-D19/22)	
Min. prominence (μV)	100
Min height (μV)	200
Peak distance (s)	0.001

Figure 7.10 shows a series of observed electrodes (D19-D23) on the MEA substrate with spiral ganglion neuron cultures. As in Section 7.2, the electrodes in the row above and below the marked row are not connected by bonds to the neuroelectronic interface.

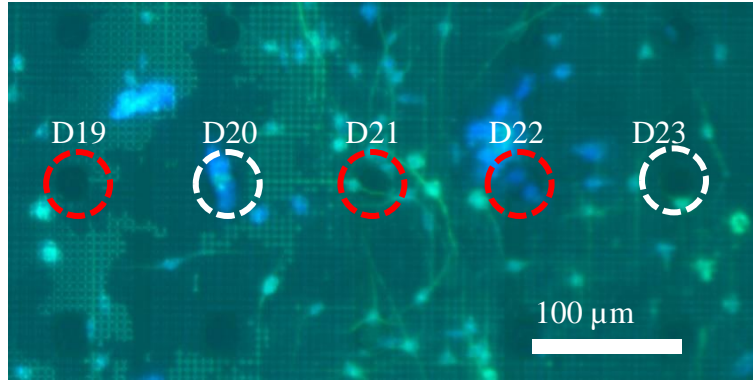


Figure 7.10 Multiple signal sources (S3-Z4-D19/22): cropped view of an electrode array on an MEA substrate with SGN cultures

Figure 7.11 shows signals on electrodes D19-D23 in the search time window with positive peaks.

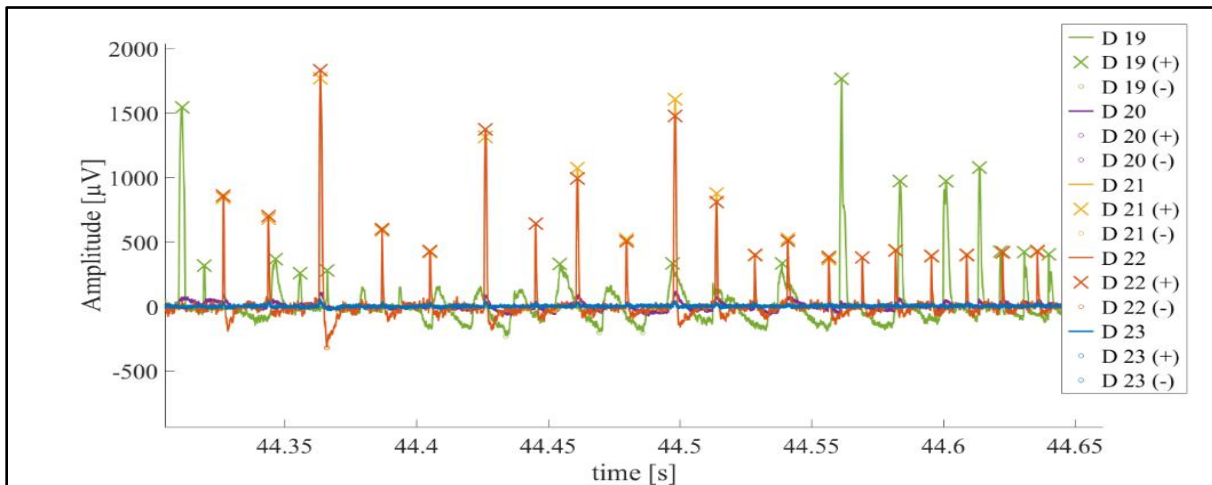


Figure 7.11 Multiple signal sources (S3-Z4-D19/22): search time window

In the presented case, two dominant patterns of bursting activity are evident, i.e., one dominant on electrode D19 (marked in green in the picture), and the other on electrodes D21 and D22 (marked in orange and yellow respectively in the picture). Figure 7.10 shows the neuronal structures that could be the source of the signal: the neurite ending at electrode D19 and the cluster of neurons between electrodes D21 and D22. The correlation measurement shown in Figure 7.12 was performed.

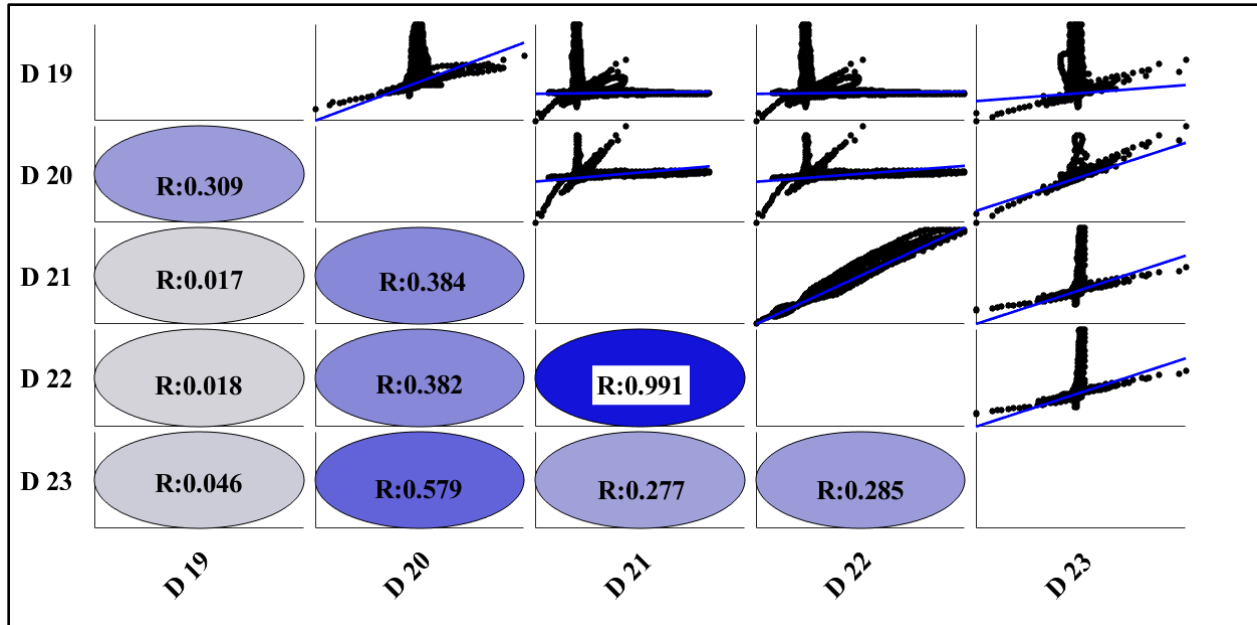


Figure 7.12 Multiple signal sources (S3-Z4-D19/22): correlogram

As expected, the left dominant electrode D19 shows the highest Pearson coefficient R for the adjacent electrode D20 ($R_{D19-D20} = 0.309$). The correlation with the other electrodes is significantly lower and ranges from $R_{D19-D23} = 0.017$ to $R_{D19-D23} = 0.046$, which is in accordance with the visual reading of the signal in Figure 7.11. Electrode D20 shows a similar correlation coefficient with all dominant electrodes. In addition to the mentioned D19, the correlation coefficients with the electrodes of the second assumed independent source are $R_{D20-D21} = 0.384$ and $R_{D20-D22} = 0.382$, which indicates their mutual similarity, but also the equal distance of the D20 electrode from both assumed sources. The highest correlation was recorded with electrode D23 ($R_{D20-D23} = 0.579$), which is located at a similar distance from the assumed source at electrodes D21 and D22. The highest degree of correlation is recorded between electrodes D21 and D22 ($R_{D21-D22} = 0.991$), which indicates a cluster of neurons between them as a potential signal source. Dominant electrodes D21 and D22 show similar correlation coefficient values with electrodes about $150 \mu\text{m}$ away from the assumed source ($R_{D21-D20} = 0.384$ and $R_{D22-D23} = 0.285$), which further supports the claim about the assumed position of the source. Accordingly, the correlation between electrodes D20 and D23, equally distant from the assumed source between D21 and D22, amounts to a relatively high $R_{D20-D23} = 0.579$. Overall, the above measurements indicate the existence of several mutually independent sources, most likely located at electrode D19 and between electrodes D21 and D22, as shown in Figure 7.10.

The comparison of the read signals of two assumed independent sources is given descriptively below, based on the case from Section 7.2. The same metrics and search parameters were used as in the case of a single signal source. The signals from electrode D19 and the signal from electrode D21 were taken for comparison, as shown in Figure 7.13.

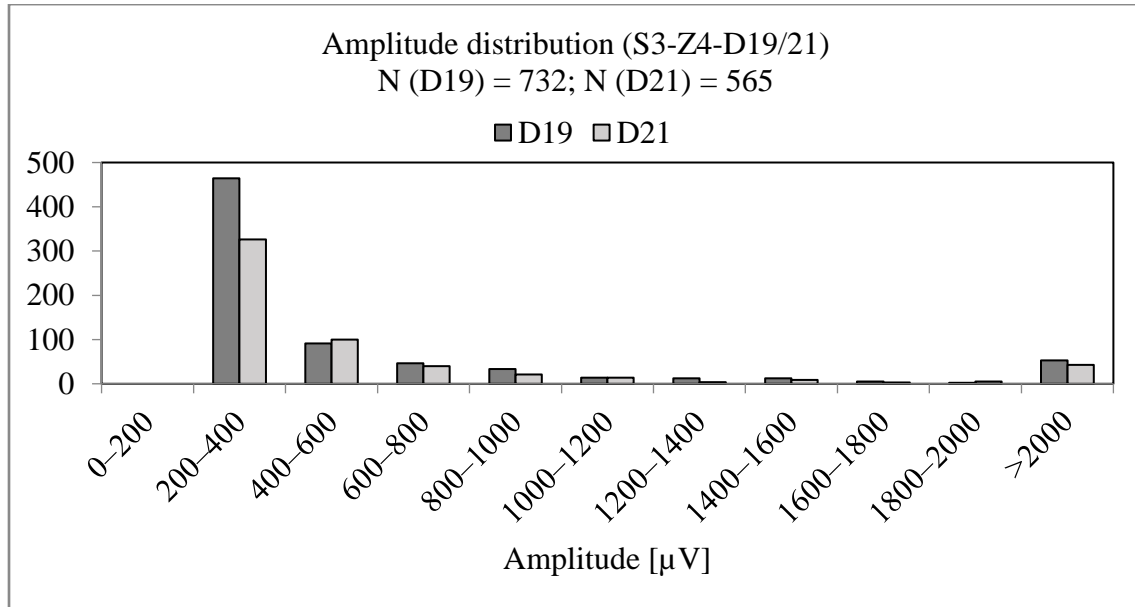


Figure 7.13 Multiple signal sources (S3-Z4-D19/21): amplitude distribution histogram

For ND19peaks = 732 the average value of the amplitude is 692.26 μV with a standard error (SE = 39.92 μV), while the median is 301.08 μV . The trimmed mean (10 %) in the value of 411.12 μV is significantly lower than the average, which is an indicator of a stronger tail of the distribution, as in the case of a single source of signal. The values of the lower (Q1 = 234.59 μV) and upper (Q3 = 589.58 μV) quartiles along with the interquartile range (IQR = 355.00 μV) suggest a distribution core of the order of several hundred μV , as in Section 7.2. The values of skewness (3.57) and kurtosis (13.02) confirm the asymmetric distribution. The 90th percentile value (P90 = 1346.73 μV) with a maximum of 6298.31 μV is consistent with the previous example, while the 10th percentile (P10 = 210.80 μV) and a minimum of 200.07 μV imply a lower detection threshold of 200 μV , which is why the lower tail cut off.

565 peaks were recorded on electrode D21, with an average of 696.65 μV with a standard error of SE = 40.82 μV . As in the previous cases, here too the median is lower than the average (363.22 μV), as well as the trimmed mean (10 %), which is 447.81 μV . The lower quartile is Q1 = 275.37 μV , and the upper Q3 = 588.84 μV with an interquartile range IQR = 313.46 μV , resulting in a

narrower central dispersion compared to D19. The right asymmetry is emphasized (skewness 3.60 and kurtosis 14.07), while the 90th percentile is 1452.37 μV . The maximum value of 6315.40 μV suggests voltage saturation on this electrode as well. Both electrodes have a similar average amplitude ($\sim 690 \mu\text{V}$) and almost identical maximum values ($\sim 6.3 \text{ mV}$), but the higher median at D21 (363 μV vs 301 μV) and the higher lower quartile (275 μV vs 235 μV) and trimmed mean (448 μV vs 411 μV) indicate a more compact distribution, as can be seen on the histogram. D19 shows a slightly wider distribution with higher interquartile range and standard deviation, and a larger number of lower amplitude signals. The lower limit of both electrodes is determined by the lower threshold at approx. 200 μV , and the upper limit of approx. 6 mV represents system saturation.

Figure 7.14 shows a histogram of the signal width of electrodes D19 and D21. For electrode D19, on a sample of 732 signals, the average is 1.62 ms, and the standard error is 0.05 ms at 95 % CL. The median value is 1.29. The interquartile range is 1.47 ms with the lower quartile $Q1 = 0.66 \text{ ms}$ and the upper quartile $Q3 = 2.13 \text{ ms}$.

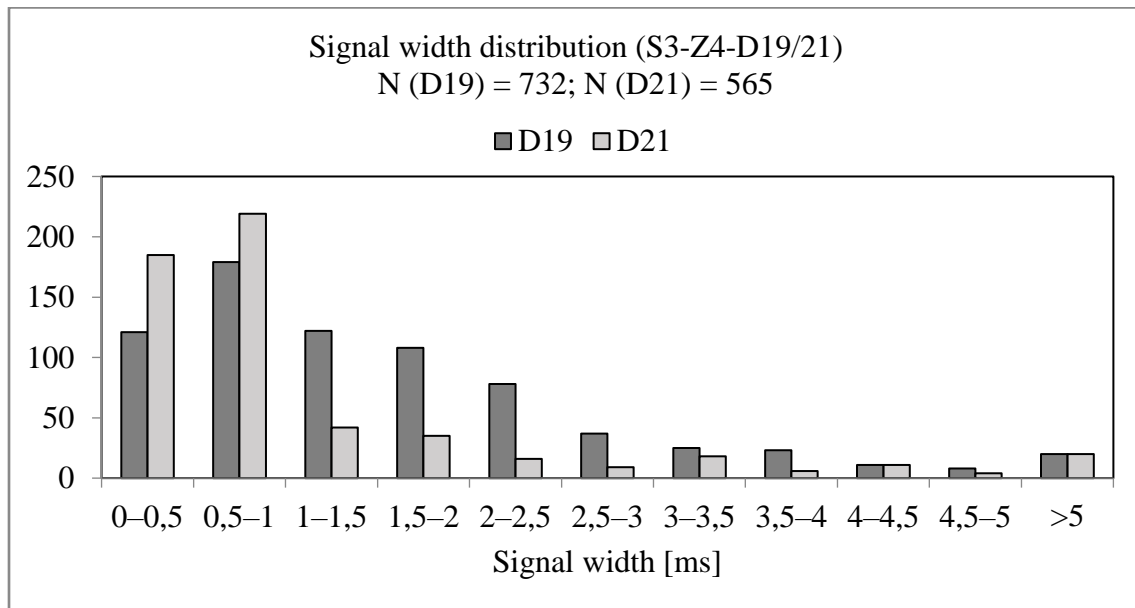


Figure 7.14 Multiple signal sources (S3-Z4-D19/21): width distribution histogram

It is obvious from the above that the width of most signals is in the interval from 0.7 to 2.1 ms with the highest density around 1 ms, which corresponds to typical values for action potentials. The skewness of the distribution is 2.77, and the kurtosis is 13.79. A smaller number of extremely wide signals reach high values (MAX = 14.40 ms), and the 90th percentile is $P90 = 3.32$, which

additionally confirms the thesis about the influence of a smaller number of signals on the distribution average.

On electrode D21, for 565 signals, an average width of 1.16 ms was measured with a standard error of $SE = 0.06$ ms. The median of 0.63 ms indicates a narrower distribution compared to electrode D19. The same conclusion follows from the interquartile range $IQR = 0.70$ ms with the lower quartile $Q1 = 0.45$ ms and the upper quartile $Q3 = 1.15$ ms. The distribution is asymmetric to the right with a skewness of 2.59, and a kurtosis of 7.49. Extreme values are smaller ($MAX = 9.48$ ms) at the 90th percentile than 3.11. The 10th percentile of P10 is 0.35 ms. Comparatively, D19 compared to D21 shows a higher median (1.29 vs 0.63 ms) and a higher interquartile range of $IQR (1.47$ vs 0.70 ms). It follows that D 19 records wider extreme activity, which is supported by the comparison of maximum values ($MAX_{D19} = 14.40$ ms vs $MAX_{D21} = 9.48$ ms). The differences in the distributions are also reflected in the average and median differences on one and the other electrode, with the difference on D19 being greater than on D21. All of the above supports the assumption of two independent sources.

Figure 7.15 shows the ISI histograms for electrodes D19 and D21 in comparison.

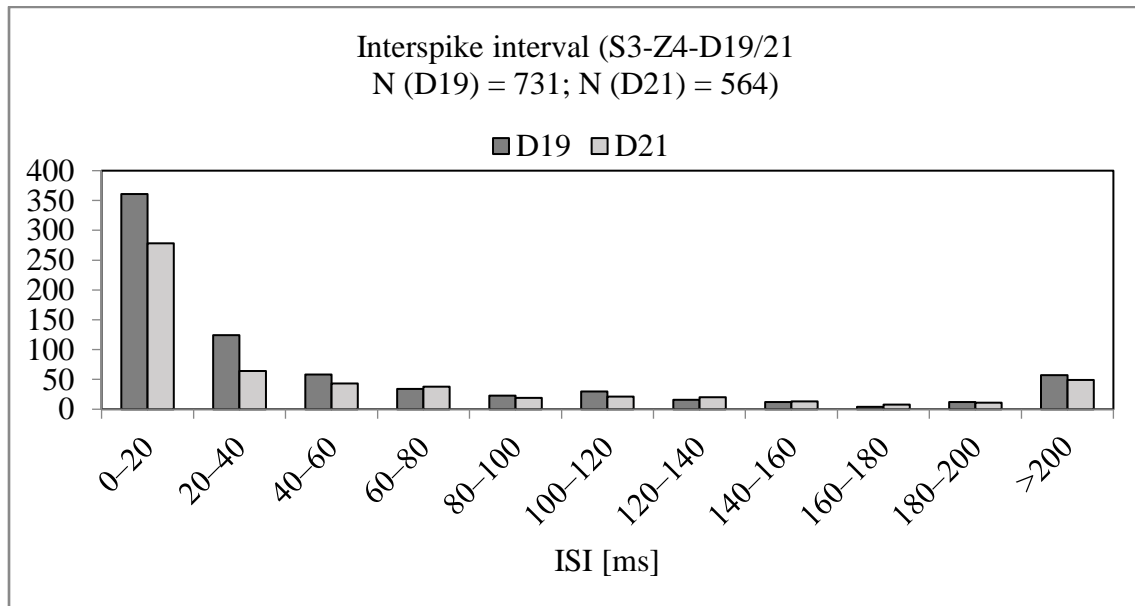


Figure 7.15 Multiple signal sources (S3-Z4-D19/21): ISI histogram

For electrode D19, at 731 intervals, the median is 20.10 ms with the lower quartile $Q1 = 5.87$ ms, the upper quartile $Q3 = 62.70$ ms, which gives an interquartile range $IQR = 56.73$ ms. The 10th

percentile value is $P_{10} = 2.07$ ms, and the 90th percentile value is $P_{90} = 164.35$ ms. Comparing the average interval (82.03 ms) with the trimmed mean (10 %) of 34.85 indicates a smaller number of long intervals that contribute to the increase in the average. The same is confirmed by the maximum interval value ($MAX = 4023.97$ ms) with a standard deviation of 251.20 ms. The skewness of the distribution is 9.16, and the kurtosis is 113.41. The minimum of 1.03 ms is limited by the refractory period of the physiological signal, but also by the detection settings (Table 7.6). In short, a large number of activities in the bursting pattern were recorded, while very wide gaps indicate the intervals between bursts.

For the D21 electrode intervals at a sample size of 564 intervals, the values follow the same trend. The median is 20.63 ms with a slightly larger interquartile range $IQR = 75.17$ ms, since the lower quartile Q_1 is 7.41 ms and the upper Q_3 is 82.57 ms. The minimum value of 1.03 ms indicates the same lower limit defined by the search parameters, and the 90th percentile of $P_{90} = 191.08$ ms shows a slightly greater spread of the distribution, which is visible in the histogram. The right tail of the distribution is even more pronounced with an average of 106.17 ms which is significantly above the median and a trimmed mean (10 %) of 42.65 ms. The maximum recorded value is 5125.03 ms with a standard deviation of 375.40 ms. Skewness is 9.66 and kurtosis is 112.50. The interpretation is the same as for electrode D19: shorter bursts dominate, and large values indicate gaps between bursts, i.e., periods of neuronal inactivity. Both electrodes show a very similar median (~20 ms) and lower core ISI (bursts), but D21 has a wider core (larger interquartile range) and more pronounced long pauses (larger mean and MAX), suggesting somewhat less frequent or irregular bursting compared to D19. In both cases, the mean–median difference and extremely high kurtosis (> 100) clearly show a mixture of short intra-burst intervals and sporadic multi-second intervals dominating the variance.

The claim that these are different sources is supported by the fact that the signals on the compared electrodes were detected at different times, which is confirmed by their correlograms. On the other hand, the claim that these are the same types of signals, in this case spontaneous action potentials as the main carriers of the electrophysiological activity of healthy neurons, is supported by the very comparable patterns of their main metrics, i.e., amplitude, spike and interspike intervals. As in the previous case, the analysis shows that the neuroelectronic interface is able to record activity that corresponds to spontaneous action potentials in terms of metrics even when they come from

different sources and quantify them separately. This case also demonstrates the tendency of the cell culture to activate multiple neurons simultaneously, which indicates that cell culturing was successfully performed.

7.4 Recording of evoked neurophysiological activity

In this section, evoked responses of neurons are briefly presented with their shape and appearance. Neurons were taken from a different population of animals compared to the previous two sections, and identical system parameters were used for signal acquisition. A bright field image of the neuronal population and observed electrodes recorded at magnification of 10 \times on zone 2 is shown in Figure 7.16.

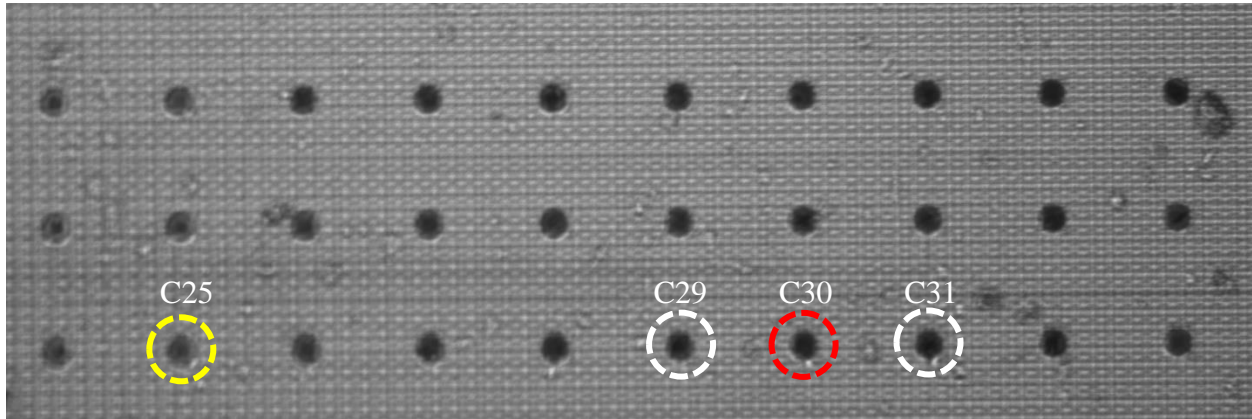


Figure 7.16 Bright field view: stimulating and recording electrodes

In the recording lasting 28 seconds with a total of 20 stimulation pulses, distributed in 4 series of 5 monophasic negative pulse trains with an amplitude of $-0.1 \mu\text{A}$ and a phase duration of $67 \mu\text{s}$ at a frequency of 5 Hz, 19 responses were recorded on the dominant electrode C30 in irregular intervals after pulse trains. The picture shows the row of electrodes in which the evoked responses were recorded. The dominant electrode C30 (marked in red) is $500 \mu\text{m}$ away from the stimulating electrode C25 (marked in yellow). Responses of negative polarity were recorded on the dominant and immediately adjacent cells, C29 and C31 (marked in white). Moving away from the C30 electrode, the signal is lost and no other response is recorded. An irregular timing pattern of signal firing without proper post-stimulation latency was recorded, therefore this example is purely demonstrative in nature. Part of the recording with the stimulating pulse and the obtained neuron response is shown in Figure 7.17. Evoked extracellular spikes recorded after delivery of a train of five monophasic negative pulses are shown in the upper graph, while the corresponding

stimulation waveform is presented in the lower graph. Each pulse had an amplitude of $-0.1 \mu\text{A}$ and a phase duration of $67 \mu\text{s}$. Panel (a) shows a magnified view of the recorded signals at the dominant electrode C30, the adjacent electrodes C29 and C31, and the stimulating electrode C25. Panel (b) presents a magnified view of the stimulation pulse.

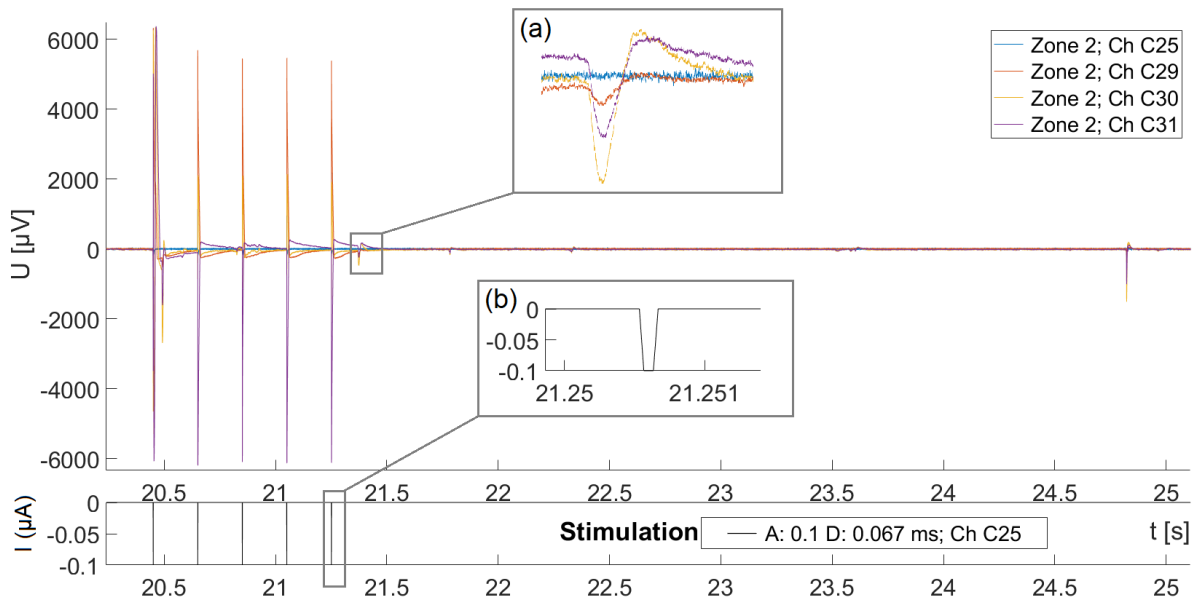


Figure 7.17 Evoked APs (upper graph); Stimulation pulses (lower graph); (a) Evoked AP: magnified (b) Stimulation pulse (magnified); Adapted from [83]

7.5 Discussion and summary

In Chapter 7, following the conclusions of Chapter 6, an analysis of spontaneous electrical activity of spiral ganglion neuron cultures on MEA substrates under in vitro mechanotactic conditions was performed. In order to validate the presence of mechanotaxis on the new set of samples used, as a necessary prerequisite for confirming the basic hypothesis of the dissertation, in addition to descriptive analysis, inferential statistical analysis was performed, according to the sampling design from Table 4.2. In addition to 5 MEA chips as substrates, sampling was also carried out evenly across four zones, with 30 ROIs selected in each zone where possible, giving 120 ROIs per chip and 600 at the level of the entire sample population for each measured parameter. In this experiment, the soma area parameter was excluded from the measurement due to its lower sensitivity to mechanotaxis and generally of less importance for the long-term application of the obtained results. It follows from the above that the total number of measured ROIs was 1 200. In addition to the application of new statistical methods, an important change compared to Chapter 6

also related to the density of neurons per chip. In this experiment, a twofold lower density was used (20 000 vs 40 000 neurons per chip) with the aim of obtaining a clearer image and ultimately more reliable measurement results.

The results showed very high values of neurite alignment (only the biaxial alignment index was used) compared to the case from Chapter 6, suggesting a strong influence of the topography of the substrate on the mentioned parameter from the aspect of descriptive statistics. Inferential statistical analysis indicated significant differences between chips in neurite alignment, suggesting the influence of microconditions on each individual substrate. In terms of neurite length, shorter neurite lengths were recorded compared to the results from Chapter 6. The differences can be attributed to the different populations of neurons that were sampled, i.e., the different animals that were used for the experiment from the sixth and seventh chapters. Unlike neurite alignment, neurite length varied less across chips. When interpreting the measured values, it is important to take into account the density of the neuronal population on the chip. On the one hand, this difference directly affects the measurement and its reliability, and on the other hand, the direct influence of the density of neurons on their morphological parameters cannot be ruled out. This interdependence certainly represents an interesting scientific question that should be taken into account in the next phase of research. Chip zones were not shown to be significant factors for neurite length and neurite alignment. All geometries of micropillars induced a strong mechanotactic effect without major mutual differences, giving primacy to the very existence of the structures regardless of their dimensions. It is important to note, and following the conclusion of Chapter 6, that when analyzing neurite alignment, the analysis was performed exclusively along the x and y axes of the substrate, i.e., at 0° and 90°, unlike the analysis in previous studies [54-56] which included other orientation angles and different dimensions of the microstructures themselves on the substrate surface. Also, in the aforementioned studies, the 90° angle showed the greatest tendency to affect neurite alignment. In order to gain better insight into the behavior of neuronal cultures under the described conditions, it would be useful and informative to examine the interdependence of the influence of the substrate on morphological parameters and the age of the cells, i.e., the time spent under in vitro conditions. In this case, as in Chapter 6, the cultures were grown in a time range that was supposed to ensure sufficient neurite development, while at the same time remaining within the prehearing period for a higher probability of recording

spontaneous electrical activity, therefore, this is the reason for using exclusively DIV 6 and DIV 7 cultures.

Spontaneous electrical activity was analyzed with respect to the characteristic features of signals of this type, i.e., amplitude and width of the signal and interspike interval. All recorded spontaneous activity was characterized by a large number of signals at the signal-source level, but a small number of different signal sources at the chip level. Given that there are no studies analyzing spontaneous electrical activity of spiral ganglion neuron cultures on such substrates, the results should be interpreted with caution, especially in light of the use of extracellular recording techniques. Unlike intracellular methods, such as patch clamp, which are highly standardized and available in the scientific literature for several decades, extracellular systems do not have this level of uniformity and standards and therefore comparison with other studies and drawing conclusions based on these comparisons is significantly more demanding. An additional factor in the case of this study is the influence of mechanotaxis through substrate topography, since no systematic investigation of the interaction of MEA substrates with a three-dimensional surface and spiral ganglion neuron cultures has been conducted so far. In light of all the above, the obtained results should be interpreted with caution. The distribution of the observed parameters, i.e., amplitude and width, and interspike interval, is consistent for a single source, as well as for isolated sources in the case of multiple signal sources. The appearance of the histogram of the width and especially the amplitude of the signal was also influenced by the voltage saturation of the system, which appeared in certain cases and caused extreme values in the distribution. These extreme values were ultimately left in the final results, because the metrics used and the visual representation were informative enough not to suggest a wrong conclusion. Identifying different signal sources in the context of this research is important for several reasons. First, successful differentiation of sources demonstrates the ability and reliability of the system for observing such phenomena. Correlation has proven to be an effective tool in differentiating sources, the correlogram of which provides a clear representation of the connection between individual signals. Second, the very appearance of different signals from multiple sources suggests the real property of neurons to be active and reduces the probability that it is some other type of activity, which is especially important to take into account when recording extracellular field potentials, a good overview of which is given in [69]. In support of the evidence that the recorded activities are spontaneous action potentials, and not some of the other neurophysiological activities described in [69], there is also a spatial decrease

of the amplitude across the electrodes, as expected considering their mutual distance. System settings are of great importance in the detection of extracellular neuronal signals, both during recording and during post processing. Signal filter settings can largely isolate the required action potentials, but their optimal value depends on the system and micro-conditions, and its accurate determination requires a large number of experiments. Detection parameters (Table 7.5 and Table 7.6), in this case in a custom-made MATLAB application, should be optimized with the same logic as the detection filter of the stimulation/recording controller: they need to include as many action potentials as possible, and as few artifacts and other signals from the cell culture as possible. For optimal values, it is also necessary to carry out a larger number of iterations. However, based on the obtained data, it can be concluded that the presented neuroelectronic interface is capable of recording electrophysiological signals of spiral ganglion neuron cultures under the described conditions and that as such it represents an experimental platform suitable for the further phase of research. Evoked neural responses in the described experiment were achieved in rare cases without a clear response pattern, therefore their presentation in this dissertation is given demonstratively. A challenge to this issue is the lack of a large number of relevant studies with spiral ganglion neuron cultures in comparable microconditions. Finding the optimal conditions and stimulation parameters to achieve a stable response of spiral ganglion neuron cultures will be an important issue in the next phase of research.

In general, and considering all the limitations of using such a system and the lack of literature with which a clear parallel can be drawn, the data should be interpreted with caution. However, based on the reliably demonstrated impact of mechanotaxis on three-dimensional MEA substrates in Chapters 6 and its validation in Chapter 7, and the rare but convincing signals of spontaneous activity, there are sufficiently strong arguments to support the claim that spiral ganglion neuron cultures are capable of electrophysiological activity under mechanotactic conditions, thus supporting the main hypothesis of this dissertation.

8 SCIENTIFIC CONTRIBUTION

The original scientific contributions of this doctoral dissertation are as follows:

- A microelectrode substrate with three-dimensional surface topography was designed and fabricated in order to promote the directed growth and development of neurites of primary auditory neurons under in vitro conditions through the mechanism of mechanotaxis.
- The uniformity of the substrate at the microscale was quantified by SEM/EDS characterization as an indicator of the fabrication process quality, which is essential for its application with primary auditory neuron cultures.
- By integrating the substrate into the neuroelectronic interface, three complementary goals were achieved: successful cultivation of spiral ganglion neurons under in vitro conditions, a functional system for simultaneous extracellular recording and stimulation of neurophysiological activity, and the use of mechanotaxis as a mechanism for neurite contact guidance.
- Knowledge was expanded on the influence of electrotaxis induced by the coil-generated electric field on primary auditory neuron cultures grown on MEA substrates integrated into the experimental magnetic field stimulator.

The overall system setup described in the dissertation represents a valuable experimental interface for further research with an innovative and integrated approach to fundamental questions in auditory prosthetics.

9 CONCLUSION

The dissertation presented an innovative approach to limitations in the current state of the art in the field of auditory prosthetics.

Through the description of the types and prevalence of hearing impairment in the world population, the significance of the subject matter is emphasized and the need for a new approach in the observed field with the aim of enabling better auditory performance for users for whom existing technological solutions do not provide satisfactory results is highlighted. The neuroanatomical gap between the primary auditory neurons in the inner ear and the implanted stimulating electrodes has been identified as one of the main obstacles to the further development of more efficient cochlear implants.

The review of the scientific and technical literature indicated the basis for a theoretical platform for an innovative approach to the described problem. Instead of the conventional approach of overcoming the neuroanatomical gap by bringing the electrodes closer to the neurons, the reverse approach was proposed: the use of mechanisms that would allow the neurons, more precisely their neurites, to approach the sources of stimulation, i.e., the electrodes. This idea was the guiding principle in the creation of two distinct but complementary interfaces based on these observed mechanisms of cell guidance that can potentially influence cell growth and development: Mechanotaxis – the mechanism of neuronal guidance by environmental cues, and electrotaxis – the mechanism of action on neurons by electrical stimuli from the environment.

For this purpose, an MEA chip with a three-dimensional surface microtopography optimized for inducing mechanotaxis was designed as a substrate for culturing primary auditory neurons *in vitro*. Such a substrate was integrated into two custom-made interfaces: a magnetic field stimulator for inducing electrotaxis through the induced electric field, and the neuroelectronic interface for extracellular recording of electrophysiological activity of spiral ganglion neurons.

The methodological approach included growing neurons *in vitro* on MEA substrates, measuring morphological parameters using an image processing software, and descriptive and inferential statistical analysis of the occurrence and impact of mechanotaxis and electrotaxis in the observed cell cultures. In addition to the analysis of the mentioned mechanisms, the characterization of the

microsubstrates themselves was carried out with the aim of verifying the reliability of the fabrication process and ensuring the quality of the analysis in further research steps.

Mechanotaxis and electrotaxis were analyzed individually and in combination, and their effects were quantified with respect to the basic morphological parameters important for neuronal behavior: soma area, neurite length, and neurite alignment. The analysis confirmed strong capacity of the substrate to mechanotactically influence the observed parameters of neuronal cultures through its surface geometry, as well as a noticeable, but weaker electrotactic effect induced by the coil. Given the different directions and modes of action, as explained in more detail in the discussion of Chapter 6, the joint action of the mentioned mechanisms did not give a significant superimposing effect.

Guided by these conclusions, an electrophysiological analysis of neuronal activity was performed using the extracellular recording method with optimization of culture cultivation parameters. It was concluded that the observed neuronal cultures under the influence of the mechanotaxis mechanism are capable of generating electrophysiological activity in the form of spontaneous action potentials, thus opening up space for the use of the described system for the purpose of further research into the interaction of neurons and substrates with three-dimensional surface microtopography that could contribute to the knowledge necessary for the improvement of auditory prosthetics.

The future perspective of the experimental system provides broad possibilities for the direction of scientific research. The first and the simplest direction is further optimization of the system with the aim of obtaining more stable and reproducible results. Varying the conditions of cell culturing with an emphasis on the density of neurons per culture and the cultivation time (for example, 7 DIV vs 14 DIV or 21 DIV were used), improving the signal filtering process and its postprocessing, eliminating noise and artifacts in the system and ultimately increasing the number of samples, are steps that could contribute to the quality of the experimental protocol and results in general.

Furthermore, a comparison of primary auditory neuron cultures with other neurons more frequently used in biological research would provide valuable insights into the nature of the neurons themselves, especially with regard to their excitability, which in this work has proven to be a serious challenge. Such a comparison could help determine whether the low excitability of

primary auditory neurons by extracellular methods under in vitro conditions is caused by cell culture and the stimulation protocol, or whether is it an intrinsic property of this type of neuron.

An interesting scientific question that can be studied in further work relates to the very nature of the origin of spontaneous action potentials in the described cultures. Namely, before electrophysiological recording, the cell cultures underwent a dissection process with a minimum of surrounding tissues extracted from the cochlea of experimental animals. Given that in the literature, most spontaneous activity of primary auditory neurons are attributed to interaction with inner hair cells, which are often extracted together with neurons as tissue explants, a comparison of these activities could open the way to numerous questions about the origin and nature of the signal itself in this type of neuron. The validated and well described mechanism of mechanotaxis could be combined with chemotaxis which is the mechanism that alters the growth and development of neurites through the application of biochemical substances. Chemotaxis is a well-tested mechanism that has not been combined with mechanotaxis in such neuronal cultures in previous research.

The main question that arises as a long-term goal of this and related research is whether the described phenomena can be implemented under in vivo conditions and thus contribute to the improvement of auditory performance for the cochlear implant users around the world. The road to the answer to the question is long and demanding, and this research represents a small but meaningful step in that direction.

REFERENCES

- [1] World Health Organization, n.d. Deafness and hearing loss. World Health Organization. Available at: https://www.who.int/health-topics/hearing-loss#tab=tab_2, Accessed: 28 February 2023.
- [2] Better Health Channel, 2017. Hearing loss – how it affects people. Department of Health, State Government of Victoria. Available at: <https://www.betterhealth.vic.gov.au/health/conditionsandtreatments/hearing-loss-how-it-affects-people>, Accessed: 15 June 2025.
- [3] Sooriyamoorthy, T. and De Jesus, O., 2025. Conductive hearing loss. In: StatPearls. Treasure Island, FL: StatPearls Publishing. Available at: <https://www.ncbi.nlm.nih.gov/books/NBK563267/>, Accessed: 3 January 2025.
- [4] Johns Hopkins Medicine, Types of hearing loss. Health Library. Available at: <https://www.hopkinsmedicine.org/health/conditions-and-diseases/hearing-loss/types-of-hearing-loss>, Accessed: 1 December 2025.
- [5] Centers for Disease Control and Prevention, 2024. Types of hearing loss. Hearing Loss in Children, 15 May. Available at: <https://www.cdc.gov/hearing-loss-children/about/types-of-hearing-loss.html>, accessed: 1 April 2024.
- [6] Karaiskos, C.A., Rachiotis, G., Simou, E. and Dounias, G., 2025. Impact of subclinical hearing loss on quality of life among industrial workers: a cross-sectional analysis utilizing the SF-36 questionnaire. Available at: <https://www.cureus.com/articles/387674-impact-of-subclinical-hearing-loss-on-quality-of-life-among-industrial-workers-a-cross-sectional-analysis-utilizing-the-sf-36-questionnaire>, Accessed: 30 November 2025.
- [7] Purves, D., Augustine, G.J., Fitzpatrick, D., Hall, W.C., LaMantia, A.-S., McNamara, J.O. and Williams, S.M., eds., 2004. Neuroscience. 3rd ed. Sunderland, MA: Sinauer Associates.
- [8] Purves, D., Augustine, G.J., Fitzpatrick, D. et al., eds., 2001. The audible spectrum. In: Neuroscience. 2nd ed. Sunderland, MA: Sinauer Associates. Available at: <https://www.ncbi.nlm.nih.gov/books/NBK10924/>, accessed: 14 July 2025.

- [9] Furness, D., n.d. Hair cells of inner ear. Digital image. Wellcome Collection. Licensed under CC BY 4.0. Available at: <https://wellcomecollection.org/works/en4kavac>, Accessed: 28 March 2025.
- [10] Herculano-Houzel, S., 2009. The human brain in numbers: a linearly scaled-up primate brain. *Frontiers in Human Neuroscience*, 3, article no. 31. doi: 10.3389/neuro.09.031.2009.
- [11] Science Facts, 2019. Parts of a neuron and their function. ScienceFacts.net. 2019. Available at: <https://www.sciencefacts.net/parts-of-a-neuron.html>, accessed: 8 July 2024.
- [12] PhysiologyWeb, n.d. Neuronal action potential. PhysiologyWeb Lecture Notes. Available at: https://www.physiologyweb.com/lecture_notes/neuronal_action_potential/neuronal_action_potential.html, accessed: 5 April 2023.
- [13] Davis, R.L. and Crozier, R.A., 2015. Dynamic firing properties of type I spiral ganglion neurons. *Cell and tissue research*, 361(1), pp.115-127.
- [14] Tritsch, N.X., Yi, E., Gale, J.E., Glowatzki, E. and Bergles, D.E., 2007. The origin of spontaneous activity in the developing auditory system. *Nature*, 450(7166), pp.50-55.
- [15] Storm, K., 2019. Hearing aid unit sales increase by 6.5% in 2019. Hearing Review. Available at: <https://hearingreview.com/inside-hearing/industry-news/hearing-aid-unit-sales-increased-by-6-5-in-2019>. Accessed: 11 August 2023.
- [16] Brand, Y., Senn, P., Dillier, N., Kompis, M. and Allum, J.H.J., 2014. Cochlear implantation in children and adults in Switzerland. *Swiss Medical Weekly*, 144, article no. w13909. doi: 10.4414/smw.2014.13909.
- [17] Seitz, P.R., 2002. French origins of the cochlear implant. *Cochlear implants international*, 3(2), pp.77-86.
- [18] Blume, S.S., 1995. Cochlear implants. In: Institute of Medicine, Sources of Medical Technology: Universities and Industry. Washington, DC: National Academies Press. Available at: <https://www.ncbi.nlm.nih.gov/books/NBK232047/>. [Accessed: 12.6.2023].
- [19] Zeng, F.G., 2022. Celebrating the one millionth cochlear implant. *JASA express letters*, 2(7).

- [20] Zeng, F.G., Rebscher, S., Harrison, W., Sun, X. and Feng, H., 2008. Cochlear implants: system design, integration, and evaluation. *IEEE reviews in biomedical engineering*, 1, pp.115-142.
- [21] Goswami, U. and Leong, V., 2013. Speech rhythm and temporal structure: converging perspectives? *Laboratory Phonology*, 4(1), pp.67–92. doi: 10.1515/lp-2013-0004.
- [22] McDermott, H.J., 2004. Music perception with cochlear implants: a review. *Trends in amplification*, 8(2), pp.49-82.
- [23] Nadol Jr, J.B., Burgess, B.J., Gantz, B.J., Coker, N.J., Ketten, D.R., Kos, I., Roland Jr, J.T., Shiao, J.Y., Eddington, D.K., Montandon, P. and Shallop, J.K., 2001. Histopathology of cochlear implants in humans. *Annals of Otolaryngology, Rhinology & Laryngology*, 110(9), pp.883-891.
- [24] Leach, J.B., Achyuta, A.K.H. and Murthy, S.K., 2010. Bridging the divide between neuroprosthetic design, tissue engineering and neurobiology. *Frontiers in Neuroengineering*, 2, article no. 18. doi: 10.3389/neuro.16.018.2009.
- [25] Nayagam, B.A., Muniak, M.A. and Ryugo, D.K., 2011. The spiral ganglion: connecting the peripheral and central auditory systems. *Hearing research*, 278(1-2), pp.2-20.
- [26] Rubinstein, J.T., 2004. How cochlear implants encode speech. *Current opinion in otolaryngology & head and neck surgery*, 12(5), pp.444-448.
- [27] Shannon, R.V., Fu, Q.-J. and Galvin, J.J. III, 2004. The number of spectral channels required for speech recognition depends on the difficulty of the listening situation. *Acta Oto-Laryngologica Supplement*, 552, pp.50–54. doi: 10.1080/03655230410017562.
- [28] Shepherd, R.K., Hatsushika, S. and Clark, G.M., 1993. Electrical stimulation of the auditory nerve: the effect of electrode position on neural excitation. *Hearing research*, 66(1), pp.108-120.
- [29] Gstoettner, W., Franz, P., Hamzavi, J., Plenk Jr, H., Baumgartner, W. and Czerny, C., 1999. Intracochlear position of cochlear implant electrodes. *Acta oto-laryngologica*, 119(2), pp.229-233.
- [30] Hahnewald, S., Tschertter, A., Marconi, E., Streit, J., Widmer, H.R., Garnham, C., Benav, H., Mueller, M., Löwenheim, H., Roccio, M. and Senn, P., 2016. Response profiles of murine spiral

ganglion neurons on multi-electrode arrays. *Journal of Neural Engineering*, 13(1), article no. 016011. doi: 10.1088/1741-2560/13/1/016011.

[31] O'Leary, S.J., Richardson, R.R. and McDermott, H.J., 2009. Principles of design and biological approaches for improving the selectivity of cochlear implant electrodes. *Journal of neural engineering*, 6(5), p.055002.

[32] Hong, G. and Lieber, C.M., 2019. Novel electrode technologies for neural recordings. *Nature Reviews Neuroscience*, 20(6), pp.330-345.

[33] Wilson, B.S. and Dorman, M.F., 2008. Cochlear implants: a remarkable past and a brilliant future. *Hearing research*, 242(1-2), pp.3-21.

[34] Weiss, P., 1934. In vitro experiments on the factors determining the course of the outgrowing nerve fiber. *Journal of Experimental Zoology*, 68(3), pp.393-448.

[35] Harrison, R.G., 1912. The cultivation of tissues in extraneous media as a method of morphogenetic study. *The Anatomical Record*, 6, pp.181–193. doi: 10.1002/ar.1090060404.

[36] Weiss, P., 1947. The problem of specificity in growth and development. *The Yale journal of biology and medicine*, 19(3), p.235.

[37] Curtis, A.S.G. and Varde, M., 1964. Control of cell behavior: topological factors. *Journal of the National Cancer Institute*, 33(1), pp.15-26.

[38] Lutolf, M.P. and Hubbell, J.A., 2005. Synthetic biomaterials as instructive extracellular microenvironments for morphogenesis in tissue engineering. *Nature biotechnology*, 23(1), pp.47-55.

[39] Bettinger, C.J., Langer, R. and Borenstein, J.T., 2009. Engineering substrate topography at the micro-and nanoscale to control cell function. *Angewandte Chemie International Edition*, 48(30), pp.5406-5415.

[40] Hoffman-Kim, D., Mitchel, J.A. and Bellamkonda, R.V., 2010. Topography, cell response, and nerve regeneration. *Annual review of biomedical engineering*, 12(1), pp.203-231.

- [41] Nguyen, A.T., Sathe, S.R. and Yim, E.K., 2016. From nano to micro: topographical scale and its impact on cell adhesion, morphology and contact guidance. *Journal of Physics: Condensed Matter*, 28(18), p.183001.
- [42] Webb, A., Clark, P., Skepper, J., Compston, A. and Wood, A., 1995. Guidance of oligodendrocytes and their progenitors by substratum topography. *Journal of cell science*, 108(8), pp.2747-2760.
- [43] Fozdar, D.Y., Lee, J.Y., Schmidt, C.E. and Chen, S., 2010. Hippocampal neurons respond uniquely to topographies of various sizes and shapes. *Biofabrication*, 2(3), p.035005.
- [44] Ferrari, A., Cecchini, M., Dhawan, A., Micera, S., Tonazzini, I., Stabile, R., Pisignano, D. and Beltram, F., 2011. Nanotopographic control of neuronal polarity. *Nano letters*, 11(2), pp.505-511.
- [45] Seo, J., Kim, J., Joo, S., Choi, J.Y., Kang, K., Cho, W.K. and Choi, I.S., 2018. Nanotopography-Promoted Formation of Axon Collateral Branches of Hippocampal Neurons. *Small*, 14(33), p.1801763.
- [46] Leclech, C., Renner, M., Villard, C. and Métin, C., 2019. Topographical cues control the morphology and dynamics of migrating cortical interneurons. *Biomaterials*, 214, p.119194.
- [47] Dowell-Mesfin, N.M., Abdul-Karim, M.A., Turner, A.M.P., Schanz, S., Craighead, H.G., Roysam, B., Turner, J.N. and Shain, W., 2004. Topographically modified surfaces affect orientation and growth of hippocampal neurons. *Journal of neural engineering*, 1(2), p.78.
- [48] Kundu, A., Micholt, L., Friedrich, S., Rand, D.R., Bartic, C., Braeken, D. and Levchenko, A., 2013. Superimposed topographic and chemical cues synergistically guide neurite outgrowth. *Lab on a Chip*, 13(15), pp.3070-3081.
- [49] Johansson, F., Carlberg, P., Danielsen, N., Montelius, L. and Kanje, M., 2006. Axonal outgrowth on nano-imprinted patterns. *Biomaterials*, 27(8), pp.1251-1258.
- [50] Bugnicourt, G., Brocard, J., Nicolas, A. and Villard, C., 2014. Nanoscale surface topography reshapes neuronal growth in culture. *Langmuir*, 30(15), pp.4441-4449.

- [51] Park, M., Oh, E., Seo, J., Kim, M.H., Cho, H., Choi, J.Y., Lee, H. and Choi, I.S., 2016. Control over neurite directionality and neurite elongation on anisotropic micropillar arrays. *Small*, 12(9), pp.1148–1152. doi: 10.1002/sml.201501896.
- [52] Chua, J.S., Chng, C.P., Moe, A.A.K., Tann, J.Y., Goh, E.L., Chiam, K.H. and Yim, E.K., 2014. Extending neurites sense the depth of the underlying topography during neuronal differentiation and contact guidance. *Biomaterials*, 35(27), pp.7750-7761.
- [53] Micholt, L., Gärtner, A., Prodanov, D., Braeken, D., Dotti, C.G. and Bartic, C., 2013. Substrate topography determines neuronal polarization and growth in vitro. *PloS one*, 8(6), p.e66170.
- [54] Mattotti, M., Micholt, L., Braeken, D. and Kovačić, D., 2015. Characterization of spiral ganglion neurons cultured on silicon micro-pillar substrates for new auditory neuro-electronic interfaces. *Journal of neural engineering*, 12(2), p.026001.
- [55] Radotić, V., Braeken, D., Drviš, P., Mattotti, M. and Kovačić, D., 2018. Advantageous environment of micro-patterned, high-density complementary metal–oxide–semiconductor electrode array for spiral ganglion neurons cultured in vitro. *Scientific reports*, 8(1), p.7446.
- [56] Radotić, V., Bedalov, A., Drviš, P., Braeken, D. and Kovačić, D., 2019. Guided growth with aligned neurites in adult spiral ganglion neurons cultured in vitro on silicon micro-pillar substrates. *Journal of neural engineering*, 16(6), p.066037.
- [57] McCaig, C.D., Rajnicek, A.M., Song, B. and Zhao, M., 2005. Controlling cell behavior electrically: current views and future potential. *Physiological Reviews*, 85(3), pp.943–978.
- [58] Patel, N.B. and Poo, M.M., 1984. Perturbation of the direction of neurite growth by pulsed and focal electric fields. *Journal of Neuroscience*, 4(12), pp.2939-2947.
- [59] Nishimura, K.Y., Isseroff, R.R. and Nuccitelli, R., 1996. Human keratinocytes migrate to the negative pole in direct current electric fields comparable to those measured in mammalian wounds. *Journal of cell science*, 109(1), pp.199-207.
- [60] Araki, S., Kawano, A., Seldon, H.L., Shepherd, R.K., Funasaka, S. and Clark, G.M., 1998. Effects of chronic electrical stimulation on spiral ganglion neuron survival and size in deafened kittens. *The laryngoscope*, 108(5), pp.687-695.

- [61] Brushart, T.M., Jari, R., Verge, V., Rohde, C. and Gordon, T., 2005. Electrical stimulation restores the specificity of sensory axon regeneration. *Experimental neurology*, 194(1), pp.221-229.
- [62] Yao, L., Pandit, A., Yao, S. and McCaig, C.D., 2011. Electric field-guided neuron migration: a novel approach in neurogenesis. *Tissue Engineering Part B: Reviews*, 17(3), pp.143-153.
- [63] Yao, L., Shanley, L., McCaig, C. and Zhao, M., 2008. Small applied electric fields guide migration of hippocampal neurons. *Journal of cellular physiology*, 216(2), pp.527-535.
- [64] Ye, H. and Steiger, A., 2015. Neuron matters: electric activation of neuronal tissue is dependent on the interaction between the neuron and the electric field. *Journal of neuroengineering and rehabilitation*, 12(1), p.65.
- [65] Li, S., Li, H. and Wang, Z., 2010. Orientation of spiral ganglion neurite extension in electrical fields of charge-balanced biphasic pulses and direct current in vitro. *Hearing research*, 267(1-2), pp.111-118.
- [66] Scanziani, M. and Häusser, M., 2009. Electrophysiology in the age of light. *Nature*, 461(7266), pp.930-939.
- [67] Vogt, A.K., 2003. Synaptic connectivity in micropatterned networks of neuronal cells. Doctoral dissertation. Max Planck Institute for Polymer Research, Max Planck Society.
- [68] Spira, M.E. and Hai, A., 2013. Multi-electrode array technologies for neuroscience and cardiology. *Nature Nanotechnology*, 8(2), pp.83–94. doi: 10.1038/nnano.2012.265.
- [69] Buzsáki, G., Anastassiou, C.A. and Koch, C., 2012. The origin of extracellular fields and currents—EEG, ECoG, LFP and spikes. *Nature reviews neuroscience*, 13(6), pp.407-420.
- [70] Thomas Jr, C.A., Springer, P.A., Loeb, G.E., Berwald-Netter, Y. and Okun, L.M., 1972. A miniature microelectrode array to monitor the bioelectric activity of cultured cells. *Experimental cell research*, 74(1), pp.61-66.
- [71] Gross, G.W., Rhoades, B.K., Azzazy, H.M. and Wu, M.C., 1995. The use of neuronal networks on multielectrode arrays as biosensors. *Biosensors and Bioelectronics*, 10(6-7), pp.553-567.

- [72] Liu, Y., Xu, S., Yang, Y., Zhang, K., He, E., Liang, W., Luo, J., Wu, Y. and Cai, X., 2023. Nanomaterial-based microelectrode arrays for in vitro bidirectional brain–computer interfaces: a review. *Microsystems & Nanoengineering*, 9(1), p.13.
- [73] Cerina, M., Piastra, M.C. and Frega, M., 2023. The potential of in vitro neuronal networks cultured on micro electrode arrays for biomedical research. *Progress in Biomedical Engineering*, 5(3), p.032002.
- [74] Frey, U., Sedivy, J., Heer, F., Pedron, R., Ballini, M., Mueller, J., Bakkum, D., Hafizovic, S., Faraci, F.D., Greve, F. and Kirstein, K.U., 2010. Switch-matrix-based high-density microelectrode array in CMOS technology. *IEEE Journal of Solid-State Circuits*, 45(2), pp.467-482.
- [75] Radivojevic, M., Jäckel, D., Altermatt, M., Müller, J., Viswam, V., Hierlemann, A. and Bakkum, D.J., 2016. Electrical identification and selective microstimulation of neuronal compartments based on features of extracellular action potentials. *Scientific reports*, 6(1), p.31332.
- [76] Ronchi, S., Fiscella, M., Marchetti, C., Viswam, V., Müller, J., Frey, U. and Hierlemann, A., 2019. Single-cell electrical stimulation using CMOS-based high-density microelectrode arrays. *Frontiers in neuroscience*, 13, p.208.
- [77] Hahnewald, S., Roccio, M., Tschertner, A., Streit, J., Ambett, R. and Senn, P., 2016. Spiral ganglion neuron explant culture and electrophysiology on multi electrode arrays. *Journal of Visualized Experiments: JoVE*, (116), p.54538.
- [78] Senn, P., Roccio, M., Hahnewald, S., Frick, C., Kwiatkowska, M., Ishikawa, M., Bako, P., Li, H., Edin, F., Liu, W. and Rask-Andersen, H., 2017. NANOCI—nanotechnology based cochlear implant with gapless interface to auditory neurons. *Otology & Neurotology*, 38(8), pp.e224–e231. doi: 10.1097/MAO.0000000000001439.
- [79] Huys, R., 2011. CMOS microelectrode arrays for neurophysiological applications: design, processing and characterization of a CMOS-chip for single-cell neuronal interfacing. Doctoral dissertation. KU Leuven, Faculty of Engineering, Arenberg Doctoral School of Science, Engineering and Technology, Leuven, Belgium.

- [80] Radotić, V., 2023. Morphological and electrophysiological characterization of spiral ganglion neurons cultured in vitro on high-density complementary semiconductor electrode array. Doctoral dissertation. University of Split, School of Medicine.
- [81] Borić, T., 2022. Morphological characterization of spiral ganglion neurons grown in the pulsating electromagnetic field. Master's thesis. University of Split, Faculty of Science, Department of Physics.
- [82] Delipetar, B., Borić, T., Žarković, J., Radotić, V., Bedalov, A. and Kovačić, D., 2024. Electromagnetic field-induced electrotaxis as a mechanism for reducing the neuroanatomical gap in cochlear implants. In: 2024 9th International Conference on Smart and Sustainable Technologies (SpliTech). IEEE, pp.1–5. doi: 10.23919/splitech61897.2024.10612394.
- [83] Delipetar, B., Žarković Krolo, J., Bedalov, A. and Kovačić, D., 2025. A neuroelectronic interface with microstructured substrates for spiral ganglion neurons cultured in vitro: proof of concept. *Biosensors*, 15(4), article no. 224. doi: 10.3390/bios15040224.
- [84] Intan Technologies, LLC, 2024. Intan Stimulation/Recording Controller User Guide: RHS2000 Intan 128ch Stimulation/Recording Controller. Updated 11 December 2024. Available at: https://intantech.com/files/Intan_Stim_Recording_Controller_user_guide.pdf, accessed: 16 April 2025.
- [85] Intan Technologies, LLC, 2021. RHS Stim SPI Interface Cable/Connector Specification. Updated 13 May 2021. Available at: https://intantech.com/files/Intan_RHS2000_Stim_SPI_cable.pdf, accessed: 16 April 2025.
- [86] TPT Wire Bonder, 2016. HB02/04/05 Wire Bonder – Operation Manual. Version 2.7, 24 November.
- [87] Griffiths, D.J., 2023. Introduction to electrodynamics. Cambridge University Press.
- [88] Szabó, Z., Harasztosi, C., Szûcs, G., Sziklai, I. and Rusznák, Z., 2003. A detailed procedure and dissection guide for the isolation of spiral ganglion cells of the guinea pig for electrophysiological experiments. *Brain research protocols*, 10(3), pp.139-147.

- [89] Vieira, M., Christensen, B.L., Wheeler, B.C., Feng, A.S. and Kollmar, R., 2007. Survival and stimulation of neurite outgrowth in a serum-free culture of spiral ganglion neurons from adult mice. *Hearing research*, 230(1-2), pp.17-23.
- [90] Mattotti, M., Alvarez, Z., Ortega, J.A., Planell, J.A., Engel, E. and Alcántara, S., 2012. Inducing functional radial glia-like progenitors from cortical astrocyte cultures using micropatterned PMMA. *Biomaterials*, 33(6), pp.1759-1770.
- [91] Euteneuer, S., Yang, K.H., Chavez, E., Leichtle, A., Loers, G., Olshansky, A., Pak, K., Schachner, M. and Ryan, A.F., 2013. Glial cell line-derived neurotrophic factor (GDNF) induces neuritogenesis in the cochlear spiral ganglion via neural cell adhesion molecule (NCAM). *Molecular and Cellular Neuroscience*, 54, pp.30-43.
- [92] Tukey, J.W., 1977. Exploratory data analysis (Vol. 2, pp. 131-160). Reading, MA: Addison-wesley.
- [93] Cliff, N., 1993. Dominance statistics: Ordinal analyses to answer ordinal questions. *Psychological bulletin*, 114(3), p.494. doi: 10.1037/0033-2909.114.3.494.
- [94] Vargha, A. and Delaney, H.D., 2000. A critique and improvement of the CL common language effect size statistics of McGraw and Wong. *Journal of Educational and Behavioral Statistics*, 25(2), pp.101-132. doi: 10.3102/10769986025002101.
- [95] Mann, H.B. and Whitney, D.R., 1947. On a test of whether one of two random variables is stochastically larger than the other. *The annals of mathematical statistics*, pp.50-60. doi: 10.1214/aoms/1177730491.
- [96] Good, P., 2005. Permutation, parametric and bootstrap tests of hypotheses. New York, NY: Springer New York.
- [97] Montgomery, D.C., 2017. Design and analysis of experiments. John wiley & sons.
- [98] Delipetar, B., Weber, I. and Kovačić, D., 2026. SEM/EDS characterisation of MEA substrates with 3D microtopography: composition uniformity metrics and salt-residue coverage. *Transactions of FAMENA*, 50(2), pp.73–86. doi: 10.21278/TOF.502086326.

CURRICULUM VITAE

Boris Delipetar was born on 15 June 1994 in Split, Republic of Croatia. After completing his primary education at Manuš Primary School and his secondary education at the Third Gymnasium in Split, he enrolled in the undergraduate university study programme in Industrial Engineering at the Faculty of Electrical Engineering, Mechanical Engineering and Naval Architecture, University of Split, in 2013. At the same Faculty, in 2018, he defended his master's thesis entitled "Introducing Rationalization into a Production System Using Lean Tools", under the supervision of Prof. Ivica Veža, PhD, and obtained the academic title of Master of Engineering in Industrial Engineering. From December 2018 to March 2023, he was employed as a research assistant at the Department of Physics, Faculty of Science, University of Split, within the STIM-REI project of the Center of Excellence for Science and Technology – Integration of Mediterranean Region (STIM), University of Split, under the project activity "The design and application of new nanostructured materials in neuro-electronic interfaces for biomedical application", led by Associate Professor Damir Kovačić, PhD. During this period, his doctoral research was funded through the Croatian Science Foundation programme "Young Researchers' Career Development Project – Training New Doctoral Students" (DOK-01-2018), financed by the European Social Fund. From June 2023 to February 2024, he was employed as a research assistant at the University of Split within the same project. From July 2025 to April 2026, he was employed as an assistant at the Department of Production Engineering, Faculty of Electrical Engineering, Mechanical Engineering and Naval Architecture, University of Split. As an assistant, he participated in teaching activities in the courses Computer-Aided Manufacturing, Machine Tools, Machine Tools and Systems, Fundamentals of CNC Programming, CNC Machine Programming, and Technology 2. Since May 2026, he has been employed at the Faculty of Electrical Engineering, Mechanical Engineering and Naval Architecture, University of Split, as a researcher on the project "ReforestTech – Enhancement of research and development capacities for globally competitive, green, and innovative technologies and services". He enrolled in the postgraduate university doctoral study programme in Mechanical Engineering at the Faculty of Electrical Engineering, Mechanical Engineering and Naval Architecture, University of Split, in 2019, under the supervision of Professor Frano Barbir, PhD, and Associate Professor Damir Kovačić, PhD.

ŽIVOTOPIS

Boris Delipetar rođen je 15. lipnja 1994. godine u Splitu, u Republici Hrvatskoj. Nakon završenoga osnovnoškolskog obrazovanja u Osnovnoj školi Manuš te srednjoškolskog obrazovanja u III. gimnaziji u Splitu, 2013. godine upisao je preddiplomski sveučilišni studij Industrijskog inženjerstva na Fakultetu elektrotehnike, strojarstva i brodogradnje Sveučilišta u Splitu. Na istom je fakultetu 2018. godine obranio diplomski rad pod naslovom „Uvođenje racionalizacija u proizvodni sustav s lean alatima”, pod mentorstvom prof. dr. sc. Ivice Veže, te stekao akademski naziv magistar inženjer industrijskog inženjerstva. Od prosinca 2018. godine do ožujka 2023. godine bio je zaposlen na Odjelu za fiziku Prirodoslovno-matematičkog fakulteta Sveučilišta u Splitu kao asistent na projektu „Znanstveni centar izvrsnosti za znanost i tehnologiju – integracija Mediteranske regije STIM-REI“ Sveučilišta u Splitu, u okviru projektne aktivnosti „Dizajn i primjena novih nanostrukturnih materijala u neuroelektroničkim sučeljima za biomedicinsku primjenu“, pod vodstvom izv. prof. dr. sc. Damira Kovačića, pri čemu je njegovo doktorsko istraživanje bilo financirano putem programa Hrvatske zaklade za znanost „Projekt razvoja karijera mladih istraživača – izobrazba novih doktora znanosti” (DOK-01-2018), financiranog iz Europskog socijalnog fonda. Od lipnja 2023. godine do veljače 2024. godine bio je zaposlen kao asistent na Sveučilištu u Splitu u sklopu istog projekta. Od srpnja 2025. godine do travnja 2026. godine bio je zaposlen kao asistent na Zavodu za proizvodno strojarstvo Fakulteta elektrotehnike, strojarstva i brodogradnje Sveučilišta u Splitu. Kao asistent sudjelovao je u održavanju nastave na kolegijima Proizvodnja podržana računalom, Obradni strojevi, Obradni strojevi i sustavi, Osnove CNC programiranja, Programiranje CNC strojeva i Tehnologija 2. Od svibnja 2026. godine zaposlen je na Fakultetu elektrotehnike, strojarstva i brodogradnje Sveučilišta u Splitu kao istraživač na projektu „ReforestTech – Unaprjeđenje istraživačko-razvojnih kapaciteta za globalno konkurentne, zelene i inovativne tehnologije i usluge“. Poslijediplomski sveučilišni studij Strojdarstva na Fakultetu elektrotehnike, strojarstva i brodogradnje Sveučilišta u Splitu upisao je 2019. godine pod mentorstvom prof. dr. sc. Frane Barbira i izv. prof. dr. sc. Damira Kovačića.